Norwegian University of Life Sciences
Faculty of Science and Technology

Philosophiae Doctor (PhD)
Thesis 2019:80

Sea level, ocean currents, and vertical land motion along the Norwegian coast

Havnivå, havstrømmer og vertikal landhevning langs Norskekysten

Martina Idžanović

Sea level, ocean currents, and vertical land motion along the Norwegian coast

Havnivå, havstrømmer og vertikal landhevning langs Norskekysten

Philosophiae Doctor (PhD) Thesis

Martina Idžanović

Norwegian University of Life Sciences
Faculty of Science and Technology

Ås (2019)

Thesis number 2019:80
ISSN 1894-6402
ISBN 978-82-575-1641-3

Supervision team

Main supervisor
Prof. Bjørn Ragnvald Pettersen
Faculty of Science and Technology (RealTek),
Norwegian University of Life Sciences (NMBU),
Ås, Norway

Co-supervisor
Dr. Christian Gerlach [1]
Geodesy and Glaciology,
Bavarian Academy of Sciences and Humanities (BAdW),
Munich, Germany

Co-supervisor
Prof. Ole Baltazar Andersen
National Space Institute, DTU Space
Technical University of Denmark (DTU),
Kgs. Lyngby, Denmark

Co-supervisor
Kristian Breili [1], PhD
Geodetic Institute,
Norwegian Mapping Authority (NMA),
Hønefoss, Norway

Evaluation Committee

First opponent
Prof. Per Knudsen
National Space Institute, DTU Space
Technical University of Denmark (DTU),
Kgs. Lyngby, Denmark

Second opponent
Dr. Luciana Fenoglio-Marc
Institute of Geodesy and Geoinformation,
University of Bonn,
Bonn, Germany

Committee coordinator
Prof. Cecilie Rolstad Denby
Faculty of Science and Technology (RealTek),
Norwegian University of Life Sciences (NMBU),
Ås, Norway

[1] Adjunct assoc. prof. at the Faculty of Science and Technology (RealTek), Norwegian University of Life Sciences (NMBU), Ås, Norway

Summary

Ocean circulation plays a fundamental role in climate and sea-level related studies due to the ocean's large heat-storage and transport capacity. Ocean circulation can be derived from numerical ocean models, which might be driven by various sets of observations, such as wind fields or water salinity and temperature. One of the most important ocean-observing systems is satellite altimetry, which allows to construct maps of the mean sea surface (MSS). The ocean's mean dynamic topography (MDT) is the height of MSS above the geoid and its inclination reveals magnitude and direction of ocean currents. A detailed picture of the marine geoid in combination with an altimetry derived MSS leads to an increased understanding of ocean circulation. The application of satellite altimetry is mostly limited to the open or deep ocean because of its peculiarities close to the coast. The presence of land in altimetric footprints makes the retrieval of radar echos difficult. Also, tidal models used to correct altimetric observations are degraded along the continental shelf border and in the coastal zone. However, coastal zones have gained increased interest in recent years by cause of their high relevance to society considering sea-level rise, shipping, and other off-shore activities. Thus, there are increased efforts in coastal altimetry, and its applicability to monitor the coastal environment was identified. The application of satellite altimetry in coastal zones has become possible, among others, due to the European Space Agency's CryoSat-2 (CS2) satellite. CS2 carries a radar altimeter, which enables the determination of coastal MDT due to its smaller footprint and delay-Doppler processing.

Precise monitoring of sea-level changes is essentially important for understanding not only climate but also social and economic aspects of sea-level rise, especially in coastal zones. Coastal cities are built upon the Earth's crust, which can be subject to uplift or subsidence. Today, vertical land motion (VLM) rates in Fennoscandia reach values of up to ~10 mm/year and are dominated by glacial isostatic adjustment (GIA), while additional signals caused, e.g., by the elastic rebound from contemporary melting of glaciers, tectonic processes or hydrological loading contribute less. GIA is the ongoing response of the Earth and oceans to the melting of late-Pleistocene ice sheets. The unloading initiated an uplift of the crust close to the centers of former ice sheets. This phenomenon affects the national height systems directly as well as observations of regional sea level and its temporal changes as measured by tide gauges along the coast.

The thesis consist of two major blocks, namely, satellite altimetry and GIA. The first part of the thesis investigates the possibilities of CS2 SAR(In) altimetry to provide observations in the Norwegian coastal zone and ad-

dresses the determination and quality assessment of the coastal MDT. The second part comprises the quantification of the Earth's response to melting of late-Pleistocene ice sheets by either modelling (i.e., solving the sea-level equation) or combining sea-surface measurements from CS2 and sea-level records from tide gauges.

It is shown that CS2 is able to provide valid observations in Norwegian coastal areas that were previously not monitored by conventional altimetry. CS2 sea-level anomalies within 45 km×45 km boxes were compared with in situ sea level at 22 tide gauges. Over all tide gauges, CS2 shows a standard deviation of differences of 16 cm with a correlation of 0.61. Ocean-tide and inverse barometer geophysical corrections were identified as most crucial, and it was noted that a large amount of observations at land-confined tide gauges were not assigned an ocean-tide value. Due to the availability of local air-pressure observations and ocean-tide predictions, the standard inverse barometer and ocean-tide corrections were replaced with local ones. The refined corrections give an improvement of 24% (to 12.2 cm) and 12% (to 0.68) in terms of standard deviations of difference and correlations, respectively.

Using new regional geoid models as well as CS2, three geodetic coastal MDT models in Norway were determined and validated against independent tide-gauge measurements as well as the operational coastal ocean model NorKyst800. The CS2 MDT models agree on a ~3-5 cm level with both tide-gauge and ocean MDT models. In addition, geostrophic surface currents were computed in order to identify errors in the used geoid models. Even though the regional geoids are all based on the latest satellite gravity data provided by GOCE (Gravity field and steady-state Ocean Circulation Explorer), the resulting circulation patterns are dependent upon geoids they were based on. It is demonstrated that some of these differences are due to erroneous or lack of marine gravity data. In addition, the coincidence of the CS2 geographical mode mask with the Norwegian Coastal Current makes it challenging to distinguish between artifacts in CS2 observations that arise during mode switches and real ocean signal.

Using ice histories from the ICE-x series (ICE-5G and ICE6G_C) along with related Earth models (VMx), vertical velocity fields as well as time series of relative sea level (RSL) change were predicted. Computations were performed with the open-source sea-level equation solver (SELEN) and validated against external data, i.e., the semi-empirical land-uplift model NKG2016LU_abs and geological RSL reconstructions. In addition, SELEN solutions were compared with published grids of vertical velocities derived by other authors in order to quantify the significance of software's assumptions and approximations. In general, all software solutions agree on a ~1 mm/year level with NKG2016LU_abs in terms of standard deviations of differences. In view of ice models, all uplift rates as well as RSL predictions calculated with ICE6G_C show a considerably better fit to NKG2016LU_abs and RSL data than model results of ICE-5G, which confirms an improvement within the ICE-x series. For both ice models, predictions of present-day vertical velocity fields based on VMx rheologies agree better with observations than predictions based on NKG rheologies. On the other hand, predictions with NKG rheologies fit better RSL data than predictions with VMx rheologies.

Applying a well known method for the determination of VLM by combining satellite altimetry and tide-gauge observations, for the first time, CS2 data (within 45 km×45 km boxes) were used for this purpose, bridging thereby the two major thesis' blocks. Hence, 7.5 years of CS2 and tide-gauge data were combined to estimate linear VLM trends at 20 tide gauges along the Norwegian coast. Monthly-averaged tide-gauge data from PSMSL (Permanent Service for Mean Sea Level) and a high-frequency tide-gauge data set with 10-minute sampling rate from NMA (Norwegian Mapping Authority) were used. Estimated VLM rates from 1 Hz CS2 and high-frequency tide-gauge data reflect well the amplitude of coastal VLM as provided by NKG2016LU_abs. A coastal average of 2.4 mm/year (average over all tide gauges) was found, while NKG2016LU_abs suggests 2.8 mm/year; the spatial correlation is 0.58.

Sammendrag

Havstrømmer spiller en grunnleggende rolle i klima- og havnivårelaterte studier på grunn av havets transportevne og store varmekapasitet. Havstrømmer kan avledes fra numeriske havmodeller basert på ulike observasjoner, så som vindfelt eller vannets saltinnhold og temperatur. Satellittaltimetri er en av de viktigste observasjonssystemene for å konstruere den geografiske fordelingen av midlere havnivå (MSS - mean sea surface). Havets midlere dynamiske topografi (MDT - mean dynamic topography) er høyden til MSS over geoiden. MSS-flatens helning i forhold til geoiden avgjør havstrømmenes styrke og retning. Et detaljert bilde av den marine geoiden kombinert med MSS avledet fra altimetri-observasjoner fører til en bedret forståelse av havstrømmene. Satellittaltimetri kan anvendes direkte over åpent dyphav, men må underkastes spesiell oppmerksomhet for data nær kysten. Radarekko fra hav og land samtidig gjør tolkningen av observasjonene vanskelig. Altimetrihøyder må korrigeres for tidevannseffekter og nær kontinentalsokler og kystsoner er modellene for tidevannsberegning mer usikre. Kystsoner fått økt oppmerksom i de senere år på grunn av den samfunnsmessige betydning for befolkning, skipsfart og off-shore virksomheter, som vil bli påvirket av endringer i havnivået. Følgelig har det vært økende aktivitet innen kystsonealtimetri med påvisning av metodens anvendelse for overvåking av kystmiljøet. Dette har særlig utviklet seg med den europeiske romfartsorganisasjonen ESAs CryoSat-2 (CS2) satellitt. CS2 har et radar-altimeter som gjør det mulig å bestemme MDT nær kysten fordi instrumentet har mindre fotavtrykk enn tidligere versjoner og ved å benytte forsinket-Doppler-prosessering av dataene.

Presis overvåking av havnivåets endringer er avgjørende viktig for å forstå ikke bare klimavariasjoner, men også samfunnsmessige og økonomiske konsekvenser av havnivåøkning, spesielt i kystsoner. Byer i kystsonen er bygget på jordklodens faste overflate, og den kan være underkastet både landhevning og innsynkning. I dag er den vertikale bevegelsen i Fennoskandia opptil ~10 mm/år og domineres av postglasial isostatisk landhevning (GIA - glacial isostatic adjustment). I tillegg er det mindre bidrag fra jordoverflatens elastiske respons forårsaket av dagens nedsmelting av isbreer, tektoniske prosesser og belastninger fra hydrologiske prosesser. GIA er jordoverflatens og havets langsomme respons på nedsmeltingen av store iskapper i sen-Pleistocene, etter siste istid. Avtagende belastning fra disse massene forårsaket en landhevning av jordoverflaten der iskappen var. Dette fenomenet påvirker nasjonale høydesystemer direkte. Observasjoner med tidevannsmålere langs kysten av regionalt havnivå og dets forandringer påvirkes også når landet hever seg med tiden.

Denne doktoravhandlingen har to hovedtemaer, nemlig satellittaltimetri og GIA. I den første delen undersøkes mulighetene for å utnytte CS2 SAR(In) interferometriske altimetri-observasjoner til bestemmelse av MDT i den norske kystsonen med kvalitetsvurderinger av resultatet. I den andre delen kvantifiseres jordoverflatens respons på avsmelting av iskapper etter siste istid, både ved modellering (dvs. løsning av havnivåligningen) og ved kombinasjon av havnivåmålinger fra CS2 satellitten og fra tidevannsmålere langs kysten.

Vi viser at CS2 bidrar med observasjoner av den norske kystsonen i områder som tidligere ikke kunne observeres med konvensjonell altimetri fra andre satellitter. Havnivå-anomalier innenfor kvadrater på 45 km×45 km avledet fra CS2 data ble sammenlignet med in situ havnivå bestemt ved 22 tidevannsmålere. Forskjellene har et standard avvik på 16 cm med en korrelasjon på 0.61. Korreksjoner for tidevannsvariasjoner og geofysiske invers barometer effekter ble identifisert som helt nødvendige for resultatet. Mange observasjonsserier på tidevannsstasjoner inne i fjorder hadde ikke tilordnede tidevannsverdier. Siden både lokalt lufttrykk og tidevannsprediksjoner var tilgjengelig, ble disse benyttet i stedet for standardmodeller for invers barometer og tidevannskorreksjoner. Det førte til en forbedring på 24% (til 12.2 cm) i standardavviket og 12% (til 0.68) i korrelasjon.

Vi benyttet tre nye regionale geoidemodeller sammen med data fra CS2 til å bestemme tre geodetiske MDT-modeller for den norske kystsonen. De ble validert mot både uavhengige tidevannsmålinger og den operasjonelle havmodellen NorKyst800. MDT-modellene overensstemmer innenfor 3-5 cm med både tidevannsmålinger og havmodell. Vi beregnet også geostrofiske overflatestrømmer i et forsøk på å identifisere feil i de anvendte geoidemodellene. Selv om alle de regionale geoidemodellene er basert på de siste gravitasjonsdataene fra GOCE-satellitten, så avhenger de beregnede strømningsmønstrene av de enkelte geoidemodellene. Vi viser at noen av forskjellene skyldes feilaktige eller mangelfulle marine tyngdedata. Dessuten har CS2 en geografisk modemaskering som faller sammen med den norske kyststrømmen. Det gjør det vanskelig å skille mellom havsignalet og særegenheter i CS2 dataene når satellitten foretar mode-endringer.

Vi benyttet tidsforløpene i ICE-x modellene (ICE-5G og ICE6G_C) sammen med geofysiske jordmodeller (VMx) til å beregne vertikale hastighetsfelt og tidsserier for relativt havnivå. Beregningene ble gjort ved hjelp av tilgjengelig (open-source) programvare til løsning av havnivåligningen (SELEN) og ble validert mot eksterne data, nemlig den semi-empiriske landhevningsmodellen NKG2016LU_abs og geologiske rekonstruksjoner av relativt havnivå. SELEN-løsningene ble også sammenlignet med vertikale hastigheter publisert av andre forfattere (som benyttet annen programvare) i et forsøk på å kvantifisere betydningen av de antagelser og tilnærminger som programvaren var bygget på. Forskjellen fra våre løsninger overensstemmer innenfor et standardavvik på ~1 mm/år med vertikalhastighetene i NKG2016LU_abs. Ismodellen ICE6G_C gir vertikale hastigheter og havnivåforløp som overensstemmer mye bedre med NKG2016LU_abs og dataserier for relative havnivåendringer enn den tidligere modellen ICE-5G. Det antyder en mer treffende beskrivelse av ishistorien. Prediksjoner av dagens vertikale hastighetsfelt basert på VMx-rheologier og ismodellene gir bedre overensstemmelse med observasjonene enn med rheologiene benyttet i NKG-modellen. Derimot gir prediksjoner av relativt havnivå bedre overensstemmelse med NKG-rheologier enn med VMx-rheologier.

Med utgangspunkt i havnivåligningen har vi for første gang bestemt den vertikale landhevningen ved å kombinere data fra satellittaltimetri og tidevannsmålere. CS2 data (i 45 km × 45 km kvadrater) knytter dermed avhandlingens to temaer sammen. Til sammen 7.5 år med CS2 data ble kombinert med data fra 20 tidevannsmålere langs norskekysten for å estimere lineære trender for vertikale hastigheter. Tidevannsmålinger ble analysert som tidsserier av månedsmidler fra PSMSL (Permanent Service for Mean Sea Level) og som tidsserier med 10 minutter oppløsning fra Kartverket. De beregnede vertikale hastigheter fra 1 Hz CS2 og den høyfrekvente tidevannsserien gjenspeiler verdiene langs kysten i NKG2016LU_abs. Et gjennomsnitt for alle tidevannsmålerne er 2.4 mm/år, mens NKG2016LU_abs gir 2.8 mm/år; den romlige korrelasjonen er 0.58.

Zusammenfassung

Meeresströmungen spielen aufgrund ihrer großen Wärmespeicher- und Transportkapazität eine grundlegende Rolle bei Klima- und Meeresspiegelstudien. Sie können aus numerischen Ozeanmodellen abgeleitet werden, welche von verschiedenen Beobachtungsdaten getrieben werden, etwa Temperatur und Salzgehalt des Wassers oder Windfeldern. Eines der wichtigsten Ozeanbeobachtungssysteme ist die Satellitenaltimetrie die es erlaubt, die mittlere Meeresoberfläche (MSS - mean sea surface) nahezu global und flächendeckend zu bestimmen. Die mittlere dynamische Topographie (MDT - mean dynamic topography) des Ozeans ist die Höhe der MSS über dem Geoid und ihre Neigung gibt die Größe und Richtung der Meeresströmungen wieder. Ein detailliertes Bild des Geoids in Kombination mit einer von der Altimetrie abgeleiteten MSS führt zu einem besseren Verständnis der Meeresströmungen. In Küstennähe treten verschiedene Störeffekte auf, so dass die Anwendung der Satellitenaltimetrie auf den offenen und tiefen Ozean beschränkt ist. Radarsignale die zumindest teilweise von Landflächen reflektiert werden, sind stark deformiert und für eine präzise Laufzeitbestimmung meist unbrauchbar. Zusätzlich nimmt die Qualität geophysikalischer Reduktionen in Küstennähe ab, speziell Gezeitenreduktionen. Die Küstengebiete haben jedoch in den letzten Jahren aufgrund ihrer hohen gesellschaftlichen Relevanz im Hinblick auf Meeresspiegelanstieg, Schifffahrt und andere küstennahe Aktivitäten zunehmend an Interesse gewonnen. Demzufolge gab es verschiedene Initiativen, um die Qualität der Küstenaltimetrie zu erhöhen. Eine durchgreifende Wende gelang hier durch das neue Messkonzept des Satelliten CryoSat-2 (CS2) der Europäischen Weltraumorganisation ESA. CS2 ist mit einem neuartigen Radaraltimeter ausgestattet, welches aufgrund einer delay-Doppler Verarbeitung einen in Flugrichtung geringeren Footprint hat und das im SARIn-Modus zusätzlich erlaubt, fehlerhafte Rückstreuungen von Landflächen zu identifizieren. Damit ist es möglich die MDT in unmittelbarer Küstennähe zu bestimmen.

Die genaue Überwachung von Meeresspiegeländerungen ist von wesentlicher Bedeutung, um nicht nur die Klima-, sondern auch die sozialen und wirtschaftlichen Aspekte des Meeresspiegelanstiegs zu verstehen, insbesondere in Küstengebieten. Hierbei ist nicht der absolute Anstieg des Meeresspiegels von Interesse, sondern der Anstieg relativ zur festen Erde welche selbst von signifikanten Hebungen oder Senkungen betroffen sein kann. Heute erreichen die vertikalen Landhebungsraten in Fennoskandien Werte bis zu etwa 10 mm/Jahr, wobei der Hauptanteil auf den glazial-istostatischen Ausgleich (GIA - glacial isostatic adjustment) zurückgeführt werden kann. Zusätzliche Signale, die z.B. durch tektonische Prozesse oder

durch elastische Reaktionen auf zeitvariable Auflasten oder den aktuellen Rückzug heutiger Gletscher verursacht werden, liefern geringere Beiträge zur Landhebung in Fennoskandien. GIA bezeichnet die laufende Reaktion der Erde und der Ozeane auf das Schmelzen der pleistozänen Eisschilde. Dieses Phänomen wirkt sich direkt auf die nationalen Höhensysteme sowie auf die Beobachtung des regionalen Meeresspiegels und seiner zeitlichen Änderungen aus, die an Pegeln entlang der Küste gemessen werden.

Die Dissertation besteht aus zwei Hauptblöcken, der Nutzung der Satellitenaltimetrie in Küstennähe und der Modellierung von GIA-induzierten Hebungsraten der Küstenregionen. Der erste Teil der Dissertation untersucht das Potenzial von CS2 SAR(In) Beobachtungen entlang der norwegischen Küste zu liefern, und befasst sich mit der Bestimmung und Qualitätsanalyse der Küsten-MDT. Der zweite Teil umfasst die Quantifizierung der Reaktion der festen Erde auf das Abschmelzen spät-pleistozäner Eisschilde durch Modellierung (nämlich durch Lösung der Meeresspiegelgleichung) oder Messungen (Kombination absoluter Meeresspiegeländerungen aus CS2 mit relativen Meerespiegeländerungen an Pegelstationen).

Es wird gezeigt, dass CS2 zuverlässige Beobachtungen in norwegischen Küstengebieten liefern kann, welche mit konventionellen Altimetern nicht überwacht werden konnten. Meeresspiegelanomalien aus CS2 innerhalb von 45 km×45 km Boxen wurden mit Meeresspiegelbeobachtungen an 22 Pegeln verglichen. Über alle Pegel hinweg ergibt sich eine Standardabweichung der Differenzen von 16 cm mit einer Korrelation von 0.61. Dabei spielen geophysikalische Korrekturen für Gezeiten und Luftdruckeffekte eine entscheidende Rolle. So wurde in der Standardprozessierung einigen der in Fjorden gelegenen Messungen keine Gezeitenreduktion zugeordnet. Zur Verbesserung der Korrekturen wurden lokale Gezeitenprädiktionen und lokale Barometermessungen verwendet. Daraus ergibt sich eine Verbesserung von 24% (auf 12.2 cm) und 12% (auf 0.68) in Bezug auf Standardabweichungen der Differenzen bzw. Korrelationen.

Aus CS2 und drei aktuellen regionalen Geoidmodellen wurden drei unterschiedliche geodätische MDT-Modelle für die norwegische Küstenzone abgeleitet. Diese wurden punktuell gegenüber geodätischen Vergleichsdaten an Gezeitenpegeln und flächenhaft gegenüber dem operationellen Ozeanströmungsmodell NorKyst800 validiert. Die CS2 MDT-Modelle stimmen auf einem Niveau von etwa 3-5 cm sowohl mit Pegeldaten als auch der aus dem Ozeanmodell abgeleiteten MDT überein. Zusätzlich wurden geostrophische Oberflächenströmungen berechnet, um Fehler in den verwendeten Geoidmodellen zu identifizieren. Da alle drei Geoide auf den neuesten globalen GOCE-Schwerefeldmodellen basieren, sind für die Unterschiede in den Geoiden hauptsächlich die jeweils verwendeten regionalen

Schwerefelddaten verantwortlich. Es wird gezeigt, dass einige der Unterschiede in den Strömungsmustern auf fehlerhafte oder fehlende Schwerefelddaten zurückgeführt werden können. Darüber hinaus ergeben sich gerade im norwegischen Küstenbereich Schwierigkeiten, da CS2 hier zwischen verschiedenen Messmodi umschaltet, wodurch es zu Artefakten in den Altimetermessungen kommen kann, die vom geophysikalischen Ozeansignal zu unterscheiden sind.

Unter Verwendung von Eismodellen der ICE-x-Serie (nämlich ICE-5G und ICE6G_C) und den dazugehörigen Rheologieprofilen (VMx) wurden vertikale Geschwindigkeitsfelder und Zeitreihen der relativen Meeresspiegeländerung (RSL - relative sea level) für Fennoskandien berechnet. Hierfür wurde die Open-Source-Software SELEN (Sea Level Equation Solver) verwendet. Ergebnisse werden gegenüber dem semi-empirischen Landhebungsmodell NKG2016LU_abs und gegenüber geologischer Küstenlinienrekonstruktionen validiert. Um den Einfluss verschiedener Software-Annahmen und Näherungen zu quantifizieren, wurden SELEN Berechnungen mit publizierten Ergebnissen anderer Gruppen verglichen, die auf anderen Softwarelösungen beruhen. Im Allgemeinen stimmen alle Softwarelösungen auf einem Niveau von etwa 1 mm/Jahr (Standardabweichungen der Differenzen) mit den Vertikalgeschwindigkeiten aus NKG2016LU_abs überein. Es zeigt sich, dass alle mit ICE6G_C berechneten Vertikalgeschwindigkeitsfelder sowie RSL-Prädiktionen eine wesentlich bessere Übereinstimmung mit NKG2016LU_abs und RSL-Daten zeigen als Modelle, die auf ICE-5G basieren, was die Verbesserung der Eishistorien innerhalb der ICE-x Serie bestätigt. Für beide Eismodelle zeigt sich, dass die auf VMx-Rheologien basierenden vertikalen Geschwindigkeitsfelder besser zu den Beobachtungsdaten passen, als die auf den NKG-Rheologien basierenden. Anders verhält es sich bei den RSL-Prädiktionen, wo die Lösungen mit NKG-Rheologien besser abschneiden als diejenigen mit VMx-Rheologien.

Erstmals wurden CS2 Daten, unter Anwendung einer bekannten Methode zur Bestimmung der Landhebung durch Kombination von Satellitenaltimetrie und Pegelbeobachtungen genutzt. Dies ermöglicht gleichzeitig die Verbindung der beiden Hauptthemen dieser Arbeit, Altimetrie und Landhebung. Aus 7.5 Jahren CS2 Daten und Pegelbeobachtungen wurden an 20 Pegeln entlang der norwegischen Küste lineare Landhebungstrends geschätzt. Dabei wurden monatlich gemittelte Pegelmessungen von PSMSL (Permanent Service for Mean Sea Level) und ein hochfrequenter Pegeldatensatz mit einer Abtastrate von 10-Minuten von NMA (Norwegische Landesvermessungsbehörde) verwendet. Geschätzte Landhebungsraten aus 1 Hz CS2 und hochfrequenten Pegeldaten spiegeln die Amplitude der Küstenlandhebung aus NKG2016LU_abs gut wider. Es wurde ein Küstenmittelwert von 2.4 mm/Jahr (Mittelwert über alle Pegel) gefunden, während sich aus NKG2016LU_abs 2.8 mm/Jahr ergeben; die räumliche Korrelation beträgt 0.58.

Sažetak

Morske struje imaju ključnu ulogu u istraživanjima vezanim uz klimu i razinu mora zbog velikog kapaciteta oceana za skladištenje topline i transport. Morske struje moguće je izvesti iz numeričkih oceanskih modela, koji su temeljeni na različitim skupinama podataka, kao što su polja vjetrova ili salinitet i temperatura vode. Jedan od najvažnijih sustava za opažanje oceana je satelitska altimetrija, koja omogućava izračun površine srednje razine mora (MSS - mean sea surface). Srednja dinamička topografija (MDT - mean dynamic topography) oceana je visina MSS-a iznad geoida te nagib otkriva iznos i smjer morskih struja. Detaljna slika geoida u kombinaciji s MSS-om dobivenim iz altimetrije pridonosi boljem razumijevanju morskih struja. Primjena satelitske altimetrije uglavnom je ograničena na otvoreni ili duboki ocean zbog poteškoća u blizini obale. Prisutnost kopna u altimetrijskim otiscima otežava rekonstrukciju radarskih odjeka. Također su modeli morskih mijena koji se koriste za korigiranje altimetrijskih opažanja degradirani duž granice kontinentalnog pojasa i u priobalnom području. Priobalna područja su međutim zadobila povećani interes posljednjih godina zbog njihove iznimne važnosti za društvo u kontekstu porasta razine mora, brodarstva i drugih aktivnosti u blizini obale. Stoga su povećane aktivnosti u području priobalne altimetrije te je prepoznata njezina primjenjivost za praćenje priobalnih područja. Primjena satelitske altimetrije u priobalnim područjima postala je moguća između ostalog zahvaljujući satelitu Europske svemirske agencije CryoSat-2 (CS2). CS2 nosi poseban radarski altimetar koji omogućava određivanje priobalnog MDT-a zahvaljujući svom manjem altimetrijskom otisku i Dopplerovoj obradi mjerenja.

Precizno praćenje promjena razine mora osobito je važno za razumijevanje ne samo klimatskih već i socijalnih te ekonomskih aspekata porasta razine mora, posebno u priobalnim područjima. Priobalni gradovi su izgrađeni na površini Zemljine kore koja je podložna uzdizanju ili slijeganju. Iznosi vertikalnih pomaka kopna u Fenoskandiji danas dosežu vrijednosti od oko 10 mm/godina i dominirani su glacijalno izostatičkim izjednačenjem (GIA - glacial isostatic adjustment), dok dodatni signali uzrokovani npr. elastičnom reakcijom uslijed suvremenog topljenja ledenjaka, tektonskim procesima ili hidrološkim opterećenjima doprinose u manjoj mjeri. GIA je neprestana reakcija Zemlje i oceana na topljenje ledenih pokrova kasnog pleistocena. Topljenje ledenih površina iniciralo je uzdizanje Zemljine kore u blizini središta nekadašnjih ledenih pokrova. Ovaj fenomen izravno utječe na nacionalne visinske sustave kao i na opažanja regionalne razine mora i njezine vremenske promjene mjerene mareografima uzduž obale.

Ovaj doktorski rad sastoji se od dva osnovna bloka, odnosno satelitske altimetrije i GIA. Prvi dio doktorskog rada istražuje mogućnosti CS2 SAR(In) altimetrije za pružanje opažanja u norveškom priobalnom pojasu te se bavi određivanjem i procjenom kvalitete priobalnog MDT-a. Drugi dio obuhvaća kvantifikaciju Zemljine reakcije na topljenje ledenih pokrova kasnog pleistocena bilo modeliranjem (tj. rješavanjem jednadžbe razine mora) ili kombiniranjem mjerenja morske površine opažane sa CS2 i mjerenja razine mora opažanih mareografima.

Pokazano je da CS2 može pružiti važeća opažanja u norveškim priobalnim područjima koja prethodno nisu bila opažana konvencionalnom altimetrijom. CS2 anomalije razine mora unutar kvadrata veličine 45 km×45 km uspoređene su s mjerenjima razine mora na lokacijama 22 mareografa. U prosjeku, CS2 pokazuje standardno odstupanje razlika od 16 cm i korelaciju od 0.61. Geofizičke korekcije za morske mijene i inverzni barometar identificirane su kao najvažnije te je ustanovljeno kako velikoj količini mjerenja u blizini mareografa okruženih kopnom nije dodijeljena vrijednost modela morskih mijena. Uslijed dostupnosti lokalnih mjerenja tlaka zraka i projekcija morskih mijena, standardne korekcije za inverzni barometar i morske mijene zamijenjene su lokalnim korekcijama. Zamjena korekcija rezultirala je smanjenjem standardnih odstupanja razlika za 24% (na 12.2 cm) i povećanjem korelacija za 12% (na 0.68).

Pomoću novih regionalnih modela geoida kao i CS2, određena su tri geodetska priobalna MDT modela za Norvešku i uspoređena s neovisnim mareografskim mjerenjima te operativnim priobalnim oceanskim modelom NorKyst800. CS2 MDT modeli podudaraju se na razini od ~3-5 cm s mareografskim i oceanskim MDT modelima. Osim toga, izračunate su geostrofičke površinske struje u svrhu identificiranja pogrešaka u korištenim modelima geoida. Iako su regionalni geoidi temeljeni na najnovijim satelitskim podacima sile teže opažanim pomoću GOCE, rezultirajući uzorci morskih struja ovise o geoidima na kojima su temeljeni. Pokazalo se da su neke od tih razlika posljedica pogrešnih pomorskih podataka sile teže ili nedostatka istih. Uz to, podudaranje CS2 geografske maske s norveškom priobalnom strujom otežava razlikovanje između CS2 artefakata prilikom prebacivanja modusa i oceanskog signala.

Koristeći modele leda iz ICE-x serije (ICE-5G i ICE6G_C) zajedno s pripadajućim reologijama (VMx), predicirana su polja vertikalnih brzina i vremenske serije promjena relativne razine mora (RSL - relative sea level). Izračuni su izvedeni pomoću softvera otvorenog koda za rješavanje jednadžbe razine mora (SELEN) te uspoređeni s eksternim podacima, tj. poluempirijskim modelom uzdizanja kopna NKG2016LU_abs i geološkim rekonstrukcijama RSL-a. Rješenja temeljena na SELEN-u dodatno su uspoređena s objavljenim gridovima vertikalnih brzina drugih autora u svrhu kvantificiranja važnosti pretpostavki i aproksimacija različitih softvera. Općenito se softverska rješenja slažu na razini od ~1 mm/godina (standardna odstupanja razlika) s NKG2016LU_abs. U pogledu modela leda, sve rate uzdizanja kopna kao i projekcije RSL-a izračunate s ICE6G_C pokazuju znatno bolje podudaranje s NKG2016LU_abs modelom i podacima RSL-a nego s rezultatima ICE-5G modela, što ukazuje na napredak unutar ICE-x serije. Projekcije današnjih polja vertikalnih brzina temeljene na VMx reologijama slažu se bolje s mjerenjima (odnosno s NKG2016LU_abs modelom) nego projekcije temeljene na NKG reologijama u slučaju oba modela leda. Projekcije s NKG reologijama se u prosjeku bolje podudaraju s podacima RSL-a nego projekcije s VMx reologijama.

Primjenjujući dobro poznatu metodu za određivanje vertikalnih pomaka kopna kombiniranjem satelitske altimetrije i mareografskih mjerenja, prvi puta su u tu svrhu korišteni CS2 podaci (unutar kvadrata veličine 45 km×45 km), premošćujući time dvije glavne teme doktorskog rada. 7.5 godina CS2 i mareografskih podataka kombinirano je u svrhu procijene linearnih trendova vertikalnih pomaka kopna na 20 mareografskih lokacija duž norveške obale. Upotrijebljeni su mjesečni osrednjeni podaci mareografa PSMSL-a (Permanent Service for Mean Sea Level) i skup visokofrekventnih podataka s uzorkovanjem u intervalima od 10 minuta od NMA (Norveška geodetska uprava). Procijenjene rate vertikalnih pomaka kopna na temelju 1 Hz CS2 podataka i visokofrekventnih mareografskih mjerenja dobro odražavaju amplitudu priobalnog prosjeka od 2.4 mm/godina (prosjek svih mareografa), dok NKG2016LU_abs predlaže 2.8 mm/godina; prostorna korelacija je 0.58.

Acknowledgments

After a four-year PhD journey, it (finally!) came to an end. I didn't do it all on my own. Many people helped and supported me on the way in different forms, and hereby, I would like to thank them. I might get emotional.

First, I would like to thank my supervisor, Prof. Bjørn Ragnvald Pettersen. The amount of support I have received from him trough all this years is beyond belief. Thank you for all your help, conversations, advises, and for taking care of me. I always knew who would continue fighting the bureaucratic confusions when I would give up the battle.

I'm obligated to my co-supervisors Dr. Christian Gerlach, Dr. Ole Baltazar Andersen, and Dr. Kristian Breili. Christian, you deserve my deepest gratitude. Thank you for always having time for me, for your unconditional help, our long phone calls and late-night emails. A special thanks to Ole, who was always interested in my work and very supportive from the beginning. Kristian, thank you for your help and support, especially at the end of my PhD journey. Overall, I was very lucky to have all of you as part of my supervision team.

A tremendous gratitude goes to my colleague Dr. Vegard Ophaug. Thank you for having me as your office-mate, for helping with this and that, reasonable and less reasonable conversations, and for becoming not only my colleague but also my friend.

Since I'm not made for sitting alone in the office, luckily, I got to share an office with PhD fellow Hasan Asyari Arief and Dr. Ivar Oveland. Guys, thank you for all our (not always) intellectual conversations and sharing of food.

I would also like to thank the members of the evaluation committee: Prof. Per Knudsen, Dr. Luciana Fenoglio-Marc, and Prof. Cecilie Rolstad Denby.

A special thanks to Christian and the staff at the Bavarian Academy of Sciences and Humanities for always welcoming me warmly as well as Ole and his colleagues at DTU Space for having Vegard and me for a four-months research visit in 2016.

Thanks to Bjørn Ragnvald for translating the thesis summary to Norwegian, and to Christian and Ivana for reading the German and Croatian versions of the summary, respectively.

My PhD fellowship was a part of the GOCODYN (GOCE for coastal ocean dynamics and geodesy) project, which was approved and supported by the Space research program of the Norwegian Research Council.

Gerti, Srećko, Margit, and Jonathan; those people accepted me as their own family member during my stays in Munich, and they didn't even know me before. I'm deeply grateful for your help, care, and friendship.

Then there are Matea, Sara, and Veka; girls, thank you for our friendship. May it be continued for at least 14 more years (or more)!

Sanja, Mare, Simi, Miki, and Marinko; my family in Norway. I'm not sure how I can express my gratitude in words. Mare and Simi, I could do anything without fear because I knew you have my back. Mare, you know everything!

At the end, I would like to express my gratitude to the two most important people in my life: my mum Dragana and my dad Pile. Those two were supporting me in every sense: in all my good (and bad) decisions, ideas, dreams. I wouldn't be the person I'm today without you two. This is for both of you!

Ås, September 3, 2019 *Martina Idžanović*

Contents

Chapter 1

Introduction

1.1 Background

The oceans are responsible for a large part of heat transport within the Earth's system. The complex interactions between oceans, atmosphere, and cryosphere make ocean circulation an important factor in the climate system. For reliable climate-model predictions, precise knowledge of ocean currents is therefore essential. Improved estimates of heat transport through ocean circulation also lead to more reliable predictions of the oceans' thermal expansion, which in turn, is a major contribution to sea-level rise (ESA, 1999).

In absence of dynamics or other external forcing, the surface of the ocean would coincide with the geoid (an equipotential surface of the Earth's gravity field that represents hydrostatic equilibrium). The deviation of the ocean's sea surface from the geoid is called dynamic ocean topography (DOT). The DOT is caused by tides, ocean currents, and changes in barometric pressure that produce the inverted barometer effect (Stewart, 2008). Ocean currents can perturb the DOT by 1-2 meters and are driven by winds, density differences in water masses caused by temperature and salinity variations, gravity, and events such as earthquakes (NOAA, 2019). The Earth's rotation results in the Coriolis effect, which also influences ocean currents (Whitehouse, 2009). Pressure changes in the atmosphere and tides alter the height of the sea surface by a similar amount over short time scales.

Understanding sea-level changes requires input from a large number of disciplines since sea-level rise results from different contributors. The changes in temperature and salinity are able to account for much of the spatial variation observed in sea level (Tamisiea et al., 2014). Since the atmosphere represents a crucial forcing to the ocean, observations of pressure, precipitation, wind, and temperature are vital. Mass loss from the Greenland and Antarctic ice sheets and glaciers as well as water-storage changes can explain the long-time-scale changes in the ocean mass. The determination of mean sea level (MSL) and coastal mean dynamic topography (MDT) is fundamentally important in geodesy as well as oceanography. Geodesy defines the geodetic vertical datum with respect to MSL observed at tide gauges (TGs). Oceanography studies the coastal MDT to understand the driving processes of MSL tilts (Higginson et al., 2015; Lin et al., 2015). Traditional levelling and satellite positioning in combination with geoid models have been used for the determination of coastal MDT at TGs. A GNSS (Global Navigation Satellite System) station collocated with a tide gauge (TG) allows the direct determination of MSL with respect to a reference ellipsoid with an accuracy of 1-2 cm (Huang, 2017). Knowing the height of the geoid with respect to the same reference ellipsoid, MDT at TGs is determined by the *geodetic approach*. The geodetic approach to MDT determination can be compared to the independent *ocean approach*, which involves the use of in situ oceanographic measurements and ocean modelling (Woodworth et al., 2015).

Satellite altimetry has become a fundamental tool to address a wide range of scientific questions, from global ocean-circulation monitoring to long-term sea-level rise or operational weather forecasting (Gommenginger et al., 2011). Satellite altimetry directly delivers the sea surface height (SSH) with respect to a reference ellipsoid, enabling the determination of the global mean sea surface (MSS). Combining observations of MSS with a geoid model allows the extension of MDT determination by the geodetic approach beyond TGs. Conventional altimeters accurately measure SSH over the open ocean but the accuracy degrades when the satellite approaches coastal regions. In the proximity of coasts, a number of issues arise, which are related to poorer geophysical corrections and artifacts in the radar echos linked to the presence of land within the altimeter footprint (Cipollini et al., 2017). ESA's (European Space Agency) CryoSat-2 (CS2) is the first sensor of its kind (ESA, 2018b), which enables the determination of coastal MDT due to its smaller footprint and delay-Doppler processing.

Satellite altimetry has shown that global MSL has been rising at a rate of 3.3±0.4 mm/yr since 1993 (glacial isostatic adjustment correction has been applied) (Beckley et al., 2017). Sea-level research has shifted from the determination of global trends to the recognition of regional and local trends and their causes (Spada, 2017). Precise monitoring of sea-level changes is vitally important for understanding not only climate but also social and economic consequences of any rise in sea level, especially in coastal zones. Coastal cities are built upon the Earth's crust, which can uplift or subside. The changes in SSH are not only driven by MDT changes but also by changes in the geoid and the Earth's crust. Therefore, to understand observed long-term sea-level changes, particularly at risky coastlines, it becomes crucial to account for both crustal motion and geoid changes (Tamisiea et al., 2014).

Many processes at different time scales cause geoid changes and crustal motion. The mass redistribution caused by these processes is not spatially uniform. Initially, the response of the Earth is nearly elastic, which means that deformations occur as soon as surface or potential load changes, and recovers as soon as the load returns to its initial state. In regions where mass loss due to ice melting occurs, the gravitational attraction is reduced, causing the geoid to lower close to the ice sheet. An altimeter would observe a sea-level fall there. In regions close to the center of ice sheets, an even larger sea-level fall would be observed due to the additional land uplift. In contrast to relative sea-level fall in the near field, sea level rises in the far field. After some time, the Earth's response stops to be purely elastic and regional mass loss will cause flow in the Earth's crust and mantle (Tamisiea et al., 2014). Thus, changes in the ice cover at the last glacial maximum (LGM) ~20 000 years ago are still driving present-day sea-level changes. This long-term response of the Earth is referred to as glacial isostatic adjustment (GIA). GIA includes changes in the Earth's shape and gravitational field caused by slow viscous mantle flow as a consequence of the Earth's response to ice melting (Bouman et al., 2016). At the LGM, Fennoscandia, British Isles, North America, Greenland, and Antarctica were covered by major ice sheets. An ocean equivalent of 115-135 m of water was stored within ice sheets during the LGM (Milne et al., 2002). Vertical land motion (VLM) in Fennoscandia is dominated by GIA and the uplift there reaches values of ~10 mm/yr. Various methods measure different aspects of the GIA problem. Relative sea-level changes are measured by TGs, sea-surface changes by satellite altimetry, and crustal motion by GNSS. TGs reflect combined effects of all geophysical processes that perturb the position of land and sea surface. Those processes include ocean's thermal expansion, volume changes in ice reservoirs, GIA, tectonics, and anthropogenic effects (e.g., subsidence due to water usage, mining, or oil drilling) (Kuo et al., 2004). TGs measure sea level relative to the solid Earth, therefore, corrections to account for vertical displacements of each marker must be made. Not all TGs have GNSS receivers available to measure vertical displacements (Figure 1.1). Other techniques to determine land movement can be, e.g., satellite altimetry in conjunction with TG data in absence of GNSS data (Nerem and Mitchum, 2002) or absolute gravity observations. GIA-modelling and its applications gained increased interest, especially during the satellite-altimetry and gravity-mission/GRACE (Gravity Recovery and Climate Experiment) era for understanding the current sea-level rise (Spada, 2017). Furthermore, projections of future sea-level variations are also dependent on the continuing isostatic disequilibrium and its quantification. Understanding past sea-level changes is important for predicting future ones (Steffen and Wu, 2011).

GIA modelling can be carried out to constrain the Earth's structure and ice history. Ice loading and its melting produce a unique pattern of sea-level changes, geoid changes, and solid Earth's changes. GIA models enable the interpretation of these patterns and help to identify past and present ice sources that cause variations. The modelling outputs serve to correct for the spatially varying GIA signal related to the LGM before interpreting the remaining signal, in order to identify the contribution of present-day ice melting to sea-level change. Another GIA contribution to the present-day sea-level budget is the solid Earth's deformation in response to post-glacial ocean loading. The deformation is increasing the capacity of ocean basins, causing thereby a sea-level fall of 0.3 mm/yr (Douglas and Peltier, 2002). GIA models can be also combined with topographic data in order to reconstruct past-shoreline positions but also predict future shoreline migration (Whitehouse, 2009).

1.2 Research objectives

The thesis explores the possibilities of MDT determination in the Norwegian coastal zone by the geodetic approach using modified retracking strategies, novel altimetry data from CS2, and improved geophysical corrections, and analyses GIA in Fennoscandia either by comparing model results with observational evidence or by combining CS2 satellite altimetry with TG data for VLM determination at TGs.

The main research objectives of this thesis are:

1. Quality assessment and refinement of coastal altimetric products along the Norwegian coast.
2. Exploration of the potential of SAR(In) altimetry.
3. Determination and quality assessment of the ocean's MDT with focus on the Norwegian coastal zone from comparison with independent data.
4. Modelling of the GIA-induced vertical velocity field and relative sea-level changes in Norway and Fennoscandia.

The research objectives resulted in the following papers:

Paper A Coastal sea level from CryoSat-2 SARIn altimetry in Norway

Paper B The coastal mean dynamic topography in Norway observed by CryoSat-2 and GOCE

Paper C Analysis of Glacial Isostatic Adjustment in Fennoscandia: Comparison of Model Results and Observational Evidence

Paper D An Attempt to Observe Vertical Land Motion along the Norwegian Coast by CryoSat-2 and Tide Gauges

The first two research objectives are addressed in **Paper A**, where the performance of CS2 was evaluated by comparing its observations with TG measurements at 22 TGs. Thereby, two major geophysical corrections, i.e., ocean tide and inverse barometer were exchanged by locally determined corrections to investigate if refined corrections would improve CS2 sea surface heights (SSHs). The same in situ analysis was performed using data from three conventional altimetry missions (Envisat, SARAL/AltiKa, and Jason-2) in order to quantify the performance of CS2 with respect to conventional altimetry.

Paper B explores the potential of CS2 observations for MDT determination in the Norwegian coastal zone, hence, focusing on objectives 2 and 3. Three state-of-the-art regional geoid models were combined with CS2 SSHs to determine geodetic mean dynamic topographies (MDTs). Geodetic MDTs were validated against an independent operational coastal ocean model as well as TG MDTs. Geostrophic ocean currents were also determined in this paper and compared to flow patterns based on the coastal ocean model.

Objective 4, i.e., modelling GIA-induced VLM as well as relative-sea level changes were addressed in **Paper C**. Ice histories and rheologies were coupled to determine the Earth's response to the melting of late-Pleistocene ice sheets in Fennoscandia. Computed predictions of present-day VLM were compared to published grids of vertical velocities by other authors in order to quantify the difference between various software solutions. In addition, GIA-modelling outputs were validated against external data, namely the semi-empirical land-uplift model for the Nordic-Baltic region NKG2016LU_abs and geological relative sea-level reconstructions.

Paper D is bridging objectives 2 and 4, where satellite altimetry was used to determine VLM (dominated by GIA) along the Norwegian coast. CS2 SARIn observations were combined with both monthly-averaged and 10-minute TG data sets in order to determine VLM rates at 20 TGs along the coast and compared with NKG2016LU_abs rates.

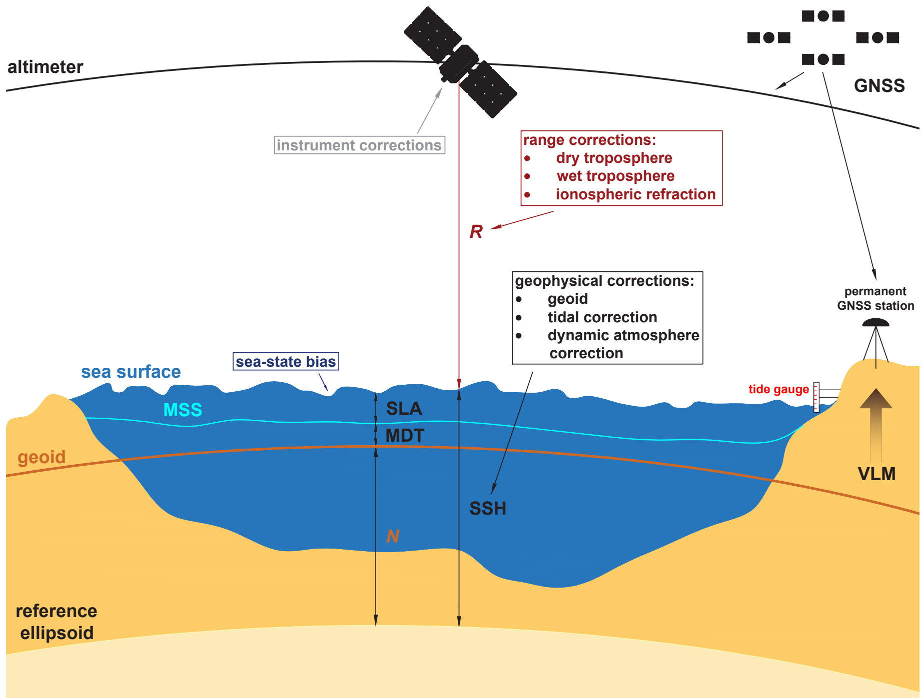

Figure 1.1. Schematic representation of geodetic measuring techniques and summary of corrections, which must be applied to the altimeter range measurement. The sea surface height (SSH) is relative to the reference ellipsoid and sea level is relative to the solid Earth. Thus, vertical land motion (VLM) is the difference between SSH and relative sea level. Tide gauges measure relative sea level, while satellite altimetry observes SSH; VLM can be observed by GNSS. All three variables include processes that may change the actual sea surface and land at any timescale. The mean dynamic topography (MDT), which is of interest for ocean-circulation studies, is obtained from the mean sea surface (MSS) by subtracting the geoid, N. Adapted from Andersen and Scharroo (2011); Chelton et al. (2001); Ophaug (2017); Simpson et al. (2015).

1.3 Talks, posters, and conferences

2019

Gerlach, Ch., V. Ophaug, O. C. D. Omang, and M. Idžanović (2019), **Quality and Distribution of Terrestrial Gravity Data for Precise Regional Geoid Modeling: A Generalized Setup**. In: International Association of Geodesy Symposia, Springer, Berlin, Heidelberg, doi: 10.1007/1345_2019_71.

2018

Interview with NMBU's rector on land-uplift determination in Norway by combining satellite altimetry and tide-gauge observations on https://www.facebook.com/mari.s.tveit/videos/10155755521657212/

Idžanović, M., K. Breili, Ch. Gerlach, and O. B. Andersen: **Land Uplift Determined by Satellite Altimetry and Tide-Gauge data in Fennoscandia**, poster presented at the "25 Years of Progress in Radar Altimetry" Symposium, September 24-29, Ponta Delgada, Portugal

Ophaug, V., M. Idžanović, and O. B. Andersen: **The Coastal Mean Dynamic Topography in Norway Observed by CryoSat-2 and GOCE**, talk given at the "25 Years of Progress in Radar Altimetry" Symposium, September 24-29, Ponta Delgada, Portugal

Gerlach, Ch., V. Ophaug, O. C. D. Omang, and M. Idžanović: **Quality and distribution of terrestrial gravity data for precise regional geoid modelling in a testbed along the Norwegian coast**, poster presented at the Hotine-Marussi Symposium 2018, June 18-22, Rome, Italy

2017

Idžanović, M. and and Ch. Gerlach: **Comparison of the semi-empirical land uplift model NKG2016LU and GIA-modelled present-day geodetic variations in Fennoscandia based on different ice models**, talk given at the Fall meeting of the German Geophysical Society, October 24-27, Blaibach, Germany

Idžanović, M. and and Ch. Gerlach: **Comparison of the semi-empirical land uplift model NKG2016LU and GIA-modelled present-day geodetic variations in Fennoscandia based on different ice models**, poster presented at the International workshop on the inter-comparison of space and ground gravity and geometric spatial measurements, October 16-18, Strasbourg, France

Andersen, O. B., M. Idžanović, V. Ophaug, and A. Aulaitijiang: **The Great Value of Cryosat-2 SAR-in for Coastal Sea Level Monitoring**, talk given at the North-American CryoSat Science Meeting, March 20-24, Banff, Alberta, Canada

Idžanović, M., V. Ophaug, and O. B. Andersen: **The Norwegian Coastal Current observed by CryoSat-2 and GOCE**, poster presented at the North-American CryoSat Science Meeting, March 20-24 Banff, Alberta, Canada

Idžanović, M., V. Ophaug, and O. B. Andersen: **The Norwegian Coastal Current observed by CryoSat-2 and GOCE**, poster presented at the 10th Coastal Altimetry Workshop, February 21-24, Florence, Italy

Idžanović, M., V. Ophaug, and O. B. Andersen: **Coastal Sea Level from CryoSat-2 SARIn Altimetry in Norway**, poster presented at the 10th Coastal Altimetry Workshop, February 21-24, Florence, Italy

Official web page of the GOCODYN project at https://www.nmbu.no/en/projects/node/31870

2016

Nordic Geodetic Commission joint WG workshop on postglacial land uplift modelling, December 1-2, Gävle, Sweden

Idžanović, M., V. Ophaug, and O. B. Andersen: **The Norwegian Coastal Current observed by CryoSat-2 and GOCE**, poster presented at the 2016 SAR Altimetry Workshop, October 31, La Rochelle, France

Idžanović, M., V. Ophaug, and O. B. Andersen: **The Norwegian Coastal Current observed by CryoSat-2 SARIn altimetry**, poster presented at the International Symposium on Gravity, Geoid and Height Systems 2016, September 19-23, Thessaloniki, Greece

Cryosat sets new standard for measuring sea levels, a popular article on ESA's Cryosat web page http://www.esa.int/Our_Activities/Observing_the_Earth/CryoSat/CryoSat_sets_new_standard_for_measuring_sea_levels

Idžanović, M., V. Ophaug, and O. B. Andersen: **Coastal Sea Level in Norway from CryoSat-2 SAR Altimetry**, poster presented at the ESA Living Planet Symposium 2016, May 9-13, Prague, Czech Republic

2015

Glacial Isostatic Adjustment Training School, Ohio State University, September 13-19, Stone Laboratory on Gibralter Island, Lake Erie, USA

1.4 Thesis structure

This thesis is divided into several chapters, which deal with the following topics.

Chapter 2 describes the first major topic of the thesis, i.e., satellite altimetry. The principal and main differences between conventional and SAR altimetry are given in Sections 2.1 and 2.2. Retracking methods are explained in Section 2.3. An essential step in the processing of altimetry data are range and geophysical corrections for which an overview is given in Section 2.4. The MDT and geostrophic surface currents are presented in Sections 2.5 and 2.6, respectively. Data and methods for **Paper A**, **Paper B**, and **Paper D** are given in detail in Section 2.7 as well as data sets for validating the results, i.e., the coastal ocean model NorKyst800 and TG observations.

Chapter 3 deals with the second major topic, GIA. The definition of the sea-level equation, including Green's functions as well as input parameters to the sea-level equation (surface loads and Earth models) are given in Section 3.1. An overview of GIA-modelling outputs is presented in Section 3.2. Models and data sets used in **Paper C** as well as data for validating modelled results are given in Section 3.3 (the semi-empirical land-uplift model NKG2016LU and geological relative sea-level data).

Chapter 4 gives on overview of results presented in the papers and consists of three sections. Section 4.1 presents results regarding SAR(In) altimetry along the Norwegian coast and ocean topographies derived from CS2 and regional geoid models. Section 4.2 comprises predictions of relative sea level as well as VLM rates in Fennoscandia derived by two different approaches. In Section 4.3, limitations to the work are discussed.

Chapter 5 lists the main conclusions of the thesis and gives a future scope of the work.

At the end of the thesis, a list of included papers is provided and four peer-reviewed journal papers are appended.

Chapter 2

Satellite altimetry and CryoSat-2

This chapter provides basic knowledge about satellite altimetry. The principle of satellite altimetry is described, heavily focusing on CS2, the altimetry mission whose data were used in this study. A brief overview of retracking methods as well as range and geophysical corrections applied onto altimetric observations is given. In addition, fundamental equations for ocean-circulation studies are presented.

Satellite altimetry is a major technique allowing global mapping of sea surface topography and measuring sea-level changes (Simpson et al., 2015). Altimetry-derived SSHs are used in climate prediction, monitoring of ocean circulation, weather forecasting, and determination of the gravity field (Jain et al., 2015). Today, satellite altimetry is able to achieve accuracies in SSH measurements of only a few centimeters thanks to technological developments and improvements in data reprocessing (Calafat et al., 2017).

Radar altimeters have been flown on a number of satellites. NASA's (National Aeronautics and Space Administration) Seasat was the first ocean-oriented mission carrying an altimeter package (including a precise orbit-determination system) for the measurement of ocean circulation and was launched in 1978. A satellite-altimetry revolution happened with the launch of the US-French Topex/Poseidon mission in 1992. Carrying two high-precision altimeters, a multi-channel microwave radiometer, and precise orbit-determination devices, it enabled the large-scale ocean circulation to be accurately measured. The European ERS-1 (from 1991) and ERS-2 (from 1995) satellites also provided long time-series of complementary altimetric observations. These observations were continued with Jason-1 (launched in 2001) and Envisat (launched in 2002) (CEOS, 2009).

Currently, there are seven altimetry missions in orbit: CS2, Jason-2, Jason-3, SARAL/AltiKa, Sentinel-3 (A & B), and HY-2. Jason-2 was launched in 2008 with the intention to continue the high-accuracy satellite-altimetry observations begun by Topex/Poseidon and Jason-1 (CEOS, 2009). As part of the Topex-family missions, Jason-2 and Jason-3 (launched in 2016) have the same orbit as Topex/Poseidon and Jason-1 with a relatively short repeat cycle of 9.9 days and widely-spaced ground tracks of 315 km at the equator (AVISO, 2019). Placed in the same 800-km polar orbit as Envisat, the French-Indian SARAL/AltiKa (launched in 2013) is the first satellite equipped with a K_a-band altimeter (which is much less affected by the ionosphere than K_u-band) for measuring SSHs with a 35-day repeat cycle (CNES, 2017). Sentinel-3 (A & B) were launched in 2016 and 2018, respectively, and have a 27-day repeat orbit. HY-2 (launched in 2011) is the second-generation ocean-monitoring satellite series approved by China National Space Administration (AVISO, 2019). Figure 2.1 shows the theoretical ground tracks for Envisat, SARAL/AltiKa, and Jason-2 whose data were compared to TG observations in **Paper A**. Not all altimetry missions cover the Norwegian coastal zone due to the low inclination (66°) of the Topex-family missions. Altimetry at high latitudes, including the northernmost coast of Norway, is therefore especially challenging.

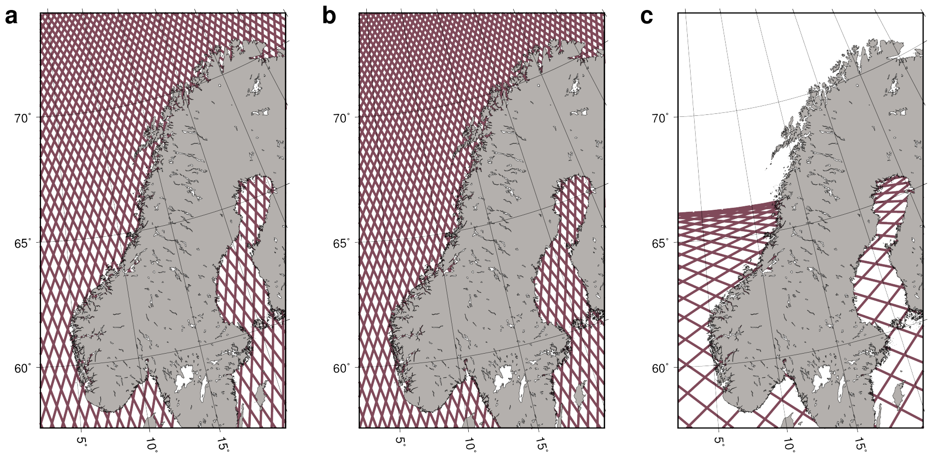

Figure 2.1. Theoretical altimeter ground tracks in the Nordic region for (**a**) Envisat Phase C (30 days), (**b**) SARAL/AltiKa (35 days), and (**c**) Jason-2 (10 days) whose data were used in **Paper A**. Inspired by Ophaug (2017).

2.1 Principle of satellite altimetry

Satellite altimeters transmit a short pulse of microwave radiation with known power towards the sea surface, where the signal interacts with the sea surface and part of the signal is returned back to the satellite. Satellite altimeters measure the round-trip travel time accurately (Vignudelli et al., 2011). The principal objective of satellite altimetry is to measure the *range* from the satellite to the sea surface (Figure 1.1). The range needs to be corrected for a variety of factors and effects (Vignudelli et al., 2011), which can be grouped into instrumental, range, and geophysical corrections. The range, $\hat{R}$, estimated from the satellite-to-surface round-trip travel time Δt is (Chelton et al., 2001)

$$\hat{R} = R_0 + \sum_i \Delta R_i, \tag{2.1}$$

where $R_0 = c \cdot \Delta t/2$ is the range computed neglecting refraction based on the speed of light c but corrected for instrument effects. Corrections for various components ΔR_i $(i = 1, \ldots)$ are described in Section 2.4. If the satellite's height, h, is known in a particular reference frame, SSH can be found by subtracting the corrected range, R, given in Eq. (2.3) from the height of the satellite:

$$\mathrm{SSH} = h - R. \tag{2.2}$$

The height of the satellite's center of mass with respect to a reference ellipsoid is normally modelled to an accuracy of 2-3 cm by using a combination of GPS (Global Positioning System) positioning, laser ranging, and the DORIS (Doppler Orbitography and Radiopositioning Integrated by Satellite) beacon/satellite receiver system (Cipollini et al., 2017).

Several frequencies are used for radar altimeters, depending upon regulations, mission objectives, and technical possibilities (AVISO, 2019). Each frequency has its advantages and disadvantages. The advantages of using K_a-band rather than K_u-band frequency are reduced ionospheric delay, narrow beamwidth enabling near-land altimetry, and a higher number of independent pulses; disadvantages are greater sensitivity to clouds and rain (Quartly and Chen, 2006), and antenna mispointing (Stammer and Cazenave, 2017).

In principle, there are two types of altimeters: (i) beam-limited and (ii) pulse-limited, depending on the width of the ground strip illuminated by the antenna. For beam-limited altimeters, the return pulse is dictated by the physical size of the antenna. For a pulse-limited altimeter, the shape of the return is dictated by the length (width) of the compressed pulse. Most missions have altimeters on-board, which use the principle of pulse-limited signals. Missions, which use synthetic aperture techniques can be seen as beam-limited instruments in the along-track direction (direction parallel to satellite's flight direction) (Cipollini et al., 2013). The main limitation of conventional nadir-pointing radar altimeters is the space-time coverage dilemma (Vignudelli et al., 2011); either the spatial sampling is coarse (Figure 2.1c) or the time sampling is poor (Figures 2.1a and 2.1b). Increased temporal resolution means decreased spatial resolution and vice versa. Ocean-oriented altimeters have a shorter repeat orbit (10 days or 35 days) in comparison to CS2 (369 days), which is constructed as a geodetic mission (spatial coverage is of higher priority than temporal resolution) (Calafat et al., 2017).

In the vertical direction, altimeters can receive echos only within a specific range window, called the *analysis window*, which is determined by the on-board tracker system. As the satellite moves along its orbit and the satellite-to-surface distance changes, the position of the analysis window is dynamically adjusted by on-board trackers to ensure that the altimeter samples at the time when the radar pulse hits the surface and that the reflected signal is kept within the analysis window (Gommenginger et al., 2011). Tracking systems can work in open and closed loops. An open-loop tracking system positions the analysis window using a priori knowledge from a high-resolution digital elevation model stored on board. Errors in the digital elevation model and variations in topography at scales higher than the digital elevation-model resolution can cause the altimeter to lose track. In a closed-loop system, the analysis window is positioned based on the on-board near real-time analysis of previous waveforms, which increases the chances for the altimeter to keep the signal inside the analysis window (Di Bella, 2019).

2.2 SAR(In) altimetry on CryoSat-2

Only few years back, conventional altimetry was not able to sample coastal zone processes and short-scale phenomena due to land contaminated footprints. This changed with the launch of CS2 and the implementation of synthetic aperture radar (SAR) altimetry. SAR altimetry was originally developed for monitoring the cryosphere by measuring variations in the ice thickness but has also proven its applicability for monitoring the ocean (Cipollini et al., 2017). SAR altimetry or delay-Doppler altimetry is a technique to process altimetric data (Raney and Phalippou, 2011). The key idea behind the SAR altimeter is to use the Doppler effect to divide the radar footprint into a number of along-track cells and average all cells illuminating the same area (Stenseng, 2011) (Figure 2.4a). Hence, the probability that the smaller footprint is contaminated by land is far less for CS2 in SAR(In) mode compared to conventional altimeters. In addition to CS2, ESA's Copernicus satellites Sentinel-3 (A

Figure 2.2. The CryoSat-2 spacecraft in orbit. Image taken from ESA (2006).

& B) are equipped with SAR altimeters. In the future, SAR altimetry will be implemented on Sentinel-3 (C & D) as well as Jason-CS/Sentinel-6 (AVISO, 2019).

CS2 (Figure 2.2) is a Earth Explorer Opportunity Mission in the Living Planet Program of ESA. It replaced CryoSat, which was lost as a result of launch failure on October 8, 2005. The replacement spacecraft was launched on April 8, 2010 from the Baikonur Cosmodrome in Kazakhstan, with some improvements. CS2 operates at an altitude of 717 km, covering areas up to 88°N/S. It operates at a K_u-band radar frequency of 13.575 GHz and has a repeat period of 369 days, with subcycles of 30 days. The 30-day subcycles provide approximately monthly global coverage. The equatorial ground-track spacing is ~8 km and the along-track resolution ~250 m (Table 2.2). CS2 carries a synthetic aperture interferometric radar altimeter (SIRAL), which can operate in (i) SAR, (ii) SAR interferometric (SARIn), and (iii) conventional low-resolution modes, introducing thereby two important improvements. First, it ensures a higher along-track resolution, and secondly, it reduces the impact of land contamination on radar echos in proximity of coasts (Dinardo et al., 2011). Two features make SIRAL different from previous space-borne altimeters (Stenseng, 2011):

- It has two antennas and two receive chains, thereby forming an interferometer in the across-track direction (direction perpendicular to satellite's flight direction) with a baseline of 1.2 m and permitting interferometric processing for enhanced ground resolution in the along-track direction. A correct antenna orientation is crucial and maintained by a trio of star trackers.

- It sends bursts of pulses separated by intervals of 50 μs; conventional altimeters have generally pulse intervals of 500 μs.

CS2 switches automatically between its three observational modes according to a geographical mode mask. The mask is updated every two weeks to account for changes in the sea-ice extent (Mertz et al., 2017). Figure 2.3 shows the geographical mode mask over the Nordic region. The SARIn zone is stretching ~40 km off the coast, where it transits to the low-resolution mode. The SAR mode is operated over the Skagerrak area.

Low-resolution mode

Conventional radar altimeters operate in the pulse-limited mode. For CS2, this mode is referred to as low-resolution mode (LRM). When in LRM, a single receive channel and a low pulse-repetition frequency are used, ensuring uncorrelated returning echos (ESA, 2007). CS2 operates in this mode over surfaces where surface slopes are small, i.e., over oceans and ice-sheet interiors (ESA, 2018a).

Synthetic aperture-radar mode

The SAR mode is operated over sea-ice areas as well as some ocean basins and coastal zones (ESA, 2018a). SAR uses a single channel, where bursts of 64 pulses at a high pulse-repetition frequency are transmitted. The high pulse-repetition frequency ensures coherent sampling, and together with pulse-to-pulse phase coherence, a series of pulses can be combined to form an equal amount of synthetic beams, with footprints much smaller in the along-track direction (Stenseng, 2011). After the burst transmission, the altimeter exploits the empty inter-burst interval to receive the echos reflected back from the surface (Dinardo, 2013). The footprints of those sub-beams are adjacent cells, about 250 m wide in the along-track direction. In the across-track direction, the resolution is still constrained by the diameter of the pulse-limited circle (Figure 2.7d).

Stacking is the collection of various Doppler beams pointing to a particular cell on the Earth's surface (Figure 2.4a). The averaging of such a stack to make a composite waveform is called multi-looking (Jain, 2005). The consequence of a small along-track footprint and multiple looks is a waveform with a steep leading edge and a fast decaying trailing edge (Figure 2.7f) as well as a response more than 10 dB stronger at the peak power in comparison to a conventional radar-altimeter waveform (Stenseng, 2011).

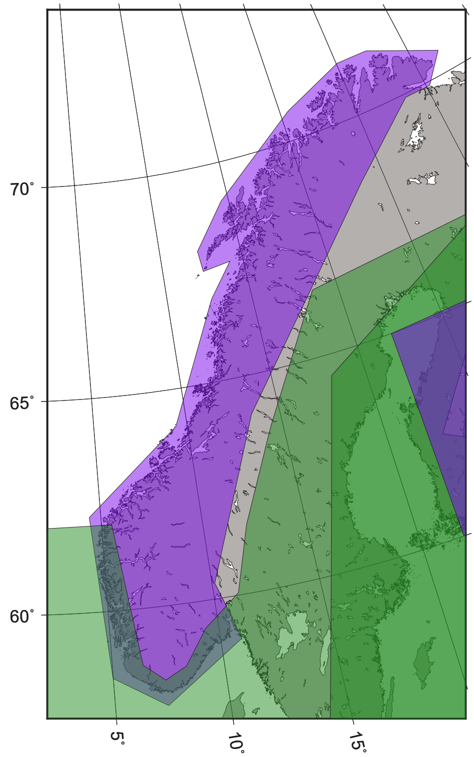

Figure 2.3. CryoSat-2 geographical mode mask version 3.9 (ESA, 2018a) over the Nordic region. The geographical mode mask is updated every year but remained constant over Norway. CryoSat-2 switches automatically to its three observational modes according to the geographical mode mask: SAR (green), SARIn (purple), and LRM (areas not covered by other modes).

Synthetic aperture-radar interferometric mode

The SARIn mode is used over ice-sheet margins, some geostrophic ocean currents, and small ice caps as well as areas of mountain glaciers. In the SARIn mode, the analysis window is four times larger than in LRM and SAR (60 m versus 240 m) due to slope variations in ice-sheet margins (ESA, 2018a). When operated in this mode, the SAR processing is combined with the interferometric feature of SARIn, which improves the echo-localization capabilities as the across-track angle of the echos can be determined. The application of two antennas in the SARIn mode allows to calculate the difference between the phase of one receiving channel with respect to the other. From the phase difference, it is possible to determine the angle of the echo at each gate, and in particular, the angle of the echo at the closest range (first return). When the range of the first scattering point to the antenna is known, the across-track distance of the scattering point can be derived. The calculated across-track distance can be applied in coastal areas to determine the origin of the radar return. Over the open ocean, the across-track distance is expected to be around zero. In presence of targets in the across-track direction, e.g., islands or steep cliffs, the across-track distance has a value different from zero, making it possible to recognize and discriminate land-originating returns from pure ocean returns (Dinardo et al., 2011) (Figure 2.4b). Due to the slanted geometry, the off-nadir Doppler beams observe a target at an apparently longer range than the range to the nadir point (Stenseng, 2011). Height retracking from such an off-nadir range measurement leads to an underestimated SSH. Hence, the off-nadir range should be corrected for SARIn applications as shown, e.g., in Abulaitijiang et al. (2015).

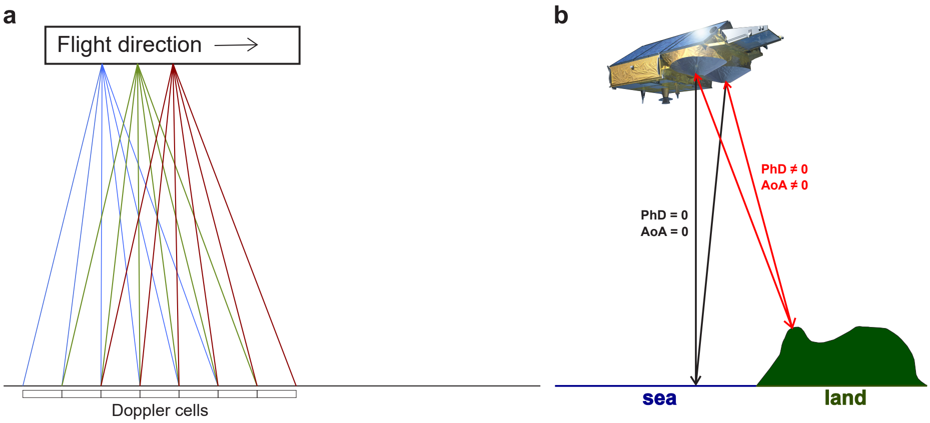

Figure 2.4. (**a**) Multi-looking of the same Doppler cells by different positions of the satellite along its flight direction. Adapted from Jain (2005). (**b**) In the SARIn mode, the across-track discrimination is based on the phase difference (PhD), i.e., angle of arrival (AoA). Adapted from Garcia-Mondájar et al. (2015).

2.3 Waveform-retracking methods

The magnitude and shape of the received echos are sampled in a time series called *waveform*, which contains information about the characteristics of the surface that caused the reflection. The delay in the signal return indicates the height of the feature below the instrument, i.e., the range; the signal amplitude records the backscatter strength of the target, σ_0, which is dependent upon the surface type and its roughness (related to wind). The waveform's shape contains information on the variation in topography within the footprint (Quartly and Chen, 2006). This information is obtained by an algorithm called *retracking* that fits an analytical waveform model to the measured waveform (Thibaut et al., 2010). Each cell within a waveform is called range *gate* or *bin* and contains a power value corresponding to a certain distance from the satellite.

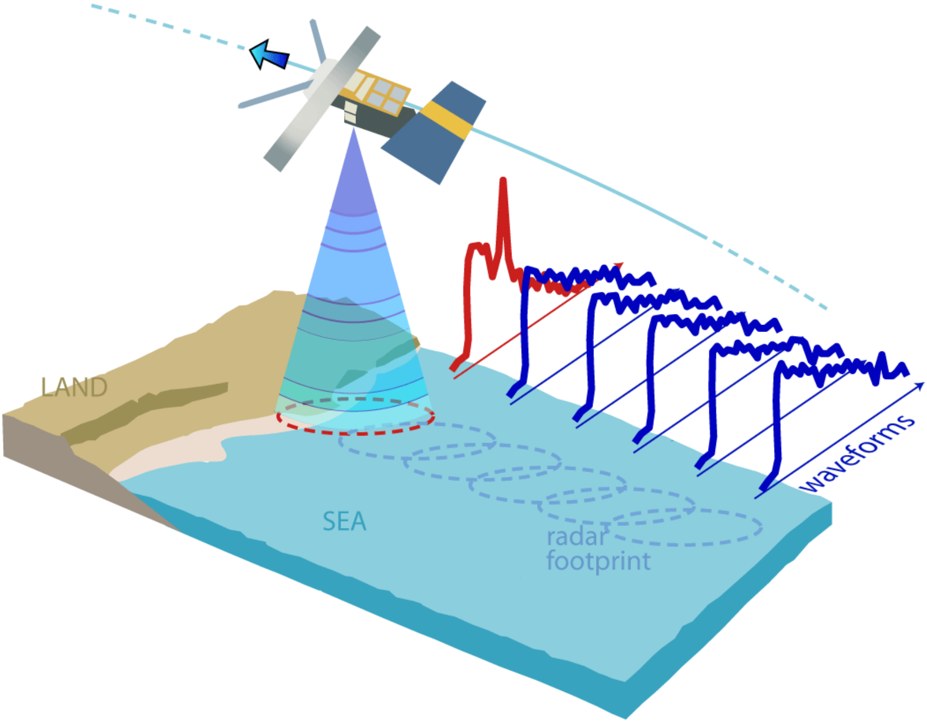

Figure 2.5. Illustration of waveform corruption when the altimeter approaches the coast. Figure taken from Cipollini et al. (2014).

Over the surface of the ocean, the waveform has a characteristic shape that can be described analytically by the Brown model, with a steep leading edge and a slowly decaying trailing edge (Figure 2.7e). Figure 2.6 shows a theoretical ocean-like or Brown-type waveform as well as parameters that can be estimated from the waveform. As long as the transmitted signal does not intercept the sea surface, the received signal is almost zero (only thermal noise, P_0, is present at the altimeter input). Due to the spherical shape of the wave front, the incidence pulse starts to intercept the sea surface at the middle of the observed area. The received signal amplitude increases to a maximum and tends to decrease accordingly to the shape of the antenna gain (Stammer and Cazenave, 2017). The presence of sea ice and coasts makes waveform retracking considerably more difficult compared to waveform retracking over the open ocean (Jain et al., 2015). The waveforms depart from the Brown model and are multipeaked (Figure 2.5). The characteristic quasi-step shape of the pulse-limited waveform is lost in SAR. SAR waveforms assume a sharp shape with a long and slow decaying tail (Figure 2.7f). Factors that impact the waveform are not only the presence of land in the altimeter footprint but also presence of ”bright targets” in the footprint such as calm water areas (Cipollini et al., 2017).

From the basic ocean-waveform shape in Figure 2.6, several parameters can be deducted (Gommenginger et al., 2011):

- τ is the epoch or time delay, i.e., the position of the waveform in the analysis window with respect to the tracking reference point determined by the on-board tracker.
- P is the amplitude of the received signal. This amplitude with respect to the emission amplitude gives the backscatter coefficient, σ_0. The backscatter coefficient is related to wind speed.
- P_0 is the thermal noise level.
- The leading-edge slope, σ_s, is related to the significant wave height.
- The trailing-edge slope is linked to any mispointing of the radar antenna ξ, i.e., any deviation from nadir.
- Skewness λ_s is related to the leading-edge curvature.

Two types of retrackers are known: (i) physical and (ii) empirical. Physical retrackers fit a mathematical model to the raw waveform and estimate the range and other physical properties with high accuracy and precision. They are suitable for ocean-type waveforms. Empirical retrackers use the waveform’s statistics to determine the retracking point, which is not related to any physical properties of the reflecting surface, giving only the range with an unknown absolute level (there can be a small offset in the estimated range depending on the retracker that was applied). In comparison to physical retrackers, empirical retrackers provide range estimates for all kinds of waveforms (Villadsen, 2016). A brief overview of retrackers is given in the following.

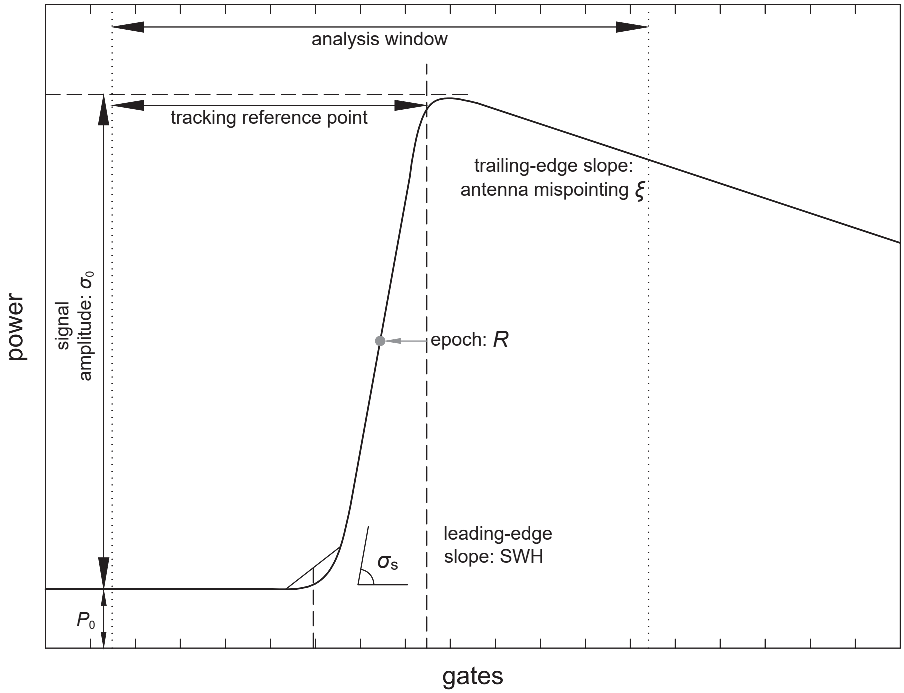

Figure 2.6. Ocean parameters that can be estimated from the altimeter echo: (i) the range between the satellite and the observed surface is related to the time (epoch) when the amplitude of the received signal represents half of the maximum amplitude in the leading edge; (ii) the significant wave height (SWH) is deducted from the slope of the leading edge; (iii) the backscatter coefficient of the ocean, σ_0, related to wind speed, is estimated from the maximum signal amplitude received. The curvature of the leading edge is linked to the wave skewness, and the slope of the trailing edge provides information on the radar-antenna mispointing with respect to nadir. Adapted from Gommenginger et al. (2011); Passaro et al. (2014).

The two traditional empirical retrackers, the offset center of gravity (OCOG) retracker (Wingham et al., 1986) and the threshold retracker (Davis, 1995) work on the complete waveform in order to locate the retracking point (Jain, 2005). They are mostly used in hydrological applications (Thibaut et al., 2017). The goal of the OCOG retracker is to find each waveform's center of gravity based on the power levels within the gates. After defining a rectangle about the effective center of gravity, the amplitude and width of the waveform as well as the gate position of the waveform's center of gravity are estimated. The threshold retracker is based on the dimensions of the rectangle computed by the OCOG method (Gommenginger et al., 2011). The threshold value is then referenced with respect to the OCOG amplitude or to a specific percentage of the waveform's maximum amplitude (Di Bella, 2019). Improved threshold retrackers distinguish between methods using external data to select the best ranging gate and methods that find the leading sub-waveform directly without additional data. Primary-peak retrackers are applied just to the primary peak (high peak that includes the leading edge and contains most of the reflection from nadir) of the reflected waveform (Jain, 2005). The β-retracker (Martin et al., 1983) is a 5- or 9-parameter functional form to fit single or double-ramped waveforms, respectively. The unknown β parameters are thermal noise level, signal amplitude, mid-point of the leading edge, waveform rise time, and slope of the trailing edge. The β parameters are estimated parameters and do not relate to physical properties (Gommenginger et al., 2011).

Physical retrackers are Brown, Hayne, and SAMOSA (SAR altimetry mode studies and applications), and applied onto the deep ocean (Thibaut et al., 2017). The formulation of the theoretical shape of an echo over the ocean was given by Brown (1977), and refined by Hayne (1980), including a fixed skewness parameter λ_{s}. To fit a model to measured waveforms, different statistical methods are used. The maximum likelihood estimator (MLE) is based on the Hayne model and fits the theoretical model-return power to the measured return power. The MLE3 algorithm estimates three parameters: range, significant wave height, and backscatter coefficient. In addition to parameters estimated by MLE3, MLE4 estimates antenna mispointing (Smith et al., 2011). The SAMOSA retracker (Ray et al., 2015) uses the Brown approach to describe the returned waveform from the delay-Doppler/pulse-limited footprint. Since it is a physically based model, it can include a number of other parameters such as significant wave height, backscatter coefficient, and antenna mispointing (Stenseng, 2011).

The retracked range is obtained by combining the range of the analysis window with the retrieved epoch obtained by retracking (Gommenginger et al., 2011)

$$R = \hat{R} + \Delta R_{\mathrm{r}}, \tag{2.3}$$

where ΔR_{r} is the retracking correction and $\hat{R}$ is given by Eq. (2.1).

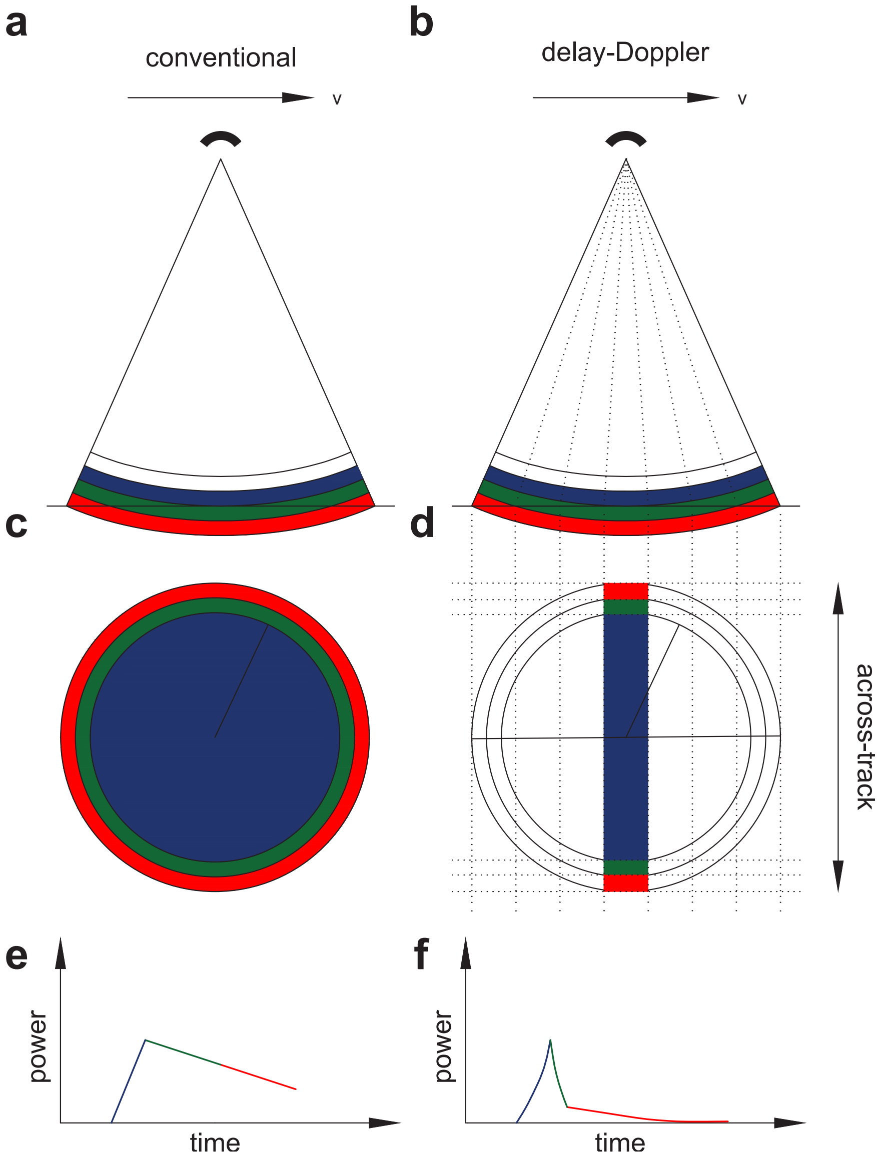

Figure 2.7. Comparison of conventional pulse-limited radar altimeters and SAR altimeters: (**a**, **b**) side view of footprints, (**c**, **d**) top view of footprints, and idealized shapes of a (**e**) conventional-altimeter echo and a (**f**) SAR-altimeter echo. Adapted from Jiang et al. (2017).

2.4 Range and geophysical corrections

The determination of SSH from altimeteric range measurements involves a number of corrections (Figure 1.1). One group of corrections concerns the behavior of the radar pulse through the atmosphere (*range corrections*), while the other group corrects for sea state and other geophysical signals (*geophysical corrections*). Some of those corrections need special attention close to the coast and in shallow-water regions (Vignudelli et al., 2011). The accuracy of derived SSHs is directly linked to the accuracy of applied corrections. In coastal zones, in addition to the refinement of statistical techniques for screening and filtering of data, the range estimation can be improved by applying specialized retracking as well as by applying improved corrections for the geophysical signals (Cipollini et al., 2017). The following overview of range and geophysical corrections is based on Andersen and Scharroo (2011). Table 2.1 provides an overview of typical mean values of time-varying range and geophysical corrections.

Range corrections, which model and adjust for the refraction and the delay of the radar signal in the atmosphere, are split into three components: (i) the dry tropospheric correction (ΔR_{dry}) accounts for dry gasses (mainly oxygen and nitrogen), (ii) the wet tropospheric correction (ΔR_{wet}) accounts for the water vapor, and (iii) the ionospheric correction (ΔR_{iono}) accounts for the presence of free electrons in the upper atmosphere. The wet tropospheric correction can be estimated from radiometer measurements or models provided by the European Centre for Medium-Range Weather Forecasts (ECMWF), which are based on pressure and temperature grids. For the dry tropospheric correction, data from operational weather models are used, e.g., ECMWF and NCEP (National Centers for Environmental Prediction). As an alternative to dual-frequency altimeter measurements, a number of climatological models have been in use to derive the ionospheric correction, e.g., the Bent model (Llewellyn and Bent, 1973) as well as GPS-derived global ionospheric maps (GIM).

The wave distribution and scattering of the radar signal by the sea surface is not Gaussian; wave troughs are more present and reflect back more of the radar signal than the crests, introducing thereby a bias. This bias is related to the local sea state (wind and wave conditions) and is called sea-state bias. The sea-state bias correction (ΔR_{ssb}) accounts for the difference between the actual scattering surface and the average of SSHs within the altimeter footprint. It refers collectively to the electromagnetic, skewness, and tracker biases (Bonnefond et al., 2011). The sea-state bias was originally modelled as a simple percentage of the significant wave height. Since the sea-state bias depends upon different wave types and wind field, a more advanced 4-

parameter model was introduced to describe the sea-state bias, referred to as the BM4 model (Andersen and Scharroo, 2011).

According to Eqs. (2.1) and (2.3), the corrected range R is

$$R = R_0 + \Delta R_r + \Delta R_{dry} + \Delta R_{wet} + \Delta R_{iono} + \Delta R_{ssb}. \quad (2.4)$$

The main focus of satellite altimetry is to study dynamical sea-surface signals, which are related to oceanographic processes. In order to isolate those signals, dominant geophysical contributions have to be removed by applying geophysical corrections. Those corrections adjust the observed SSH for the largest time-variable contributors: (i) tides (h_{tides}) and (ii) the dynamic atmosphere (h_{atm}). These effects must be modelled and removed in order to investigate the actual SSH, which can be split into geoid height, N, and DOT:

$$\text{SSH} = \text{DOT} + h_{tides} + h_{atm} + N. \quad (2.5)$$

The tidal correction, h_{tides}, is the dominant contributor to temporal SSH variations. The ocean tide (OT) is responsible for more than 80% of the tidal signal variance and is the largest tidal component. The tidal correction also includes smaller tidal signals, i.e., ocean-tide loading (OTL), solid Earth tide (SET), and pole tide (PT), and can be written as the sum of its contributors:

$$h_{tides} = h_{OT} + h_{OTL} + h_{SET} + h_{PT}. \quad (2.6)$$

Global OT models have an accuracy of ~1-2 cm over the open ocean. The tidal range is much larger in the coastal regions than in the open ocean, and coastal tidal waves are more complex. Global OT models have errors of 10-20 cm close to the coast (Ray, 2008). In some places, the OT correction is not available in coastal regions (**Paper A**). A commonly used model for the OT correction is FES2004 (Lyard et al., 2006). The SET is computed using closed formulas as described in Cartwright and Taylor (1971) and Cartwright and Edden (1973), and assumed to be very accurate. The PT is computed as described by, e.g., Wahr (1985) to high accuracy.

The dynamic atmosphere correction, h_{atm}, corrects the SSH for variations due to time-varying atmospheric pressure loading. The atmosphere exerts a downward force on the sea surface and lowers it when the pressure is high and vice versa. h_{atm} combines a static response (inverse barometer) of the ocean to atmospheric forcing for low-frequency signals (periods longer than 20 days) as well as a correction for high-frequency variations (periods shorter than 20 days). For the low-frequency contribution, the classical inverse barometer (IB) correction is used to account for the response of the sea surface to changes in atmospheric pressure

$$h_{\text{ib}} \approx -0.99484\,(P_0 - P_{\text{ref}}), \tag{2.7}$$

where P_0 may be derived from the dry tropospheric correction, and P_{ref} is the global mean pressure, i.e., reference pressure. Traditionally, a constant value of 1013.3 hPa has been used, which is the average surface pressure over the globe. However, the mean pressure over the globe is not identical to the mean pressure over the ocean. The mean pressure over the ocean is closer to 1011 hPa (Andersen and Scharroo, 2011). The low-frequency part should be combined with the high-frequency contribution (short-period air-pressure changes and wind effects). The high-frequency contribution is available from models, e.g., MOG2D (Carrère and Lyard, 2003). The standard deviation of the IB correction ranges from 10 to 15 cm at high latitudes. Combining the IB correction with the high-frequency part reduces the SSH signal additionally for 1.0-1.5 cm (Andersen and Scharroo, 2011). Large variations in atmospheric pressure along the coast and complex tidal patterns degrade the geophysical corrections for dynamic atmosphere and OT (Andersen and Scharroo, 2011). In addition, Norway has the world's second longest coastline of 103 000 km, with many islands, steep mountains, and deep, narrow fjords. All this makes the application of coastal altimetry particularly challenging in Norway.

Table 2.1. Typical mean values of time-varying range and geophysical corrections. The mean values were computed from six years of Jason-1 data. The geoid and MSS are assumed to have no significant temporal variation and mean values are therefore not shown. Taken from Andersen and Scharroo (2011).

Range or geophysical correction	Mean [cm]	Observation or model
Dry troposphere	−231	ECMWF (model) NCEP (model)
Wet troposphere	−16	Radiometer ECMWF (model)
Ionosphere	−8	Radiometer - smoothed dual frequency JPL GIM (model)
Sea-state bias	−5	BM4 (model) CLS NPARAM-GDRC (model)
Tides	~0-2	FES2004 (model) GOT4.7 (model)
Dynamic atmosphere	~0-2	IB (model, local pressure) MOG2D_IB (model)
Geoid/MSS	-	EGM2008 (geoid) DTU15 (MSS)

2.5 Mean dynamic topography

If we average Eq. (2.5) over a specific time period after applying geophysical corrections, SSH will give the MSS and DOT the MDT for that period, hence

$$\mathrm{MSS} = \mathrm{MDT} + N. \tag{2.8}$$

For ocean-circulation studies, MDT is the fundamental parameter, which will give an accurate picture of surface geostrophic currents and ocean mass transport (Bingham et al., 2008), and is given as

$$\mathrm{MDT} = \mathrm{MSS} - N. \tag{2.9}$$

Consequently, a better estimation of the geoid and MSS will improve the determination of the mean ocean circulation (Andersen and Knudsen, 2009).

Both MDT and physical heights over land, H, refer to the same reference surface, i.e., the geoid. With known geoid heights and ellipsoidal heights obtained by GNSS, physical heights are given as

$$H = h - N, \tag{2.10}$$

or can be obtained by spirit levelling. The connection between MDT over open ocean and physical heights over land along the coast is achieved through MSL measurements by TGs. The definition of MDT at TGs is analog to Eq. (2.10)

$$\mathrm{MDT} = h_{\mathrm{MSL}} - N, \tag{2.11}$$

where h_{MSL} is the ellipsoidal height of MSL. Eqs. (2.9) and (2.11) represent the geodetic approach of MDT determination, where the marine geoid is of crucial importance for using satellite altimetry in the determination of MDT and ocean currents (**Paper B**).

2.6 Geostrophic surface currents

Surface currents that flow horizontally in the ocean's surface layers (at depths of less than 100 to 200 m) are primarily driven by winds (Segar, 2018). Their patterns are determined by wind direction, Coriolis force from the Earth's rotation, and the position of landforms that interact with the currents (NOAA, 2019). Deep-ocean currents describe water-movement patterns far below the ocean's surface and the influence of winds. Deep-ocean currents are driven by density differences between ocean-water masses, which are caused by temperature and salinity variations (Segar, 2018).

The dominant forces in the horizontal are the pressure gradient and the Coriolis force. Within the ocean's interior away from the boundary layers, for time scales exceeding a few days and spatial resolutions exceeding a few tens of kilometers, the horizontal pressure gradient is balanced by the Coriolis force (Figure 2.8a). This balance is known as *geostrophic balance*. The equations for geostrophic balance are derived from the equations of motion assuming that (i) the flow has no acceleration, (ii) horizontal velocities are much larger than vertical, (iii) the only external force is gravity, and (iv) friction is small (Stewart, 2008).

The geostrophic approximation applied at the surface relates the MDT slope to geostrophic surface currents (Stewart, 2008) (Figure 2.8b). In terms of geodetic coordinates, the two velocity components of geostrophic surface currents are given by (e.g., Wunsch and Stammer, 1998)

$$u_\mathrm{s} = -\frac{g}{fR}\frac{\partial \mathrm{MDT}}{\partial \varphi} \tag{2.12}$$

and

$$v_\mathrm{s} = \frac{g}{fR\cos\varphi}\frac{\partial \mathrm{MDT}}{\partial \lambda}, \tag{2.13}$$

where u_s and v_s are the zonal (east-west) and meridional (north-south) components, respectively. R is the Earth's mean radius, g is gravity, φ is latitude, λ is longitude, and $f = 2\omega\sin\varphi$ is the Coriolis parameter, of which the angular velocity of the Earth ω forms a part.

Important limitations to the geostrophic assumptions are: (i) geostrophic currents cannot evolve with time because the balance ignores acceleration of the flow, (ii) the geostrophic balance does not apply within ~2° of the equator where the Coriolis force goes to zero (because $\sin\varphi = 0$), and (iii) the geostrophic balance ignores the influence of friction (Stewart, 2008).

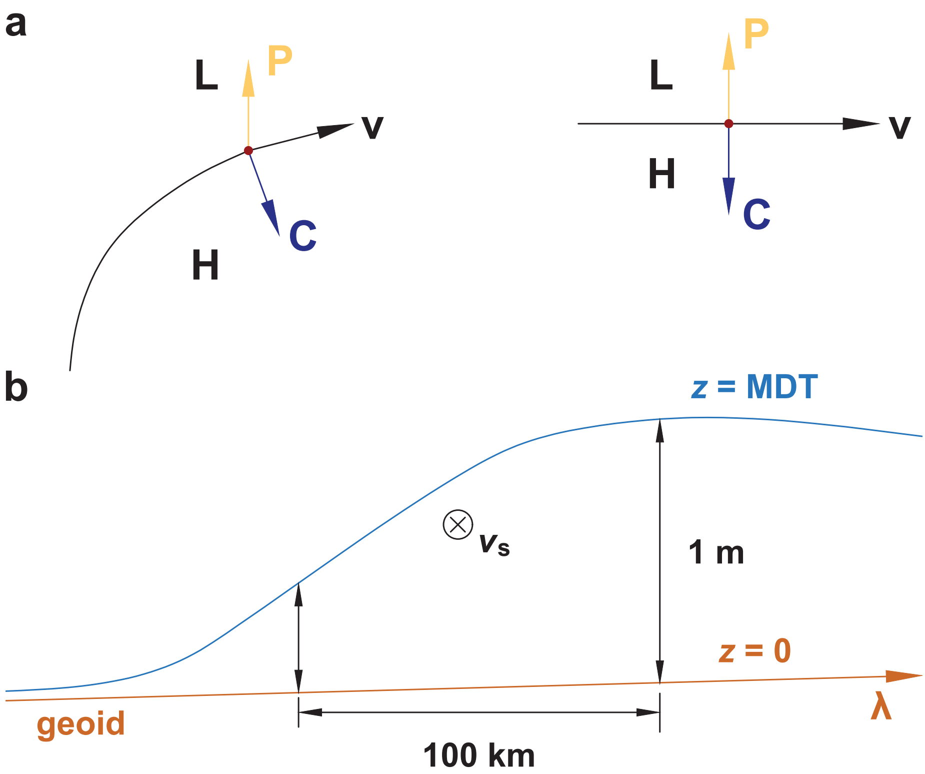

Figure 2.8. (**a**) Schematic representation of a geostrophic flow **v** initiated by a force balance between the pressure gradient **P** and the Coriolis force **C**. (**b**) Geostrophic surface currents are proportional to the slope of the MDT, a quantity that can be measured by satellite altimetery if the geoid is known. A slope of 1 m per 100 km gives a current magnitude of ~1 cm/s. In the northern hemisphere, v_s is into the paper. Adapted from Ophaug (2017); Segar (2018); Stewart (2008).

2.7 Data and methods

2.7.1 Paper A

The potential of SAR(In) altimetry along the Norwegian coast as well as the availability and quality of range and geophysical corrections applied onto CS2 SARIn observations were investigated in **Paper A**. 20 Hz CS2 SARIn observations for the 2010-2014 period were obtained from the Technical University of Denmark (DTU) Space retracking system (Stenseng and Andersen, 2012) and extracted within 45 km×45 km boxes around 22 TGs (Figure 2.10). The NARV TG was left out due to few CS2 observations. The 20 Hz *sea-level anomalies* were computed referring SSHs to DTU15 MSS and applying range and geophysical corrections listed in Table 2.3. Since the off-nadir range correction was not applied, the SARIn observations are degraded-SARIn observations excluding the phase information. A two-step outlier detection was employed: (i) CS2 observations over land were removed by applying a land mask and (ii) a within-track outlier detection was performed onto sea-level anomalies using a multiple t test. Since within-track CS2 observations are sampled very close in time, 20 Hz observations belonging to the same track were averaged. The availability of local OT predictions and air-pressure data (see Section 2.7.4) allowed the substitution of standard OT and IB corrections provided by FES2004 and ECMWF, respectively with local ones.

To quantify the performance of CS2 with respect to conventional altimeters, Jason-2, Envisat, and SARAL/AltiKa 1 Hz data were extracted from RADS (Radar Altimeter Database System) (Scharroo et al., 2013), with standard corrections applied (Table 2.3). Only data up to 66°N are available for Jason-2 due to its orbit configuration (Figure 2.1c). For each altimeter, the two nearest tracks to the TG were considered. As for CS2, a 45 km×45 km box was centered on the TG and shifted westwards by 0.1°. All observations within a box were averaged. For some TGs (HELG, TREG, MALO, TROM), the search radius had to be extended to find a valid track. TGs that lie further inside fjords than TGs closer to the open ocean have been assigned the same altimeter tracks as the latter. The time periods of conventional altimetry data were adapted as far as possible to the CS2 time period and are given in Table 4.1.

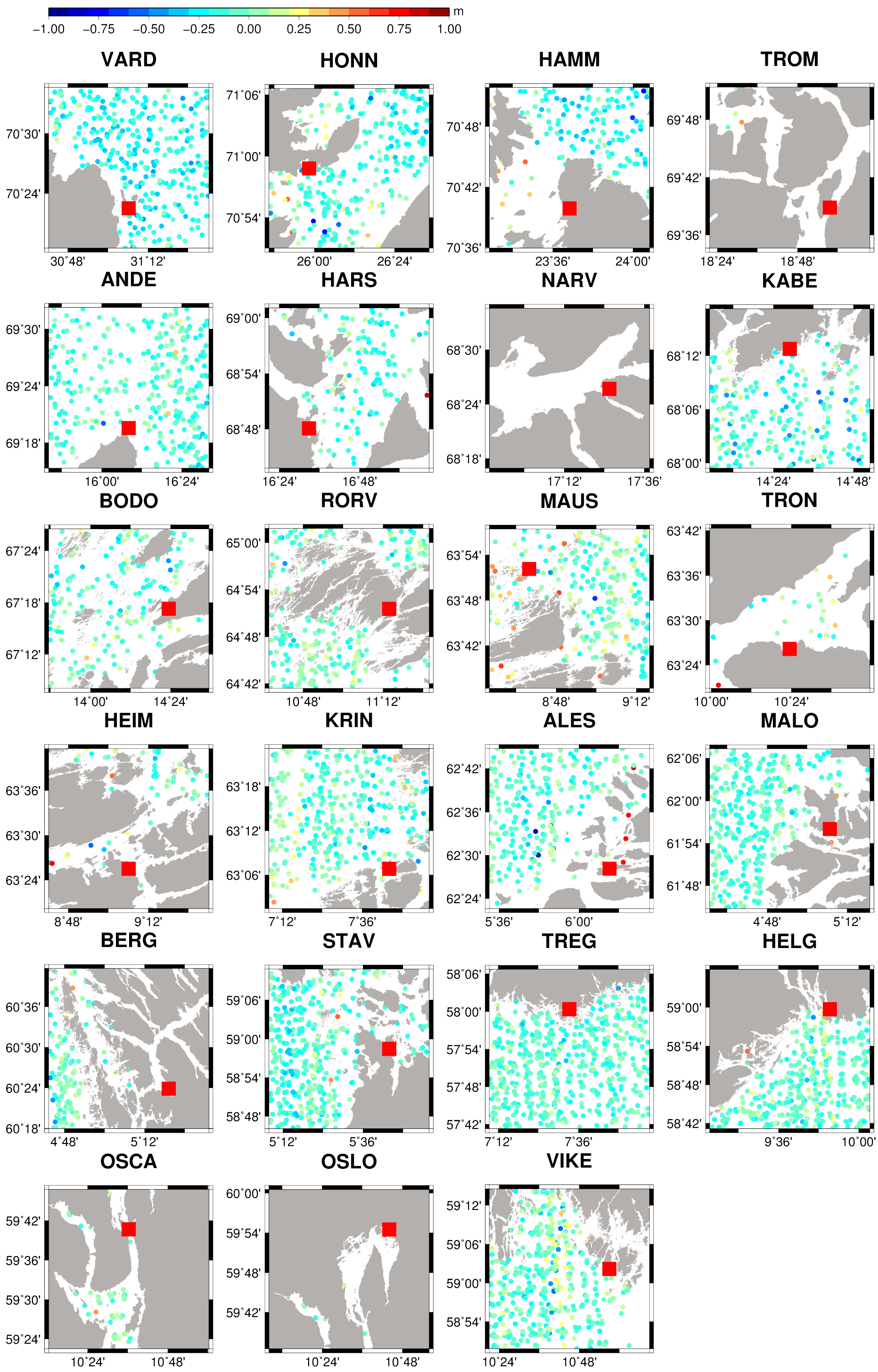

Figure 2.9. 1 Hz CryoSat-2 SARIn sea-level anomalies around 23 Norwegian tide gauges in 45 km×45 km boxes. Red squares indicate tide-gauge locations.

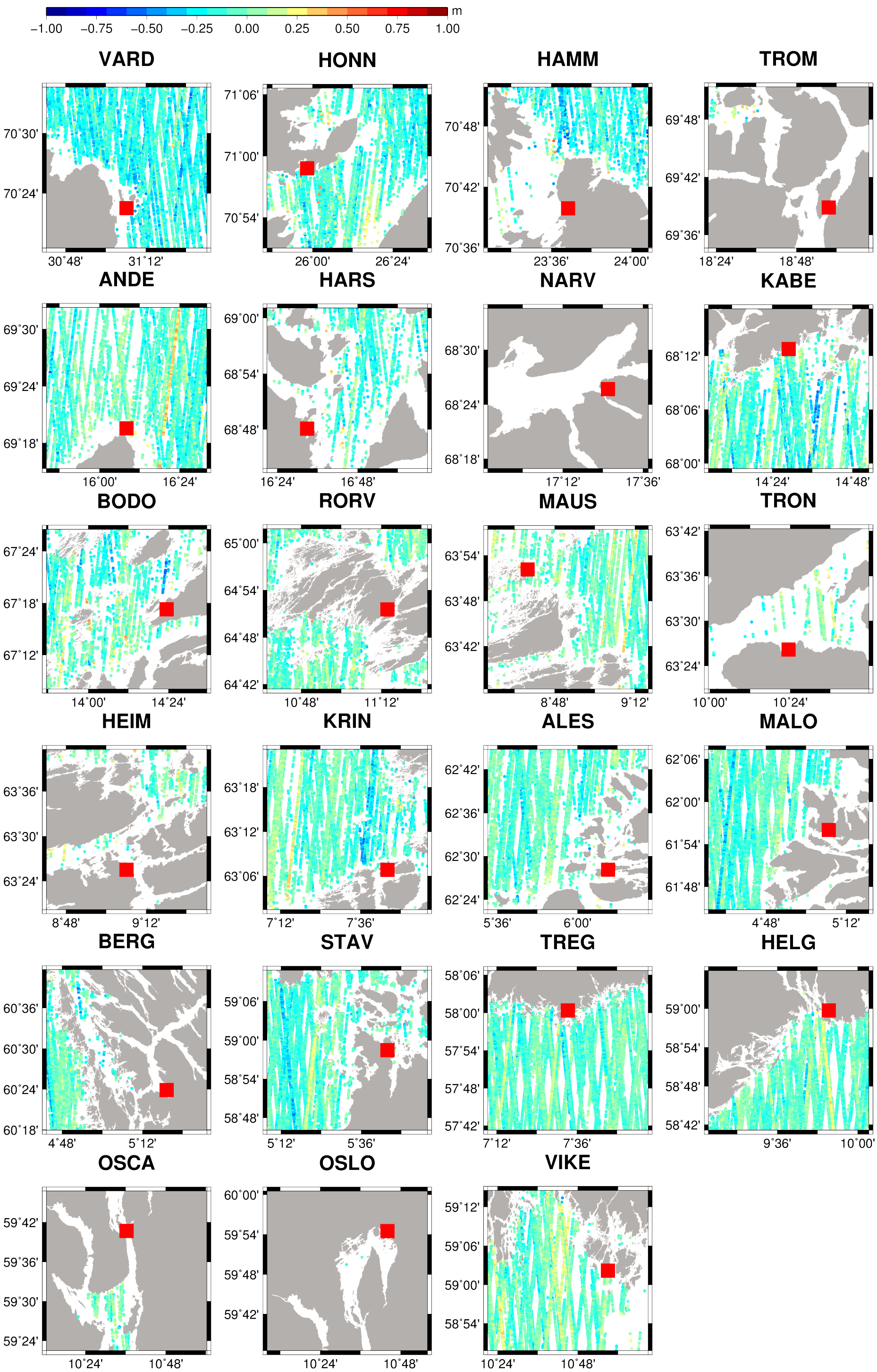

Figure 2.10. Same as Figure 2.9 but with 20 Hz CryoSat-2 SARIn sea-level anomalies.

Table 2.2. Mission specification for used altimeters in **Paper A**, **Paper B**, and **Paper D**: Envisat, Jason-2, SARAL/AltiKa, and CryoSat-2 (Jiang et al., 2017; Stammer and Cazenave, 2017; Vignudelli et al., 2011; Webb and Hall, 2016; Wingham et al., 2006).

	Envisat	Jason-2	SARAL	CryoSat-2
Mission duration	March 2002 - April 2012	June 2008 - present	February 2013 - present	April 2010 - present
Waveband	K_u- [a] and S-band [b]	K_u- and C-band [c]	K_a-band [d]	K_u-band
Latitudinal limit	81.45°	66°	81.45°	88°
Orbit type	near-circular, sun-synchronous	circular, non-sun-synchronous	sun-synchronous, LEO [e]	near-circular, polar, LEO
Altitude	782 km	1336 km	800 km	717 km
Inclination	98.55°	66°	98.55°	92°
Repeat period	35 (30 in phase C) days	9.9 days	35 days	369 (30) days
Footprint size along-track	2-10 km	8 km	8 km	2-10 km (250-400 m for SAR)
Equatorial ground-track spacing	80 km	315 km	80 km	7.7 km
Footprint area	183.7 km^2	287.0 km^2	102.0 km^2	173.0 km^2 (4.9 km^2 for SAR)
Altimeter	RA-2	Poseidon-3	AltiKa	SIRAL
Mode(s)	LRM	LRM	SAR	LRM, SAR, SARIn

[a] 13.575 GHz, [b] 3.2 GHz, [c] 5.3 GHz, [d] 35.75 GHz
[e] Low Earth orbit

Table 2.3. Range and geophysical corrections applied onto CryoSat-2 (Webb and Hall, 2016), SARAL/AltiKa, Envisat/C, and Jason-2 (Scharroo et al., 2013) data.

Correction	Observation or model for			
	CryoSat-2	SARAL/AltiKa	Envisat/C	Jason-2
Dry troposphere	ECMWF	ECMWF	ECMWF	ECMWF
Wet troposphere	ECMWF	Radiometer	Radiometer	Radiometer
Ionosphere	GIM	GIM	GIM	Dual frequency
Inverse barometer	ECMWF	ECMWF	ECMWF	ECMWF
High-frequency atmospheric variations	MOG2D	MOG2D	MOG2D	MOG2D
Ocean tide	FES2004	FES2004	FES2004	FES2004
Ocean-tide loading	FES2004	FES2004	FES2004	FES2004
Solid Earth tide	Cartwright/Edden	Cartwright/Edden	Cartwright/Edden	Cartwright/Edden
Pole tide	Wahr (1985)	Wahr (1985)	Wahr (1985)	Wahr (1985)
Mean sea surface	DTU15MSS	DTU13MSS	DTU13MSS	DTU13MSS
Bias	1.38 [a]	-	-	-

[a] Includes the difference between TOPEX and WGS84 ellipsoids as well as the SARIn range bias, which must be applied to baseline B products (Scagliola and Fornari, 2017).

2.7.2 Paper B

To determine MDTs in **Paper B**, LRM, SAR, and SARIn data from 2010 to 2015 were combined in the Norwegian coastal zone (Figure 2.3). LRM and SAR data were obtained through RADS, where SAR-mode observations are provided as so-called reduced-SAR (pseudo-LRM) observations; they are reduced-SAR observations because they were processed similarly to LRM data using incoherent processing of pulse-limited echos. SARIn data were obtained from the ESA Grid Processing on Demand (G-POD) service (Benveniste et al., 2016). The off-nadir range correction (Armitage and Davidson, 2014; Abulaitijiang et al., 2015) was applied onto the SARIn observations. Due to the geodetic orbit of CS2, DOT values were spatially averaged to get a temporal mean and avoid striping effects. Hence, observations in all three modes were combined and averaged in 20 km×20 km bins, and then interpolated onto a regular grid with 30″ resolution using least-squares collocation.

Three regional geoid models were used, namely, the operational regional geoid model for Norway, NMA2014, as described in Ophaug et al. (2015), the Nordic Geodetic Commission NKG2015 model (Ågren et al., 2015), and the European Gravimetric Geiod EGG2015 (Denker, 2016) (Table 2.4). All are based on the fifth release data from GOCE (Gravity Field and Steady-State Ocean Circulation Explorer). Geoid heights were transformed from the zero-tide system to the mean-tide system using Ekman (1989, Eq. (17)), and refer to the WGS84 ellipsoid. CS2 MDTs based on NKG2015, EGG2015, and NMA2014 are in the following referred to as $CS2_{NKG}$, $CS2_{EGG}$, and $CS2_{NMA}$, respectively. In **Paper B**, NARV, TRON, OSCA, and OSLO were omitted due to insufficient coverage by altimetry.

Table 2.4. Coverage and grid spacing of used geoid models.

Geoid model	φ [°]	λ [°]	$\Delta\varphi$ [°] × $\Delta\lambda$ [°]
NMA2014	$53° \leq \varphi \leq 77.99°$	$-15° \leq \varphi \leq 40°$	$0.01° \times 0.02°$
NKG2015	$53° \leq \varphi \leq 73°$	$0° \leq \varphi \leq 34°$	$0.01° \times 0.02°$
EGG2015	$25.01° \leq \varphi \leq 84.99°$	$-49.99° \leq \varphi \leq 69.99°$	$0.017° \times 0.017°$

2.7.3 Paper D

For the determination of VLM at TG locations in **Paper D**, 1 and 20 Hz SARIn observations for the 2010-2018 period were extracted in 45 km×45 km boxes around 20 TGs as shown in Figures 2.9 and 2.10, respectively. TGs in TROM, NARV, and OSLO did not have enough CS2 observations available for trend computations. Both 1 and 20 Hz SARIn data were obtained from G-POD with applied off-nadir range correction.

VLM signals from GIA can be computed by solving the sea-level equation (see Chapter 3 for more details):

$$\dot{S} = \dot{N} - \dot{U}. \tag{2.14}$$

The dot indicates time differentiation. All three quantities of the sea-level equation can be determined directly by time-series analysis of geodetic observations. TG records constrain relative sea-level change ($\dot{S}$), which is the variation of the sea surface relative to the solid Earth (Kuo et al., 2004). TGs are attached to the Earth's crust making their measurements affected by VLM. On the other hand, satellite altimetry and GPS provide independent measurements of absolute sea-level change $\dot{N}$ and VLM $\dot{U}$ with respect to a global geocentric reference frame, respectively. Based on Eq. (2.14), the combination of SSH from altimetry and relative sea-level records from TGs can be used to isolate the VLM component $\dot{U}$ (Nerem and Mitchum, 2002) as

$$\dot{U}(\varphi,\lambda) = \dot{N}(\varphi,\lambda) - \dot{S}(\varphi,\lambda), \tag{2.15}$$

where φ is latitude and λ is longitude.

Two TG data sets were combined with CS2 observations for VLM determination: (i) Permanent Service for Mean Sea Level (PSMSL) and (ii) Norwegian Mapping Authority (NMA) (see Section 2.7.4 for more details). Both were interpolated using nearest-neighbor interpolation onto 1 and 20 Hz time stamps of CS2 SARIn observations. VLM rates and standard deviations of residuals, s_e, were then computed by fitting a linear regression model to the differences. To account for serial correlation in time series, final rate uncertainties, σ, were estimated by

$$\sigma = s_e\sqrt{\frac{1+r^1}{1-r^1}}, \tag{2.16}$$

where r^1 is the lag-1 autocorrelation coefficient computed from residuals of the regression (Wilks, 2006). In the following, $\mathrm{VLM}_{\mathrm{1HzPSMSL}}$ and $\mathrm{VLM}_{\mathrm{1HzNMA}}$ refer to VLM rates estimated from TG observations from PSMSL and NMA, respectively, and 1 Hz CS2 data. Similarly, $\mathrm{VLM}_{\mathrm{20HzPSMSL}}$ and $\mathrm{VLM}_{\mathrm{20HzNMA}}$

are calculated from 20 Hz CS2 observations.

2.7.4 Validation data sets

Two validation data sets were used in **Paper A** and **Paper B**: (i) TG observations provided by both PSMSL and NMA as well as (ii) the numerical coastal ocean model NorKyst800 of the Norwegian Meteorological Institute. Both TG data sets were applied in **Paper D** for the determination of VLM in combination with CS2 observations.

Numerical coastal ocean model NorKyst800

Numerical ocean models give the part of SSH that arises from the ocean's circulation, i.e., sea level relative to an implicit geopotential surface. Thus, an average of such heights over a given time period will be equivalent to MDT.

The operational coastal ocean model in Figure 2.11a, NorKyst800 (Ådlandsvik et al., 2014), is based on the Regional Ocean Modeling System (ROMS) (Haidvogel et al., 2008). It was obtained from http://met.no/Hav_og_is/English/Access_to_data/, where it is available in form of daily mean values since July 2, 2012.

NorKyst800 is a free-surface, terrain-following hydrostatic numerical ocean model using finite difference horizontal and vertical coordinate systems. It is vertically discretized into 35 levels, where vertical coordinates follow a smoothed bathymetry. Moreover, it is forced by atmospheric data sets (mean sea-level pressure, wind, temperature, specific humidity, total cloud cover, and precipitation), where the equations of motion determine the model's response to these forces.

NorKyst800 uses a polar stereographic grid delimited by $55.81° \leq \varphi \leq 75.24°$ and $-1.56° \leq \lambda \leq 38.03°$, at an eddy-resolving resolution of 800 m. The NorKyst800 version of ROMS differs from the original version in that it replaces the atmospheric forcing by that of Røed and Debernard (2004), and additionally considers a sea-ice component (Budgell, 2005). It includes tidal forcing from the global TPXO model (Egbert and Erofeeva, 2002) and freshwater runoff from a hydrological model discharge at 256 main catchment areas.

To make our validation easier, NorKyst800 was resampled to a regular grid with $30''$ resolution using the NEARNEIGHBOR routine of Generic Mapping Tools (Wessel et al., 2013). The nearest-neighbor algorithm is favorable due to its simplicity and because it does no extrapolation at the coast. Typically the coastal grid point of the native ocean model grid is used, relieving us from any special treatment of the coastal points.

As NorKyst800 is forced by atmospheric pressure, it includes the IB effect. NorKyst800 was corrected for the IB effect applying the method by Wunsch and Stammer (1998) to a 0.25°×0.25° mean sea-level pressure field for the 2012-2015 period, obtained from ECMWF Interim Reanalysis (Dee et al., 2011).

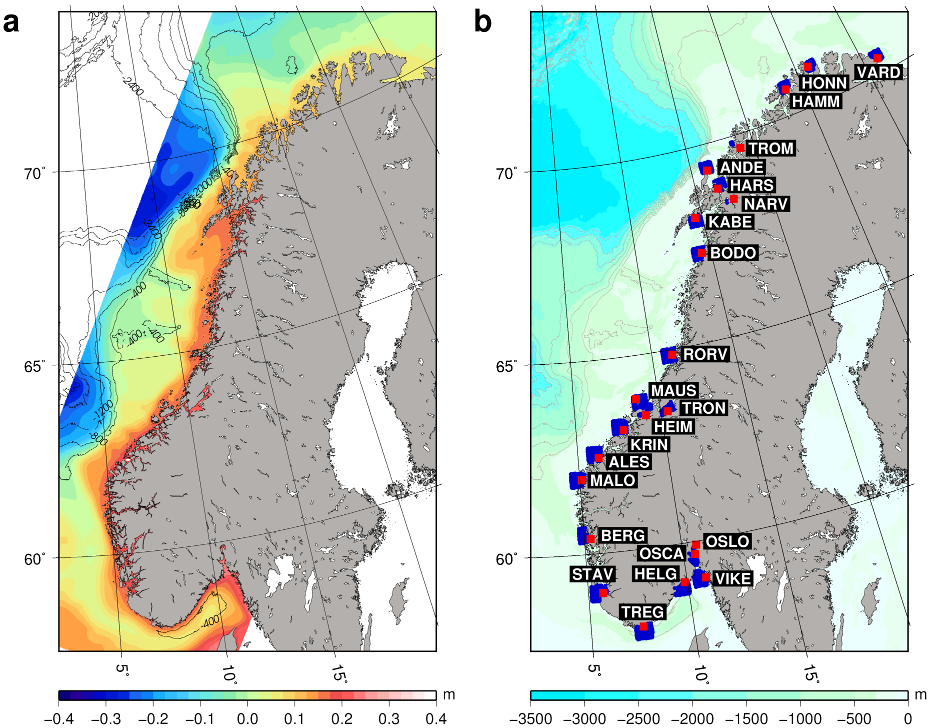

Figure 2.11. Validation data sets used in **Paper A** and **Paper B**. (**a**) Operational coastal ocean model NorKyst800 (Ådlandsvik et al., 2014). The mean value has been removed. (**b**) 23 tide gauges along the Norwegian coast. Red squares indicate the tide-gauge locations and blue squares the CryoSat-2 boxes. Bathymetry is from the General Bathymetric Charts of the Oceans (GEBCO) 2019 grid (GEBCO, 2019). In both (a-b), 400 m isobaths from the GEBCO 2019 grid are shown. In **Paper A**, the NARV tide gauge was left out due to few CryoSat-2 observations. In **Paper B**, NARV, TRON, OSCA, and OSLO were omitted due to the insufficient coverage by altimetry. In **Paper D**, tide gauges in TROM, NARV, and OSLO did not have enough CryoSat-2 observations available for trend computations.

Tide-gauge data

There are in total 23 TGs along the Norwegian coast (Figure 2.11b). Two TG data sets were used in this thesis: (i) monthly averaged sea-level observations obtained from PSMSL (Holgate et al., 2013) at http://www.psmsl.org/data/obtaining/ and (ii) 10-minute sea-level observations obtained from the NMA database. The PSMSL data are given as monthly averages in revised local reference (RLR). The NMA TG data are given as observed water levels referred to TG zero and include local air-pressure observations as well as predicted OT. The OT corrections were estimated in a harmonic analysis of several years of water-level observations from the current TG. An overview of applied TG data sets and their time spans in different papers is given in Table 4.1.

In **Paper B**, mean sea-level observations were given as heights in the national height system Normalnull 2000 (NN2000), H_{MSL}. As none of the considered TGs have a tie between TG benchmark and GNSS benchmark, ellipsoidal heights of MSL, h_{MSL}, were determined using the Norwegian reference surface HREF2016A (Solheim, 2000) and the simple relation: $h_{\mathrm{MSL}} = H_{\mathrm{MSL}} + \mathrm{HREF}$. NKG2015, EGG2015, and NMA2014 were linearly interpolated onto the TG locations, and by Eq. (2.11), $\mathrm{TG}_{\mathrm{NKG}}$, $\mathrm{TG}_{\mathrm{EGG}}$, and $\mathrm{TG}_{\mathrm{NMA}}$ were determined, respectively.

Chapter 3

Glacial isostatic adjustment

The following overview of theoretical basics of the sea-level equation (SLE) is based on Farrell and Clark (1976); Mitrovica and Milne (2003); Spada and Stocchi (2006); Spada (2017); Whitehouse (2009). The task of the SLE is to describe sea-level changes as a function of ice-thickness changes and rheology that were assumed for mantle and lithosphere. The main GIA-modelling parameters, i.e., rheology and surface loads are presented as well as modifications to the SLE. In addition, a brief overview of GIA-modelling outputs is given.

GIA is the ongoing response of the Earth to mass redistribution during a glacial cycle. Each glacial cycle lasts ~100 000 years (100 ka, 1000 years = 1 ka), including a long glaciation phase of ~90 ka and a much shorter deglaciation phase. The deglaciation phase of the current ice age started ~20 ka before present (BP), at the LGM, and ended ~6 ka BP (Tsuji et al., 2009), when most of the Pleistocene ice sheets have melted. As shown in Figure 3.3, Canada, northeastern United States, British Isles, Fennoscandia, as well as Greenland and Antarctica were covered by major ice sheets (Tsuji et al., 2009; Steffen and Wu, 2011). During a glacial phase, lower temperatures result in the growth of ice sheets, thereby removing water from the oceans and causing a relative sea-level fall. In a deglaciation phase, ice sheets melt, water flows back into the oceans, and relative sea level rises. The transfer of water from oceans to ice sheets resulted in a sea-level fall of ~130 m. Water and ice masses act as time-variable load. The Earth deforms in response to this load, either subsiding under the load of ice sheets or filled oceanic basins, or rebounding once the ice sheets melt or water is removed from the oceanic basins. The deformation is isostatic, which means that it happens in the attempt to return the Earth to a state of equilibrium (Whitehouse, 2009). GIA does not only describe the ongoing viscous response to past ice-sheet changes but also includes other effects. It is related to (i) global and regional temporal variations of the Earth's gravity field, (ii) three-dimensional (3D) displacements of the Earth's surface in the near and far field of former ice sheets, (iii) stress variations in the crust and mantle due to loading and unloading, and (iv) fluctuations of the Earth's rotational axis (lateral movements of the pole and changes in the length of day) (Spada, 2017).

The absolute sea level (SL) is given as an offset between two surfaces

$$SL(\omega, t) = R_{\mathrm{SS}}(\omega, t) - R_{\mathrm{SE}}(\omega, t), \tag{3.1}$$

where $\omega \equiv (\varphi, \lambda)$, φ is latitude and λ longitude, t is time, and R_{SS} and R_{SE} are radii of the equipotential sea surface (SS) and the solid surface of the Earth (SE), respectively, relative to the Earth's center of mass. The SLE does not directly involve SL; rather it involves the variation of absolute sea level relative to an initial reference value at time t_0, i.e., the *sea-level change* S. Hence, the sea-level change S at a given time BP, t_{BP}, is

$$S(\omega, t_{\mathrm{BP}}) = SL(\omega, t_{\mathrm{BP}}) - SL(\omega, t_0). \tag{3.2}$$

For the present time, t_{P}, we can similarly write

$$S(\omega, t_{\mathrm{P}}) = SL(\omega, t_{\mathrm{P}}) - SL(\omega, t_0). \tag{3.3}$$

For studies of past sea-level variations, it is convenient to introduce *relative sea level* (RSL)

$$\mathrm{RSL}(\omega, t_{\mathrm{BP}}) = SL(\omega, t_{\mathrm{BP}}) - SL(\omega, t_{\mathrm{P}}), \tag{3.4}$$

which refers sea level to the present datum. According to Eqs. (3.2) and (3.3), RSL in Eq. (3.4) can be directly related to the sea-level change S as

$$\mathrm{RSL}(\omega, t_{\mathrm{BP}}) = S(\omega, t_{\mathrm{BP}}) - S(\omega, t_{\mathrm{P}}). \tag{3.5}$$

The sea-level change in Eq. (3.2) can be written in a new form by introducing the *sea-surface variation* N

$$N(\omega, t) = R_{\mathrm{SS}}(\omega, t) - R_{\mathrm{SS}}(\omega, t_0), \tag{3.6}$$

also referred to as *absolute sea-level change*, and the *vertical displacement* of the Earth's solid surface U

$$U(\omega, t) = R_{\mathrm{SE}}(\omega, t) - R_{\mathrm{SE}}(\omega, t_0), \tag{3.7}$$

which along with Eq. (3.1) gives

$$S(\omega, t) = N(\omega, t) - U(\omega, t). \tag{3.8}$$

3.1 The sea-level equation

Redistribution of mass on the Earth's surface caused by cryosphere and other climate phenomena, such as wind stress, ocean currents, and land-water storage perturbs the gravitational and centrifugal (rotational) potential of the Earth (Adhikari et al., 2016). In case of a rigid or elastic Earth, sea-level changes assume instantaneous changes following a redistribution of ice masses. In reality, the viscous properties of the mantle result in a delayed response to loading/unloading. This delayed response occurs since the mantle material flows back to areas previously covered by ice or away from a glaciated region, and in turn, changes the mass distribution in the Earth's interior, i.e., the gravitational potential. Continuously changing gravitational potential causes variations in the separation between the solid and fluid surface, and hence, variations in sea level. Accordingly, the perturbation to the gravitational potential Φ is used to determine the resulting change in sea level at all points on the surface of the Earth. In the following, the definition of the SLE is given along with an overview of Green's functions; starting from a rigid Earth model through an elastic one to a final viscoelastic Earth model.

3.1.1 The Green's functions

The Green's functions (GFs) quantify the variation of the gravitational potential and 3D displacements when a point-wise, impulsive load is applied to the surface of a spherically symmetric, layered Earth. For multi-layered models, the GFs are computed numerically by means of load-deformation coefficients (LDCs). The Green's function (GF) approach holds for elastic and viscoelastic Earth models. Once the viscoelastic GFs have been constructed, the response of the Earth to the surface loads of arbitrary geometries and time histories can be obtained by spatio-temporal convolution (Spada and Stocchi, 2006). The type of GFs depends on the rheology profile adopted for the Earth model (Table 3.1). Here, GFs for the three components of the displacement field as well as the perturbation gravitational potential are introduced for a rigid, elastic, and viscoelastic Earth model.

Rigid Earth

The gravitational potential exerted by a localized mass on the Earth's surface is

$$\Phi^r(d,t) = \frac{G\mu(t)}{d}, \tag{3.9}$$

where G is the gravitational constant ($\sim 6.674 \cdot 10^{-11}$ m^{3}kg^{-1}s^{-2}), μ the dynamic mass ($\mu(t) = \delta(t)\, m_{\mathrm{s}}$, where $\delta(t)$ is Dirac's delta and m_{s} the static mass), and d the distance between the point load and computation point. The superscript r denotes that we are dealing with a rigid Earth. Since Φ^r only results from the gravitational attraction of the imposed point mass, it is referred to as *direct gravitational potential*. By simple trigonometry,

$$d(\alpha) = 2\,a \sin\left(\frac{\alpha}{2}\right), \tag{3.10}$$

where α is the spherical distance between the computation point with respect to the point load, and a the Earth's radius. This allows to rewrite Eq. (3.9) as

$$\Phi^r(\alpha, t) = \frac{a\,\gamma\,m_\mathrm{s}\,\delta(t)}{2\,M_\mathrm{E}\,\sin\left(\frac{\alpha}{2}\right)}, \tag{3.11}$$

where

$$\gamma = \frac{G\,M_\mathrm{E}}{a^2} \tag{3.12}$$

is the surface gravity acceleration in spherical approximation, and M_E is the mass of the Earth. The GF for the direct gravitational potential of a rigid Earth G^r_Φ is defined as the potential variation per unit mass

$$\begin{aligned} G^r_\Phi(\alpha, t) &= \frac{\Phi^r(\alpha, t)}{m_\mathrm{s}} \\ &= \frac{a\,\gamma\,\delta(t)}{2\,M_\mathrm{E}\,\sin\left(\frac{\alpha}{2}\right)}. \end{aligned} \tag{3.13}$$

An equivalent expression for the GF can be obtained using the Legendre sum

$$\sum_{n=0}^{\infty} P_n(\cos\alpha) = \frac{1}{2\,\sin\left(\frac{\alpha}{2}\right)}, \tag{3.14}$$

where $P_n(\cos\alpha)$ is the Legendre polynomial of harmonic degree n. Hence, the spectral form of G^r_Φ in Eq. (3.13) is

$$G^r_\Phi(\alpha, t) = \delta(t) \sum_{n=0}^{\infty} \Phi^r_n\, P_n(\cos\alpha), \tag{3.15}$$

with

$$\Phi^r_n = \frac{a\,\gamma}{M_\mathrm{E}}. \tag{3.16}$$

Elastic Earth

A unit mass placed on the Earth's surface causes two effects in case an elastic Earth is considered. First, the Earth yields under the load and a displacement field arises as a consequence. Secondly, there is a variation of gravitational potential following the change of the Earth's shape, which adds to the direct potential and is termed *perturbation gravitational potential.* In analogy with Eq. (3.15), the corresponding GF can be written as

$$G^e_\Phi(\alpha,t) = \delta(t)\sum_{n=0}^{\infty}\Phi^e_n P_n(\cos\alpha), \tag{3.17}$$

which is in phase with G^r_Φ as a consequence of elasticity. In addition, the spectral coefficients Φ^e_n are degree-wise proportional to Φ^r_n

$$\Phi^e_n = k^e_n\Phi^r_n, \tag{3.18}$$

where the non-dimensional number k^e_n is the *elastic load-deformation coefficient* (LDC) for the perturbation potential. The total GF for the gravitational potential stems from a rigid and elastic component

$$G^E_\Phi(\alpha,t) = G^r_\Phi(\alpha,t) + G^e_\Phi(\alpha,t). \tag{3.19}$$

Substituting Eqs. (3.15) and (3.17) into the above expression gives the spectral form for G^E_Φ

$$G^E_\Phi(\alpha,t) = \delta(t)\frac{a\gamma}{M_\mathrm{E}}\sum_{n=0}^{\infty}(1+k^e_n)P_n(\cos\alpha). \tag{3.20}$$

At the surface of the Earth, the elastic displacement induced by the applied load can be expressed as

$$\vec{u}(\alpha,t) = G^e_\mathrm{U}(\alpha,t)\,\hat{r} + G^e_\mathrm{V}(\alpha,t)\,\hat{\alpha}, \tag{3.21}$$

where $\hat{r}$ and $\hat{\alpha}$ are unit vectors in the directions of the increasing radius and spherical distance. G^e_U and G^e_V are related to vertical and horizontal components of the displacement, respectively. We write the displacement GFs in analogy to Eq. (3.19) as

$$G^E_\mathrm{U}(\alpha,t) = G^r_\mathrm{U}(\alpha,t) + G^e_\mathrm{U}(\alpha,t) \tag{3.22}$$

and

$$G^E_\mathrm{V}(\alpha,t) = G^r_\mathrm{V}(\alpha,t) + G^e_\mathrm{V}(\alpha,t) \tag{3.23}$$

where $G^r_\mathrm{U}(\alpha,t) = G^r_\mathrm{V}(\alpha,t) = 0$ since the Earth is rigid. The spectral form of the vertical and horizontal components of displacement by means of appropriate

LDCs can be expressed as

$$G_{\mathrm{U}}^{e}(\alpha,t)=\delta(t)\sum_{n=0}^{\infty}u_n^e\,P_n(\cos\alpha) \tag{3.24}$$

and

$$G_{\mathrm{V}}^{e}(\alpha,t)=\delta(t)\sum_{n=0}^{\infty}v_n^e\,\frac{\partial P_n(\cos\alpha)}{\partial\alpha}, \tag{3.25}$$

where

$$u_n^e=h_n^e\,\frac{\Phi_n^r}{\gamma} \tag{3.26}$$

and

$$v_n^e=l_n^e\,\frac{\Phi_n^r}{\gamma} \tag{3.27}$$

define the elastic LDCs for the vertical and horizontal displacement. From above, the GFs associated to vertical and horizontal displacement are

$$G_{\mathrm{U}}^{e}(\alpha,t)=\delta(t)\,\frac{a}{M_{\mathrm{E}}}\sum_{n=0}^{\infty}h_n^e\,P_n(\cos\alpha) \tag{3.28}$$

and

$$G_{\mathrm{V}}^{e}(\alpha,t)=\delta(t)\,\frac{a}{M_{\mathrm{E}}}\sum_{n=0}^{\infty}l_n^e\,\frac{\partial P_n(\cos\alpha)}{\partial\alpha}, \tag{3.29}$$

respectively. Along with Eq. (3.20), they create the basic set of GFs for an elastic Earth.

Viscoelastic Earth

Viscoelasticity introduces a delayed response of the Earth to the surface load. For a spherically symmetric, layered, and linear viscoelastic Earth, the GF relative to the total perturbation potential is

$$G_{\Phi}^{VE}(\alpha,t)=G_{\Phi}^{E}(\alpha,t)+G_{\Phi}^{v}(\alpha,t). \tag{3.30}$$

The instantaneous elastic component is given by Eq. (3.20), and the delayed viscous component G_{Φ}^{v} by

$$G_{\Phi}^{v}(\alpha,t)=H(t)\,\frac{a\gamma}{M_{\mathrm{E}}}\sum_{n=0}^{\infty}\left(\sum_{m=1}^{M}k_{nm}^{v}\,e^{s_{nm}t}\right)P_n(\cos\alpha), \tag{3.31}$$

where

$$H(t)=\begin{cases}0 & t<0\\ 1 & t\geq 0\end{cases}$$

is the Heaviside step function, k^{v}_{nm} are the *viscous* LDCs for the total perturbation potential, and

$$s_{nm} = \frac{-1}{\tau_{nm}}. \tag{3.32}$$

The term s_{nm} describes the relaxation of the Earth to the imposed impulsive unit load. In the case of an incompressible viscoelastic body, the terms s_{nm} are the roots of an algebraic equation of degree M, with M depending on the number of layers of the Earth model employed and the nature of the interfaces between the layers. The parameters τ_{nm} in Eq. (3.32) are the *relaxation times* of the adopted Earth model (Spada, 2003). The couple $\{k^{v}_{nm}, s_{nm}\}$ ($n = 0, 1, \ldots$ and $m = 1, 2, \ldots, M$) represents the m-th *viscoelastic mode* of degree n. Substituting Eqs. (3.20) and (3.31) into (3.30), the complete form of the viscoelastic GF for the total perturbation potential follows as

$$G^{VE}_{\Phi}(\alpha, t) = \frac{a\gamma}{M_{\mathrm{E}}} \sum_{n=0}^{\infty} \left(\delta(t)\,(1 + k^{e}_{n}) + H(t) \sum_{m=1}^{M} k^{v}_{nm}\, e^{s_{nm} t} \right) P_n(\cos\alpha). \tag{3.33}$$

The GFs for vertical and horizontal components of displacement can be similarly written as the sum of elastic and viscous parts

$$G^{VE}_{\mathrm{U}}(\alpha, t) = G^{E}_{\mathrm{U}}(\alpha, t) + G^{v}_{\mathrm{U}}(\alpha, t) \tag{3.34}$$

and

$$G^{VE}_{\mathrm{V}}(\alpha, t) = G^{E}_{\mathrm{V}}(\alpha, t) + G^{v}_{\mathrm{V}}(\alpha, t). \tag{3.35}$$

The elastic components are given in Eqs. (3.28) and (3.29), and viscous components are

$$G^{v}_{\mathrm{U}}(\alpha, t) = H(t)\, \frac{a}{M_{\mathrm{E}}} \sum_{n=0}^{\infty} \left(\sum_{m=1}^{M} h^{v}_{nm}\, e^{s_{nm} t} \right) P_n(\cos\alpha) \tag{3.36}$$

and

$$G^{v}_{\mathrm{V}}(\alpha, t) = H(t)\, \frac{a}{M_{\mathrm{E}}} \sum_{n=0}^{\infty} \left(\sum_{m=1}^{M} l^{v}_{nm}\, e^{s_{nm} t} \right) \frac{P_n(\cos\alpha)}{\partial\alpha}, \tag{3.37}$$

where h^{v}_{nm} and l^{v}_{nm} are the *viscous* LDCs relative to the radial and horizontal components of displacement, respectively. The total GFs for the components of displacement are

$$G^{VE}_{\mathrm{U}}(\alpha, t) = \frac{a}{M_{\mathrm{E}}} \sum_{n=0}^{\infty} \left(\delta(t)\, h^{e}_{n} + H(t) \sum_{m=1}^{M} h^{v}_{nm}\, e^{s_{nm} t} \right) P_n(\cos\alpha) \tag{3.38}$$

and

$$G_{\mathrm{V}}^{VE}(\alpha,t) = \frac{a}{M_{\mathrm{E}}} \sum_{n=0}^{\infty} \left(\delta(t)\, l_n^e + H(t) \sum_{m=1}^{M} l_{nm}^v \, e^{s_{nm} t} \right) \frac{P_n(\cos\alpha)}{\partial \alpha}. \tag{3.39}$$

A more compact form for the GFs of a viscoelastic Earth can be established introducing the time-dependent LDCs

$$\begin{Bmatrix} k_n^{VE} \\ h_n^{VE} \\ l_n^{VE} \end{Bmatrix} (t) = \begin{Bmatrix} 1 + k_n^e \\ h_n^e \\ l_n^e \end{Bmatrix} \delta(t) + \sum_{m=1}^{M} H(t) \begin{Bmatrix} k_{nm}^v \\ h_{nm}^v \\ l_{nm}^v \end{Bmatrix} e^{s_{nm} t}, \tag{3.40}$$

which finally allows to write

$$\begin{Bmatrix} \frac{1}{\gamma} G_{\Phi}^{VE} \\ G_{\mathrm{U}}^{VE} \\ G_{\mathrm{V}}^{VE} \end{Bmatrix} (\alpha, t) = \frac{a}{M_{\mathrm{E}}} \sum_{n=0}^{\infty} \begin{Bmatrix} k_n^{VE} \\ h_n^{VE} \\ l_n^{VE} \end{Bmatrix} (t) \begin{Bmatrix} 1 \\ 1 \\ \partial_\alpha \end{Bmatrix} P_n(\cos\alpha) \tag{3.41}$$

with $\partial_\alpha \equiv \frac{\partial}{\partial \alpha}$. In addition, a systematic overview of GFs for different kinds of Earth models is given in Table 3.1.

Load-deformation coefficients For each Legendre degree n, the equation for the static equilibrium of the Earth under all elastic and gravitational forces is solved. Solving this equation with an appropriate boundary condition leads to three constants, i.e., LDCs. The LDCs are obtained by the normal modes technique. They depend on degree n and the structure of the employed Earth model, and have a simple physical interpretation. The LDCs represent a transfer function between some load applied onto the surface and the Earth's response. The response is given in terms of

(i) vertical displacement h_n^{VE},

(ii) horizontal displacement l_n^{VE}, and

(iii) potential perturbation k_n^{VE}.

The elastic LDCs k_n^e, l_n^e, and h_n^e describe the response to the impulsive unit load. Therefore, their amplitude does not depend on the viscosity profile of the mantle but only on the the density and shear-modulus profile. k_{nm}^v, l_n^v, and h_{nm}^v are viscous amplitudes (or viscous residuals) of the LDCs, and their values depends on viscosity, density, and rigidity (Spada, 2003).

Table 3.1. Systematization of Green's functions for rigid, elastic, and viscoelastic Earth models.

	Green's functions
Rigid Earth	$G^r_\Phi(\alpha,t)=\frac{a\gamma}{M_\mathrm{E}}\delta(t)\sum_{n=0}^{\infty}P_n(\cos\alpha)$
Elastic Earth	$\left\{\begin{matrix}\frac{1}{\gamma}G^E_\Phi\\ G^E_U\\ G^E_V\end{matrix}\right\}(\alpha,t)=\frac{a}{M_\mathrm{E}}\sum_{n=0}^{\infty}\left\{\begin{matrix}k_n\\ h_n\\ l_n\end{matrix}\right\}(t)\left\{\begin{matrix}1\\ 1\\ \partial_\alpha{}^{\mathrm{a}}\end{matrix}\right\}P_n(\cos\alpha)$, where $\left\{\begin{matrix}k_n\\ h_n\\ l_n\end{matrix}\right\}(t)=\left\{\begin{matrix}1+k^e_n\\ h^e_n\\ l^e_n\end{matrix}\right\}\delta(t)$
Viscoelastic Earth	$\left\{\begin{matrix}\frac{1}{\gamma}G^{VE}_\Phi\\ G^{VE}_U\\ G^{VE}_V\end{matrix}\right\}(\alpha,t)=\frac{a}{M_\mathrm{E}}\sum_{n=0}^{\infty}\left\{\begin{matrix}k_n\\ h_n\\ l_n\end{matrix}\right\}(t)\left\{\begin{matrix}1\\ 1\\ \partial_\alpha\end{matrix}\right\}P_n(\cos\alpha)$, where $\left\{\begin{matrix}k_n\\ h_n\\ l_n\end{matrix}\right\}(t)=\left\{\begin{matrix}1+k^e_n\\ h^e_n\\ l^e_n\end{matrix}\right\}\delta(t)+\sum_{m=1}^{M}H(t)\left\{\begin{matrix}k^v_{nm}\\ h^v_{nm}\\ l^v_{nm}\end{matrix}\right\}e^{\frac{-t}{\tau_{nm}}}$

[a] $\partial_\alpha\equiv\frac{\partial}{\partial\alpha}$

The sea-level Green's function for a viscoelastic Earth

The sea-level GF for a viscoelastic Earth is then

$$\frac{G^{VE}_\mathrm{S}}{\gamma}(\alpha,t)=\frac{G^{VE}_\Phi}{\gamma}-G^{VE}_\mathrm{U}. \tag{3.42}$$

Substituting Eqs. (3.30) and (3.34) into Eq. (3.42), we obtain

$$\frac{G^{VE}_\mathrm{S}}{\gamma}(\alpha,t)=\frac{G^r_\Phi}{\gamma}+\left(\frac{G^e_\Phi}{\gamma}-G^e_\mathrm{U}\right)+\left(\frac{G^v_\Phi}{\gamma}-G^v_\mathrm{U}\right), \tag{3.43}$$

where the first, second, and third term represent rigid, elastic, and viscoelastic components of G^{VE}_S, respectively. Finally, the sea-level GF for a viscoelastic

Earth is given as

$$\frac{G_{\mathrm{S}}^{VE}}{\gamma}(\alpha,t)=\frac{a}{M_{\mathrm{E}}}\Bigg(\sum_{n=0}^{\infty}(1+k_n^e-h_n^e)\,P_n(\cos\alpha)\,\delta(t)\\ +\sum_{n=0}^{\infty}\bigg(\sum_{m=1}^{M}(k_{nm}^{v}-h_{nm}^{v})\,e^{s_{nm}t}\bigg)P_n(\cos\alpha)\,H(t)\Bigg). \tag{3.44}$$

The rheological properties are contained in the GFs. The GFs work for any kind of linear (i.e., spherically symmetric or one-dimensional (1D)) viscoelastic body, in which all its geophysical properties

- elastic model parameters (shear modulus or modulus of rigidity $\mu(r)$ and Lame's first parameter $\lambda(r)$),
- density $\rho(r)$, and
- the rheological parameter, i.e., viscosity $\eta(r)$

depend on the radius r.

3.1.2 Derivation of the sea-level equation

According to Farrell and Clark (1976), the sea-surface variation N in Eq. (3.6) can be written as

$$N(\omega,t)=G(\omega,t)+c(t), \tag{3.45}$$

where the *geoid height variation*, $G(\omega,t)$, is given by

$$G(\omega,t)=\frac{\Phi}{\gamma}. \tag{3.46}$$

Inserting Eq. (3.45) into Eq. (3.8) gives

$$S(\omega,t)=\frac{\Phi}{\gamma}-U+c. \tag{3.47}$$

To determine c, we impose the constrain of mass conservation. Since the mass of the Earth is constant, the total mass of the system (oceans and ice) must be the same in the reference state as well as in the current state

$$M_{\mathrm{I}}(t)+M_{\mathrm{O}}(t)=0, \tag{3.48}$$

where

$$M_{\mathrm{I}}(t)=\int_{\mathrm{I}}\rho_{\mathrm{I}}\,I\,\mathrm{d}A \tag{3.49}$$

is the mass variation of the ice sheets, ρ_I the ice density (~920 kg/m^3), dA the element of area. The integral is defined over the ice-covered regions, and

$$I(\omega, t) = T(\omega, t) - T(\omega, t_0), \tag{3.50}$$

is the variation of the thickness T of the continental ice sheets. Additionally,

$$M_\mathrm{O}(t) = \int_\mathrm{O} \rho_\mathrm{w} S \,\mathrm{d}A \tag{3.51}$$

is the mass variation of the oceans over which the integral is defined, and ρ_w is the ocean-water density (~1000 kg/m^3). Substituting Eqs. (3.49) and (3.51) into (3.48) using (3.47) gives

$$c(t) = S^E - \left\langle \frac{\Phi}{\gamma} - U \right\rangle, \tag{3.52}$$

where the notation $\langle\rangle$ is used to denote the mean value of a variable over oceans and A_O is the (constant) area covered by oceans. The term

$$S^E = -\frac{M_\mathrm{I}}{\rho_\mathrm{w} A_\mathrm{O}}$$

represents the initial approximation, i.e., the *eustatic term* of the SLE. From Eqs. (3.47) and (3.52), the SLE takes the following form

$$S(\omega, t) = \left(\frac{\Phi}{\gamma} - U\right) + S^E - \left\langle \frac{\Phi}{\gamma} - U \right\rangle. \tag{3.53}$$

We define a space-time *loading function*, L, which incorporates all masses (water and ice). The space-time loading function equals $\rho_\mathrm{w} S$ over oceans and $\rho_\mathrm{I} I$ over ice for unit time

$$L(\omega, t) = \rho_\mathrm{I} I + \rho_\mathrm{w} S. \tag{3.54}$$

The total variation of the gravitational potential stems from two terms

$$\Phi(\omega, t) = \rho_\mathrm{I} G_\Phi^{VE} \otimes_\mathrm{I} I + \rho_\mathrm{w} G_\Phi^{VE} \otimes_\mathrm{O} S, \tag{3.55}$$

where G_Φ^{VE} is the GF for the total perturbation potential given in Eq. (3.33), and $\otimes_\mathrm{I}$ and $\otimes_\mathrm{O}$ are spatio-temporal convolutions over the ice- and ocean-covered regions, respectively. Similarly, the vertical displacement is

$$U(\omega, t) = \rho_\mathrm{I} G_U^{VE} \otimes_\mathrm{I} I + \rho_\mathrm{w} G_U^{VE} \otimes_\mathrm{O} S, \tag{3.56}$$

where G_U^{VE} is the corresponding GF given in Eq. (3.38).

Convolving the GF with the mass distribution function L gives the total change in sea level. Substituting Eqs. (3.55) and (3.56) into (3.53) we obtain

$$S(\omega,t) = \frac{\rho_\mathrm{I}}{\gamma} G_S^{VE} \otimes_\mathrm{I} I + \frac{\rho_\mathrm{w}}{\gamma} G_S^{VE} \otimes_\mathrm{O} S + S^E - \frac{\rho_\mathrm{I}}{\gamma} \left\langle G_S^{VE} \otimes_\mathrm{I} I \right\rangle - \frac{\rho_\mathrm{w}}{\gamma} \left\langle G_S^{VE} \otimes_\mathrm{O} S \right\rangle, \tag{3.57}$$

which represents the form of SLE for geophysical applications. The quantity that enters directly into the SLE is the sea-level GF given in Eq. (3.44). This form of the SLE was first obtained by Farrell and Clark (1976), and is referred to as *gravitationally self-consistent* since the sea-level variations predicted by SLE are consistent with the variations of the gravitational field induced by the time-evolving surface loads.

The evaluation of the SLE based on the viscoelastic LDC theory using the (pseudo)spectral method (Mitrovica and Pelier, 1991) in a spherical-harmonic domain has been the standard approach (Adhikari et al., 2016). Most spectral methods are based on the normal-mode formalism (Peltier, 1974; Wu, 1978), in which LDCs are derived, and hence, GFs for the perturbation potential and the displacement field (Whitehouse, 2009). Since Peltier (1974) showed that the constitutive equations for a linearly viscoelastic Earth turn into an elastic problem in the Laplace-transform domain and can be solved there, this method has been predominant (Olsson, 2013).

The key-point of the spectral method is the introduction of the *reduced sea-level change* Z as

$$Z(\omega,t) = SC, \tag{3.58}$$

where C is the *ocean function* (Munk and MacDonald, 1960). The ocean function given by

$$C(\omega) = \begin{cases} 1 & \omega \in \text{ocean} \\ 0 & \omega \notin \text{ocean} \end{cases}$$

is a step function in two dimensions that is equal to 1 across the oceans (ocean height is equivalent to sea level) and 0 across the land (ocean height vanishes outside oceans). It insures that the ocean loading is applied only if the location lies within the ocean. The introduction of Z allows to transform Eq. (3.57) into (Spada and Stocchi, 2006)

$$S(\omega,t) = \frac{\rho_\mathrm{I}}{\gamma} G_S^{VE} \otimes_\mathrm{E} I + \frac{\rho_\mathrm{w}}{\gamma} G_S^{VE} \otimes_\mathrm{E} Z + S^E - \frac{\rho_\mathrm{I}}{\gamma} \left\langle G_S^{VE} \otimes_\mathrm{E} I \right\rangle - \frac{\rho_\mathrm{w}}{\gamma} \left\langle G_S^{VE} \otimes_\mathrm{E} Z \right\rangle, \tag{3.59}$$

where we have substituted $G_S^{VE} \otimes_\mathrm{I} I$ with $G_S^{VE} \otimes_\mathrm{E} I$ (I vanishes outside the region I) and $G_S^{VE} \otimes_\mathrm{O} S$ with $G_S^{VE} \otimes_\mathrm{E} Z$.

The SLE is a fundamental tool in GIA modelling. The integral equation describes the response of the Earth to surface loads characterized by any time scale. Hence, it can be used for predicting geodetic quantities associated with both late-Pleistocene ice sheets or present-day melting of continental ice sheets (Spada, 2017). The SLE is solved iteratively.

3.1.3 Input parameters to the sea-level equation

The first input to a GIA model is the ice model. The ice models determine the ocean-loading history via the SLE by assuming mass conservation and a gravitationally-consistent redistribution of water over the Earth's surface (Whitehouse, 2009). The second input parameter is the Earth model on which the combined surface load (ice and ocean) is applied, and which describes the response of the Earth to loading. The way the Earth model is implemented depends on the method used to solve the SLE. Since two components, an ice model and an Earth model, are needed to model the GIA process, together they are termed GIA model (Figure 3.1).

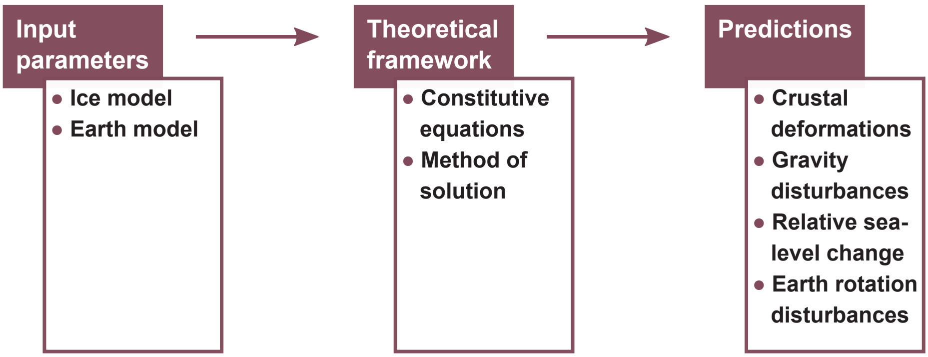

Figure 3.1. Schematic representation of GIA modelling. Adapted from Olsson (2013).

Earth model

The Earth's interior is layered in spherical shells. The classification of the internal structure of the Earth in terms of the *chemical composition* comprises the crust, mantle, and core. The crust has an average thickness of 35 km beneath the continents and 7-8 km beneath the oceans (Whitehouse, 2009). The transition from crust to mantle takes place across the Mohorovičić discontinuity. The mantle may be separated into two layers, the upper and lower mantle. At the bottom of the lower mantle lies the core-mantle boundary. The core has a radius of ~3450 km and is divided into the outer and inner core (classification on the left-hand side in Figure 3.2).

In addition to the classification of the Earth's interior from a chemical point of view, the classification can be defined in terms of *mechanical* and *physical (rheological) properties*. It does not distinguish between crust and mantle but comprises the crust and uppermost mantle to the lithosphere. The lithosphere is typically ~100 km thick, and is the part of the Earth participating in plate tectonics (Whitehouse, 2009). The lithosphere is followed by the asthenosphere, which refers to non-lithospheric mantle material at depths between approximately 100 and 700 km. Beneath the lithosphere lies the mesospheric mantel, which refers to the part of the Earth's mantle below the lithosphere and asthenosphere but above the outer core, with an upper boundary defined at a depth of 660 km (Condie, 2001). The core is subdivided into an inner solid and outer liquid core (classification on the right-hand side in Figure 3.2).

The properties of the crust, lithosphere, and mantle determine the response of the solid Earth to GIA-related surface loading. The base of the lithosphere may be delimited by the change in seismic, thermal, or mechanical properties, resulting in different estimates for lithospheric thickness (LT). When the lithosphere is deformed by a glacially-related load, the mantle flow plays a role in compensating for. The depth to which the mantle responds to surface loading depends on the size of the load. The largest ice sheets cause deformation in the lower mantle. The mantle's viscosity is a measure of its strength and determines to what degree surface loading is supported (Whitehouse, 2009). The transition from the upper to the lower mantle happens at a depth of ~660 km. In GIA modelling, the lower mantle has 1 to 2 orders of magnitude higher viscosity than the upper mantle.

In GIA studies, the most common Earth models use spherical geometry to represent the whole Earth. The models consist of an elastic lithosphere of constant thickness, and between 1 and ~20 viscolelastic mantle layers. The number of mantle layers depends on whether the mantle is represented as a single layer of uniform viscosity, divided into upper and lower mantle, or a multi-layered structure. In each case, the viscosity of each layer is taken to be uniform (Whitehouse, 2009). In all models which use spherical geometry, the Preliminary reference Earth model (PREM) (Dziewonski and Anderson, 1981) is used to determine the elastic model parameters as well as density. The continental LT usually ranges between 70 and 200 km, while mantle viscosities range between 10^{19} and 10^{24} Pa·s. The 1D spherical models vary in the radial direction, while 3D models allow lateral variations in LT and/or in viscosity at each depth.

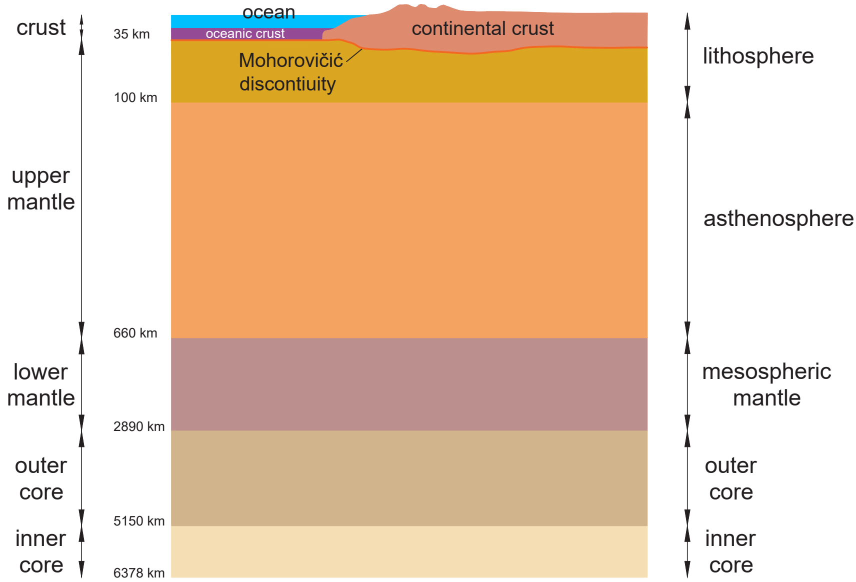

Figure 3.2. Classification of Earth's internal structure in terms of chemical composition (left-hand side) and mechanical properties (right-hand side). Adapted from Encyclopedia Britannica (2019).

Surface loads

Ice models Ice models represent the change of ice thickness as a function of position and time. Ice loading in GIA-modelling is generally applied in a series of time steps, with each time step covering between ~0.5 and ~10 ka, depending upon the required temporal and spatial resolution. The ice extent and ice thickness are defined at each time step (Whitehouse, 2009). The accuracy of a GIA model is strongly dependent on the accuracy of the input ice model.

GIA modellers used two ways to constrain early ice models. Observations of RSL at locations far from ice sheets at the LGM are good proxies for eustatic sea level. This allows to constrain the total volume of ice locked up in an ice sheet at a given time during the deglaciation. In addition, an iterative method was used for solving the SLE. A first estimate of the ice model was used to calculate the RSL change, which was then compared to observations. The misfits between predictions and observations were used to re-adjust the ice model in turn to improve the fit (Whitehouse, 2009).

In GIA, two approaches of ice modelling exist: (i) classical and (ii) thermo-mechanical. Ice models determined by the classical approach are adjusted with the SLE where the solution fits RSL and TG data (Steffen, 2014). Ice models of the ICE-x series, i.e., ICE-3G (Tushingham and Peltier, 1991), ICE-4G (Peltier, 1994), ICE-5G (Peltier, 2004), and ICE6G_C (Argus et al., 2014; Peltier et al., 2015) (Figure 3.3a) are ice models of the first kind. The ICE-x suit consists of global models based on dated observations of ice-sheet margins, RSL curves, and the global MSL curve (Schmidt et al., 2014). Considering individual ice sheets, Antarctica is the least well constrained since a small number of observations is available in this area. Hence, Antarctica has been mainly used as a buffer to ensure that a fit to the global MSL is achieved. Parallel to the development of ICE-x models, the respective VMx Earth models have been developed. In the inversion of VMx Earth models, the ICE-x models have been used as predefined loading. Those Earth models were then used in the construction of the next-generation ICE-x models (Schmidt et al., 2014), making them highly dependent on Earth model information. Further, the spatial and temporal distribution of observational data strongly affects the inferred 1D viscosity profiles (Steffen and Wu, 2011).

Another family of global GIA models developed by the National Australian University (ANU) implements a detailed definition of the ocean load in the SLE. The ANU model, also known as RSES, is a collection of individual ice-sheet models that together comprise a global model (Schmidt et al., 2014). The RSES ice model (Lambeck et al., 1998) combines the Fennoscandian part fom FBK8 (Lambeck et al., 1998), the Laurentide and Greenland parts from ICE-1 (Peltier and Andrews, 1976), the BK4 British Isles model (Lambeck, 1993b), and the ANT3 Antarctic model (Nakada and Lambeck, 1988). This model has not been published as a single data set (Whitehouse, 2009). The spatial resolution of the model is $0.5° \times 0.25°$. In time, the model is sampled on varying length intervals (0.45-5 ka), capturing the time of important change in the ice-sheet evolution (Schmidt et al., 2014). As a starting model, ice thickness is computed from simple glaciological assumptions. The final solution is obtained through a series of iterations involving the fit to different parts of the constraining data or to newly added data while optimizing either via a scale factor or Earth model parameters. Thus, in addition to the ice sheet, the output is also an estimate of the LT and the viscosities of the upper and lower mantle. In contrast, the Earth's structure is assumed to be known prior to the reconstruction of ICE-x models (Schmidt et al., 2014). Both groups assume a spherically symmetric Earth, characterized by a layered Maxwell rheology. However, they differ in the a priori assumption of the Earth model, RSL data sets they were constrained by, and approaches for solving the SLE (Spada, 2017).

In the second approach, 3D thermo-mechanically climate-forced models are tuned to ice-margin information, present-day uplift, and RSL records. They contain Earth model information mainly due to topography information (Steffen, 2014). The GLAC-1 ice model (Figure 3.3b) by Tarasov et al. (2012) is an example of ice models calculated by the second approach. Another example is the UMISM ice-sheet reconstruction (Näslund, 2010), which is a version of the thermo-mechanical University of Maine ice-sheet model. The ice sheet constitutes three main subsystems: (i) mass balance, (ii) ice movement, and (ii) ice temperature for which the model solves the conservation of mass, momentum and energy equations, respectively (Schmidt et al., 2014).

Water loads The discretization of ocean basins is done by breaking the ocean load into small pieces, e.g., symmetric discs for its practical implementation. Early GIA models used fixed ocean areas to determine the redistribution of water throughout the oceans. Current models use bathymetry and topography data to determine the changes in the ocean areas during a glacial cycle.

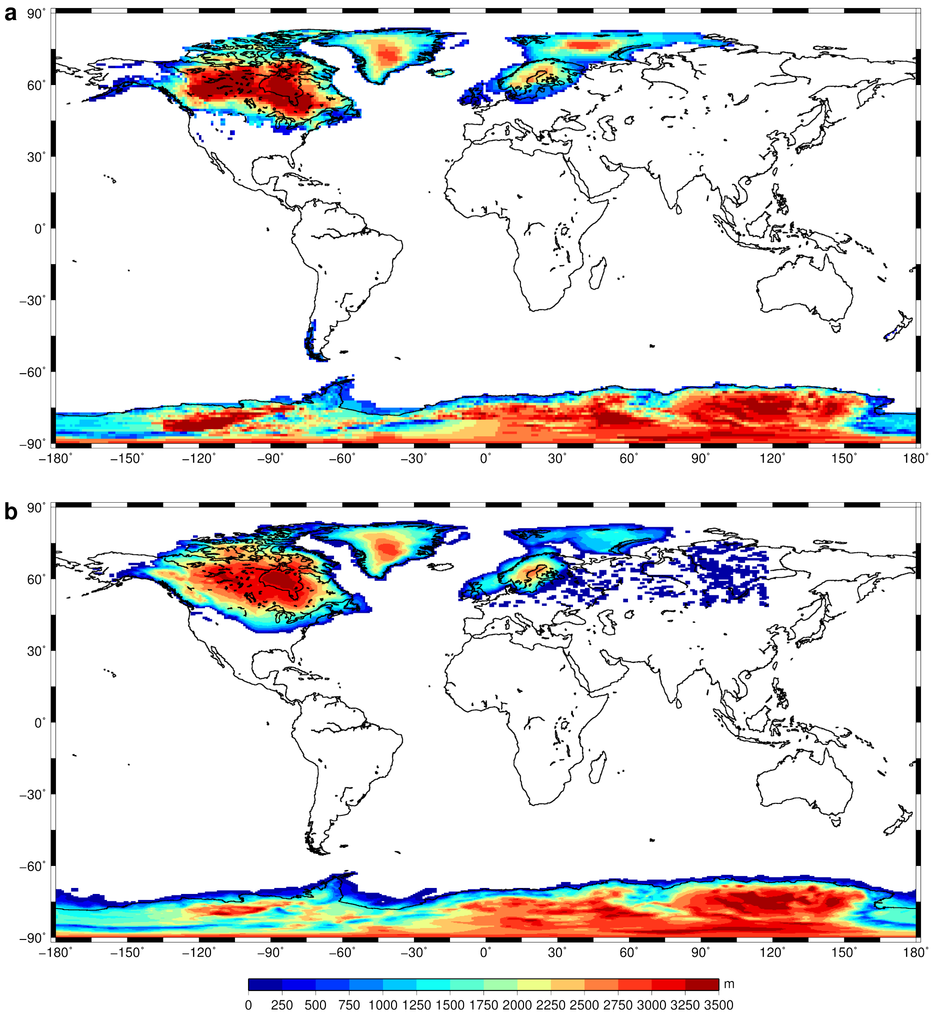

Figure 3.3. Distribution and thickness of ice (in m) at the LGM for global ice models calculated by two different modelling approaches. (**a**) The classical ice model ICE6G_C (Argus et al., 2014; Peltier et al., 2015). (**b**) The thermo-mechanical ice model GLAC-1 (Tarasov et al., 2012).

3.1.4 Modifications to the sea-level equation

Several processes were neglected in the original definition of the SLE by Farrell and Clark (1976). Modifications to the SLE include shoreline migration (Lambeck and Nakada, 1990), presence of grounded or floating ice (Lambeck et al., 2003), rotational feedback (Milne and Mitrovica, 1998), and Earth's 3D structure (Whitehouse, 2009).

The original SLE assumes a constant area of ocean basins. However, as sea level rises, shorelines migrate inland, while as sea level falls, the shorelines migrate towards the ocean. The implementation of a time-varying ocean geometry is done by using a time-varying ocean function $C(\omega, t)$ within the SLE. The change in ocean coverage depends on the underlying topography/bathymetry. At steep continental margins, the horizontal migration of the shoreline will be small compared to the migration of shorelines across a low-gradient continental shelf for the same change in RSL. Hence, the knowledge of topography, which also varies due to surface loading is necessary to determine the geometry of the time-varying ocean function. Sea level is redefined using the time-varying ocean function as

$$Z(\omega, t) = S(\omega, t)\, C(\omega, t). \tag{3.60}$$

In models, which do not account for shoreline migration, the ocean function is separating between regions, which are subject to ocean-loading and the ones which are not. In models that do include the time-varying ocean function, an additional iterative loop must be carried out when solving the SLE in order to determine the change in the distribution of the ocean function at each time step. For the first solution, fixed ocean geometry is assumed, e.g., present-day geometry. The relative sea level ΔS between the present-day and each past time, t_j, is calculated as

$$\Delta S(\omega, t_j) = S(\omega, t_j) - S(\omega, t_\mathrm{P}), \tag{3.61}$$

where $j = 1, \dots, N$, and N is the number of loading time steps. The paleotopography distribution may then be calculated at each position and for each time step as

$$T(\omega, t_j) = T(\omega, t_\mathrm{P}) - \Delta S(\omega, t_j), \tag{3.62}$$

where $T(\omega, t_\mathrm{P})$ is the present-day topography distribution. The coastline at time t_j will follow the zero height paleotopography distribution, hence, the sign of $T(\omega, t_j)$ is used to define the new ocean function at each time step;

$C(\omega, t_j)$ takes the value 1 over the oceans, and the value 0 over land

$$C(\omega, t_j) = \begin{cases} 1 & \text{where } T(\omega, t_j) < 0 \\ 0 & \text{where } T(\omega, t_j) > 0. \end{cases}$$

The ocean function is now uniquely defined for each time step. The SLE is resolved for the whole glacial cycle, using the newly-defined time-dependent ocean function. The process is repeated until the ocean function converges for all time steps (Whitehouse, 2009).

The presence of floating and marine-grounded ice adds further modifications to the SLE. An ice sheet is marine grounded if the mass of ice is greater than the mass of water in the ocean column, i.e.,

$$\rho_\mathrm{I} I > \rho_\mathrm{w} Z.$$

The retreat of grounded ice results in migration of ocean water to the former ice region. The process where water replaces ice results in a global sea-surface fall. As marine-grounded ice retreats, changes of local ice- and ocean-loading, perturbations to the gravitational potential due to water mass influx, and mass conservation should be considered. To include variations in the marine-grounded ice configuration, an extra term in the SLE is introduced

$$T(\omega, t) = C(\omega, t)\, S(\omega, t)\, \beta(\omega, t), \tag{3.63}$$

where $\beta(\omega, t)$ has the value 1 where there is no grounded ice and 0 where there is grounded ice. If the ice thickness is greater than zero at a location that lies within the ocean, i.e.,

$$\rho_\mathrm{I} I > 0 \text{ and } C(\omega, t) = 1,$$

but

$$\rho_\mathrm{I} I < \rho_\mathrm{w} Z,$$

then the ice will float. The total contribution to ocean loading from floating ice is given by

$$M_{floating} = \rho_\mathrm{I} \int_\Omega I(\omega, t)\, C(\omega, t)\, \beta(\omega, t)\, \mathrm{d}\Omega, \tag{3.64}$$

where $\mathrm{d}\Omega$ is an element of area. The mass of grounded ice at time t that directly acts as a load upon the Earth's surface is

$$M_{grounded}(t) = M_{total}(t) - M_{floating}(t), \tag{3.65}$$

where the total ice volume M_{total} can be determined at any time t since the ice history is given a priori.

The theory presented in Farrell and Clark (1976) is valid for a non-rotating Earth. Changes in the Earth's surface load (ice and ocean) perturb the Earth's rotation vector. The change in the Earth's rotation deforms the geoid and the solid surface, and hence, RSL and Earth's surface loads. Expressions for the solid surface and geoid height must be rewritten to account for the rotation-induced changes in RSL as

$$U(\omega, t) = G_{\mathrm{U}}^{VE}(\omega, t) \otimes L(\omega, t) + G_{\mathrm{U}}^{VE}(\omega, t) \otimes \Lambda(\omega, t) \tag{3.66}$$

$$\Phi(\omega, t) = G_{\Phi}^{VE}(\omega, t) \otimes L(\omega, t) + G_{\Phi}^{VE}(\omega, t) \otimes \Lambda(\omega, t), \tag{3.67}$$

where $\Lambda(\omega, t)$ is the time-varying rotational potential.

Early expressions of the SLE used only 1D Earth models and did not include the effect of Earth's lateral structure. Lateral variations in Earth's elastic and viscous properties affect the response of the solid Earth to loading. It has been shown that lateral variations in LT and in asthenospheric viscosity do influence model predictions of paleo-shorelines and crustal motions (Steffen and Kaufmann, 2005). Hence, recent work has focused on using a modified version of the original SLE that can account for the effect of lateral Earth structure (e.g., Steffen and Kaufmann (2005); Whitehouse et al. (2006)). The modification of the SLE involves redefining the Earth's properties to vary with depth as well as lateral position and requires solution methods, which use a fully 3D spherical solution domain (Whitehouse, 2009).

Neglecting any of the processes mentioned above introduces errors into the GIA calculations. Largest errors occur due to omitting shoreline migration. In regions of shoreline migration, the RSL change since the LGM can be under- or over-estimated by up to 125 m (Whitehouse, 2009), which equals to the eustatic sea-level change since the LGM. The errors will be much smaller in regions with steep topography at shorelines, because the topography limits the expansion of shoreline migration, e.g., in Fennoscandia. The difference between the SLE solution incorporating shoreline migration and solving the SLE with fixed shorelines gives a discrepancy of 0.15 μGal/yr (Olsson et al., 2012, Figure 8) in terms of gravity rates. This value corresponds to ~0.9 mm/yr in terms of VLM and was calculated using the modelled relation between gravity and height rates of change of -0.163 μGal/mm for GIA (Olsson et al., 2015, Table 5). The source for the second largest error in GIA calculations is the incorrect treatment of marine-grounded ice. Especially in regions that contained marine-grounded ice at the LGM, such as Hudson Bay or the Gulf of Bothnia, predictions of RSL change can be wrong by up to 100 m (Kendall et al., 2005). Neglecting rotational feedback introduces an error of up to 0.15 mm/yr in predictions of present-day sea-level change (Whitehouse, 2009). Errors due to neglecting the lateral Earth's structure have the most complicated spatial patterns.

3.2 GIA-modelling outputs

A set of geophysical quantities associated with GIA can be obtained from the SLE: (i) relative sea-level rates, (ii) absolute sea-level variations, and (iii) horizontal and vertical crustal rates of displacement. Global maps of those fields, as shown in Figure 3.4, define GIA *fingerprints*, which can be used to identify the ice sources responsible for geodetic variations. The GIA fingerprints also provide means for evaluating *GIA corrections*, which are fundamental for the assessment of secular global MSL rise fromTG observations (Spada, 2017). All of these outputs can be compared to observations, e.g., RSL, TG records, levelling, GPS, gravity observations, as well as satellite altimetry. In GIA studies, time derivatives, i.e., rates of S, N, and U evaluated at present time $\dot{S}$, $\dot{N}$, and $\dot{U}$ are considered.

3.2.1 Data sets to constrain GIA models

Data sets used to constrain GIA models cover different time spans and geographical areas. GIA models are constrained by combining these data sets (Whitehouse, 2009).

Geological relative sea-level data

RSL records cover the longest time span, dating back several thousand years. RSL data record the height of the sea-land interface from the deglaciation to present day. Classical RSL data consist of dated paleo-shorelines, which may be identified by biological sea-level markers, i.e., sea-level indicators. Sea-level indicators are dated samples of shells, corals, wood, whale bones and pollen, with the exact location and relation to former and present-day sea level (Steffen and Wu, 2011). Most samples are dated by the radiocarbon-controlled method and need to be calibrated (see Section 3.3.2). Sea-level indicators only few kilometers apart should be combined to form a sea-level curve since the shape of sea-level curves varies with location (Figure 3.5). RSL records are scattered through the literature but regional data sets have been compiled, e.g., for the British Isles (Lambeck, 1993a,b), the Atlantic coast of the United States (Engelhart and Horton, 2012), or the Pacific coast of central North America (Engelhart et al., 2015). There are also few initiatives to compose global RSL databases, e.g., Tushingham and Peltier (1992) or Kopp et al. (2016).

Geological RSL records can separate between effects of ice history and rheology (Steffen and Wu, 2011). Generally, RSL curves at particular locations vary with distance to the former ice sheet. We distinguish between three groups, depending on the distance to former ice sheets: (i) regions of ice-sheet margin, (ii) near-field, and (iii) far-field regions. Near-field (N) locations are those that occur within the limits of the former ice sheets. At those sites, the dominant contribution to sea-level change is the ice-load term, where the RSL curve has an exponential fall up to the present (Figure 3.5a). For the ice-sheet margin (M) sites, the contribution of the ice load and the Earth model are of similar amplitude but of opposite sign. An initially rapid fall in sea level, followed by a period of relative stability at ~10 ka, and a rise in sea level until ~6 ka BP characterizes these sites. After 6 ka BP, the sea level falls uniformly to present day (Lambeck, 1993c) (Figure 3.5b). Far-field (F) sites are those far away from the ice-sheet center, e.g., Pacific Ocean islands. Sea-level was 115-135 m below present-day sea level when the ice-sheet thickness was at its maximum. A rapid sea-level rise started at the time ice sheets melted and the ocean volume increased. After the ice-sheet melting terminates, ~6 ka BP, sea level reached a small high stand after which it nearly uniformly fell from this high stand until present day (Lambeck, 1993c) (Figure 3.5c). Crustal tilting induced by ocean loading accounts for sea levels higher than present-day sea level in the last 6 ka BP (Steffen and Wu, 2011). The RSL data in the far-field are relatively insensitive to the source of melting and the istostatic component is small. Therefore, the far-field data are able to capture the eustatic sea-level change, and thus, the total volume of ice contained in the ice sheets (Steffen and Wu, 2011). Sea levels can be recorded as soon as the ice retreats and becomes replaced by ocean water. Since the ice vanishes earlier in the ice-margin regions, the observational period starts earlier than at the ice-sheet centers. In the far field, the observational period over the whole deglaciation is possible (Steffen and Wu, 2011).

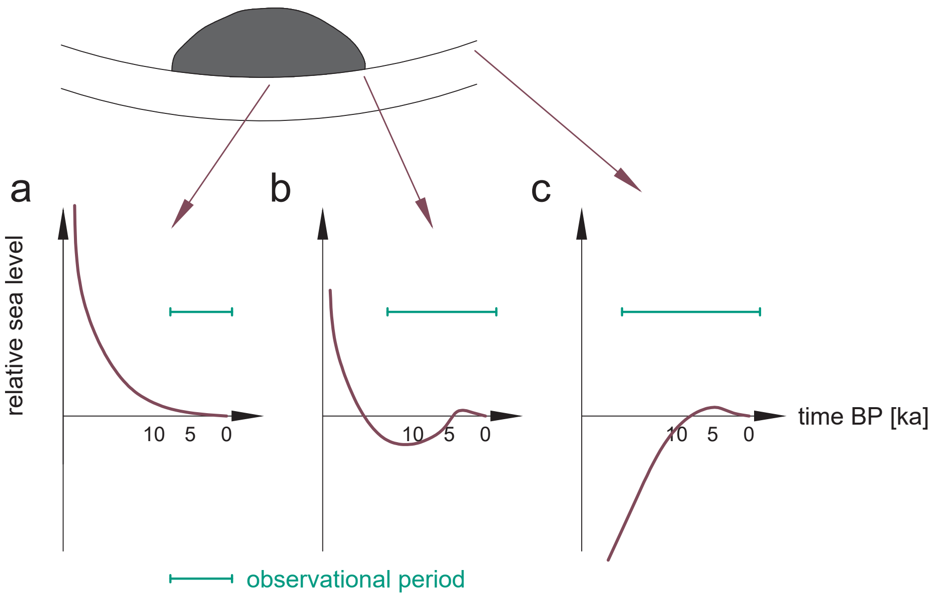

Figure 3.5. Typical patterns of sea-level records at different distances to the ice sheet: (**a**) near field, (**b**) margin, and (**c**) far field. Adapted from Steffen and Wu (2011).

Geodetic data

TG observations capture both VLM as well as variations of the sea surface. VLM and changing sea levels result from a complex interplay of thermal expansion of ocean water, changing ice reservoirs, GIA, tectonic motion, and anthropogenic effects (Kuo et al., 2004). The analysis of long-term TG records allows direct estimation of RSL change (Steffen and Wu, 2011). Kuo et al. (2004) combined satellite altimetry data from TOPEX/POSEIDON with long-term TG data (>40 years) in the Baltic Sea region to obtain estimates of VLM. The estimated VLM rates showed only small differences to independent solutions from GPS sites.

VLBI (Very Long Baseline Interferometry), SLR (Satellite Laser Ranging), GNSS, and other space geodetic techniques are used to determine present-day deformation rates. They provide a better spatial coverage in comparison to RSL data but a much shorter time span. Geodetic data covering the longest time span are levelling data. They have been used in combination with TG data to construct maps of VLM, e.g., in Bjerhammar (1980). Ekman (1996) constructed a map of the apparent uplift (VLM relative to MSL) in Fennoscandia on the basis of sea-level records (spanning 60 years or more), lake-level records, and repeated high-precision levelling. VLBI data is used to validate predictions of GIA-related horizontal motions (Haas et al., 2003). Thorough analysis of GPS data can indicate the uplift center and horizontal crustal motions (Steffen and Wu, 2011). The BIFROST (Baseline Inferences for Fennoscandian Rebound, Sea Level, and Tectonics) GPS network (Johansson et al., 2001) measures crustal deformation in Fennoscandia for geodynamic, sea-level, and tectonic studies since August 1993.

Gravity observations provide complementary information on the rate of VLM by measuring gravity variations with terrestrial or satellite gravimetry. NASA's GRACE mission, operated from 2002 to 2017, provided measurements of Earth's gravity field changes. The GRACE Follow-On (GRACE-FO) is a continuation of the GRACE mission with near-identical hardware launched in May 2018. In June 2019, the GRACE-FO project released their first Level-2 data products (Dahle et al., 2019). GRACE(-FO) measures mass transport within the Earth's system and monthly solutions can be used to calculate time-varying gravity trends over the whole Earth. The GIA signal is detectable within these trends (Tamisiea et al., 2007). The use of GOCE gravity data for purposes of GIA includes estimation of the crustal thickness, modelling the lithospheric structure, or investigation of deeper mantle sources (Ebbing et al., 2018). Terrestrial gravity measurements in Fennoscandia provide a reasonably long time span of gravity data but their spatial extent is limited.

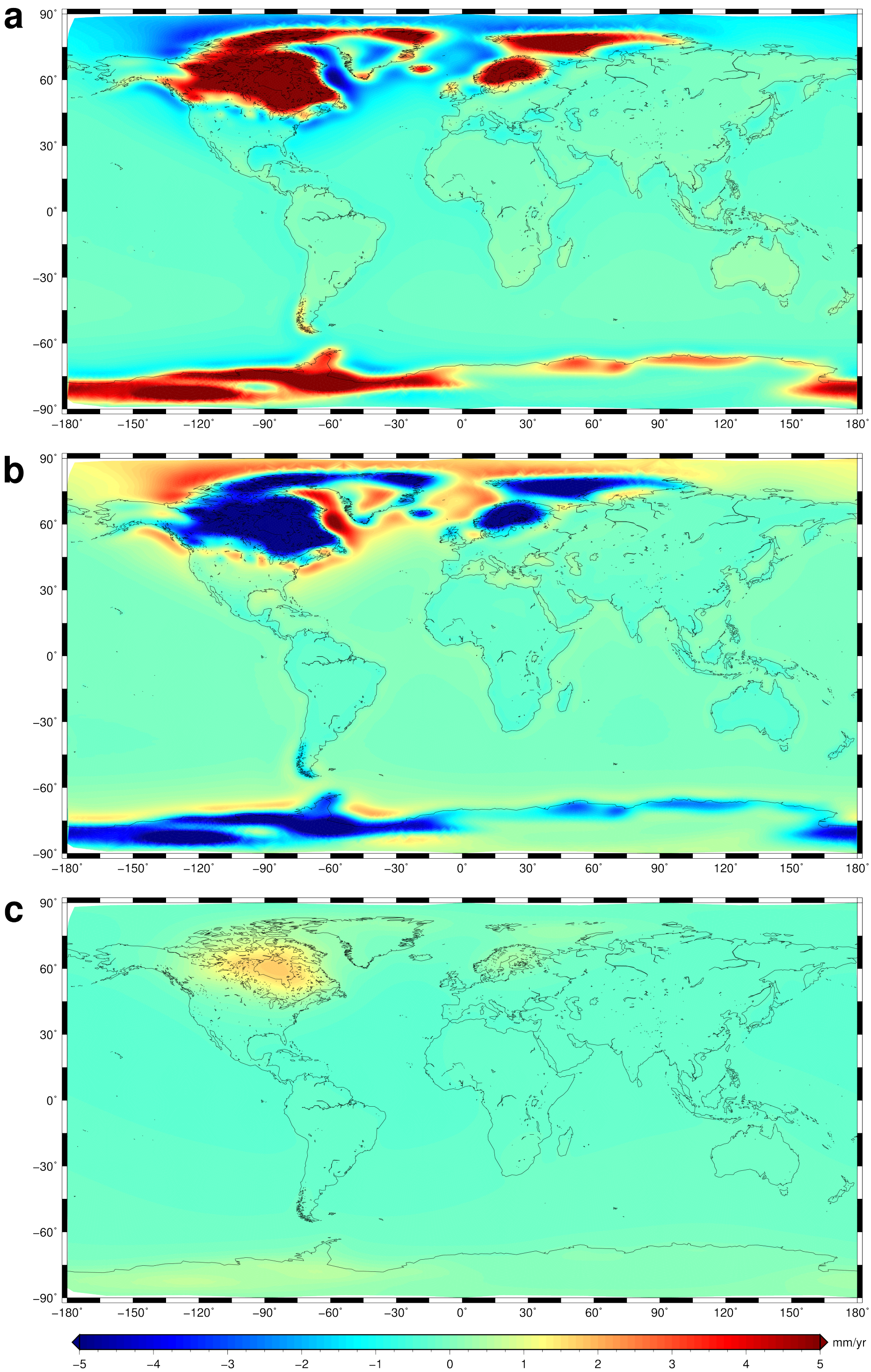

Figure 3.4. Global GIA fingerprints (in mm/yr) from SELEN based on ICE6G_C (VM5a). (**a**) Map of GIA-induced vertical land motion $\dot{U}$. (**b**) Map of the present-day rate of sea-level change $\dot{S}$ associated with GIA. (**c**) Rate of sea-surface variation induced by GIA relative to the Earth's center of mass $\dot{N}$.

3.3 Models and data: ice models, Earth models, and validation data

3.3.1 Paper C

The open-source program SELEN (Spada and Stocchi, 2006, 2007; Spada et al., 2012) solves numerically the SLE for a spherical, layered Earth with Maxwell viscoelastic rheology. SELEN can compute vertical and horizontal surface displacements, gravity variations, and sea-level changes on a global and regional scale. The pseudospectral approach introduced by Mitrovica and Pelier (1991) and Mitrovica et al. (1994) is implemented in SELEN (Spada and Melini, 2015). SELEN obtains a gravitationally self-consistent response to a prescribed ice load by iteratively solving the SLE in the spherical-harmonic domain. Internally, the time-dependent fields are represented as piece-wise constant functions, with a time-step of 0.5 ka. The spatial domain is discretized with an equal-area, icosahedron-based grid of disc-shaped pixels (Tegmark, 1996), which represents a natural quadrature set for the spherical-harmonic representations of fields (Martinec et al., 2018). Resulting spatial grids presented in this thesis consist of 75 692 pixels, with each pixel corresponding to a disc of 46.3 km radius.

In SELEN 2.9 a non-rotating Earth with fixed shorelines is assumed. A new version of SELEN (version 4) includes a rotational feedback according to Milne and Mitrovica (1998), migrating coastlines (according to the formulation of Mitrovica and Milne (2003)), and properly handles the transition between floating and grounded ice sheets (Martinec et al., 2018). At the time of this study, the SELEN version 4 was not publicly available. Consequently, all SELEN runs presented in this thesis were performed using the SELEN 2.9 version.

Rheology profiles are employed as n-parameter models and LDCs are calculated by TABOO using the viscoelastic normal-mode method. The models differ in LT as well as in the number and viscosity values of mantle layers. Figure 3.6 gives a logarithmic representation of Earth models employed in the thesis. The corresponding Earth model for ICE-3G is VM1 (dark red line in Figure 3.6), for ICE-5G VM2a (dashed blue line in Figure 3.6), and for ICE6G_C VM5a (coral pink line in Figure 3.6). Their lithospheric thicknesses (LTs) range between 65 and 120 km. VM1, VM2a, and VM5a have between two and four layers. VM5a has a transition zone defined between the upper and lower mantle, with a viscosity half of that for the lower mantle. Earth models corresponding to ICE-x models are termed VMx rheologies in the following.

In addition to VMx rheologies, two other Earth models from the Nordic geodetic commission (NKG) were used, namely GIA_prel0306 (dashed green line in Figure 3.6) and GIA_prel0907 (H. Steffen, personal communication, 2017, gray line in Figure 3.6), with LTs of 160 and 120 km, respectively. GIA_prel0306 was found as the best fitting model (in central Fennoscandia) to GNSS uplift rates and Fennoscandian RSL data (Vestøl et al., 2016). VM5a and GIA_prel0907 have a thin layer (35 km for VM5a and 90 km for GIA_prel0907) below the lithosphere. This additional layer in GIA_prel0907 was introduced to tune a 1D model towards a good fit to horizontal velocities (Vestøl et al., 2016). The most obvious difference between NKG rheologies compared to VMx profiles is the much higher viscosity for the lower mantle. The upper-lower mantle boundary is defined at 670 km depth for all Earth models. Elastic-model parameters as well as densities are volume-averaged mean values of PREM for all Earth models used in the thesis.

In addition to the Earth models used in **Paper C**, another Earth model was added to the thesis, namely the M_1 rheology profile proposed in Colli et al. (2018) (yellow line in Figure 3.6). The M_1 rheology profile includes a 70 km thick lithosphere and a 30 km thick layer with a viscosity of 10^{23} Pa·s. The value of the lower-mantle viscosity is $5 \cdot 10^{22}$ Pa·s and based on studies of Earth's rotational variations and deglaciation-induced true polar wonder (Matsuyama et al., 2010; Nakada et al., 2015).

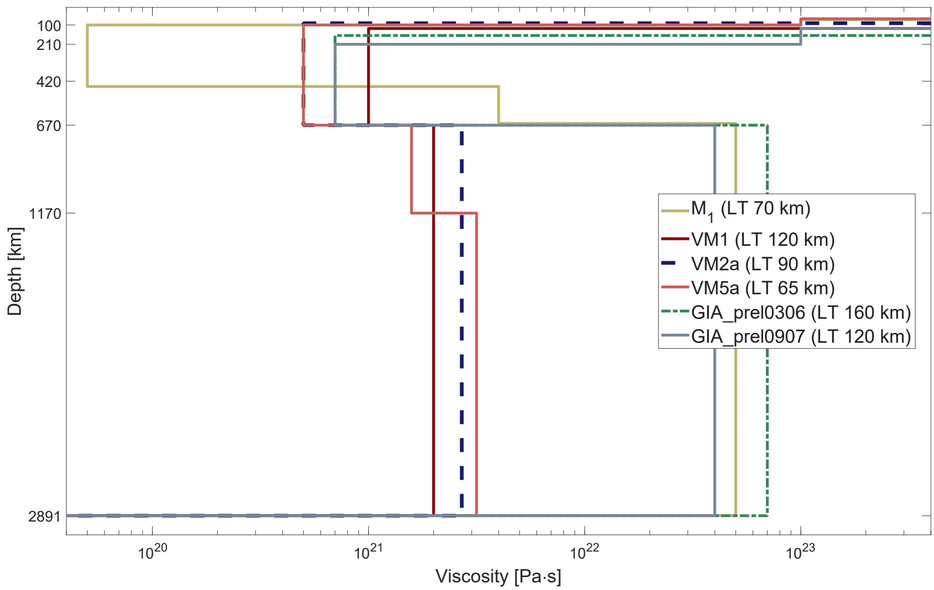

Figure 3.6. Logarithmic representation of rheological profiles used in this study: M_1 (Colli et al., 2018), VM1 (Tushingham and Peltier, 1991), VM2a (Peltier, 2004), VM5a (Peltier et al., 2015; Purcell et al., 2016), GIA_prel0306 (Steffen et al., 2016), and GIA_prel0907 (H. Steffen, personal communication, 2017).

Figure 3.7 shows the ICE-x models at the LGM in Fennoscandia. They are given on a global grid and describe ice-thickness changes of major ice sheets over North America and Greenland, Fennoscandia, the Barents Sea, British Isles, and Antarctica from the LGM to present in time steps of 1 ka. ICE-4G (Peltier, 1994), ICE-5G (Peltier, 2004), and ICE6G_C (Argus et al., 2014; Purcell et al., 2016) are updated versions of ICE-3G (Tushingham and Peltier, 1991). ICE-5G and ICE6G_C (used in this study) are given on global $1°\times1°$ grids. In the Fennoscandian study region, the delimitation of ice-covered areas in the different ice models is similar, with smaller deviations at the ice bridge between the Scottish and Norwegian ice sheets. ICE-4G and ICE-5G have ice-sheet maxima of 3649 and 3084 m at the LGM, respectively. ICE-6G and ICE6G_C are less thick with 1905 and 2694 m, respectively. For ICE-3G, the ice-sheet maximum is located in central Finland. In all other ice models, the ice-sheet maxima are shifted to central Sweden and the Gulf of Bothnia. In comparison to older ICE-x model versions, an extensive set of geodetic data (e.g., GPS and GRACE) was used to constrain the ICE6G_C reconstruction (Abe-Ouchi et al., 2015). The difference in ice thickness between ICE-5G and ICE6G_C is reflected in their eustatic sea levels, where ICE-5G assumes a RSL rise of 127.1 m and ICE6G_C 116.9 m (both values are outputs from SELEN runs). All SELEN computations have been performed by three iterations of the SLE. A further version of ICE6G_C (VM5a) was produced, namely ICE6G_D (VM5a) (Peltier et al., 2018) but not used in the thesis.

The validation of model results is achieved by forming differences ϵ between external data and model results. These differences are empirical measures of errors in the validation data sets as well as in the model results. Modelling errors can be further attributed to errors in ice histories and rheologies, as well as the approximations of the applied software packages. Additional discrepancies may arise from non-GIA related processes, such as tectonics, which contribute to the observed temporal variations. Thus, we may write

$$\epsilon = \epsilon_{\mathrm{NKG2016LU\_abs}} + \epsilon_{\mathrm{ice}} + \epsilon_{\mathrm{rheo}} + \epsilon_{\mathrm{soft}} + \epsilon_{\mathrm{non\text{-}GIA}}, \tag{3.68}$$

where $\epsilon_{\mathrm{NKG2016LU\_abs}}$ represents errors of NKG2016LU_abs and depends on the accuracy of the included geodetic data and the underlying GIA model NKG2016GIA_prel0306, ϵ_{ice} and ϵ_{rheo} are errors of the ice and Earth models. ϵ_{soft} are approximations in the software, including approximations in the mathematical model and its numerical implementation as well as temporal and spatial discretization; $\epsilon_{\mathrm{non\text{-}GIA}}$ are contributions of non-GIA effects. Hence, Eq. (3.68) represents the full empirical error budget.

In addition to the validation with external data, comparisons of different model results were performed. Thereby, terms of the full error budget in Eq. (3.68), which are identical in both model runs, drop out. When comparing uplift rates between different software solutions that include same input parameters (ice and Earth model), the error budget in Eq. (3.68) reduces to ϵ_{soft}, thus allowing to quantify the significance of the software component in the full error budget. Determining differences of uplift rates calculated with the same software, varying ice/Earth model combinations, gives insight into the sensitivity of results to ice models and/or Earth models.

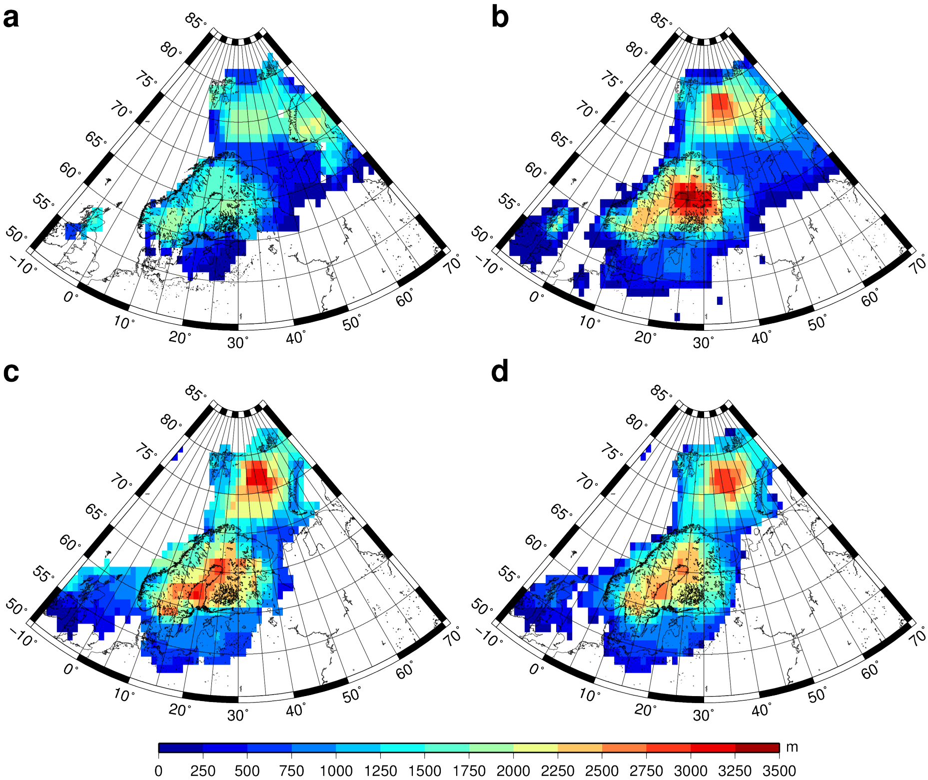

Figure 3.7. Ice models given as ice thickness (in m) at the LGM in Fennoscandia. (**a**) ICE-3G (Tushingham and Peltier, 1991), (**b**) ICE-4G (Peltier, 1994), (**c**) ICE-5G (Peltier, 2004), and (**d**) ICE6G_C (Argus et al., 2014; Peltier et al., 2015).

Table 3.2. Overview of parameters used when calculating uplift rates using ICE-5G (VM2/VM2a) and ICE6G_C(VM5a), and statistics of differences to NKG2016LU_abs (in mm/yr).

Vertical uplift rates		VLM_{ICE5G}	VLM_{ICE5G_S}	VLM_{ICE6G_C}	VLM_{ICE6G_ANU}	VLM_{ICE6G_S}
Software package		Peltier (2004)	SELEN (Spada and Stocchi, 2007)	Peltier (2004)	CALSEA (version 33) (Lambeck et al., 2003)	SELEN
Method		pseudo-spectral	pseudo-spectral	pseudo-spectral	-	pseudo-spectral
Rheology		VM2	VM2a [a]	VM5a	VM5a	VM5a
Truncation degree		256	256	512	256	256
$\Delta\varphi \times \Delta\lambda$		$1^\circ \times 1^\circ$	r=44 [b]	$1^\circ \times 1^\circ$	$1^\circ \times 1^\circ$	r=44
Number of iterations		-	3	-	-	3
Shoreline migration		Yes (Peltier, 2004)	No	Yes (Peltier, 2004)	Yes (Lambeck et al., 2003)	No
Paleo-topography and grounded ice		Yes	No	Yes	GEBCO_08/ BEDMAP [c]	No
Rotational feedback		Yes	No	Yes	Yes [d]	No
Differences to NKG2016LU_abs [e]	**min**	−2.2	−4.2	−1.5	−2.1	−2.2
	max	2.9	1.0	2.6	2.0	2.2
	mean	0.1	−0.7	0.2	0.0	0.0
	std	1.2	1.0	1.0	0.9	0.9

[a] a volume-averaged version of the VM2 viscosity profile (Spada and Melini, 2015)
[b] corresponds to a disc of radius 0.4°, see Spada and Melini (2015) for more details
[c] GEBCO_08 was used north of 60°S and BEDMAP south of 60°S
[d] the applied geoid velocity corrections are: $\dot{C}_{21}^{rot} = -1.75\times10^{-9}$, $\dot{S}_{21}^{rot} = -1.75\times10^{-8}$ (Purcell et al., 2016)
[e] over land points within an area delimited by $49^\circ < \varphi < 73^\circ$ and $4^\circ < \lambda < 35^\circ$

3.3.2 Validation data sets

Semi-empirical land-uplift model NKG2016LU

NKG2016LU (Vestøl et al., 2019) is a semi-empirical land-uplift model, released by NKG, representing an improved version of NKG2005LU. It combines an empirical model with a GIA model by applying a remove-compute-restore technique. First, the empirical model was directly computed from BIFROST GNSS velocities (Kierulf et al., 2014) and levelling by least-squares collocation with unknown parameters and does not include TG data, i.e., apparent land uplift. Secondly, a GIA model was removed from the empirical model in the observation points and least-squares collocation was applied to model the residual surface. Finally, the GIA model was added back to the residual-surface grid to get the final land-uplift grid NKG2016LU_abs in ITRF2008 (Figure 3.8a). The levelled land-uplift relative to the geoid NKG2016LU_lev (Figure 3.8b) is given as (Vestøl et al., 2016)

$$\text{NKG2016LU\_lev} = \text{NKG2016LU\_abs} - \text{NKG2016GIA\_prel0306}, \tag{3.69}$$

where NKG2016GIA_prel0306 is the geoid rise from the GIA model.

The underlying GIA model, NKG2016GIA_prel0306 (Steffen et al., 2016) in Figure 3.8c, was computed applying the ICEAGE software (Kaufmann, 2004), using the viscoelastic normal-mode method. The spherical-harmonic expansion was truncated at degree 192. For the rheology, the three-layered GIA_prel0306 model was used (dashed green line in Figure 3.6). The GLAC-71340 ice history for Fennoscandia and the Barents Sea by L. Tarasov was used in the calculation, while other parts of the world were taken from ICE-5G (Vestøl et al., 2016). The GLAC-71340 ice history is a 3D thermo-mechanical ice model. It is tuned to ice-margin information, present-day uplift, and RSL records. This type of model is dynamically more consistent than the ICE-x models because it represents the dynamic response of a real ice sheet to climate forcing. Despite the fact that thermo-mechanical models are also based on some certain rheology, there is a smaller interdependency between ice model and rheology (Schmidt et al., 2014) than in case of ICE-x and VMx, which are iteratively tuned to fit geological and/or geodetic data using the SLE. The uncertainty of the VLM rates from NKG2016LU_abs was calculated to 0.6 mm/yr by Olsson et al. (2019), taking into account internal uncertainty (0.2 mm/yr) as well as drifts in the ITRF2008 reference frame's origin (0.5 mm/yr) and scale (0.3 mm/yr).

Table 3.3. Statistics of NKG2016LU_abs, NKG2016LU_lev, and NKG2016GIA_prel0306 signal (in mm/yr) illustrated in Figure 3.8.

Model	min	max	mean	std
NKG2016LU_abs	−4.6	10.3	0.9	3.1
NKG2016LU_lev	−4.7	9.6	0.7	3.0
NKG2016GIA_prel0306	−0.1	0.7	0.2	0.2

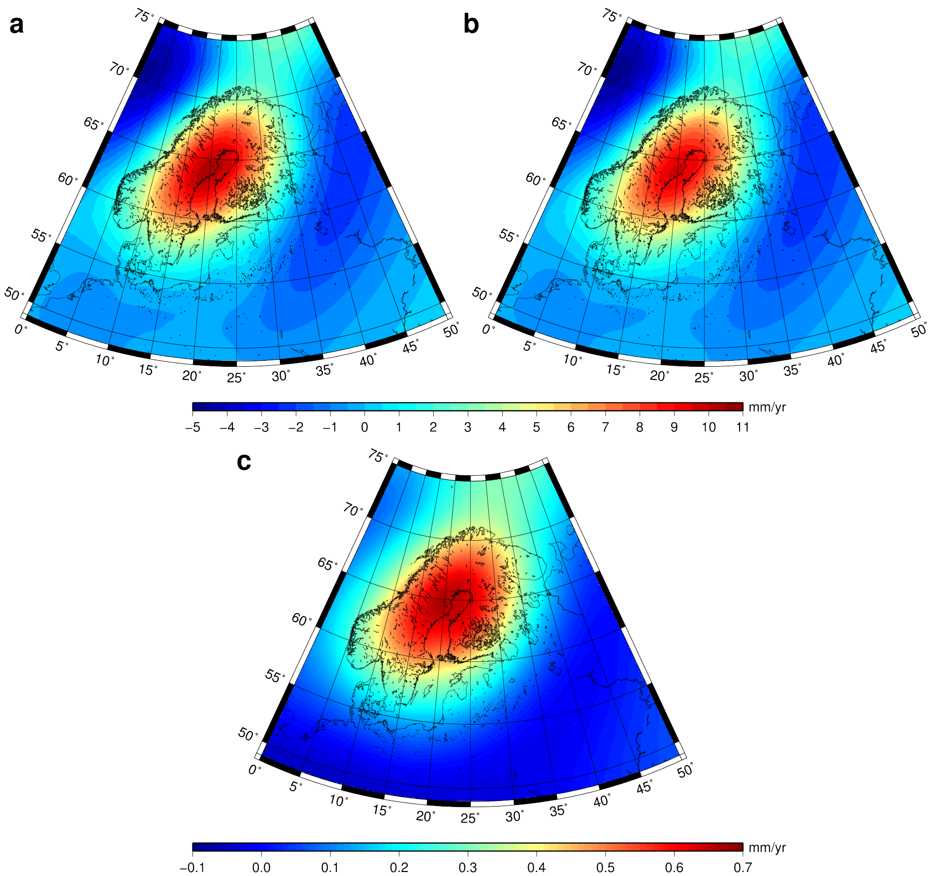

Figure 3.8. Validation data used in **Paper C** and **Paper D**. (**a**) Absolute land-uplift model NKG2016LU_abs in ITRF2008. (**b**) Levelled land-uplift model NKG2016LU_lev relative to the geoid. (**c**) Rate of geoid change NKG2016GIA_prel0306 (a−b) (Vestøl et al., 2019).

Geological relative sea-level records in Fennoscandia

In the Tushingham and Peltier (1992) database, 392 globally non-uniformly distributed ^{14}C/radiocarbon-controlled RSL histories are available, covering a time span of 0-15 ^{14}C ka BP. Relict shoreline deposits were identified and dated radiometrically from associated carbonate or organic material by geomorphological methods, and are given as relative heights in meters referenced to modern MSL (Tushingham and Peltier, 1992), i.e., as RSL. RSL observations in this context are of the ancient sea level relative to land (Vestøl et al., 2016). For the comparison, 55 RSL sites from the Tushingham and Peltier (1992) database have been used, within an area delimited by $49° < \varphi < 75°$ and $0° < \lambda < 50°$ (Figure 3.9a).

The RSL ages were given as ^{14}C ages and were therefore calibrated to calendar years using the CALIB 7.1 program (Stuiver and Reimer, 1993) following the approach in Alves et al. (2018). Organisms from marine environments have been exposed to different levels of ^{14}C than their counterparts in the atmosphere. Radiocarbon dates of terrestrial and marine organism of equivalent ages have a difference of ~400 radiocarbon years. The marine calibration incorporates this time-dependent global ocean-reservoir correction of ~400 radiocarbon years. To accommodate local effects, the difference ΔR in reservoir age of the local region of interest with respect to the global ocean should be determined (Stuiver and Reimer, 1993). Hence, the Marine13 radiocarbon age-calibration curve and a regional mean reservoir correction based on 125 data points inside the NKG2016LU boundaries were employed (Figure 3.9b) from the Marine Reservoir Database (http://calib.org/calib/, and references for each value therein). The 55 RSL sites for Fennoscandia have a varying number of observations and cover different time spans, ranging between ~17.3 and ~3.9 ka BP (Figure 3.9a).

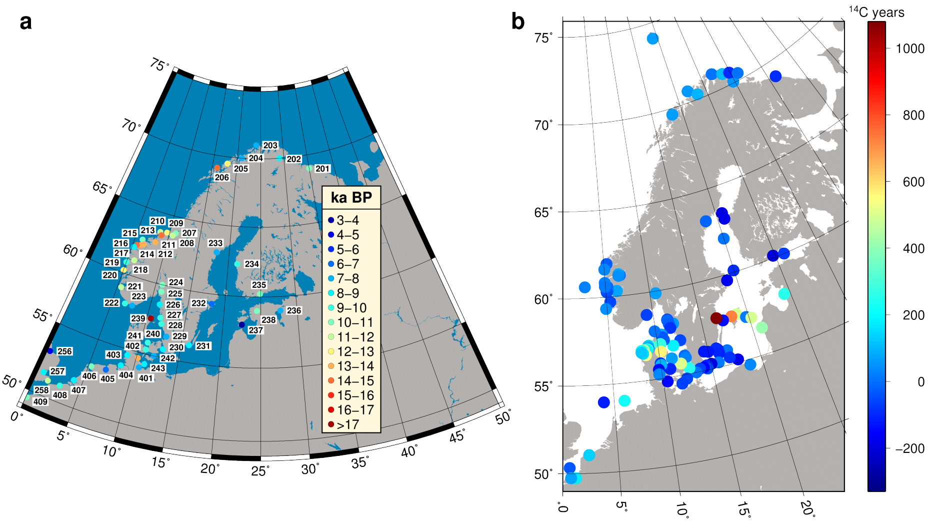

Figure 3.9. Validation data set used in **Paper C**. (**a**) Geological relative-sea level sites from the Tushingham and Peltier (1992) database and their geographical distribution in Fennoscandia. The calibrated age BP (in ka) of the oldest available observation per relative sea-level site is marked with a colored dot. The corresponding name for each relative sea-level site can be found in Tushingham and Peltier (1992). (**b**) ΔR values (in ^{14}C years) for Fennoscandia from the Marine Reservoir Database, which also holds references for each value. For the selected region, the employed weighted mean of ΔR was 24 ^{14}C years with a standard deviation of 155 ^{14}C years.

Chapter 4

Results and discussion

The following chapter gives an overview and gathers results presented in **Paper A**, **Paper B**, **Paper C**, and **Paper D**. The focus of Section 4.1 is the quality assessment of CS2 data and MDT determination. Section 4.2 focuses on comparisons of VLM rates determined by different approaches. Limitations to the research are listed in Section 4.3. In Table 4.1, an outline of data sets used in all papers is given.

4.1 Coastal altimetry and mean dynamic topography

Results from **Paper A** and **Paper B** are gathered in this section. **Paper A** investigates the performance of SARIn (without phase information) altimetry in the Norwegian coastal zone. 20 Hz CS2 observations within 45 km×45 km boxes at 22 TGs (Figure 2.10, except NARV) were compared to TG data with a 10-minute sampling rate provided by NMA. The same comparison was done using three conventional altimeters to quantify the performance of CS2 with respect to conventional altimetry. In **Paper B**, three state-of-the-art regional geoid models as well as CS2 data in the Norwegian coastal zone were combined to determine coastal MDT models. The MDT models were validated against PSMSL TG observations as well as the state-of-the-art operational coastal ocean model NorKyst800.

Table 4.1. Overview of data sets used in **Paper A**, **Paper B**, **Paper C**, and **Paper D**. Inspired by Ophaug (2017).

Paper	Data set	Coverage	Time period	Note
	Geoid models			
B	NMA2014	regional	-	based on DIR5
	NKG2015	regional	-	
	EGG2015	regional	-	
	Tide-gauge data			
A	NMA	22 TGs	2010-2014	10-minute, relative
B	PSMSL	19 TGs	2012-2015	monthly, NN2000
D	PSMSL	20 TGs	2010-2018	monthly, RLR
	NMA	20 TGs	2010-2018	10-minute, relative
	Relative sea-level data			
C	Tushingham and Peltier (1992)	regional (55 sites)	~17.3-3.9 ka BP	
	Satellite altimetry			
A	CryoSat-2	45 km boxes	2010-2014	20 Hz degraded SARIn [a]
	SARAL/AltiKa	specific tracks	2013-2016	
	Envisat	specific tracks	2010-2013	Phase C
	Jason-2	specific tracks	2010-2016	
	DTU13MSS	global	1993-2012	
B	CryoSat-2	regional	2010-2015	LRM, SAR [b], SARIn [c]
A, D	DTU15MSS	global	1993-2014	
D	CryoSat-2	45 km boxes	2010-2018	1 and 20 Hz SARIn [c]
	Ocean models			
B	NorKyst800	regional	2010-2012	
	Land-uplift models			
C, D	NKG2016LU_abs	regional	-	
	Ice models			
D	ICE-5G (VM2)	global	-	
	ICE6G_C (VM5a)	global	-	
	Earth models			
D	VM1	global	-	
	VM2/VM2a	global	-	
	VM5a	global	-	
	GIA_prel0306	regional	-	
	GIA_prel0907	regional	-	
	M_1	global	-	

[a] simple threshold retracker, the SARIn/off-nadir range correction was not applied
[b] reduced-SAR, data acquired in SAR mode and reduced to a sequence of LRM-like echoes
[c] SAMOSA2

4.1.1 Comparison of altimetry and tide-gauge data along the Norwegian coast

Table 4.2 gives the statistics of differences between both CS2 and conventional altimeters and TG observations in 45 km×45 km boxes. CS2 ranges were retracked by either applying the simple threshold retracker (**Paper A**) or SAMOSA2 (**Paper D**). In general, CS2 agrees well with TG observations. The agreement between CS2 (retracked applying simple threshold retracker) and TG time series is better at TGs close to the open ocean than at TGs located inside fjords. Using standard corrections, standard deviations of differences are 20 cm or more at land-confined TGs, while TGs to the open ocean have standard deviations of differences of 9 cm or less. Similar behavior holds for correlations. The mean standard deviation of differences is 16.0 cm with a mean correlation of 0.61 over 22 TGs applying standard corrections. A decrease of standard deviations of differences is noted at 19 out of 22 TGs (exceptions are ALES, MALO, and OSCA) when exchanging standard corrections by local ones. Applying local corrections, the mean standard deviation of differences is 12.2 cm with a mean correlation of 0.68. The correction swap led to an average improvement of ~24% in standard deviations of differences and ~12% for correlations. If land-confined TGs (TROM, TRON, HEIM, BERG) are omitted from the analysis, CS2 shows a mean standard deviation of 12.0 cm and a mean correlation of 0.69 (applying standard corrections), and a mean standard deviation of 10.0 cm with a mean correlation of 0.74 (applying local corrections). In **Paper D**, a mean standard deviation of 12.1 cm and a mean correlation of 0.77 were obtained between 20 Hz CS2 SARIn data (off-nadir range corrected and retracked applying SAMOSA2) and TG data from NMA at 20 TGs. In **Paper A**, for the same subset of TGs as in **Paper D**, a mean standard deviation of 14.7 cm with a mean correlation of 0.64 were obtained applying the simple threshold retracker and standard CS2 corrections.

All three conventional altimeters perform similarly. Envisat, SARAL/AltiKa, and Jason-2 show mean standard deviations of differences of 10.0, 10.6, and 11.0 cm, and mean correlations of 0.58, 0.64, and 0.56, respectively. Similar to CS2, the mean correlation of the conventional altimeters with TGs is 0.60 with a slightly lower mean standard deviation of differences of 11 cm. There is a tendency that correlation decreases and standard deviation of differences increases with increasing distance to TGs for all conventional altimeters.

Table 4.2. Overview of the number of available altimeter observations in 45 km×45 km boxes and the overall agreement (mean Spearman's rank correlation coefficient ρ and mean standard deviation of differences σ) between altimetric and tide-gauge time series at Norwegian tide gauges. Results from **Paper A** and **Paper D** are combined in this table.

Paper	Altimeter	Retracker	No. of obs. mean	Sampling	monthly PSMSL mean ρ	monthly PSMSL mean σ [cm]	10-minute NMA mean ρ	10-minute NMA mean σ [cm]	No. of TGs	Type of applied corrections
A	CryoSat-2	simple threshold	4208	20 Hz	-	-	0.61	16.0	22	standard
	CryoSat-2	simple threshold	4192	20 Hz	-	-	0.68	12.2	22	local
	Envisat	Hayne	15	1 Hz	-	-	0.58	10.0	22	standard
	SARAL/AltiKa	MLE4	30	1 Hz	-	-	0.64	10.6	22	standard
	Jason-2	MLE4	200	1 Hz	-	-	0.56	11.0	14	standard
	CryoSat-2	simple threshold	4593	20 Hz	-	-	0.64	14.7	20	standard
D	CryoSat-2	SAMOSA2	218	1 Hz	0.53	17.6	0.82	11.9	20	standard
	CryoSat-2	SAMOSA2	3359	20 Hz	0.50	16.7	0.77	12.1	20	standard

4.1.2 Validation of mean dynamic topographies

Figure 4.1 shows coastal ocean MDTs. The CS2 MDTs (Figures 4.1b-4.1d) are generally consistent with NorKyst800 (Figure 4.1a). They show slightly larger values in the coastal zone and smaller values to the open ocean. Compared to NorKyst800, $CS2_{EGG}$ shows a slightly larger standard deviation of differences of ~7 cm than $CS2_{NKG}$ and $CS2_{NMA}$ (~6 cm, Table 4.3). All geodetic MDTs show some areas along the coast with smaller values than one would expect. The most striking coastal feature of $CS2_{EGG}$ and $CS2_{NMA}$ is an MDT low seen in the area between Lofoten-Vesterålen area and Senja island, roughly at 69°N between 15 and 20°E, which is much less visible in $CS2_{NKG}$.

Coastal ocean and geodetic MDT profiles are illustrated in Figure 4.2. The coastal MDT profile obtained from NorKyst800 is smoother compared to geodetic MDT profiles. According to the findings in Ophaug et al. (2015), from north to south a 10 cm rise towards KABE, a flattening towards STAV, and another 10 cm rise towards VIKE is observed. The largest differences are observed in the Lofoten-Vesterålen area (~10 cm). At some TGs, the geodetic MDTs show a large spread (e.g., HAMM, ANDE, and BODO) but show a good agreement at HONN, MAUS, HEIM, and STAV. In addition, a scattering of TG and CS2 MDTs is noted at some TGs. NorKyst800 agrees better with TG MDTs than with CS2 MDTs at TROM, RORV, and ALES, and vice versa at BODO and BERG. Table 4.4 gives the statistics of differences between ocean and geodetic MDTs over 19 TG sites. In comparison with TG MDTs, CS2 MDTs show a mean profile standard deviation of differences of 4.4 cm. NorKyst800 shows a mean profile standard deviation of differences of 3.4 cm to CS2 MDTs and of 4.2 cm to TG MDTs.

Geostrophic surface currents are shown in Figure 4.3. The general pattern of the Norwegian Sea circulation is evident in all MDTs. The strongest and best defined currents are visible in NorKyst800. $CS2_{NMA}$ shows the strongest currents and most distinct pattern of the geodetic MDTs, followed closely by $CS2_{NKG}$. $CS2_{EGG}$ shows the Norwegian Coastal Current but the open-ocean circulation pattern is more or less absent, apart from the hot spot in the Lofoten-Vesterålen area.

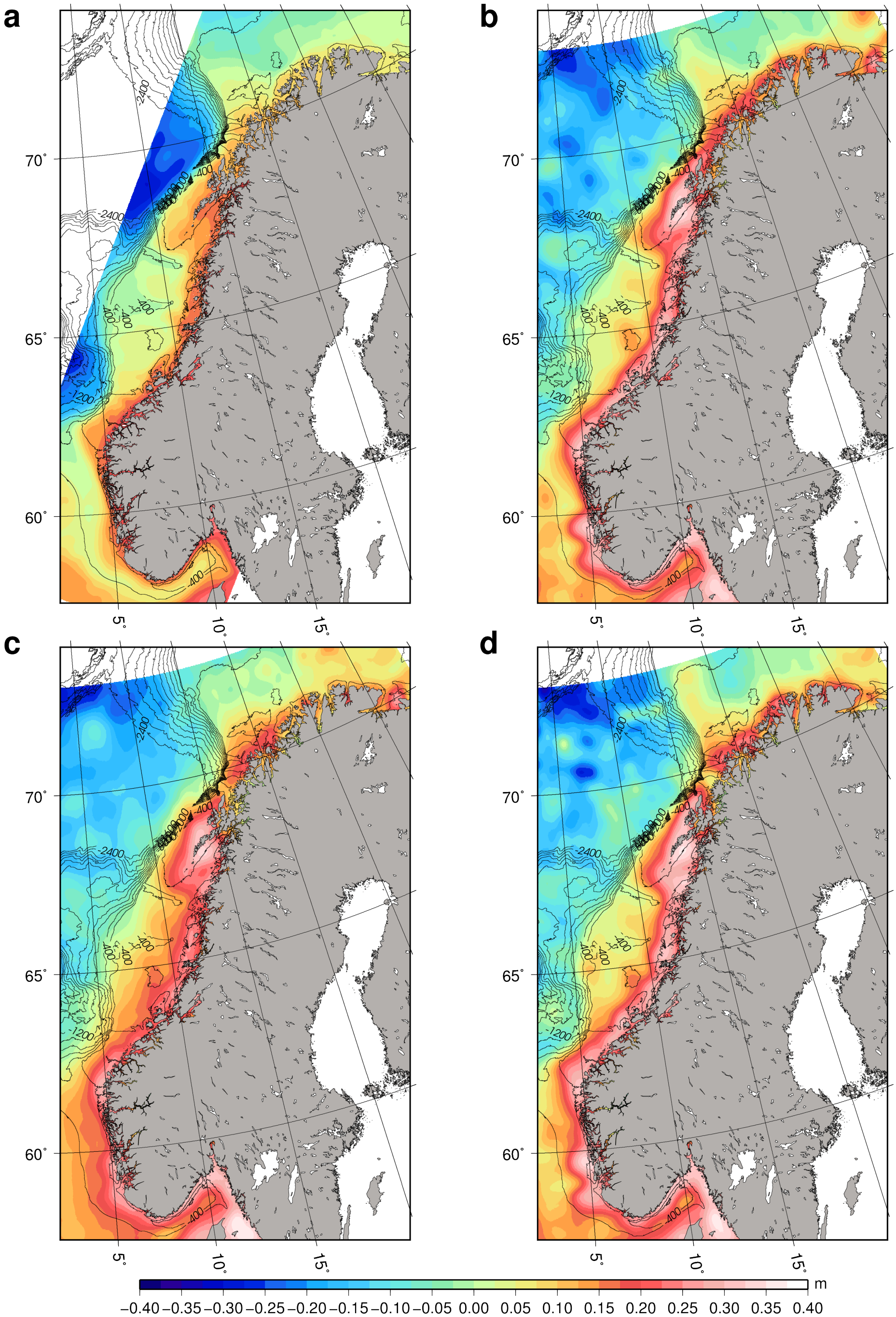

Figure 4.1. Coastal MDTs in Norway. (**a**) Ocean MDT, based on NorKyst800. Geodetic MDTs based on (**b**) $CS2_{NKG}$, (**c**) $CS2_{EGG}$, and (**d**) $CS2_{NMA}$. The mean value has been removed in all cases. In all figures (a-d), 400 m isobaths from the GEBCO 2019 grid (GEBCO, 2019) are shown.

Table 4.3. Statistics of MDTs and of their differences (in cm).

Model	min	max	mean	std
NorKyst800	−67.6	−7.6	−36.6	11.8
$CS2_{NKG}$	−37.5	43.4	8.2	14.3
$CS2_{EGG}$	−29.3	48.1	11.1	13.8
$CS2_{NMA}$	−30.4	47.7	11.2	14.3
$CS2_{NKG}$ − NorKyst800	−20.6	25.2	6.7	5.8
$CS2_{EGG}$ − NorKyst800	−33.5	32.6	7.9	6.5
$CS2_{NMA}$ − NorKyst800	−29.4	27.9	7.9	5.9

Table 4.4. Statistics of differences between tide-gauge MDT profiles (in cm).

Model	min	max	std
TG_{NKG} − $CS2_{NKG}$	−8.4	7.0	4.4
TG_{EGG} − $CS2_{EGG}$	−9.5	10.2	4.7
TG_{NMA} − $CS2_{NMA}$	−7.2	7.5	3.9
NorKyst800 − $CS2_{NKG}$	−6.1	6.1	3.6
NorKyst800 − $CS2_{EGG}$	−4.3	6.3	3.3
NorKyst800 − $CS2_{NMA}$	−6.0	5.9	3.2
NorKyst800 − TG_{NKG}	−5.3	11.5	4.1
NorKyst800 − TG_{EGG}	−6.0	11.4	4.6
NorKyst800 − TG_{NMA}	−10.0	10.4	3.9

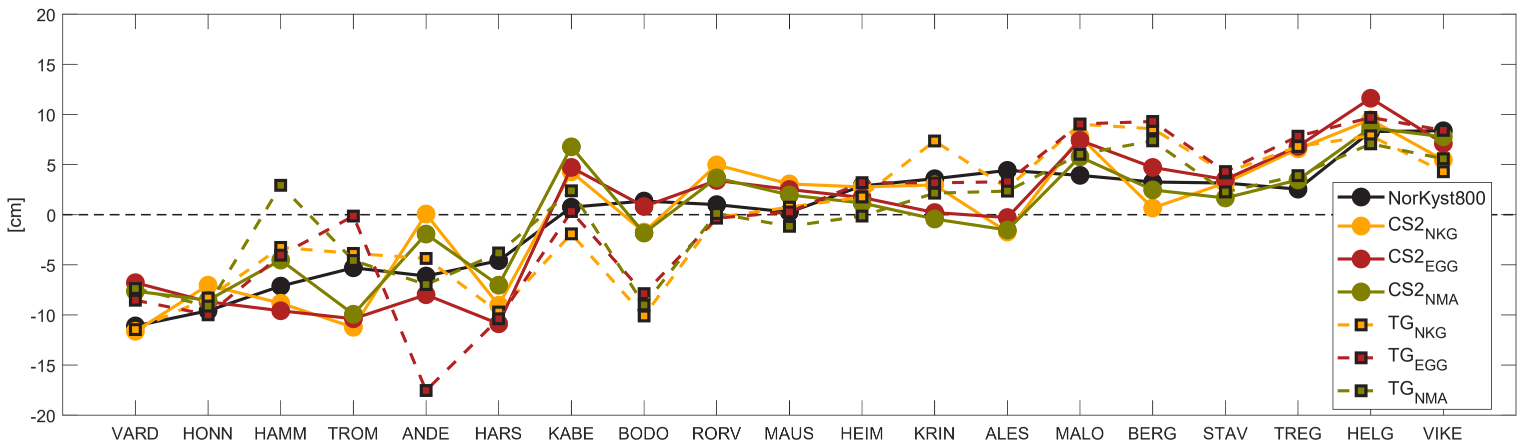

Figure 4.2. Tide-gauge MDT profiles using geodetic and ocean estimates, arranged from north to south. Tide-gauge locations are shown in Figure 2.11b.

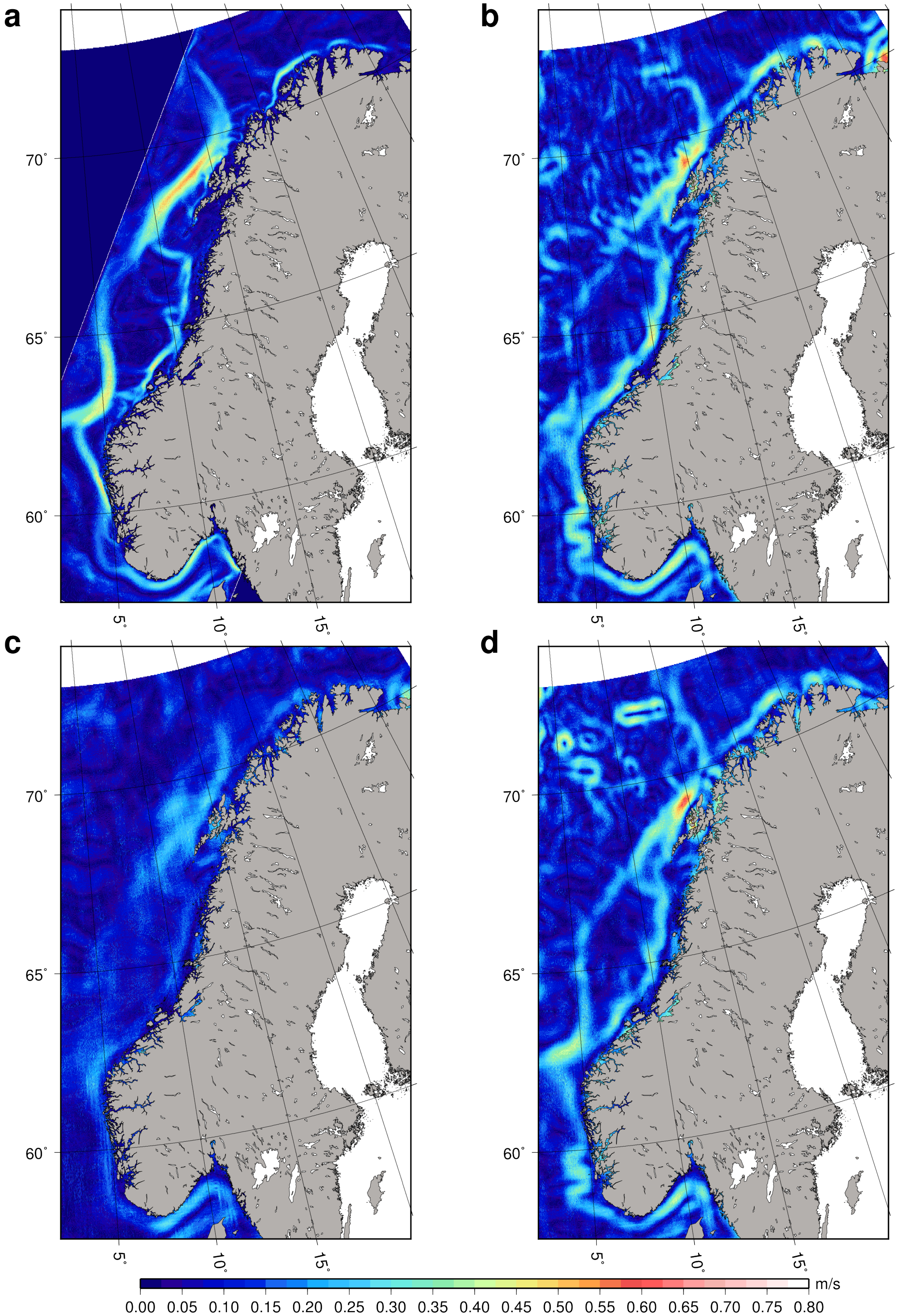

Figure 4.3. Geostrophic ocean surface currents derived from (**a**) NorKyst800, (**b**) $CS2_{NKG}$, (**c**) $CS2_{EGG}$, and (**d**) $CS2_{NMA}$.

4.2 Vertical land motion in Fennoscandia

The following sections gather results from **Paper C** and **Paper D**. In **Paper C**, ice histories from the ICE-x series along with VMx and NKG rheology profiles were used to predict vertical velocity fields as well as time series of RSL change. Predictions based on an additional rheology profile, namely, M_1 (Colli et al., 2018) are also included in this thesis. Computations were performed with SELEN and validated against the semi-empirical land-uplift model NKG2016LU_abs as well as geological RSL reconstructions from the global Tushingham and Peltier (1992) database. In **Paper D**, 7.5 years of CS2 satellite altimetry were combined with TG data to estimate linear VLM rates at 20 TGs along the Norwegian coast. Monthly-averaged PSMSL and 10-minute TG data from NMA were used. VLM estimates were validated against NKG2016LU_abs rates.

4.2.1 Vertical land motion and relative sea levels from GIA modelling

Comparison of various software solutions

The present-day radial velocity field based on ICE-5G from Peltier (2004) is denoted VLM_{ICE5G} and the one calculated with SELEN VLM_{ICE5G_S}. In addition, the present-day radial velocity field based on ICE6G_C from Peltier et al. (2015) is denoted VLM_{ICE6G_C}, the CALSEA solution VLM_{ICE6G_ANU}, and the one calculated using SELEN VLM_{ICE6G_S}. The parameter overview for determining vertical displacements and RSL changes is given in Table 3.2.

The statistics for all uplift-rate differences between NKG2016LU_abs and modelled values was calculated over land points within an area delimited by $49° < \varphi < 73°$ and $4° < \lambda < 35°$ because only there is NKG2016LU_abs constrained by geodetic observations. Figures 4.4a-4.4c present differences between NKG2016LU_abs and uplift rates calculated with ICE6G_C. Comparing Figures 4.4a and 4.4b, similar geographical structures with an offset between the velocity fields are noted. This is also reflected in their differences in Figure 4.4d and in the corresponding statistics in Table 4.5. The SELEN solution (Figure 4.4c) gives a less correlated velocity field but still reflects the main features, having a standard deviation of differences of ~0.6 mm/yr when compared to Lambeck's solution (Figure 4.4e). Differences between NKG2016LU_abs and vertical-uplift rates using ICE-5G (VM2/VM2a) in Table 3.2 vary between −4.2 and 2.9 mm/yr. Differences based on ICE6G_C (VM5a) range from −2.2 to 2.6 mm/yr.

Based on the statistics in Table 3.2, it was not observed that the less complex software (SELEN) gives worst results in all cases. In terms of the average velocity field, Peltier's solution fits NKG2016LU_abs better than SELEN when using ICE-5G (VM2). However, applying ICE6G_C (VM5a) results in the worst fit of Peltier's solution, while the ANU and SELEN solutions give a much better fit. In terms of standard deviations of differences to NKG2016LU_abs, a slightly different picture is found but still no clear deficiency of SELEN compared to the other software packages.

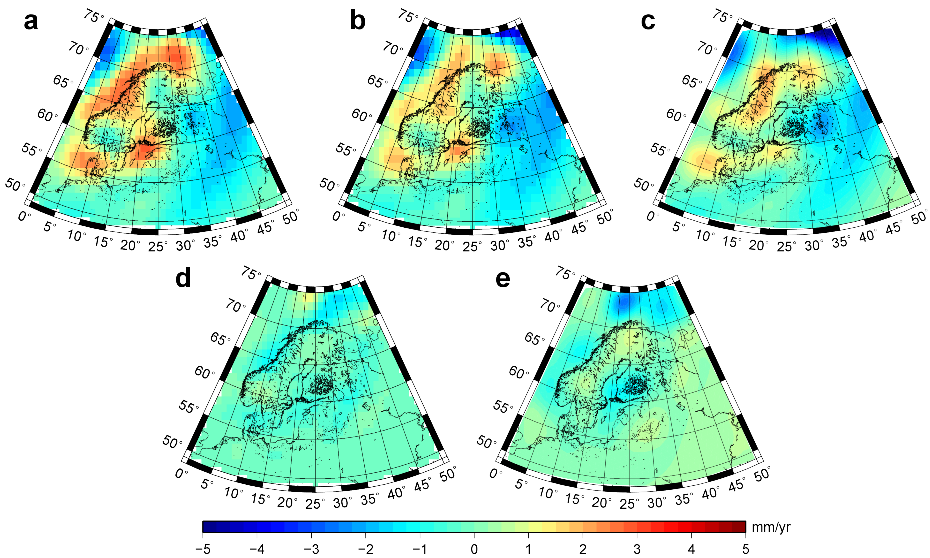

Figure 4.4. The first row shows differences between NKG2016LU_abs and (**a**) VLM_{ICE6G_C}, (**b**) VLM_{ICE6G_ANU}, and (**c**) VLM_{ICE6G_S}. The second row shows differences between software solutions (**d**) VLM_{ICE6G_C} and VLM_{ICE6G_ANU} (a−b), and (**e**) VLM_{ICE6G_ANU} and VLM_{ICE6G_S} (b−c).

Table 4.5. Statistics of differences (in mm/yr) between VLM_{ICE5G} and VLM_{ICE5G_S}, VLM_{ICE6G_C} and VLM_{ICE6G_ANU} (Figure 4.4d) as well as VLM_{ICE6G_ANU} and VLM_{ICE6G_S} (Figure 4.4e).

Model	min	max	mean	std
$VLM_{ICE5G} - VLM_{ICE5G\_S}$	−4.4	1.3	−0.6	1.2
$VLM_{ICE6G\_C} - VLM_{ICE6G\_ANU}$	−1.6	1.1	−0.2	0.4
$VLM_{ICE6G\_ANU} - VLM_{ICE6G\_S}$	−2.7	0.8	−0.1	0.6

Comparison of different ice/Earth model combinations

Vertical uplift rates Statistics of the external comparison is given in Table 4.6, the internal one in Table 4.7. Corresponding geographical maps of differences are shown in Figures 4.5 (external) and 4.6 (internal). Only maps based on ICE-5G are shown because maps based on ICE6G_C show very similar geographical patterns. The VM1-based combinations are chosen as reference solutions for the internal comparisons because they fit NKG2016LU_abs best in terms of average velocity fields for both ice models (Table 4.6).

Figure 4.5 shows the comparison of calculated SELEN uplift rates (using ICE-5G) with NKG2016LU_abs. Similar geographical patterns for the group of velocity fields calculated using VMx rheologies are notable (Figures 4.5a-4.5c). The group of NKG and M_1 rheologies also results in similar patterns (Figures 4.5d-4.5e). In Figures 4.5a-4.5c, a low over Finland and the Barents Sea is noted, while this low is more significant in Figures 4.5d-4.5f and expands over the Gulf of Bothnia and the Norwegian Sea. The comparison of mean values in Table 4.6 reveals an offset in the order of ~0.5 mm/yr between ICE6G_C and ICE-5G solutions. The average velocity fields based on ICE6G_C fit better NKG2016LU_abs than ICE-5G solutions. All SELEN solutions predict greater present-day uplift rates than NKG2016LU_abs, implying a too slow relaxation process. In terms of standard deviations of differences to NKG2016LU_abs, Table 4.6 shows smaller values for ICE6G_C than for ICE-5G. This indicates that not only the total ice load but also the spatial distribution and deglaciation history of ICE6G_C are more realistic than of ICE-5G.

In general, uplift rates calculated with VM1 are smaller in comparison to other uplift rates. In Figure 4.6, two groups of geographical patterns are observed: the first for VMx rheologies and the second for NKG rheologies and M_1. Few high peaks appear when calculating differences between VM1 and the other two VMx rheologies (Figures 4.6a and 4.6b). Negative values along the ice-sheet margin occur when forming differences to NKG rheologies and M_1 (Figures 4.6c-4.6e), which all have one-magnitude higher lower-mantle viscosities than VM1. A decreasing similarity from VM2a over VM5a, GIA_prel0306, GIA_prel0907 to M_1 with VM1 is notable for both ice models. Except the difference to $\mathrm{VLM}_{\mathrm{I6G(VM2a)}}$ and $\mathrm{VLM}_{\mathrm{I6G(M_1)}}$, all differences calculated with ICE6G_C show slightly smaller standard deviations of differences than the ones determined with ICE-5G.

Uplift rates calculated with NKG and M_1 rheologies show a significant offset in comparison to NKG2016LU_abs as well as large standard deviations, which is also reflected in the internal comparison. VMx Earth models were used in the reconstruction of ICE-x models and tuned to various data sets, making ice models highly dependent upon Earth model information. This could explain the significant offsets when combining ICE-x models with other uncorrelated Earth models.

Table 4.6. Statistics of differences between land-uplift rates based on observations and GIA modelling (in mm/yr).

NKG2016LU_abs – … [a]	min	max	mean	std
$\mathrm{VLM}_{\mathrm{I5G(VM1)}}$	−4.7	1.5	−0.4	1.3
$\mathrm{VLM}_{\mathrm{ICE5G(VM2a)}}$	−4.2	1.0	−0.7	1.0
$\mathrm{VLM}_{\mathrm{I5G(VM5a)}}$	−3.8	1.9	−0.5	1.1
$\mathrm{VLM}_{\mathrm{I5G(prel0306)}}$	−5.1	0.9	−1.4	1.7
$\mathrm{VLM}_{\mathrm{I5G(prel0907)}}$	−6.5	1.1	−1.6	2.2
$\mathrm{VLM}_{\mathrm{I5G(M_1)}}$	−8.0	1.0	−2.1	2.5
$\mathrm{VLM}_{\mathrm{I6G(VM1)}}$	−2.4	1.8	0.0	0.7
$\mathrm{VLM}_{\mathrm{I6G(VM2a)}}$	−1.7	1.6	−0.1	0.7
$\mathrm{VLM}_{\mathrm{ICE6G(VM5a)}}$	−2.2	2.2	0.0	0.9
$\mathrm{VLM}_{\mathrm{I6G(prel0306)}}$	−3.8	0.8	−0.9	1.1
$\mathrm{VLM}_{\mathrm{I6G(prel0907)}}$	−4.7	0.9	−1.2	1.5
$\mathrm{VLM}_{\mathrm{I6G(M_1)}}$	−5.8	0.8	−1.6	1.9
$\dot{h}_{\mathrm{empirical\_obs}} - \dot{h}_{\mathrm{NKG2016GIA\_prel0306}}$ [b]	-1.2	1.2	-0.1	0.3

[a] over land points within an area delimited by $49° < \varphi < 73°$ and $4° < \lambda < 35°$

[b] in observation points (Vestøl et al., 2016)

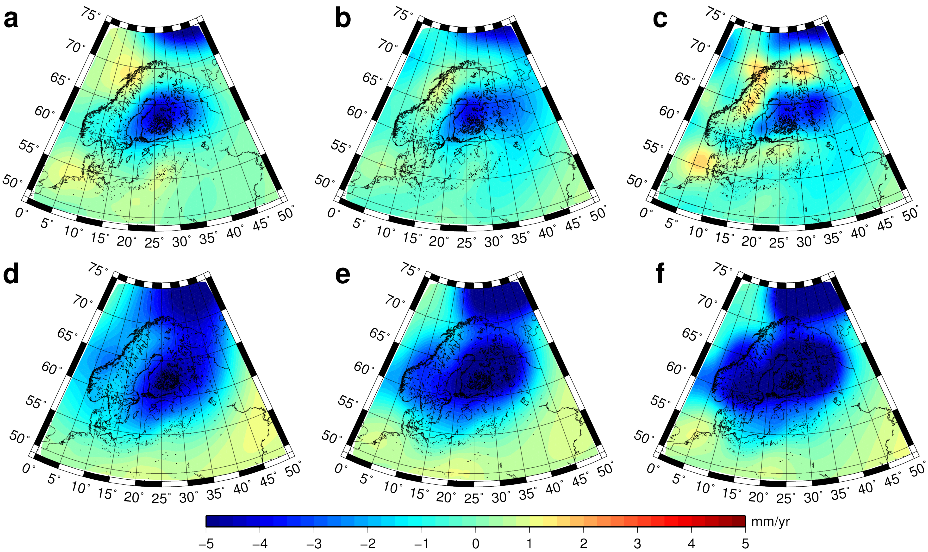

Figure 4.5. Differences between NKG2016LU_abs and modelled uplift rates: (**a**) $\mathrm{VLM}_{\mathrm{I5G(VM1)}}$, (**b**) $\mathrm{VLM}_{\mathrm{I5G(VM2a)}}$, (**c**) $\mathrm{VLM}_{\mathrm{I5G(VM5a)}}$, (**d**) $\mathrm{VLM}_{\mathrm{I5G(prel0306)}}$, (**e**) $\mathrm{VLM}_{\mathrm{I5G(prel0907)}}$, and (**f**) $\mathrm{VLM}_{\mathrm{I5G(M_1)}}$.

Table 4.7. Statistics of differences between calculated VLM rates based on ICE-5G and ICE6G_C (in mm/yr). The rheology profile VM1 was chosen as a reference and differences relative to it were computed.

$\mathbf{VLM}_{\mathrm{I5G(VM1)}} - \ldots$ [a]	min	max	mean	std
$\mathrm{VLM}_{\mathrm{I5G(VM2a)}}$	−1.7	0.9	−0.4	0.6
$\mathrm{VLM}_{\mathrm{I5G(VM5a)}}$	−1.6	2.2	−0.1	0.9
$\mathrm{VLM}_{\mathrm{I5G(prel0306)}}$	−3.8	1.0	−0.7	1.2
$\mathrm{VLM}_{\mathrm{I5G(prel0907)}}$	−3.8	0.7	−1.3	1.3
$\mathrm{VLM}_{\mathrm{I5G(M_1)}}$	−4.4	0.5	−1.8	1.6
$\mathbf{VLM}_{\mathrm{I6G(VM1)}} - \ldots$ [a]				
$\mathrm{VLM}_{\mathrm{I6G(VM2a)}}$	−1.7	1.2	−0.3	0.6
$\mathrm{VLM}_{\mathrm{I6G(VM5a)}}$	−1.2	2.3	−0.1	0.8
$\mathrm{VLM}_{\mathrm{I6G(prel0306)}}$	−3.4	1.0	−0.6	1.1
$\mathrm{VLM}_{\mathrm{I6G(prel0907)}}$	−3.5	0.6	−1.2	1.2
$\mathrm{VLM}_{\mathrm{I6G(M_1)}}$	−4.0	0.5	−1.6	1.6

[a] over land points within an area delimited by $49° < \varphi < 73°$ and $4° < \lambda < 35°$

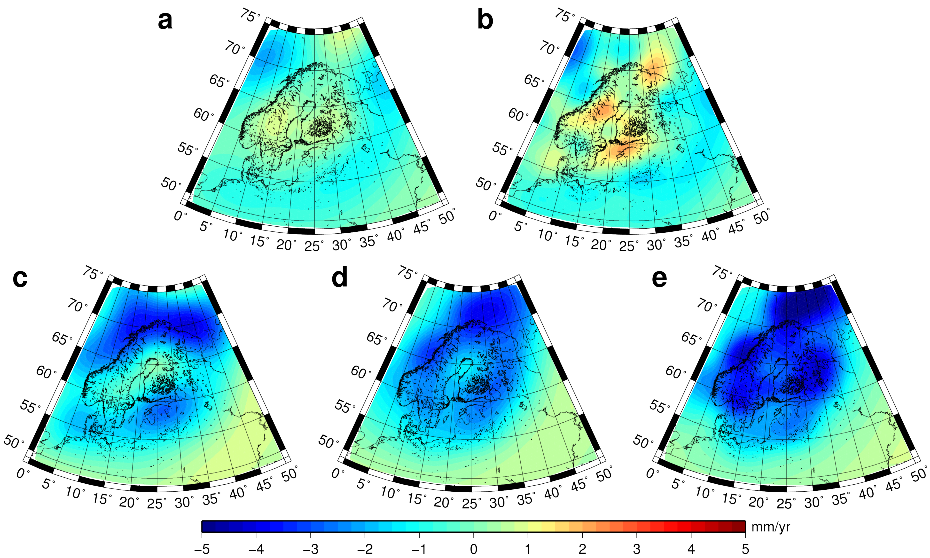

Figure 4.6. Comparison of uplift rates calculated with SELEN where ICE-5G was used. The rheology profile VM1 was chosen as a reference and differences to calculated VLM rates based on (**a**) VM2a, (**b**) VM5a, (**c**) GIA_prel0306, (**d**) GIA_prel0907, and (**e**) M_1 are shown.

Relative sea levels Differences between geological RSL data and RSL predictions from SELEN using different ice histories and rheologies at 55 sites in Fennoscandia, illustrated in Figure 3.9a, were computed. Differences vary between −147.01 and 89.43 m (**Paper C**, Table 6). In general, ICE6G_C solutions give a considerably better fit to RSL data than ICE-5G solutions in terms of both mean values as well as standard deviations of differences. In view of mean values and standard deviations of differences, the RSL predictions based on NKG rheologies show a better agreement to RSL data than the ones based on VMx and M_1 rheologies.

Figure 4.7 shows the fit between RSL data and calculated RSL curves using ICE-5G and ICE6G_C with different rheology profiles at chosen sites. The presented sites were chosen depending on the distance to the former ice sheet. A slight grouping of RSL-prediction curves according to the applied ice model and its ice-sheet distribution/thickness is observed. RSL predictions obtained using ICE-5G (red-nuanced curves) show larger RSL changes than predictions based on ICE6G_C (blue-nuanced curves) due to thicker ice-sheets of ICE-5G (compare Figures 3.7c and 3.7d). At the ice-sheet margin and near-field area, two branches of RSL-prediction curves are noted (Figures 4.7a-4.7e). The first branch gathers RSL curves of VMx rheologies and the second one gathers RSL curves based on NKG rheologies. The RSL curves based on M_1 are between those two groups. The variations of RSL-prediction curves within each branch in the ice-margin area are harder to distinguish than in the near-field region. Significant differences of RSL predictions in the near field (which is dominated by land uplift) are highly dependent on rheology. The LT, asthenosphere, and lower-mantle viscosity are affecting the behavior of RSL-prediction curves there. First, RSL curves are gathering according to the LT; a larger LT (Figure 3.6) results in smaller RSL changes. Secondly, GIA_prel0907 that assumes an additional layer under the lithosphere shows smaller RSL predictions in comparison to GIA_prel0306, although the first has a thinner lithosphere. Finally, RSL predictions based on GIA_prel0306, GIA_prel0907, and M_1 with one-magnitude higher lower-mantle viscosities show smallest RSL-change values.

The smoother NKG-based RSL-prediction curves in Figure 4.7 show a slower reaction to the unloading with consequently smaller mean values that fit the RSL data better than the VMx- and M_1-based predictions. Due to the slower relaxation process, NKG-based land-uplift rates show greater present-day rates (Table 4.6 and Figure 4.5).

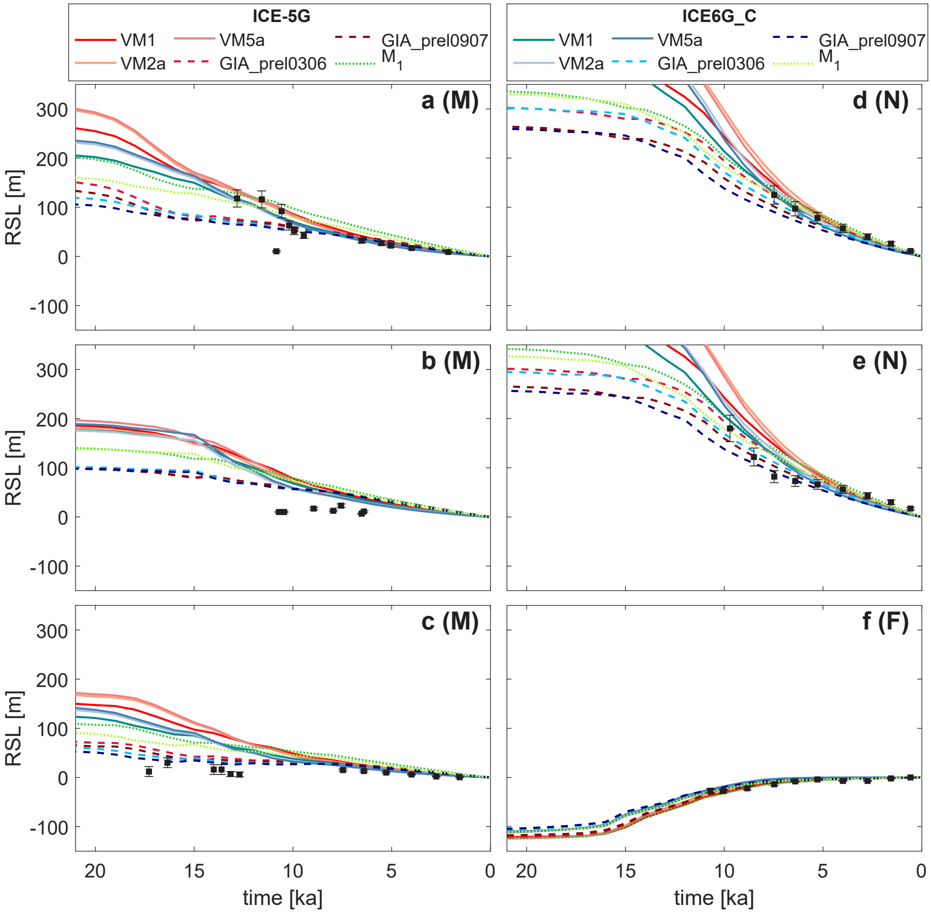

Figure 4.7. Variation of relative sea-level curves at sites (**a**) 209, (**b**) 237, (**c**) 239, (**d**) 233, (**e**) 234, and (**f**) 409, and their comparison to geological relative sea-level data (including relative sea-level error bars). See Figure 3.9a for site locations. Red nuances represent relative sea-level curves calculated using ICE-5G, while blue-nuanced relative sea-level curves are computed applying ICE6G_C. Dotted green-nuanced relative sea-level curves are calculated applying M_1 rheology and ICE-5G/ICE6G_C. M, N, and F define site locations with respect to the former ice sheet: M stands for ice-sheet margin, N for near field, and F for far field.

4.2.2 Vertical land motion from satellite altimetry and tide-gauge records

Linear rates of VLM at 20 TGs from NKG2016LU_abs and CS2 combined with TG records over the period 2010-2018 are illustrated in Figure 4.8. NKG2016LU_abs shows positive rates (from 1.3 mm/year at MALO to 4.7 mm/year at TRON) for all 20 TGs. This is also confirmed by the majority of estimated VLM rates. Uncertainties (**Paper D**, Figure 3), which take into account serial correlations of measurements range from 3.1 to 27.1 mm/yr when using 1 Hz CS2 sea-level anomalies, and from 1.1 to 18.5 mm/yr when using 20 Hz CS2 data. Largest uncertainties occur at TGs with few CS2 observations available, i.e., at TRON, HEIM, OSCA, and HAMM (Figures 2.9 and 2.10).

VLM rates based on both 1 and 20 Hz CS2 data in combination with NMA TG measurements (VLM_{1HzNMA} and $VLM_{20HzNMA}$) agree with NKG2016LU_abs within uncertainties for most of the sites. Their differences range from −13.9 to 8.1 mm/yr. When using PSMSL TG data for the VLM estimation ($VLM_{1HzPSMSL}$ and $VLM_{20HzPSMSL}$), differences range between −23.2 and 16.3 mm/yr. Standard deviations of differences between NKG2016LU_abs and rates of VLM based on PSMSL TG records are twice as large as the standard deviations between NKG2016LU_abs and rates from NMA TG data. This could be explained by different sampling rates of PSMSL (monthly) and NMA (10-minute) TG data. 1 and 20 Hz sampling frequencies of CS2 imply that altimetry observations include ocean signals, which are averaged to nearly zero in monthly TG data. Consequently, differential ocean signal might be introduced into differences between CS2 and monthly TG time series.

NKG2016LU_abs has a coastal average of 2.8 mm/yr over all 20 TGs (**Paper D**, Table 2). $VLM_{1HzPSMSL}$ shows a coastal average of 4.4 mm/yr and VLM_{1HzNMA} of 2.4 mm/yr. VLM rates based on 20 Hz CS2 data show coastal averages of 5.5 mm/yr ($VLM_{20HzPSMSL}$) and 3.4 mm/yr ($VLM_{20HzNMA}$). The mean Spearman's rank correlation coefficient (see **Paper A** for more details) between VLM estimates based on PSMSL data and NKG2016LU_abs is 0.53 when using 1 Hz CS2 data and 0.46 when using the 20 Hz CS2 observation. Employing NMA TG records, the mean correlation between VLM rates and NKG2016LU_abs over all TGs is 0.58 and 0.43 for 1 and 20 Hz CS2 data, respectively.

High discrepancies between NKG2016LU_abs and VLM rates from CS2 and TG data are found at both TGs that are land-confined and located to the open ocean. For all four solutions, the largest misfits to NKG2016LU_abs are observed at TRON, HEIM, and OSCA, all located deeply inside fjords. Leaving out these TGs, the coastal average of NKG2016LU_abs drops from 2.8 to

2.6 mm/yr. Excluding TRON, HEIM, and OSCA from the comparison reduces the minima and standard deviations of differences for all VLM solutions considerably (Table 4.8). A decrease in the coastal averages of estimated VLM rates is noted as well as reduced uncertainties. $\mathrm{VLM}_{1\mathrm{HzPSMSL}}$ and $\mathrm{VLM}_{1\mathrm{HzNMA}}$ differ on average 1.4 and 1.5 mm/yr from NKG2016LU_abs, respectively. $\mathrm{VLM}_{20\mathrm{HzPSMSL}}$ differs on average 0.1 mm/yr from NKG2016LU_abs and $\mathrm{VLM}_{20\mathrm{HzNMA}}$ 0.3 mm/yr. The agreement of mean values of differences between estimated VLM rates and NKG2016LU_abs is also reflected in the agreement between their coastal averages. VLM rates based on 1 Hz CS2 data show coastal averages of 1.2 mm/yr ($\mathrm{VLM}_{1\mathrm{HzPSMSL}}$) and 1.1 mm/yr ($\mathrm{VLM}_{1\mathrm{HzNMA}}$), while estimates of VLM based on 20 Hz data have coastal averages of 2.5 mm/yr ($\mathrm{VLM}_{20\mathrm{HzPSMSL}}$) and 2.3 mm/yr ($\mathrm{VLM}_{20\mathrm{HzNMA}}$).

Table 4.8. Statistics of differences between NKG2016LU_abs and vertical land-motion rates (in mm/yr) represented in Figure 4.8 and calculated over 20 tide gauges along the Norwegian coast. Vertical land-motion rates result from either GIA modelling (**Paper C**) or combining CryoSat-2 observations with tide-gauge data (**Paper D**). In addition, Spearman's rank correlation coefficient ρ between NKG2016LU_abs and vertical land-motion rates is given. The last column shows coastal averages of vertical land motion calculated over tide gauges along the Norwegian coast.

Paper	NKG2016LU_abs − ...	min	max	mean	std	ρ	coastal average
C	$\mathrm{VLM}_{\mathrm{I5G(VM2a)}}$	−0.5	0.7	−0.2	0.4	0.89	3.0
	$\mathrm{VLM}_{\mathrm{I6G(VM5a)}}$	−0.3	2.1	0.8	0.6	0.87	2.0
	$\mathrm{VLM}_{\mathrm{I5G(GIA\_prel0306)}}$	−4.1	−1.7	−2.4	0.7	0.84	5.2
	$\mathrm{VLM}_{\mathrm{I6G(GIA\_prel0306)}}$	−3.0	−0.7	−1.5	0.7	0.83	4.4
	$\mathrm{VLM}_{\mathrm{I5G(GIA\_prel0907)}}$	−4.0	−1.4	−2.8	0.8	0.89	5.6
	$\mathrm{VLM}_{\mathrm{I6G(GIA\_prel0907)}}$	−2.9	−0.9	−1.8	0.6	0.92	4.6
	$\mathrm{VLM}_{\mathrm{I5G(M_1)}}$	−4.7	−1.6	−3.6	1.0	0.86	6.4
	$\mathrm{VLM}_{\mathrm{I6G(M_1)}}$	−3.5	−0.9	−2.3	0.9	0.93	5.2
D	$\mathrm{VLM}_{1\mathrm{HzPSMSL}}$	−23.2	16.3	−1.5	11.0	0.53	4.4
	$\mathrm{VLM}_{1\mathrm{HzNMA}}$	−13.9	8.1	0.4	4.8	0.58	2.4
	$\mathrm{VLM}_{20\mathrm{HzPSMSL}}$	−23.2	14.5	−2.7	10.0	0.46	5.5
	$\mathrm{VLM}_{20\mathrm{HzNMA}}$	−10.5	6.5	−0.5	4.1	0.43	3.4
	$\mathrm{VLM}_{1\mathrm{HzPSMSL}}$ [a]	−12.3	16.3	1.4	8.7	0.29	1.2
	$\mathrm{VLM}_{1\mathrm{HzNMA}}$ [a]	−3.9	8.1	1.5	3.5	0.40	1.1
	$\mathrm{VLM}_{20\mathrm{HzPSMSL}}$ [a]	−13.1	14.5	0.1	7.7	0.19	2.5
	$\mathrm{VLM}_{20\mathrm{HzNMA}}$ [a]	−5.5	6.5	0.3	3.4	0.24	2.3

[a] TRON, HEIM, and OSCA were excluded

4.2.3 Vertical land-motion rates calculated by different approaches

In addition to VLM rates from NKG2016LU_abs as well as from combining CS2 with TGs in **Paper D**, Figure 4.8 shows rates from selected SELEN runs in **Paper C**. Modelled vertical-velocity fields in **Paper C** were interpolated onto 20 TG locations (same TG sites as used in **Paper D**). The corresponding statistics is given in the upper part of Table 4.8.

At 20 TGs, differences between NKG2016LU_abs and SELEN runs range from −4.7 to 2.1 mm/yr, and standard deviations of differences from 0.4 to 1.0 mm/yr. $VLM_{I5G(VM2a)}$ and $VLM_{I6G(VM5a)}$ show the best fit to NKG2016LU_abs in terms of mean differences and standard deviations (Table 4.8). Rates based on ICE6G_C and NKG and M_1 rheologies follow the form of NKG2016LU_abs rates in Figure 4.8 but show an offset of ~1.9 mm/yr (considering mean values in Table 4.8). Rates based on the same rheologies but ICE-5G show an offset of ~2.9 mm/yr. In terms of coastal averages, $VLM_{I5G(VM2a)}$ and $VLM_{I6G(VM5a)}$ reflect well the amplitude of coastal VLM provided by NKG2016LU_abs showing values of 3.0 and 2.0 mm/yr, respectively. Other SELEN solutions have coastal averages ranging from 4.4 to 6.4 mm/yr.

In general, the spread of rates from combining CS2 with TGs is larger than that of NKG2016LU_abs or of rates modelled by SELEN (Figure 4.8). This is especially notable for PSMSL-based VLM rates, where the combination of CS2 with PSMSL TG records does not observe VLM at some TGs. However, NMA-based solutions show a much smaller spread of differences to NKG2016LU_abs and a high spatial correlation. At HONN, KABE, RORV, MAUS, and VIKE, differences between VLM rates based on NMA TG data and NKG2016LU_abs are within the uncertainty of NKG2016LU_abs (~0.6 mm/yr). Correlations of NKG2016LU_abs to VLM rates from SELEN are considerably higher (ranging from 0.83 to 0.93) than to VLM rates estimated from CS2 and TGs.

Kuo et al. (2004) combined TOPEX/POSEIDON data with TG observations, where both data sets covered the same time span from 1992 to 2001 to estimate VLM at 25 TGs in the Baltic Sea region. NKG2016LU_abs was interpolated onto locations of 25 TGs used in Kuo et al. (2004) and differences to their estimated VLM rates were calculated. Differences range from −4.7 to 7.4 mm/yr and have a standard deviation of 3.4 mm/yr. These values are comparable to VLM estimates based on 1 Hz CS2 observations and NMA TG data covering the 2010-2018 period (Table 4.8).

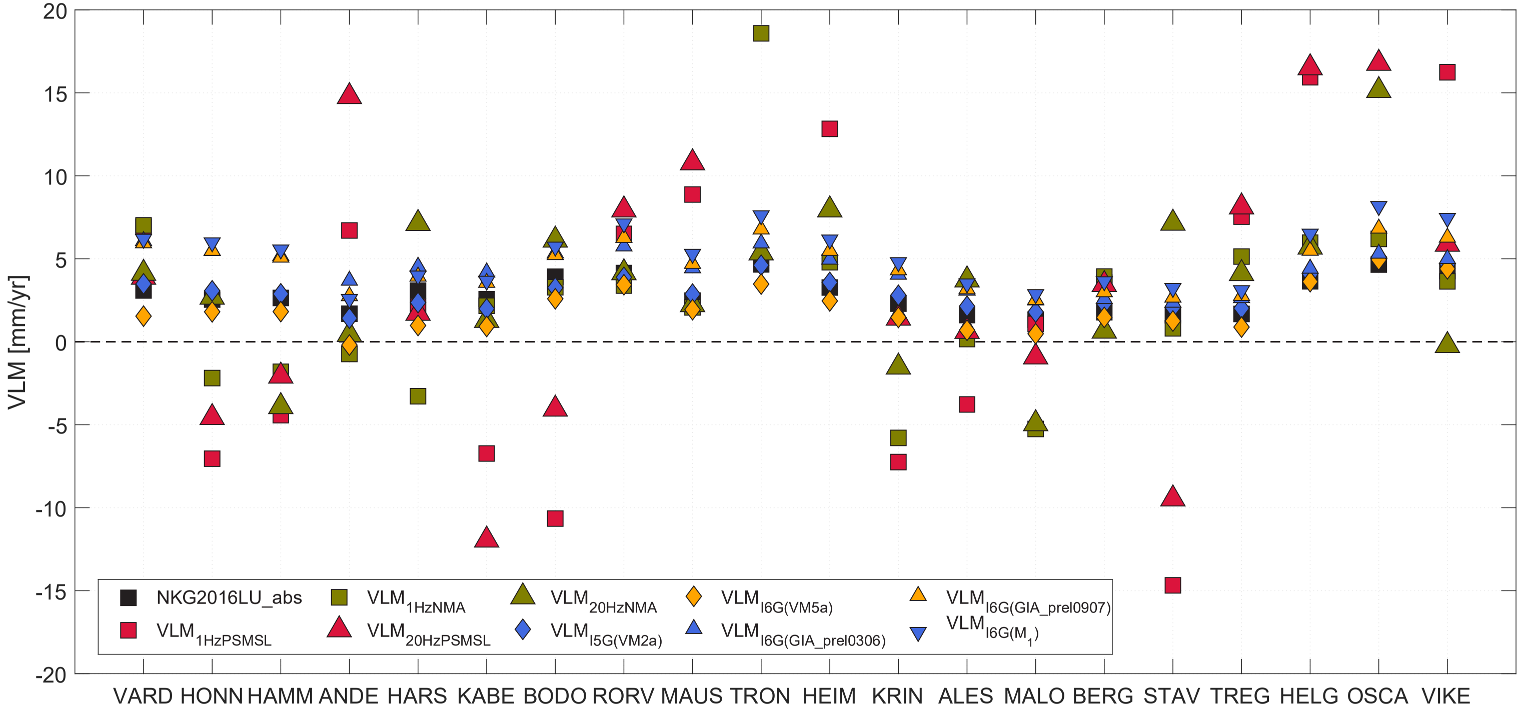

Figure 4.8. Rates of vertical land motion at 20 Norwegian tide gauges. Black squares represent rates from NKG2016LU_abs. Red squares and triangles represent vertical land motion calculated from tide-gauge data provided by PSMSL and NMA, respectively, and 1 Hz CryoSat-2 sea-level anomalies. Similarly, green squares and triangles represent rates calculated from 20 Hz CryoSat-2 observations. Vertical land-motion rates represented by diamonds, smaller upward- and downward-pointing triangles are uplift rates modelled using SELEN, and interpolated onto tide-gauge locations. Input parameters were ICE-5G and ICE6G_C ice histories with their corresponding Earth models as well as GIA_prel0306, GIA_prel0907, and M_1. Results from **Paper C** and **Paper D** are combined in this figure.

4.3 Limitations to the research

At the time of data processing, the off-nadir range correction was not implemented in the DTU Space retracking system. Consequently, SARIn observations in **Paper A** are degraded-SARIn observations excluding phase information. Usually, SSHs and sea-ice freeboard acquired in SARIn mode are processed using a SAR-like approach with degraded noise levels. By using the phase information from the SARIn mode to range correct off-nadir measurements, the accuracy and precision of the estimated SSHs is improved by increasing the number of valid waveforms despite the degraded noise level (Quartly et al., 2019). This is reflected in the comparison with TG observations and the better performance of off-nadir range corrected SSHs in **Paper D** than of degraded-SARIn SSHs in **Paper A**. One has to keep in mind that those two data sets were retracked by different retrackers (SAMOSA2 versus simple threshold retracker). The editing criteria for CS2 SARIn data was crude, where only ~60% of data were kept after omitting points over land and the within-track outlier detection. This shows that not only a considerable amount of data did not pass the editing but also demonstrates that CS2 targets along the Norwegian coast are generally noisy.

Coastal geodetic MDT models determined in **Paper B** are highly dependent on the used regional geoid models and show different artifacts related to the resolution and accuracy of marine geoids. The three regional geoid models are based on GOCE release five gravity data and slightly varying terrestrial gravity data. Hence, different interpolation methods and weighting used for their determination are likely to affect the observed variations in geodetic MDTs. NKG2015 and NMA2014 are both almost completely free of altimetry-derived gravity information and therefore independent of altimetry data they are subtracted from. On the other hand, EGG2015 is heavily based on altimetry-derived gravity data. CS2 MDTs based on NKG2015 and NMA2014 fit NorKyst800 and TG MDTs better than the CS2 MDT based on EGG2015. Consequently, the circulation pattern in $CS2_{EGG}$ is less emphasized and north-south flows are less distinct. Another challenge is the CS2 geographical mode mask. The SARIn zone stretches out only ~40 km off the coast and the border between SARIn and LRM/SAR modes largely overlaps with the Norwegian Coastal Current in the Norwegian coastal zone. This makes the combination of CS2 data acquired in different modes more difficult. In addition, CS2 observations are sparse and more uncertain in areas where SIRAL is switching modes. Furthermore, due to the missing tie between TG benchmark and GNSS benchmark, ellipsoidal heights of MSL were determined using HREF. This procedure makes ellipsoidal heights dependent on HREF, which is in turn dependent on GNSS/levelling and the geoid it is based on.

In **Paper C**, a software for a linear, incompressible, non-rotating Earth with fixed shorelines was used, which possibly introduces errors into the predictions. Ice models determined by the classical approach were used for SELEN runs in the thesis. Those ice models strongly contain Earth model information since their determination is based on a particular initial Earth model, which is then iteratively refined through inversion (Steffen and Wu, 2011). In addition, radially-varying (1D) Earth models, which assume the Earth's mantle to be uniformly layered in terms of viscosity were used. Whitehouse et al. (2006) found that neglecting lateral variations in LT and in mantle viscosity can introduce a bias of up to 3 mm/yr into predictions of present-day uplift rates in Fennoscandia, 1 mm/yr for horizontal rates, or 70 m for predictions in RSL at 10 ka BP. All these errors peak at the center of former ice sheets. According to Wu (1998), geodetic quantities are more affected by lateral variations in the asthenopshere than by lateral variations in LT (Steffen and Wu, 2011). Considering the spatial scale, ice models that were optimally fitted to global data sets were used and we looked into variations at regional scales, which do not have to reflect the same behavior as global variations. Moreover, Earth models that fit RSL data over a time scale of thousands of years do not necessarily need to agree with present-day geodetic observations.

Different OT corrections applied to CS2 SARIn observations (FES2004) and NMA TG measurements (local OT corrections) in **Paper D** are possible reasons for the misfit between NKG2016LU_abs and estimated VLM rates at some TGs. Particularly at HAMM, TRON, HEIM, and KRIN, discrepancies between signal standard deviations of FES2004 and local OT corrections within CS2 boxes are ranging between 6.7 and 28.5 cm. The largest differences to NKG2016LU_abs are also found at these TGs. The wide spread of estimated VLM rates not seen in NKG2016LU_abs might be due to an insufficient number of CS2 observations within CS2 boxes, instrumental noise, and complex ocean or coastal processes (e.g., local subsidence not seen by NKG2016LU_abs). In addition, estimated errors of VLM rates are strongly dependent on the number of CS2 observations available in each box. Consequently, mean uncertainty estimates based on 20 Hz data are much smaller than those based on 1 Hz data.

Chapter 5

Summary, conclusions, and outlook

5.1 Summary and conclusions

The thesis provides the following conclusions:

- New generation SAR(In)-altimetry, i.e., CS2 observes the sea surface in areas previously uncovered by conventional altimetry and demonstrates the possibility of mapping local coastal topographies in a rugged, steep, and narrow coast like in Norway.

- Compared with 10-minute TG measurements at 22 TGs, standard deviations of differences are between 7 and 20 cm, with largest variations at TGs located deep inside fjords with only few observations.

- Exchanging standard tidal and atmospheric corrections with local corrections determined from predicted tides and air-pressure observations, respectively, a decrease in standard deviations of differences is noted at 19 out of 22 TGs. The correction swap led to an average improvement of ~24% in standard deviations of differences (from 16 cm to 12.2 cm) and ~12% for correlations (from 0.61 to 0.68).

- Off-nadir range corrected SARIn observations retracked using SAMOSA2 perform better in the comparison to TG observations than degraded-SARIn observations retracked applying the simple threshold retracker without phase information.

- The general circulation pattern in the Norwegian Sea is revealed in geodetic MDTs.

- Compared to NorKyst800, $CS2_{EGG}$ shows a slightly larger standard deviation of differences of ~7 cm than $CS2_{NKG}$ and $CS2_{NMA}$ with standard deviations of ~6 cm.
- At TGs, the fit between coastal geodetic and oceanographic MDT models is on the 3-5 cm level.
- For the first time, the Norwegian Coastal Current is revealed by geodetic techniques.
- The circulation patterns are dependent on geoids they are based on, i.e., their resolution and accuracy. All geoid models that were used are based on GOCE, hence, their variations are related to the quality of included terrestrial data.
- An equivalent to GNSS/levelling for geoid validation over land is the determination of circulation patterns over ocean. The geostrophic surface currents can be used to reveal errors (observational or interpolation errors) and data gaps in regional geoid models.
- New regional geoid models as well as CS2 have improved the coastal MDT models and demonstrate the potential of coastal MDT determination, especially for coastal regions, which are not monitored by TGs.
- Uplift rates resulting from three software packages (which differ in methods, approximations, and assumptions) show similar geographical structures when compared to NKG2016LU_abs. NKG2016LU_abs and all software solutions (for both ice models and their related Earth models) agree on average on a ~1 mm/yr level in terms of standard deviations of differences.
- Considering that the NKG2016LU_abs signal standard deviation is 3.5 mm/yr, a misfit of 1 mm/yr seems quite large. However, one has to consider that the employed ice histories and rheologies are derived from a best fit towards geological and geodetic data in a global sense, while the comparison is restricted to Fennoscandia.
- In general, land-uplift rates calculated with SELEN using both ICE-5G and ICE6G_C show larger values than observations in NKG2016LU_abs reflect, indicating that the ice history/rheology combinations show a too slow relaxation process for Fennoscandia, i.e., larger land-uplift rates at present day.
- Based on the validation against NKG2016LU_abs and geological relative sea-level data, the ice load, its spatial distribution, and ice-melting history seem more realistic for ICE6G_C than for ICE-5G.

- Modelled uplift rates are not sensitive to variations of lithospheric thickness and the inclusion of asthenosphere, but more sensitive to lower mantle-viscosity variations, while the opposite holds for relative sea-level predictions.

- A higher viscosity for the lower mantle results in slowing down the rebound over the whole deglaciation phase, implying higher present-day velocities (e.g., GIA_prel0306, GIA_prel0907, and M_1).

- Vertical velocity fields calculated with VMx rheologies have a better agreement with NKG2016LU_abs than the ones calculated with NKG rheologies in terms of standard deviations of differences. The opposite holds for the agreement between RSL predictions and relative sea-level observations, where NKG rheologies agree slightly better.

- NKG2016LU_abs shows an average signal of 2.8 mm/yr at 20 TGs along the Norwegian coast, while the coastal averages of estimated VLM rates (based on 10-minute TG observations) are 2.4 mm/yr and 3.4 mm/yr with 1 and 20 Hz CS2 data, respectively.

- A mean correlation of 0.58 between VLM_{1HzNMA} and NKG2016LU_abs over 20 TGs is found. This good agreement indicates that there are no systematic errors in the Norwegian national sea-level observing system.

- Combining satellite altimetry and TGs represents an independent solution, which can be used to determine VLM at TGs where there are no nearby GPS receivers nor rates available from VLM models.

- The agreement of VLM estimates with external rates from NKG2016LU_abs also demonstrates the coastal accuracy of CS2 data and its SAMOSA2 retracker.

5.2 Recommendations for further work

In **Paper A**, the CS2 ice baseline-B processor was used. A tailored ocean processing of CS2, the CryoSat Ocean Processing baseline-C, was released in 2017 (Bouffard et al., 2017). In future coastal applications of CS2, this baseline should be considered. In the editing of CS2 SARIn data, ~40% of the raw CS2 data were omitted. A more elaborate statistical data editing, such as that employed by Nielsen et al. (2015), could provide a larger amount of valid observations. Also, a large amount of CS2 observations inside fjords did not have a valid OT correction, as they are outside the coverage of the standard global OT model. Considering local OT corrections as demonstrated in **Paper A** can lead to a larger number of valid observations. A more elaborate modelling of the dynamic atmosphere correction (including high-frequency atmospheric variations as in Bouffard et al. (2011)) and an improved wet tropospheric correction using the national GNSS network (e.g., Obligis et al., 2011) could be included.

An additional validation method of geostrophic velocities is their comparison with in situ drifter measurements. The Global Drifter Program of NOAA's Atlantic Oceanographic and Meteorological Laboratory collects satellite-tracked drifting buoys (drifter) measurements of upper ocean currents and sea-surface temperatures around the world (Albertella et al., 2012). Currents determined from geodetic MDTs in **Paper B** should be compared to the surface geostrophic component of drifter currents in the future. Also, the SARIn zone should be expanded further out from the coast to avoid overlapping of the geographical mode mask with the Norwegian Coastal Current.

Extension of the CS2 data span would improve the accuracy of the estimated VLM rates in **Paper D**. A next step in the VLM estimation from CS2 and TGs should be a link of relative VLM between TGs, as presented in Kuo et al. (2004, 2008), using additional constrains and taking advantage of long-term TG records available in Fennoscandia. Replacing the standard CS2 OT correction with a local one, as demonstrated in **Paper A**, could possibly lead to a better agreement of estimated VLM rates with NKG2016LU_abs. Especially at TGs, where discrepancies between standard and local OT corrections are large (e.g., HAMM, TRON, HEIM, and KRIN). Furthermore, expanding the estimation of VLM rates using CS2 and TG measurements to the Baltic Sea region could be considered in the future, where the VLM signal reaches values of up to ~10 mm/yr. The usage of tailored coastal products of SARAL/AltiKa, e.g., PEACHI (Prototype for Expertise on AltiKa for Coastal, Hydrology and Ice) (Valladeau et al., 2016) distributed through AVISO for VLM determination could be considered in the future. The comparison of estimated VLM rates in **Paper D** with independent rates acquired by SAR images represents a further step in the validation of VLM based on CS2 and TGs. InSAR measurements of ground motion by Sentinel-1 satellites are available for entire Norway and provided by the Norwegian Ground Motion Service (https://www.ngu.no/en/topic/insar-norway). This observation type could be explored in future studies of VLM.

Earth models with a thin elastic lithosphere and a low-viscosity asthenosphere are known for more than 100 years, e.g., Cathles (1975) (W. Fjeldskaar, personal communication, 2019). According to Fjeldskaar (2017), a thick elastic lithosphere could not explain the tilted paleo-shorelines in Norwegian coastal regions and a much thinner lithosphere would be a possible option. The integration of this kind of Earth model into SELEN could be considered in the future. Also, the use of a SLE-solver, which includes shoreline migration and rotational feedback should be considered in order to quantify the effect of neglecting those features. The application of thermo-mechanical ice models in GIA modelling would be of advantage. NKG2016GIA_prel0306, which is based on a thermo-mechanical ice model for Fennoscnadia (other parts of the world were taken from ICE-5G) shows a better fit to the empirical model (in observation points) than ICE-x based land-uplift rates (over land points) in terms of mean values and standard deviations of differences (Table 4.6). By including such an ice model, a larger independence from Earth model information would be achieved. Since seismological results show that mantle viscosity and LT vary laterally in Fennoscandia (Janik et al., 2009), the importance of 3D Earth models increases.

References

Abe-Ouchi, A., F. Saito, M. Kageyama, P. Braconnot, S. P. Harrison, K. Lambeck, B. L. Otto-Bliesner, W. R. Peltier, L. Tarasov, J.-Y. Peterschmitt, and K. Takahashi (2015), Ice-sheet configuration in the CMIP5/PMIP3 Last Glacial Maximum experiments, *Geosci. Model Dev.*, **8**, 3621-3637, doi: 10.5194/gmd-8-3621-2015.

Abulaitijiang, A., O. B. Andersen, and L. Stenseng (2015), Coastal sea level from inland CryoSat-2 interferometric SAR altimetry, *Geophys. Res. Lett.*, **42**, 1841-1847, doi: 10.1002/2015GL063131.

Adhikari, S., E. R. Ivins, and E. Larour (2016), ISSM-SESAW v1.0: mesh-based computation of gravitationally consistent sea-level and geodetic signatures caused by cryosphere and climate driven mass change, *Geosci. Model Dev.*, **9**, 1087-1109, doi: 10.5194/gmd-9-1087-2016.

Albertella, A., R. Savcenko, T. Janjić, R. Rummel, W. Bosch, and J. Schröter (2012), High resolution dynamic ocean topography in the Southern Ocean from GOCE, *Geophys. J. Int.*, **190**(2), 922-930, doi: 10.1111/j.1365-246X.2012.05531.x.

Alves, E. Q., K. Macario, P. Ascough, and C. Bronk Ramsey (2018), The Worldwide Marine Radiocarbon Reservoir Effect: Definitions, Mechanisms, and Prospects, *Rev. Geophys.*, **56**(1), 278-305, doi: 10.1002/2017RG000588.

Andersen, O. B. and P. Knudsen (2009), DNSC08 mean sea surface and mean dynamic topography models, *JGR Oceans*, **114**, C11001, doi: 10.1029/2008JC005179.

Andersen, O. B. and R. Scharroo (2011), Range and geophysical corrections in coastal regions: And implications for mean sea surface determination. In: Vignudelli, S., A. Kostianoy, P. Cipollini, and J. Benveniste (Eds.), Coastal Altimetry, Springer, Berlin Heidelberg, pp. 103-145, doi: 10.1007/978-3-642-12796-0_5.

Argus, D. F., W. R. Peltier, R. Drummond, and A. W. Moore (2014), The Antarctica component of postglacial rebound model ICE-6G_C (VM5a) based on GPS positioning, exposure age dating of ice thicknesses, and relative sea level histories, *Geophys. J. Int.*, **198**(1), 537-563, doi: 10.1093/gji/ggu140.

Armitage, T. W. K. and M. W. J. Davidson (2014), Using the interferometric capabilities of the ESA CryoSat-2 mission to improve the accuracy of sea ice freeboard retrievals, *IEEE Trans. Geosci. Remote Sens.*, **52**(1), 529-536, doi: 10.1109/TGRS.2013.2242082.

AVISO (2019), Satellite Altimetry Data. Online at https://www.aviso.altimetry.fr/en/home.html (as of 09 June 2019).

Beckley, B. D., P. S. Callahan, D. W. Hancock, G. T. Mitchum, and R. D. Ray (2017), On the "Cal-Mode" Correction to TOPEX Satellite Altimetry and Its Effect on the Global Mean Sea Level Time Series, *JGR Oceans*, **122**(11), 8371-8384, doi: 10.1002/2017JC013090.

Benveniste, J., A. Ambrózio, M. Restano, and S. Dinardo (2016), SAR processing on demand service for CryoSat-2 and Sentinel-3 at ESA G-POD, Geophysical Research Abstracts vol. 18, EGU2016-13084 presented at 2016 EGU General Assembly, Vienna Austria, 17-22 April.

Bingham, R. J., K. Haines, and C. W. Hughes (2008), Calculating the Ocean's Mean Dynamic Topography from a Mean Sea Surface and a Geoid, *J. Atmos. Oceanic Technol.*, **25**, 1808-1822, doi: 10.1175/2008JTECHO568.1.

Bjerhammar, A. (1980), Postglacial uplifts and geopotentials in Fennoscandia. In: Mörner, N.-A. (Ed.), Earth Rheology, Isostasy and Eustasy, Wiley & Sons, pp. 323-326.

Bonnefond, P., B. J. Haines, and C. Watson (2011), In situ Absolute Calibration and Validation: A Link from Coastal to Open-Ocean Altimetry. In: Vignudelli, S., A. Kostianoy, P. Cipollini, and J. Benveniste (Eds.), Coastal Altimetry, Springer, Berlin Heidelberg, pp. 259-296, doi: 10.1007/978-3-642-12796-0_11.

Bouffard, J., L. Roblou, F. Birol, A. Pascual, L. Fenoglio-Marc, M. Cancet, R. Morrow, and Y. Ménard (2011), Introduction and Assessment of Improved Coastal Altimetry Strategies: Case Study over the Northwestern Mediterranean Sea. In: Vignudelli, S., A. Kostianoy, P. Cipollini, and J. Benveniste (Eds.), Coastal Altimetry, Springer, Berlin Heidelberg, pp. 297-330, doi: 10.1007/978-3-642-12796-0_12.

Bouffard, J., M. Naeije, C. J. Banks, F. M. Calafat, P. Cipollini, H. M. Snaith, E. Webb, A. Hall, R. Mannan, P. Féménias, and T. Parinello (2017), CryoSat ocean product quality status and future evolution, *Adv. Space Res.*, **62**(6), 1549-1563, doi: 10.1016/j.asr.2017.11.043.

Bouman, J., J. Ebbing, M. Fuchs, J. Sebera, V. Lieb, W. Szwillus, R. Haagmans, and P. Novak (2016), Satellite gravity gradient grids for geophysics, *Sci. Rep.*, **6**, 21050, doi: 10.1038/srep21050.

Brown, G. (1977), The average impulse response of a rough surface and its applications, *IEEE Trans. Antennas Propag.*, **25**(1), 67-74, doi: 10.1109/TAP.1977.1141536.

Budgell, W. P. (2005), Numerical simulation of ice-ocean variability in the Barents Sea region. Towards dynamical downscaling, *Ocean Dyn.*, **55**(3-4), 370-387, doi: 10.1007/s10236-005-0008-3.

Calafat, F. M., P. Cipollini, J. Bouffard, H. Snaith, and P. Féménias (2017), Evaluation of new CryoSat-2 products over the ocean, *Remote Sens. Environ.*, **191**, 131-144, doi: 10.1016/j.rse.2017.01.009.

Carrère, L. and F. Lyard (2003), Modeling the barotropic response of the global ocean to atmospheric wind and pressure forcing - comparisons with observations, *Geophys. Res. Lett.*, **30**(6), 1275, doi: 10.1029/2002GL016473.

Cartwright, D. E. and R. J. Taylor (1971), New Computations of the Tide-generating Potential, *Geophys. J. Int.*, **23**(1), 45-73, doi: 10.1111/j.1365-246X.1971.tb01803.x.

Cartwright, D. E. and A. C. Edden (1973), Corrected Tables of Tidal Harmonics, *Geophys. J. Int.*, **33**(3), 253-264, doi: 10.1111/j.1365-246X.1973.tb03420.x.

Cathles, L. M. (1975), Viscosity of the Earth's Mantle, Princeton Univ. Press., Princeton, 414 pp.

Chelton, D. B., J. C. Ries, B. J. Haines, L.-L. Fu, and P. S. Callahan (2001), Satellite altimetry. In: Fu, L.-L and A. Cazenave (Eds.), Satellite altimetry and Earth Sciences: A Handbook of Techniques and Applications, Vol. 69 of International Geophysics Series, Academic Press, pp. 1-122.

Cipollini, P. and H. Snaith (2013), A short course on Altimetry, paper presented at the 3rd European Space Agency Advanced Training on Ocean Remote Sensing, Cork, Ireland, 23-27 September.

Cipollini, P., R. Scarrott, and H. Snaith (2014), Product Data Handbook: Coastal Altimetry, Issue 2.0, D180G_HB_SL1, 2.0, Coastal & Marine Research Centre, University College Cork, Ireland.

Cipollini, P., F. M. Calaft, S. Jevrejeva, A. Melet, and P. Prandi (2017), Monitoring Sea Level in the Coastal Zone with Satellite Altimetry and Tide Gauges, *Surv. Geophys.*, **38**(1), 33-57, doi: 10.1007/s10712-016-9392-0.

Colli, L., S. Ghelichkhan, H.-P. Bunge, and J. Oeser (2018), Retrodictions of Mid Paleogene mantle flow and dynamic topography in the Atlantic region from compressible high resolution adjoint mantle convection models: Sensitivity to deep mantle viscosity and tomographic input model, *Gondwana Res.*, **53**, 252-272, doi: 10.1016/j.gr.2017.04.027.

Committee on Earth Observation Satellites (2009), CEOS EO HANDBOOK – EARTH OBSERVATION SATELLITE CAPABILITIES AND PLANS. Online at http://www.eohandbook.com/eohb2009/earth_altimeters.html (as of 25 June 2019).

Condie, K. C. (2001), Mantle Plumes and Their Record in Earth History, Cambridge University Press, Cambridge, doi: 10.1017/CBO9780511810589.

Dahle, C., F. Flechtner, M. Murböck, G. Michalak, H. Neumayer, O. Abrykosov, A. Reinhold, and R. König (2019), GRACE-FO Geopotential GSM Coefficients GFZ RL06. V. 6.0. GFZ Data Services, doi: 10.5880/GFZ.GRACEFO_06_GSM.

Davis, C. H. (1995), Growth of the Greenland ice sheet: a performance assessment of altimeter retracking algorithms, *IEEE Trans. Geosci. Remote Sens.*, **33**(5), 1108-1116, doi: 10.1109/36.469474.

Dee, D. P., S. M. Uppsala, A. J. Simmons, P. Berrisford, P. Poli, S. Kobayashi, U. Andrae, M. A. Balmaseda, P. Bauer, P. Bechtold, A. C. M. Beljaars, L. van de Berg, J. Bidlot, N. Bormann, C. Delsol, R. Dragani, M. Fuentes, A. J. Geer, L. Haimberger, S. B. Healy, H. Hersbach, E. V. Hólm, L. Isaksen, P. Kållberg, M. Köhler, M. Matricardi, A. P. McNally, B. M. Monge-Sanz, J.-J. Morcrette, B.-K. Park, C. Peubey, P. de Rosnay, C. Tavolato, J.-N. Thépaut, and F. Vitart (2011), The ERA-Interim reanalysis: configuration and performance of the data assimilation system, *Quart. J. R. Met. Soc.*, **137**(656), 553-597, doi: 10.1002/qj.828.

Denker, H. (2016), A new European gravimetric (quasi)geoid EGG2015, paper presented at the IAG Symposium on Gravity, Geoid and Height Systems, Thessaloniki, Greece, 19-23 September.

Di Bella, A. (2019), Measurement of Arctic sea ice from satellite altimetry: the potential and limitations of CryoSat-2 SARIn mode. PhD thesis, DTU Space, Technical University of Denmark, Copenhagen.

Dinardo, S., B. Lucas, and J. Benveniste (2011), SAR Altimetry in Open and Coastal Sea Water: Performances, Limits, Perspectives, paper presented at the OSTST 2011 meeting, San Diego, California, USA, October 21-23.

Dinardo, S. (2013), Guidelines for the SAR (Delay-Dopller) L1b Processing, XCRY-GSEG-EOPS-TN-14-0042, ESRIN, Italy.

Douglas, B. and R. Peltier (2002), The Puzzle of Global Sea-Level Rise, *Physics Today*, **55**(3), 35, doi: 10.1063/1.1472392.

Dziewonski, A. M. and D. L. Anderson (1981), Preliminary reference Earth model, *Phys. Earth Planet. Inter.*, **25**(4), 297-356, doi: 10.1016/0031-9201(81)90046-7.

Ebbing, J., P. Haas, F. Ferraccioli, F. Pappa, W. Szwillus, and J. Bouman (2018), Earth tectonics as seen by GOCE - Enhanced satellite gravity gradient imaging, *Sci. Rep.*, **8**, 16356, doi: 10.1038/s41598-018-34733-9.

Egbert, G. D. and S. Y. Erofeeva (2002), Efficient Inverse Modeling of Barotropic Ocean Tides, *J. Atmos. Oceanic Technol.*, **19**(2), 183-204, doi: 10.1175/1520-0426(2002)019<0183:EIMOBO>2.0.CO;2.

Ekman, M. (1989), Impacts of geodynamic phenomena on systems for height and gravity, *Bull. Geod.*, **63**(3), 281-296, doi: 10.1007/BF02520477.

Ekman, M. (1996), A consistent map of the postglacial uplift of Fennoscandia, *Terra Nova*, **8**(2), 158-165, doi: 10.1111/j.1365-3121.1996.tb00739.x.

Encyclopædia Britannica (2007), A cross section of Earth's outer layers, from the crust through the lower mantle. Online at https://www.britannica.com/science/upper-mantle/media/618804/100516 (as of 5 April 2019).

Engelhart, S. E. and B. P. Horton (2012), Holocene sea level database for the Atlantic coast of the United States, *Quat. Sci. Rev.*, **54**, 12-25, doi: 10.1016/j.quascirev.2011.09.013.

Engelhart, S. E., M. Vacchi, B. P. Horton, A. R. Nelson, and R. E. Kopp (2015), A sea-level database for the Pacific coast of central North America, *Quat. Sci. Rev.*, **113**, 78-92, doi: 10.1016/j.quascirev.2014.12.001.

European Space Agency (1999), Gravity Field and Steady-State Ocean Circulation Mission. Report for Mission Selection, ESA SP-1233(1).

European Space Agency (2006), Artist's impression of CryoSat in orbit. Online at http://www.esa.int/spaceinimages/Images/2006/02/Artist_s_impression_of_CryoSat_in_orbit (as of 19 March 2019).

European Space Agency (2007), CryoSat Mission and Data Description, Technical Note 3.0, CS-RP-ESA-SY-0059.

European Space Agency (2018a), Geographical Mode Mask. Online at https://earth.esa.int/web/guest/-/geographical-mode-mask-7107 (as of 25 January 2018).

European Space Agency (2018b), Cryosat-2 Product Handbook, Baseline D 1.0, C2-LI-ACS-ESL-5319.

Farrell, W. E. and J. A. Clark (1976), On Postglacial Sea Level, *Geosphys. J. Int.*, **46**(3), 647-667, doi: 10.1111/j.1365-246X.1976.tb01252.x.

Fjeldskaar, W. and A. Amantov (2017), Tilted Norwegian post-glacial shorelines require a low viscosity asthenosphere and a weak lithosphere, *Regional Geology and Metallogeny*, **70**, 48-59.

Garcia-Mondéjar, A., B. Martínez-Val, M. J. Escorihuela, P. García, C. Martin-Puig, J. Yang, and J. Liao (2015), Measuring lake level evolution with SAR altimeters, paper presented at the 2015 DRAGON 3 SYMPOSIUM, Interlaken, Switzerland, 22-26 June.

GEBCO Compilation Group (2019), GEBCO 2019 Grid, doi: 10.5285/836f016a-33be-6ddc-e053-6c86abc0788e.

Gommenginger, C., P. Thibaut, L. Fenoglio-Marc, G. Quartly, X. Deng, J. Gómez-Enri, P. Challenor, and Y. Gao (2011), Retracking Altimeter Waveforms Near the Coasts: A Review of Retracking Methods and Some Applications to Coastal Waveforms. In: Vignudelli, S., A. Kostianoy, P. Cipollini, and J. Benveniste (Eds.), Coastal Altimetry, Springer, Berlin Heidelberg, pp. 61-101, doi: 10.1007/978-3-642-12796-0_4.

Haas, R., A. Nothnagel, J. Campbell, and E. Gueguen (2003), Recent crustal movements observed with the European VLBI network: geodetic analysis and results, *J. Geodyn.*, **35**(4-5), 391-414, doi: 10.1016/S0264-3707(03)00003-6.

Haidvogel, D. B., H. Arango, W. P. Budgell, B. D. Cornuelle, E. Curchitser, E. Di Lorenzo, K. Fennel, W. R. Geyer, A. J. Hermann, L. Lanerolle, J. Levin, J. C. McWilliams, A. J. Miller, A. M. Moore, T. M. Powell, A. F. Shchepetkin, C. R. Sherwood, R. P. Signell, J. C. Warner, and J. Wilkin (2008), Ocean forecasting in terrain-following coordinates: Formulation and skill assessment of the Regional Ocean Modeling System, *J. Comp. Phys.*, **227**(7), 3595-3624, doi: 10.1016/j.jcp.2007.06.016.

Hayne, G. (1980), Radar altimeter mean return waveforms from near-normal-incidence ocean surface scattering, *IEEE Trans. Antennas Propag.*, **28**(5), 687-692, doi: 10.1109/TAP.1980.1142398.

Higginson, S., K. R. Thompson, P. L. Woodworth, and C. W. Hughes (2015), The tilt of mean sea level along the east coast of North America, *Geophys. Res. Lett.*, **42**(5), 1471-1479, doi: 10.1002/2015GL063186.

Holgate, S. J., A. Matthews, P. L. Woodworth, L. J. Rickards, M. E. Tamisiea, E. Bradshaw, P. R. Foden, K. M. Gordon, S. Jevrejeva, and J. Pugh (2013), New Data Systems and Products at the Permanent Service for Mean Sea Level, *J. Coastal Res.*, **29**(3), 493-504, doi: 10.2112/jcoastres-d-12-00175.1.

Huang, J. (2017), Determining Coastal Mean Dynamic Topography by Geodetic Methods, *Geophys. Res. Lett.*, **44**(21), 11125-11128, doi: 10.1002/2017GL076020.

Jain, M. (2005), Improved sea level determination in the Arctic regions through development of tolerant altimetry retracking. PhD thesis, DTU Space, Technical University of Denmark, Kgs. Lyngby, Denmark.

Jain, M., O. B. Andersen, J. Dall, and L. Stenseng (2015), Sea surface height determination in the Arctic using Cryosat-2 SAR data from primary peak empirical retrackers, *Adv. Space Res.*, **55**(1), 40-50, doi: 10.1016/j.asr.2014.09.006.

Janik, T., E. Kozlovskaya, P. Heikkinen, J. Yliniemi, and H. Silvennoinen (2009), Evidence for preservation of crustal root beneath the Proterozoic Lapland-Kola orogen (northern Fennoscandian shield) derived from P and S wave velocity models of POLAR and HUKKA wide-angle reflection and refraction profiles and FIRE4 reflection transect, *JGR Solid Earth*, **114**(B6), B06308, doi: 10.1029/2008JB005689.

Jiang, L., R. Schneider, O. B. Andersen, and P. Bauer-Gottwein (2017), CryoSat-2 Altimetry Applications over Rivers and Lakes, *Water*, **9**(3), 211, doi: 10.3390/w9030211.

Johansson, J. M., J. L. Davis, H.-G. Scherneck, G. A. Milne, M. Vermeer, J. X. Mitrovica, R. A. Bennett, B. Jonsson, G. Elgered, P. Elósegu, H. Koivula, M. Poutanen, B. O. Rönnäng, and I. I. Shapiro (2001), Continuous GPS measurements of postglacial adjustment in Fennoscandia 1. Geodetic results, *JGR Solid Earth*, **107**(B8), ETG 3-1-ETG 3-27, doi: 10.1029/2001JB000400.

Kaufmann, G. (2004), Program package ICEAGE, Version 2004, Manuscript, Institut für Geophysik, Universität Göttingen, 40 pp.

Kendall, R. A., J. X. Mitrovica, and G. A. Milne (2005), On post-glacial sea level – II. Numerical formulation and comparative results on spherically symmetric models, *Geophys. J. Int.*, **161**(3), 679-706, doi: 10.1111/j.1365-246X.2005.02553.x.

Kierulf, H. P., H. Steffen, M. J. R. Simpson, M. Lidberg, P. Wu, and H. Wang (2014), A GPS velocity field for Fennoscandia and a consistent comparison to glacial isostatic adjustment models, *JGR Solid Earth*, **119**(8), 6613-6629, doi: 10.1002/2013JB010889.

Kopp, R. E., A. C. Kemp, K. Bittermann, B. P. Horton, J. P. Donnelly, W. R. Gehrels, C. C. Hay, J. X. Mitrovica, E. D. Morrow, and S. Rahmstorf (2016), Temperature-driven global sea-level variability in the Common Era, *Proc. Natl. Acad. Sci. USA*, **113**(11), E1434-E1441, doi: 10.1073/pnas.1517056113.

Kuo, C. Y., C. K. Shum, A. Braun, and J. X. Mitrovica (2004), Vertical crustal motion determined by satellite altimetry and tide gauge data in Fennoscandia, *Geophys. Res. Lett.*, **31**(1), L01608, doi: 10.1029/2003GL019106.

Kuo, C. Y., C. K. Shum, A. Braun, K. C. Cheng, and Y. Yi (2008), Vertical Motion Determined Using Satellite Altimetry and Tide Gauges, *Terr. Atmos. Ocean. Sci.*, **19**(1-2), 21-35, doi: 10.3319/TAO.2008.19.1-2.21(SA).

Lambeck, K. and M. Nakada (1990), Late Pleistocene and Holocene sea-level change along the Australian coast, *Palaeogeog. Palaeoclimat. Palaeoecol.*, **89**(1-2), 143-176, doi: 10.1016/0031-0182(90)90056-D.

Lambeck, K. (1993a), Glacial rebound of the British Isles-I. Preliminary model results, *Geophys. J. Int.*, **115**(3), 941-959 doi: 10.1111/j.1365-246X.1993.tb01503.x.

Lambeck, K. (1993b), Glacial rebound of the British Isles-II. A high-resolution, high-precision model, *Geophys. J. Int.*, **115**(3), 960-990, doi: 10.1111/j.1365-246X.1993.tb01504.x.

Lambeck, K. (1993c), Glacial rebound and sea-level change: an example of a relationship between mantle and surface processes, *Tectonophysics*, **223**(1-2), 15-37, doi: 10.1016/0040-1951(93)90155-D.

Lambeck K., C. Smither, and P. Johnston (1998), Sea-level change, glacial rebound and mantle viscosity for northern Europe, *Geophys. J. Int.*, **134**(1), 102-144, doi: 10.1046/j.1365-246x.1998.00541.x.

Lambeck, K., A. Purcell, P. Johnston, M. Nakada, and Y. Yokoyama (2003), Water-load definition in the glacio-hydro-isostatic sea-level equation, *Quat. Sci. Rev.*, **22**(2-4), 309-318, doi: 10.1016/S0277-3791(02)00142-7.

Lin, H., K. R. Thompson, J. Huang, and M. Véronneau (2015), Tilt of mean sea level along the Pacific coasts of North America and Japan, *JGR Oceans*, **120**(10), 6815-6828, doi: 10.1002/2015JC010920.

Llewellyn, S. K. and R. B. Bent (1973), Documentation and description of the Bent ionospheric model, Rep. AFCRL-TR-73-0657, Air Force Geophysics Laboratory, Hanscom Air Force Base, Massachusetts, USA.

Lyard, F., F. Lefevre, T. Letellier, and O. Francis (2006), Modelling the global ocean tides: modern insights from FES2004, *Ocean Dynam.*, **56**(5-6), 394-415, doi: 10.1007/s10236-006-0086-x.

Martin, T. V., H. J. Zwally, A. C. Brenner, and R. A. Bindschadler (1983), Analysis and retracking of continental ice sheet radar altimeter waveforms, *JGR Oceans*, **88**(C3), 1608-1616, doi: 10.1029/JC088iC03p01608.

Martinec, Z., V. Klemann, W. van der Wal, R. E. M. Riva, G. Spada, Y. Sun, D. Melini, S. B. Kachuck, V. Barletta, K. Simon, G. A., and T. S. James (2018), A benchmark study of numerical implementations of the sea level equation in GIA modelling, *Geophys. J. Int.*, **215**(1), 389-414, doi: 10.1093/gji/ggy280.

Matsuyama, I., J. X. Mitrovica, A. Daradich, and N. Gomez (2010), The rotational stability of a triaxial ice-age Earth, *JGR Solid Earth*, **115**(B5), B05401, doi: 10.1029/2009JB006564.

Mertz, F., J. P. Dumontm, and S. Urien (2017), Baseline-C Cryosat Ocean Processor: Ocean Product Handbook, Version 4.0, ESRIN, Italy.

Milne, G. A. and J. X. Mitrovica (1998), Postglacial sea-level change on a rotating Earth, *Geophys. J. Int.*, **133**(1), 1-19, doi: 10.1046/j.1365-246X.1998.1331455.x.

Milne, G. A., J. X. Mitrovica, and D. P. Schrag (2002), Estimating past continental ice volume from sea-level data, *Quat. Sci. Rev.*, **21**(1-3), 361-376, doi: 10.1016/S0277-3791(01)00108-1.

Mitrovica, J. X. and W. R. Peltier (1991), On postglacial geoid subsidence over the equatorial oceans, *JGR Solid Earth*, **96**(B12), 20053-20071, doi: 10.1029/91JB01284.

Mitrovica, J. X., J. L. Davis, and I. I. Shapiro (1994), A spectral formalism for computing three-dimensional deformations due to surface loads: 1. Theory, *JGR Solid Earth*, **99**(B4), 7057-7073, doi: 10.1029/93JB03128.

Mitrovica, J. X. and G. A. Milne (2003), On post-glacial sea level: I. General theory, *Geophys. J. Int.*, **154**(2), 253-267, doi: 10.1046/j.1365-246X.2003.01942.x.

Munk, W. H. and G. J. F. MacDonald (1960), *The Rotation of the Earth*, Cambridge University Press, New York.

Nakada, M. and K. Lambeck (1988), The melting history of the late Pleistocene Antarctic ice sheet, *Nature*, **333**, 36-40.

Nakada, M., J. Okuno, K. Lambeck, and A. Purcell (2015), Viscosity structure of Earth's mantle inferred from rotational variations due to GIA process and recent melting events, *Geophys. J. Int.*, **202**(2), 976-992, doi: 10.1093/gji/ggv198.

National Centre for Space Studies (2017), SARAL/ALTIKA. Online at https://altika-saral.cnes.fr/en/SARAL/index.htm (as of 25 June 2019).

National Oceanic and Atmospheric Administration (2019), Learning Ocean Science through Ocean Exploration. Online at https://oceanexplorer.noaa.gov/edu/curriculum/section3.pdf (as of 08 August 2019).

Nerem, R. S. and G. T. Mitchum (2002), Estimates of vertical crustal motion derived from differences of TOPEX/POSEIDON and tide gauge sea level measurements, *Geophys. Res. Lett.*, **29**(19), 40-1-40-4, doi: 10.1029/2002GL015037.

Nielsen, K., L. Stenseng, O. B. Andersen, H. Villadsen, and P. Knudsen (2015), Validation of CryoSat-2 SAR mode based lake levels, *Rem. Sens. Environ.*, **171**, 162-170, doi: 10.1016/j.rse.2015.10.023.

Näslund, J.-O. (2010), Climate and climate-related issues for the safety assessment SR-Site, Technical Report TR-10-49, Swedish Nuclear Fuel and Waste Management Co, Sweden.

Obligis, E., C. Desportes, L. Eymard, M. J. Fernandes, C. Lázaro, A. L. Nunes (2011), Tropospheric corrections for coastal altimetry, S. Vignudelli, et al. (Eds.), Coastal Altimetry, Springer, Berlin Heidelberg, pp. 147-176, doi: 10.1007/978-3-642-12796-0_6.

Olsson, P.-A., J. Ågren, and H.-G. Scherneck (2012), Modelling of the GIA-induced surface gravity change over Fennoscandia, *J. Geodyn.*, **61**, 12-22, doi: 10.1016/j.jog.2012.06.011.

Olsson, P.-A. (2013), On modelling of postglacial gravity change. PhD thesis, Department of Earth and Space Sciences, Chalmers University of Technology, Gothenburg, Sweden.

Olsson, P.-A., G. Milne, H.-G. Scherneck, and J. Ågren (2015), The relation between gravity rate of change and vertical displacement in previously glaciated areas, *J. Geodyn.*, **83**, 76-84, doi: 10.1016/j.jog.2014.09.011.

Olsson, P.-A., K. Breili, V. Ophaug, H. Steffen, M. Bilker-Koivula, E. Nilsen, T. Oja, and L. Timmen (2019), Postglacial gravity change in Fennoscandia – three decades of repeated absolute gravity observations, *Geophys. J. Int.*, **217**(2), 1141-1156, doi: 10.1093/gji/ggz054.

Ophaug, V., K. Breili, and C. Gerlach (2015), A comparative assessment of coastal mean dynamic topography in Norway by geodetic and ocean approaches, *JGR Oceans*, **120**(12), 7807-7826, doi: 10.1002/2015JC011145.

Ophaug, V. (2017), Geodetic observations and modeling of gravity field, sea level, and ocean dynamics in the Norwegian coastal zone. PhD thesis, Faculty of Science and Technology, Norwegian University of Life Sciences, Ås, Norway.

Passaro, M., P. Cipollini, S. Vignudelli, G. D. Quartly, and H. M. Snaith (2014), ALES: A multi-mission adaptive subwaveform retracker for coastal and open ocean altimetry, *Remote Sens. Env.*, **145**, 173-189, doi: 10.1016/j.rse.2014.02.008.

Peltier, W. R. (1974), The impulse response of a Maxwell Earth, *Rev. Geophys.*, **12**(4), 649-669, doi: 10.1029/RG012i004p00649.

Peltier, W. R. and J. T. Andrews (1976), Glacial-Isostatic Adjustment-I. The Forward Problem , *Geophys. J. Int.*, **46**(3), 605-646, doi: 10.1111/j.1365-246X.1976.tb01251.x.

Peltier, W. R. (1994), Ice Age Paleotopography, *Science*, **265**(5169), 195-201, doi: 10.1126/science.265.5169.195.

Peltier, W. R. (2004), GLOBAL GLACIAL ISOSTASY AND THE SURFACE OF THE ICE-AGE EARTH: The ICE-5G (VM2) Model and GRACE, *Ann. Rev. Earth and Planet. Sci.*, **32**, 111-149, doi: 10.1146/annurev.earth.32.082503.144359.

Peltier, W. R., D. F. Argus, and R. Drummond (2015), Space geodesy constrains ice age terminal deglaciation: The global ICE-6G_C (VM5a) model, *JGR Solid Earth*, **120**(1), 450-487, doi: 10.1002/2014JB011176.

Peltier, W. R., D. F. Argus, and R. Drummond (2018), Comment on "An Assessment of the ICE-6G_C (VM5a) Glacial Isostatic Adjustment Model" by Purcell et al., *JGR Solid Earth*, **123**(2), 2019-2028, doi: 10.1002/2016JB013844.

Purcell, A., P. Tregoning, and A. Dehecq (2016), An assessment of the *ICE6G_C(VM5a)* glacial isostatic adjustment model, *JGR Solid Earth*, **121**(5), 3939-3950, doi: 10.1002/2015JB012742.

Quartly, G. and G. Chen (2006), Introduction to the Special Issue on ”Satellite Altimetry: New Sensors and New Applications”, *Sensors*, **6**(6), 616-619, doi: 10.3390/s6060616.

Quartly, G. D., E. Rinne, M. Passaro, O. B. Andersen, S. Dinardo, S. Fleury, A. Guillot, S. Hendricks, A. A. Kurekin, F. L. Müller, R. Ricker, H. Skourup, and M. Tsamados (2019), Retrieving Sea Level and Freeboard in the Arctic: A Review of Current Radar Altimetry Methodologies and Future Perspectives, *Remote Sens.*, **11**(7), 881, doi: 10.3390/rs11070881.

Raney, K. R. and L. Phalippou (2011), The Future of Coastal Altimetry. In: Vignudelli, S., A. Kostianoy, P. Cipollini, and J. Benveniste (Eds.), Coastal Altimetry, Springer, Berlin Heidelberg, pp. 535-560, doi: 10.1007/978-3-642-12796-0_20.

Ray, R. D. (2008), Tide corrections for shallow-water altimetry: a quick overview, paper presented at the at Second coastal altimetry workshop, Pisa, Italy, 6-7 November.

Ray, C., C. Martin-Puig, M. P. Clarizia, G. Ruffini, S. Dinardo, C. Gommenginger, and J. Benveniste (2015), SAR altimeter backscattered waveform model, *IEEE Trans. Geosci. Remote Sens.*, **53**(2), 911-919, doi: 10.1109/TGRS.2014.2330423.

Røed, L. P. and J. Debernard (2004), Description of an integrated flux and sea-ice model suitable for coupling to an ocean and atmosphere model, met.no Report 4/2004, Norwegian Meteorological Institute, Oslo, Norway.

Scagliola, M. and M. Fornari (2017), Known biases in CryoSat-2 Level 1b Products. DOC: C2-TN-ARS-GS-5135, 2.1.

Scharroo, R., E. W. Leuliette, J. L. Lillibridge, D. Byrne, M. C. Naeije, G. T. Mitchum (2013), RADS: consistent multi-mission products. In: Proceedings of the Symposium on 20 Years of Progress in Radar Altimetry, ESA SP-710, ESA Publications Division, European Space Agency, Noordwijk, The Netherlands, 4 pp.

Schmidt, P., B. Lund, J.-O. Näslund, and J. Fastook (2014), Comparing a thermomechanical Weichselian Ice Sheet reconstruction to reconstructions based on the sea level equation: aspects of ice configurations and glacial isostatic adjustment, *Solid Earth*, **5**, 371-388, doi: 10.5194/se-5-371-2014.

Segar, D. A. (2018), Introduction to Ocean Sciences, 4th edition. Retrieved from http://www.reefimages.com/oceans/SegarOcean4Book.pdf.

Simpson, M. J. R., J. E. Ø. Nilsen, O. R. Ravndal, K. Breili, H. Sande, H. P. Kierulf, H. Steffen, E. Jansen, M. Carson, and O. Vestøl (2015), Sea level change for Norway: Past and present observations and projections to 2100, Norwegian Cent. for Clim. Serv. Rep. 1/2015, Norwegian Cent. for Clim. Serv., Oslo, Norway.

Smith, W. H. F., R. Scharroo, J. L. Lillibridge, and E. W. Leuliette (2011), Retracking CryoSat waveforms for Near-Real-time ocean forecast products and platform attitude, paper presented at the American Geophysical Union Fall Meeting 2011, San Francisco, California, USA, 5-9 December.

Solheim, D. (2000), New height reference surfaces for Norway. In: Torres, J A. and H. Hornik (Eds.), Report on the Symposium of the IAG Subcommission for Europe (EUREF), pp. 154-158, Verlag der Bayerischen Akademie der Wissenschaften, Munich, Germany.

Spada, G. (2003), The theory behind TABOO, Release 1.0, Samizdat Press, Vermont.

Spada, G. and P. Stocchi (2006), The Sea Level Equation, Theory and Numerical Examples, Aracne, Rome.

Spada, G. and P. Stocchi (2007), SELEN: A Fortran 90 program for solving the "sea-level equation", *Comput. Geosci.*, **33**(4), 538-562, doi: 10.1016/j.cageo.2006.08.006.

Spada, G., D. Melini, G. Galassi, and F. Colleoni (2012), Modeling the sea level changes and geodetic variations by glacial isostasy: the improved SELEN code (https://arxiv.org/abs/1212.5061).

Spada, G. and D. Melini (2015), SELEN: a program for solving the "Sea Level Equation", User manual for version 2.9. Retrieved from https://geodynamics.org/cig/software/selen/selen-manual.pdf.

Spada, G. (2017), Glacial Isostatic Adjustment and Contemporary Sea Level Rise: An overview, *Surv. Geophys.*, **38**(1), 153-185, doi: 10.1007/s10712-016-9379-x.

Stammer, D. and A. Cazenave (2017), Satellite Altimetry Over Oceans and Land Surfaces, CRC Press, Boca Raton.

Steffen, H. and G. Kaufmann (2005), Glacial isostatic adjustment of Scandinavia and northwestern Europe and the radial viscosity structure of the Earth's mantle, *Geophs. J. Int.*, **163**(2), 801-812, doi: 10.1111/j.1365-246X.2005.02740.x.

Steffen, H. and P. Wu (2011), Glacial isostatic adjustment in Fennoscandia—A review of data and modeling, *J. Geodyn.*, **52**(3-4), 169-204, doi: 10.1016/j.jog.2011.03.002.

Steffen, H. (2014), On the accuracy of Glacial Isostatic Adjustment models with special attention to ice models, paper presented at the EUREF 2014 Symposium, Vilnius, Lithuania, 3-7 June.

Steffen, H., V. Barletta, K. Kollo, G. A. Milne, M. Nordman, P.-A. Olsson, M. J. R. Simpson, L. Tarasov, and J. Ågren (2016), NKG201xGIA – first results for a new model of glacial isostatic adjustment in Fennoscandia, paper presented at the European Geosciences Union General Assembly 2016, Vienna, Austria, 17-22 April.

Stenseng, L. (2011), Polar Remote Sensing by CryoSat-type Radar Altimetry. PhD thesis, DTU Space, Technical University of Denmark, Kgs. Lyngby, Denmark.

Stenseng, L. and O. B. Andersen (2012), Preliminary gravity recovery from CryoSat-2 data in the Baffin Bay, *Adv. Space Res.*, **50**(8), 1158-1163, doi: 10.1016/j.asr.2012.02.029.

Stewart, R. H. (2008), Introduction to Physical Oceanography. Dept. of Oceanography, Texas A & M University, College Station, Texas.

Stuiver, M. and P. J. Reimer (1993), Extended ^{14}C Data Base and Revised CALIB 3.0 ^{14}C Age Calibration Program, *Radiocarbon*, **35**(1), 215-230, doi: 10.1017/S0033822200013904.

Tamisiea, M. E., J. X. Mitorvica, and J. L. Davis (2007), GRACE Gravity Data Constrain Ancient Ice Geometries and Continental Dynamics over Laurentia, *Science*, **316**(5826), 881-883, doi: 10.1126/science.1137157.

Tamisiea, M. E., C. W. Hughes, S. D. P. Williams, and R. M. Bingley (2014), Sea level: measuring the bounding surfaces of the ocean, *Philos. Trans. Royal Soc. A*, **372**(2025), 20130336, doi: 10.1098/rsta.2013.0336.

Tarasov, L., A. S. Dyke, R. M. Neal, and W. R. Peltier (2012), A data-calibrated distribution of deglacial chronologies for the North American ice complex from glaciological modeling, *Earth Planet. Sci. Lett.*, **315-316**, 30-40, doi: 10.1016/j.epsl.2011.09.010.

Tegmark, M. (1996), An Icosahedron-based Method for Pixelizing the Celestial Sphere, *Astrophys. J. Lett.*, **470**(2), L81-L84.

Thibaut, P., J. C. Poisson, E. Bronner, and N. Picot (2010), Relative Performance of the MLE3 and MLE4 Retracking Algorithms on Jason-2 Altimeter Waveforms, *Mar. Geod.*, **33**(sup1), 317-335, doi: 10.1080/01490419.2010.491033.

Thibaut, P., J. C. Poisson, T. Moreau, F. Piras, S. Le Gac, F. Boy, and N. Picot (2017), From Deep Ocean to Inland Water: Homogeneous Retracker Solution for Continuous Observations, paper presented at the 10th Coastal Altimetry Workshop, Florence, Italy, 21-24 February.

Tsuji, L. J. S., N. Gomez, J. X. Mitrovica, and R. Kendall (2009), Post-Glacial Isostatic Adjustment and Global Warming in Subarctic Canada: Implications for Islands of the James Bay Region, *Arctic*, **62**(4), 458-467, doi: 10.14430/arctic176.

Tushingham, A. M. and W. R. Peltier (1991), Ice-3G: A new global model of Late Pleistocene deglaciation based upon geophysical predictions of post-glacial relative sea level change *JGR Solid Earth*, **96**(B3), 4497-4523, doi: 10.1029/90JB01583.

Tushingham, A. M. and W. R. Peltier (1992), Validation of the ICE-3G Model of Würm-Wisconsin Deglaciation Using a Global Data Base of Relative Sea Level Histories, *JGR Solid Earth*, **97**(B3), 3285-3304, doi: 10.1029/91JB02176.

Valladeau, G., P. Thibaut, B. Picard, J. C. Poisson, N. Tran, N. Picot, and A. Guillot (2015), Using SARAL/AltiKa to Improve Ka-band Altimeter Measurements for Coastal Zones, Hydrology and Ice: The PEACHI Prototype, *Marine Geodesy*, **38**(sup1), 124-142, doi: 10.1080/01490419.2015.1020176.

Vestøl, O., J. Ågren, H. Steffen, H. Kierulf, M. Lidberg, T. Oja, A. Rüdja, T. Kall, V. Saaranen, K. Engsager, C. Jepsen, I. Liepins, E. Paršeliūnas, and L. Tarasov (2016), NKG2016LU, an improved postglacial land uplift model over the Nordic-Baltic region, paper presented at the NKG Joint WG Workshop on Postglacial Land Uplift Modelling, Gävle, Sweden, 1-2 December.

Vestøl, O., J. Ågren, H. Steffen, H. Kierulf, and L. Tarasov (2019), NKG2016LU: a new land uplift model for Fennoscandia and the Baltic Region, *J. Geod.*, doi: 10.1007/s00190-019-01280-8.

Vignudelli, S., A. G. Kostianoy, P. Cipollini, and J. Benveniste (Eds.) (2011), Coastal altimetry, Springer, Berlin, doi: 10.1007/978-3-642-12796-0.

Villadsen, H. (2016), Satellite altimetry for land hydrology - CryoSat-2 for inland water monitoring. PhD thesis presentation, DTU Space, Technical University of Denmark, Kgs. Lyngby, Denmark.

Wahr, J. M. (1985), Deformation induced by polar motion, *JGR Solid Earth*, **90**(B11), 9363-9368, doi: 10.1029/JB090iB11p09363.

Webb, E. and A. Hall (2016), Geophysical Corrections in Level 2 CryoSat Data Products, IDEAS-VEG-IPF-MEM-1288 Version 5.1, ESRIN, Italy.

Wessel, P., W. H. F. Smith, R. Scharroo, J. Luis, and F. Wobbe (2013), Generic Mapping Tools: Improved Version Released, *EOS Trans. AGU*, **94**(45), 409-410, doi: 10.1002/2013EO450001.

Whitehouse, P., K. Latychev, G. A. Milne, J. X. Mitrovica, and R. Kendall (2006), Impact of 3-D Earth structure on Fennoscandian glacial isostatic adjustment: Implications for space-geodetic estimates of present-day crustal deformations, *Geophys. Res. Lett.*, **33**(13), L13502, doi: 10.1029/2006GL026568.

Whitehouse, P. (2009), Glacial isostatic adjustment and sea-level change, State of the art report, Technical Report TR-09-11, Swedish Nuclear Fuel and Waste Management Co, Sweden.

Wilks, D. S.(2006), Statistical Methods in the Atmospheric Sciences, International Geophysics Series, pp. 131-177, Academic Press, San Diego.

Wingham, D. J., C. G. Rapley, and H. Griffiths (1986), New techniques in satellite altimeter tracking systems. In: Proceedings of IGARSS 86 Symposium, Zurich, Switzerland.

Wingham, D. J., C. R. Francis, S. Baker, C. Bouzinac, D. Brockley, R. Cullen, P. de Chateau-Thierry, S. W. Laxon, U. Mallow, C. Mavrocordatos, L. Phalippou, G. Ratier, L. Rey, F. Rostan, P. Viau, and D. W. Wallis (2006), CryoSat: A mission to determine the fluctuations in Earth's land and marine ice fields, *Adv. Space Res.*, **37**(4), 841-871, doi: 10.1016/j.asr.2005.07.027.

Woodworth, P. L., G. Médéric, M. Marcos, G. Wöppelmann, and C. W. Hughes (2015), The status of measurement of the Mediterranean mean dynamic topography by geodetic techniques, *J. Geod.*, **89**(8), 811-827, doi: 10.1007/s00190-015-0817-1.

Wu, P. (1978), The response of a Maxwell Earth to applied surface loads: Glacial Isostatic Adjustment. MSc thesis, University of Toronto, Toronto, Canada.

Wu, P. (1998), Will earthquake activity in eastern Canada increase in the next few thousand years?, *Can. J. Earth Sci.*, **35**(5), 562-568, doi: 10.1139/e97-125.

Wunsch, C. and D. Stammer (1998), SATELLITE ALTIMETRY, THE MARINE GEOID, AND THE OCEANIC GENERAL CIRCULATION, *Annu. Rev. Earth Planet. Sci.*, **26**, 219-253, doi: 10.1146/annurev.earth.26.1.219.

Ådlandsvik, B., J. Albretsen, L. Asplin, and K. Fjellheim (2014), NorKyst-800 and the Norwegian Current Information System, paper presented at the 2014 ROMS User Workshop, Rovinj, Croatia, 26-29 May.

Ågren, J., G. Strykowski, M. Bilker-Koivula, O. Omang, S. Märdla, R. Forsberg, A. Ellmann, T. Oja, I. Liepinš, E. Paršeliūnas, J. Kaminskis, L. E. Sjöberg, and G. Valsson (2015), The NKG2015 gravimetric geoid model for the Nordic-Baltic region, paper presented at the 1st Joint Commission 2 and IGFS Meeting, Thessaloniki, Greece, 19-23 September.

Errata

Page	Line	Original text	Corrected text	Type
4	-9	... at TGs. The main ...	... at TGs. The main ...	New paragraph
9	-2	... four journal papers ...	... four peer-reviewed journal papers ...	Clarification
14	-4	... cells, and average ...	... cells and average ...	Typo
24	-20	The tropospheric correction ...	The wet tropospheric correction ...	Clarification
24	-9	... by the sea surface is not Gaussian; ...	... by the sea surface are not Gaussian; ...	Typo
24	-7	... conditions), and is called ...	... conditions) and is called ...	Typo
38	-6	... tide-gauge locations.	... tide-gauge locations and blue squares the CryoSat-2 boxes.	Clarification
41	-12	During the glacial phase, ...	During a glacial phase, ...	Typo
41	-6	... or filed oceanic basins, ...	... or filled oceanic basins, ...	Typo
45	-6	... GFs in analog to ...	... GFs in analogy to ...	Typo
61	15	... focused on using of a modified version ...	... focused on using a modified version ...	Typo
61	21	... of these processes introduces ...	... of the processes mentioned above introduces ...	Clarification
64	-6	**?**	Ekman (1996)	Reference missing
67	17	... grids presented in this thesis consists of ...	... grids presented in this thesis consist of ...	Typo
67	-2	... namely GIA_prel 0306 ...	... namely GIA_prel0306 ...	Typo
68	7	... differences between of the NKG rheologies ...	... differences between NKG rheologies ...	Typo
93	-9	... 20 Hz CS2 observation.	... 20 Hz CS2 observations.	Typo

List of appended peer-reviewed papers

Paper A

Idžanović, M., V. Ophaug, and O. B. Andersen (2018), Coastal sea level from CryoSat-2 SARIn altimetry in Norway, *Adv. Space Res.*, **62**(6), 1344-1357, doi: 10.1016/j.asr.2017.07.043.

Paper B

Idžanović, M., V. Ophaug, and O. B. Andersen (2017), The coastal mean dynamic topography in Norway observed by CryoSat-2 and GOCE, *Geophys. Res. Lett.*, **44**(11), 5609-5617, doi: 10.1002/2017GL073777.

Paper C

Idžanović, M. and Ch. Gerlach (2018), Analysis of Glacial Isostatic Adjustment in Fennoscandia: Comparison of Model Results and Observational Evidence, *avn*, **125**(7), 230-243.

Paper D

Idžanović, M., Ch. Gerlach, K. Breili, and O. B. Andersen (2019), An Attempt to Observe Vertical Land Motion along the Norwegian Coast by CryoSat-2 and Tide Gauges, *Remote Sens.*, **11**(7), 744, doi: 10.3390/rs11070744.

Paper A

Available online at www.sciencedirect.com

ScienceDirect

Advances in Space Research 62 (2018) 1344–1357

ADVANCES IN SPACE RESEARCH (a COSPAR publication)

www.elsevier.com/locate/asr

Coastal sea level from CryoSat-2 SARIn altimetry in Norway

Martina Idžanović [a,*], Vegard Ophaug [a], Ole Baltazar Andersen [b]

[a] Faculty of Science and Technology, Norwegian University of Life Sciences (NMBU), Drøbakveien 31, N-1430 Ås, Norway
[b] DTU Space, Technical University of Denmark, Elektrovej, DK-2800 Kgs. Lyngby, Denmark

Received 16 August 2016; received in revised form 26 July 2017; accepted 30 July 2017
Available online 7 August 2017

Abstract

Conventional (pulse-limited) altimeters determine the sea surface height with an accuracy of a few centimeters over the open ocean. Sea surface heights and tide-gauge sea level serve as each other's buddy check. However, in coastal areas, altimetry suffers from numerous effects, which degrade its quality. The Norwegian coast adds further challenges due to its complex coastline with many islands, mountains, and deep, narrow fjords.

The European Space Agency CryoSat-2 satellite carries a synthetic aperture interferometric radar altimeter, which is able to observe sea level closer to the coast than conventional altimeters. In this study, we explore the potential of CryoSat-2 to provide valid observations in the Norwegian coastal zone. We do this by comparing time series of CryoSat-2 sea level anomalies with time series of in situ sea level at 22 tide gauges, where the CryoSat-2 sea level anomalies are averaged in a 45-km area around each tide gauge. For all tide gauges, CryoSat-2 shows standard deviations of differences and correlations of 16 cm and 61%, respectively. We further identify the ocean tide and inverted barometer geophysical corrections as the most crucial, and note that a large amount of observations at land-confined tide gauges are not assigned an ocean tide value. With the availability of local air pressure observations and ocean tide predictions, we substitute the standard inverted barometric and ocean tide corrections with local corrections. This gives an improvement of 24% (to 12.2 cm) and 12% (to 68%) in terms of standard deviations of differences and correlations, respectively.

Finally, we perform the same in situ analysis using data from three conventional altimetry missions, Envisat, SARAL/AltiKa, and Jason-2. For all tide gauges, the conventional altimetry missions show an average agreement of 11 cm and 60% in terms of standard deviations of differences and correlations, respectively. There is a tendency that results improve with decreasing distance to the tide gauge and a smaller footprint, underlining the potential of SAR altimetry in coastal zones.

Keywords: CryoSat-2; SARIn altimetry; Tide gauges

1. Introduction

Satellite altimetry is a well-proven and mature technique for observing the sea surface height (SSH) with an accuracy of a few centimeters over the open ocean (Chelton et al., 2001). The effective footprint of an altimeter is controlled by the pulse duration and width of the analysis window, and is typically between 2 and 7 km, depending on the sea state (Gommenginger et al., 2011). These classic pulse-limited altimeter systems are often termed conventional altimeters (Vignudelli et al., 2011). For such altimeters and typical wave heights of 3–5 m, a circular footprint of $\sim$100 km^2 is obtained, depending on the satellite orbit (Chelton et al., 1989).

The coastal zone is particularly relevant to society considering, e.g., sea-level rise, shipping, fishery, and other offshore activities (Pugh and Woodworth, 2014). The application of satellite altimetry is difficult close to the coast due to land and calm-water (bright target) contami-

* Corresponding author.
E-mail address: maid@nmbu.no (M. Idžanović).

http://dx.doi.org/10.1016/j.asr.2017.07.043
0273-1177/© 2017 COSPAR. Published by Elsevier Ltd.

nation of the radar echoes. This, in combination with a degradation of key range (wet troposphere) and geophysical corrections (high-frequency atmospheric and ocean signals, and tides), results in observation gaps in these zones (Vignudelli et al., 2005, 2011; Saraceno et al., 2008; Gómez-Enri et al., 2010). Large variations in atmospheric pressure along the coast and complex tidal patterns degrade the geophysical corrections for dynamic atmosphere and ocean tides (Andersen and Scharroo, 2011). Considering that Norway has the world's second longest coastline of 103,000 km, with many islands, steep mountains, and deep narrow fjords, the application of coastal altimetry is especially challenging there. An impression of the conventional altimetry observation gap along the Norwegian coast is given in a recent comparison of conventional altimetry with tide gauges (TGs). The average distance between valid points of crossing conventional altimetry tracks and local TGs was ~54 km (Ophaug et al., 2015).

The European Space Agency (ESA) CryoSat-2 (CS2) is the first new-generation altimetry satellite carrying a synthetic aperture interferometric radar altimeter (SIRAL) (Wingham et al., 2006). CS2 can operate in synthetic aperture radar (SAR), interferometric SAR (SARIn), as well as conventional low resolution (LR) modes. At high latitudes, the satellite operates in all three modes following geographically delimited masks. Along the Norwegian coast, in a narrow strip with a typical width of less than ~40 km, CS2 operates in SARIn mode (Fig. 1a). A Delay-Doppler modulation of the altimeter signal creates a synthetic footprint in this mode. The footprint is nominally 0.3 km by 8 km in respectively along- and across-track directions (Table 1). Hence, the risk that the footprint is contaminated by land is far less for CS2 in this mode compared to conventional altimeters.

The main goal of this study is to evaluate CS2 along the Norwegian coast, which comprises degraded SARIn data (without phase information, see Section 2.1). We explore the potential for these data to provide valid sea-level observations closer to the coast than conventional pulse-limited altimetry by comparing time series of CS2 observations with observations from an array of TGs along the Norwegian coast. The same tide-gauge (TG) comparison is also done using three conventional altimetry missions to quantify the performance of CS2 with respect to conventional altimetry. The data and methods are introduced in Section 2, comparison results are shown and discussed in Section 3, and conclusions are presented in Section 4.

2. Data and methods

2.1. CryoSat-2 20 Hz SARIn data processing

Satellite altimetry is normally distributed through initiatives like AVISO (http://www.aviso.altimetry.fr), OpenADB (http://openadb.dgfi.badw.de), PODAAC (http://podaac.jpl.nasa.gov), and RADS (http://rads.tudelft.nl), focusing on the regular distribution of homogenized and quality-controlled 1 Hz data. However, these archives do not process and/or distribute the CS2 SARIn data. ESA provides CS2 data in two levels, Level 1 (L1) and Level 2 (L2). L1 data contain orbit information and waveforms, while L2 data contain range and geophysical corrections, as well as height estimates. The 20 Hz L1b SARIn dataset was retracked using the simple threshold retracker (Nielsen et al., 2015), whereby the bin that contains 80% of the maximum power is taken as the retracking point. The SARIn dataset was obtained by the Technical University of Denmark (DTU) Space retracker system (Stenseng and Andersen, 2012) for the period from 2010 to 2014, which, at the time of this study, was based on the ice baseline B processor. Since then, it has been replaced by the CS2 baseline C processor (Bouffard et al., 2015). According to Webb and Hall (2016), the altimeter range R is given by

$$R = R_{wd} + R_{retrack} + R_{corr}, \tag{1}$$

where R_{wd} is the window delay, $R_{retrack}$ is the correction obtained in the retracking. R_{corr} are range and geophysical corrections including wet and dry troposphere, ionosphere, and atmospheric and tidal oceanic variations. In turn, the SSH is given by

$$SSH = h - R, \tag{2}$$

where h is the altitude of the satellite. 20 Hz sea level anomalies (SLAs) were computed referencing the sea surface heights (SSHs) to the DTU15 Mean Sea Surface (MSS) (Andersen et al., 2015) and applying range and geophysical corrections (see Section 2.4 and Table 3).

At the time of data processing, the SARIn/cross-track correction (Armitage and Davidson, 2014; Abulaitijiang et al., 2015) was not implemented in the retracker system. Consequently, the SARIn observations are degraded SARIn observations excluding phase information. Because the burst mode pulse repetition frequency in SAR mode is four times that of SARIn mode, the SARIn data are expected only to have half the precision of normal SAR altimetry (Wingham et al., 2006). As this study is a first validation of CS2 along the Norwegian coast, with the most important goal being to explore the potential of SAR altimetry missions (such as Sentinel-3 and Jason-CS/Sentinel-6), we still believe that a study of degraded SARIn CS2 observations is of value.

A suite of editing and outlier detection criteria are normally used to edit the altimeter data for the computation of 1 Hz data, see, e.g., Scharroo et al. (2013). As most of these are not available for the CS2 L1 data, we employed a two-step outlier detection. After discarding all CS2 observations over land using a high-resolution coastline (1:50,000 map scale, provided by the Norwegian Mapping Authority (NMA)) as a mask, the first step in the outlier detection was to remove all observations deviating more than ±1 m from DTU15 MSS. This first step led to a 28% data rejection. The second step of our outlier detection was based on a within-track gross error search using a multiple t test

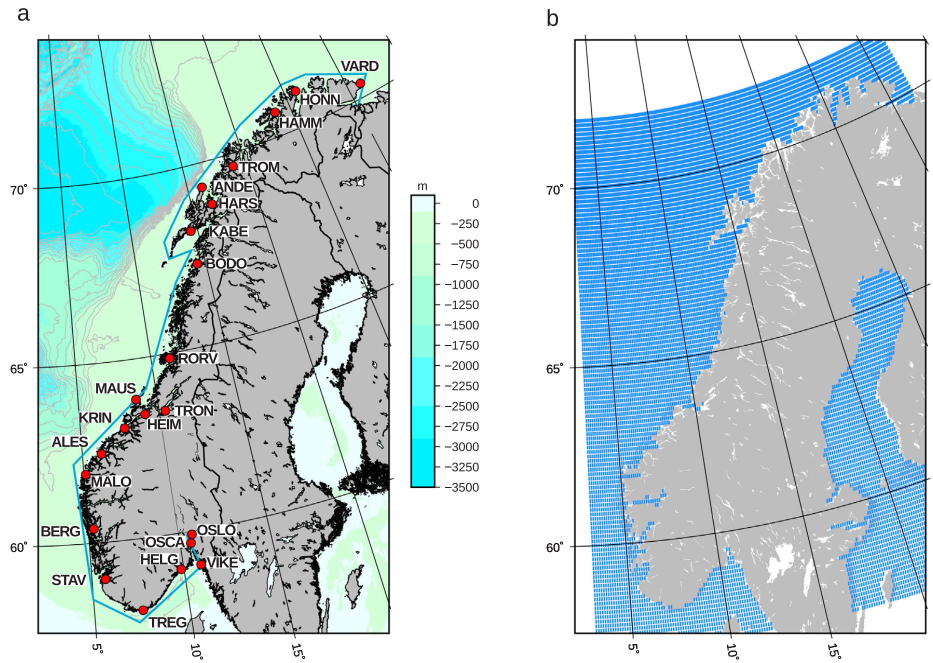

Fig. 1. (a) The 22 Norwegian TGs considered in this study. The blue line shows the CS2 SARIn mode border, using the geographical mode mask version 3.8 (European Space Agency, 2016). Bathymetry and 400 m isobaths are from the 2014 General Bathymetric Charts of the Oceans (GEBCO) (Weatherall et al., 2015). (b) FES2004 grid cells around Norway.

Table 1
CryoSat-2 mission specifications (Webb and Hall, 2016).

	CryoSat-2
Mission duration	8 April 2010 – present
Frequency	13.57 GHz
Latitudinal limit	88°
Orbit type	Near circular, polar, Low Earth Orbit
Altitude	717 km
Inclination	92°
Repeat period	396 (30) days
Footprint size along-track	2–10 km (250–400 m for SAR)
Footprint size across-track	7.7 km
Footprint area	185.1 km^2 (4.9 km^2 for SAR)

(Koch, 1999; Revhaug, 2007), applied to the SLAs. Thus, we allow our SLAs $\mathbf{l}$ $(n \times 1)$ to contain gross errors ∇ $(q \times 1)$, and see that the observation vector can be corrected for those gross errors by the subtraction $\mathbf{l} - \mathbf{E} \cdot \nabla$. Consequently, we extend the linear model by introducing a gross-error term:

$$\mathbf{l} - \mathbf{E} \cdot \nabla + \tilde{\mathbf{v}} = \mathbf{A} \cdot \tilde{\mathbf{x}}, \tag{3}$$

where $\mathbf{E}$ is an $(n \times q)$ matrix containing ones where a gross error is present (at (n, q)) and zeros elsewhere. $\mathbf{A}$ is the well-known $(n \times e)$ design matrix. Correcting for gross errors, we obtain new estimates for the residuals $\mathbf{v}$ $(n \times 1)$ and unknowns $\mathbf{x}$ $(e \times 1)$, annotated as $\tilde{\mathbf{v}}$ and $\tilde{\mathbf{x}}$.

A statistical outlier test based on Eq. (3) is obtained if the null hypothesis $H_0 : \nabla = 0$ (all outliers equal zero) is tested against the alternative hypothesis $H_1 : \nabla = \nabla_1 \neq 0$. The least-squares solution for Eq. (3) gives:

$$\mathbf{Q}_{\nabla} = \left(\mathbf{E}^T \cdot \mathbf{P} \cdot \mathbf{Q}_v \cdot \mathbf{P} \cdot \mathbf{E}\right)^{-1}, \tag{4}$$

$$\nabla = -\mathbf{Q}_{\nabla} \cdot \mathbf{E}^T \cdot \mathbf{P} \cdot \mathbf{v}, \tag{5}$$

where $\mathbf{Q}_v$ and $\mathbf{Q}_{\nabla}$ are cofactor matrices of $\mathbf{v}$ and ∇, respectively, and $\mathbf{P}$ the weight matrix. Applying the multiple t test, one observation at a time can be tested, with an estimated standard deviation of ∇:

$$\tilde{s}^2_{\nabla} = \frac{1}{f-1} \cdot \left(\mathbf{v}^T \cdot \mathbf{P} \cdot \mathbf{v} - \frac{\nabla^2}{\mathbf{Q}_{\nabla}}\right), \tag{6}$$

where f represents the degrees of freedom.

First, we assume a solution without gross errors, after which we perform the outlier test. Without the presence of gross errors, ∇ is small and the observations are normally distributed, i.e., $\mu = \mathrm{E}\{\nabla\} = 0$. Then, the t-statistic can be written as:

$$t = \frac{\nabla}{s_{\nabla}}, \tag{7}$$

where s_∇ is the estimated standard deviation of the gross error. If there is no gross error present, t in Eq. (7) will follow the t distribution. Thus, if the absolute value of t is smaller than the threshold value (two-tailed, with $\alpha = 0.05$ and $f = n - 1$), we accept the observation, otherwise we classify it as an outlier. For further details, see Koch (1999). On average, ~21% of the data points were classified as outliers (Table 2).

2.2. Tide-gauge data

We have considered 22 out of 23 TGs on the Norwegian mainland as shown in Fig. 1a, leaving out the Narvik TG due to few CS2 observations. The TG data were provided by NMA (K. Breili, personal communication) with a 10-min sampling rate, and include predicted ocean tides as well as local air pressure observations.

Both inverse barometer (IB) and ocean tide (OT) corrections were applied to the TG observations, making them comparable with the altimeter data. Before this was done, the annual astronomical tidal contribution, $\mathbf{S_a}$, was estimated from the OT predictions and removed, as it includes seasonal effects that to a large extent are already accounted for in the IB correction (Pugh and Woodworth, 2014). All TG observations were corrected for the IB effect using Wunsch and Stammer (1997) with respect to a reference value of 1011.4 mbar (Woodworth et al., 2012). At HAMM TG, no local pressure observations were available, and pressure data from a nearby meteorological station were used instead. Those pressure observations were obtained from the eKlima database of the Norwegian Meteorological Institute, at https://eklima.met.no/.

2.3. CryoSat-2 tide gauges

Treating CS2 like a 369-day repeat altimeter would only give four observations per point for the 2010–2014 period. Consequently, we consider a different approach. We established 45 × 45 km boxes around each TG containing CS2 observations and forming "CS2 tide gauges" (CS2TGs), shown in Figs. 7 and 8. The CS2TGs were positioned around each TG depending on topography, such that they cover as much marine area as possible, but still keep a minimum distance of 0.2° between the TG and the edge of the CS2 tide-gauge (CS2TG) box. The 45-km distance was chosen based on the geodetic orbit and temporal resolution of CS2. A CS2 orbit repetition cycle includes 13 sub-cycles. To include one CS2 repetition cycle (observations over a whole year, not only seasonal tracks) in our CS2TG box, and taking the CS2 across-track distance of 8 km at the equator into account, we need a 100 × 100 km CS2TG box. For Norway, with a mean latitude of 65°, we end up with a 45-km box. At TGs close to the open ocean, more than enough observations were available within the CS2TGs, while a more critical situation was found at TGs located inside fjords. Fig. 2 shows the data situation within the CS2TGs at three TGs to the open ocean (BODO, KABE, and VIKE), as well as three TGs well inside fjords (OSLO, OSCA, VIKE). We take the 45-km distance to be a trade-off between having enough points to have a sufficient temporal resolution for deriving meaningful statistics, as well as being close enough such that CS2 still observes the same ocean signal as the TG (see also Section 2.4).

As mentioned in Section 2.1, we did not downsample the 20 Hz observations to 1 Hz. This is normally done by the

Table 2
CS2TGs at 22 Norwegian TGs.

Tide-gauge	Tide-gauge code	No. obs.	No. obs. $\in [-1, 1]$ m DTU15	Used no. obs.	$t > t_{(\alpha/2,f)}$ [%]	No. tracks
Vardø	VARD	6111	5710	4639	19	93
Honningsvåg	HONN	6546	4457	3498	22	79
Hammerfest	HAMM	5611	3669	2947	20	90
Tromsø	TROM	2438	587	494	16	36
Andenes	ANDE	8023	7662	6318	18	95
Harstad	HARS	6010	4031	3034	25	83
Kabelvåg	KABE	7319	6639	5256	21	92
Bodø	BODO	7463	5909	4680	21	85
Rørvik	RORV	7940	7060	5410	23	102
Mausund	MAUS	7489	6678	5214	22	94
Trondheim	TRON	4826	1940	1495	23	56
Heimsjø	HEIM	5018	3030	2458	19	89
Kristiansund	KRIN	9949	9125	7422	19	97
Ålesund	ALES	9653	7352	5869	20	89
Måløy	MALO	9246	6411	5321	17	70
Bergen	BERG	5820	3962	3157	20	74
Stavanger	STAV	9365	8433	6731	20	94
Tregde	TREG	7695	7453	6118	18	92
Helgeroa	HELG	7496	7121	5824	21	92
Oscarsborg	OSCA	2346	1747	1377	21	49
Oslo	OSLO	493	255	224	12	21
Viker	VIKE	7407	6219	4960	20	67

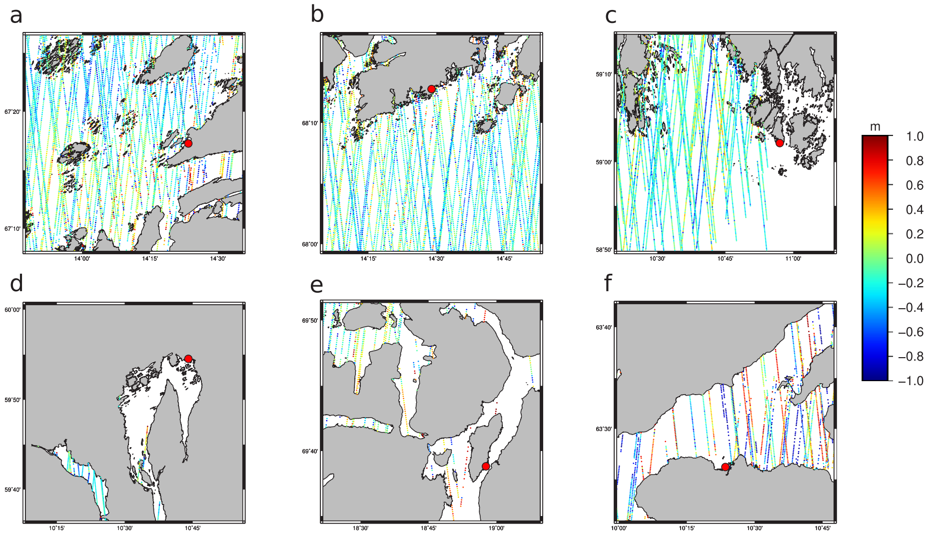

Fig. 2. SLAs in CS2TGs at (a) BODO, (b) KABE, (c) VIKE, (d) OSLO, (e) OSCA, and (f) TRON. The red dots denote the TGs. Note that OSLO and VIKE TGs are situated just outside the SARIn geographical mode mask (Fig. 1a), giving less observations in parts of the respective CS2TGs.

space agencies using iterative editing and averaging, which will increase the data accuracy. Since the CS2 observations within a track are sampled very closely in time (all CS2 observations within a track would be assigned the same TG observation), we averaged all 20 Hz observations within a track, and linearly interpolated the TG observations to the time of the averaged CS2 observations using a nearest-neighbor approach. On average, 79 CS2 tracks were available in each CS2TG. In addition to standard deviations of differences between CS2TG and TG time series, Spearman's (distribution-free) rank correlation coefficient, ρ, was computed. Spearman's ρ is a non-parametric method for detecting relations between two variables. Non-parametric methods are relatively insensitive to outliers, and do not assume that the observations are normally distributed (Hollander et al., 2013). It is a slightly more conservative value than the well-known Pearson correlation coefficient.

Table 2 summarizes the processing results for the 22 CS2TGs. In some cases, there are slight differences of the resulting number of valid SLAs depending on whether standard or local corrections are applied. Consequently, the three rightmost columns in Table 2 are average values from both cases.

2.4. Range and geophysical corrections

As opposed to the Jason-2, Envisat, and SARAL/AltiKa altimetry satellites, CS2 does not carry a radiometer. Therefore, the corrections for the wet (WET) and dry (DRY) tropospheric refraction must be derived using models, where CS2 uses the ECMWF model (Dee et al., 2011). CS2 is furthermore a single-frequency altimeter, hence the correction for the ionospheric refraction (IONO) is also provided by a model, i.e., the GPS-based global ionospheric model (GIM) (Komjathy and Born, 1999). In general, these corrections are believed to be only slightly less accurate than the instrument-derived corrections applied on conventional altimeters (Andersen and Scharroo, 2011).

The CS2 dynamic atmosphere correction (DAC) consists of a high-frequency part provided by MOG2D (Carrère and Lyard, 2003) and a low-frequency part, IB, provided by ECMWF (IB_{ECMWF}). The tide correction consists of OT, nodal tide (NT), ocean tide loading (OTL), solid Earth tide (SET), and pole tide (PT). The CS2 OT correction ($OT_{FES2004}$) is provided by the FES2004 global OT model (Lyard et al., 2006), which is similar to those used in conventional satellites. See Table 3 for an overview of applied corrections.

Fig. 3b shows the signal standard deviations of the range and geophysical corrections in all CS2TGs. The DRY, WET, and IONO range corrections show smooth correction curves along the coast, with values of less than 6 cm, while NT, OTL, SET, and PT show values of ~8 cm or less. We note that by far the largest contributors to the corrections are OT (up to ~80 cm at the northernmost TGs) and IB (~12 cm), in accordance with Andersen and Scharroo (2011). Here, $OT_{FES2004}$ and IB_{ECMWF} are the standard OT and IB corrections for CS2. Fig. 3a shows the percentage of CS2 observations not having a FES2004 OT correction assigned to them within the CS2TGs. In accordance with the findings of Abulaitijiang et al. (2015), there is a considerable amount of global OT values missing at TGs well inside fjords, particularly at TROM, TRON, and OSLO. Looking at Fig. 1b we note that these TGs are outside the coverage of the

Table 3
Range and geophysical corrections for CS2 (Webb and Hall, 2016), SARAL/AltiKa, Envisat/C, and Jason-2 (Scharroo et al., 2013).

Correction	Observation or model for			
	CS2	SARAL/AltiKa	Envisat/C	Jason-2
Dry troposphere	ECMWF	ECMWF	ECMFW	ECMWF
Wet troposphere	ECMWF	Radiometer	Radiometer	Radiometer
Ionosphere	GIM	GIM	GIM	Dual frequency
Inverse barometric correction	ECMWF	ECMWF	ECMWF	ECMWF
High-frequency atmospheric variations	MOG2D	MOG2D	MOG2D	MOG2D
Ocean tide	FES2004	FES2004	FES2004	FES2004
Ocean tide loading	FES2004	FES2004	FES2004	FES2004
Long-period tide	FES2004	FES2004	FES2004	FES2004
Solid Earth	Cartwright/Edden	Cartwright/Edden	Cartwright/Edden	Cartwright/Edden
Pole tide	Wahr	Wahr	Wahr	Wahr
Mean sea surface	DTU15 MSS	DTU13 MSS	DTU13 MSS	DTU13 MSS
Bias	1.38 m[a]	–	–	–

[a] Includes the difference between TOPEX and WGS84 ellipsoids as well as the SARIn range bias, which must be applied to baseline B products (Scagliola and Fornari, 2017).

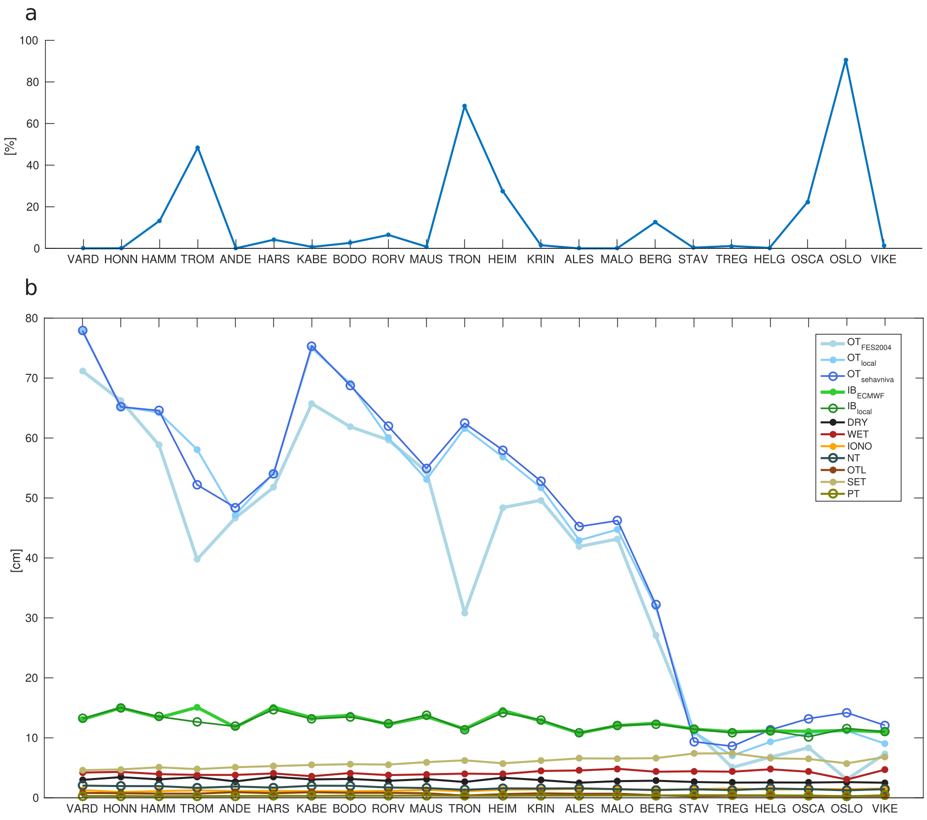

Fig. 3. (a) Percentage of CS2 observations missing the FES2004 OT correction within CS2TGs. (b) Signal standard deviations of CS2 range and geophysical corrections within CS2TGs.

FES2004 grid, where the standard OT correction is consequently set to zero.

The substitution of standard corrections with locally refined corrections in the post-processing of coastal altimetry data has proven to be a successful strategy (e.g., Bouffard et al., 2011; Birol et al., 2017). The availability of local OT predictions and pressure data (Section 2.2) allowed us to substitute the standard OT and IB corrections ($OT_{FES2004}$ and IB_{ECMWF}) with OT_{local} and IB_{local} derived from TGs. The substituted corrections are termed local corrections in the following. Fig. 3b reveals that the IB_{ECMWF} and IB_{local} curves are very similar. Since the IB is the low-frequency part of the total DAC correction, we did not expect in situ pressure observations to show large differences to ECMWF model pressure. The agreement between the ECMWF model pressure and the locally observed pressure suggests that the ECMWF model pressure is sufficiently accurate for the areas considered along the Norwegian coast.

However, we observe a larger difference between the $OT_{FES2004}$ and OT_{local} curves. As expected, the most prominent differences appear at TGs where a considerable amount of FES2004 OT values is missing. There is also a larger discrepancy between standard and local OT signal at KABE, which mainly contains valid FES2004 OT values. A possible explanation is that FES2004 does not fully capture the complex OT signal in that area.

To support our CS2TG choice we explored the OT signal variability within the CS2TGs. This was done by computing OT corrections for the CS2TGs using the tide and sea-level web service of NMA ($OT_{sehavniva}$, http://www.kartverket.no/sehavniva/). Using $OT_{sehavniva}$, each CS2 observation is assigned an individual OT correction, determined by a spatial interpolation of OT using site-specific scaling factors and time delays to observations from the nearest permanent and temporary TGs. This contrasts OT_{local}, which simply assigns the TG OT prediction value to all observations within the CS2TG. An agreement of $OT_{sehavniva}$ with OT_{local} thus suggests that the CS2TG indeed covers an area showing similar ocean variability.

In Fig. 3b we note that $OT_{sehavniva}$ and OT_{local} generally agree well, especially in areas with a large amount of observations. It suggests that the CS2TGs represent areas that are compatible with the TGs. Larger discrepancies are seen in TROM, OSCA, and OSLO, i.e., at TGs that are already problematic due to few CS2 observations (Figs. 2d–f), and where the CS2TG approach is not ideal.

2.5. Conventional altimeter data

Jason-2, Envisat, and SARAL/AltiKa 1 Hz altimetry data were extracted from the radar altimeter database system (RADS) (Scharroo et al., 2013), with standard corrections applied. Due to the orbit configuration of Jason-2, only data up to 66°N are available. For each altimeter, the two nearest tracks to the TG were considered. For consistency with the CS2TGs, for each track, a 45×45 km box was centered on the TG and then shifted westwards by 0.1°. Next, all altimeter observations within the box were averaged. In the following, when referring to conventional altimetry sites, it is the average location of the observations within the box that is meant. For some TGs (HELG, TREG, MALO, TROM), the search radius had to be extended to find a valid track. The time period of the conventional altimetry data was adapted as far as possible to the CS2 time period. For Jason-2, its entire 2010–2016 period was used, while for Envisat only the period between 2010 and 2012 (phase C) was used, where the satellite was in a 30-day repeat orbit. For SARAL/AltiKa the period after 2013 could be used. We are aware of the fact that SARAL/AltiKa is not strictly a conventional altimeter, as it has a smaller footprint and lower noise due to its lower altitude, antenna pattern, and Ka-band frequency (Verron et al., 2015). In this study, however, we use the term conventional altimetry only to distinguish pulse-limited altimetry from SAR altimetry.

The number of observations from the conventional altimeters will generally not correspond with the expected number of observations considering the number of repeats for each altimeter time period. This is due to the averaging box and that the RADS data are not resampled to reference tracks. For Jason-2 $\sim$200 observations were averaged, while for SARAL/AltiKa and Envisat $\sim$30 and $\sim$15 observations were averaged, respectively. Furthermore, TGs that lie further inside fjords than TGs closest to the open ocean, have been assigned the same altimeter tracks as the latter. This is because the tracks around the open-ocean TGs are also the closest to the TGs inside fjords. Consequently, (HARS, ANDE), (TRON, HEIM, MAUS), and (OSLO, OSCA, VIKE) are compared with the same altimeter tracks. In addition, at VIKE, roughly the same site was chosen for each track in case of Envisat and SARAL/AltiKa, as the two tracks are crossing there. For consistency, the SSHs were extracted from RADS using the same geophysical corrections as for CS2 (Table 3).

Several experimental coastal altimetry projects exist, such as Jason-2/PISTACH (Mercier et al., 2008), Envisat/COASTALT (Dufau et al., 2011), multi-mission/CTOH (Roblou et al., 2011), or the recent coastal altimetry product based on SARAL/AltiKa (Valladeau et al., 2015). Some of these are distributed through AVISO. In their study along the Norwegian coast, Ophaug et al. (2015) found that tailored coastal altimetry products based on Jason-2 and Envisat offered only marginal improvements over the conventional observations, thus we did not consider coastal altimetry products in this study.

3. Results

3.1. Comparison of CryoSat-2 with tide gauges along the Norwegian coast

Fig. 4 shows time series of SLAs from CS2TGs and sea level from TGs between 2010 and 2014 at 22 sites, using standard CS2 corrections. Generally, the two time series agree well, with a mean standard deviation of differences of 16.0 cm and a mean correlation of 61%. Fig. 5 shows the same time series using local CS2 corrections. These two time series agree better than the ones in the standard case, with a mean standard deviation of differences of 12.2 cm and a mean correlation of 68%. The time series at TGs close to the open ocean (e.g., VARD, ANDE, STAV, VIKE) agree better than the time series at land-confined TGs (e.g., TROM, TRON, HEIM, BERG).

Fig. 6 shows standard deviations of differences and correlations between the TGs and CS2, using both standard and local corrections. Using standard corrections (solid lines in Fig. 6), the standard deviations of differences are 20 cm or more at land-confined TGs (e.g., TROM, TRON, HEIM, BERG), while TGs to the open ocean (e.g., VARD, ANDE, STAV, VIKE) have standard deviations of differences of 9 cm or less. Related behavior is seen for correlations in Fig. 6b. A comparison of curves in Figs. 3a and 6a reveals that deviating locations are due to missing $OT_{FES2004}$ values.

Using local corrections (dashed lines in Fig. 6), we observe an improvement in standard deviations of differences at 19 out of 22 TGs (exceptions are ALES, MALO, and OSCA). Local corrections yield an average improvement of ~24% in standard deviations of differences and ~12% for correlations. Applying local corrections, large decreases in standard deviations of differences are observed at HAMM, KABE, BODO, RORV, TRON, and HEIM, i.e., at TGs that are both land-confined and to the open ocean. Among land-confined TGs with few observations, TRON and TROM show large drops in standard deviations of differences, and the correlation increases. These CS2TGs are characterized by a small number of valid observations. Among TGs to the open ocean with many observations, BODO, KABE, and VIKE show significant drops in standard deviations of differences and increased correlation. This indicates a gain in determining the OT correction by a local approach.

3.2. Comparison of conventional altimetry with tide gauges along the Norwegian coast

Figs. 7 and 8 show standard deviations of differences and correlations between time series of SLAs from the conventional altimetry missions (Envisat, SARAL/AltiKa, and Jason-2) and sea level from TGs. In addition, the CS2TGs are shown, to give an overview of the spatial distribution of the data used in this study.

We first note that the mean distance from the conventional altimetry sites and TGs is 53 km, which agrees with the findings of Ophaug et al. (2015). Due to the lower spa-

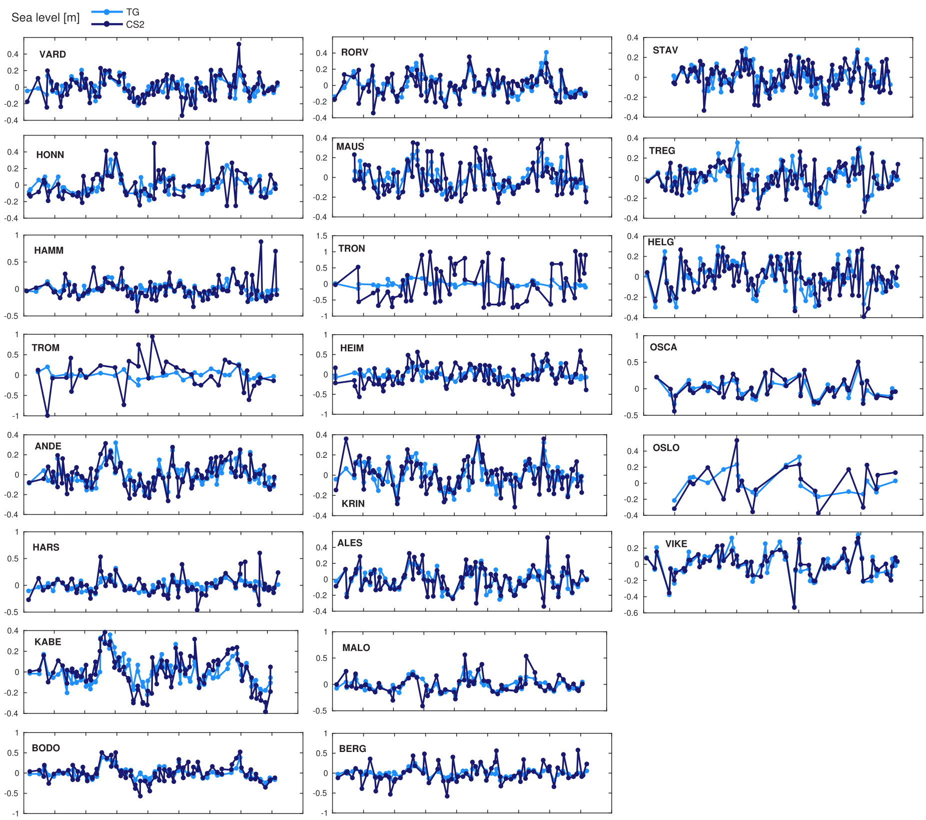

Fig. 4. Comparison of CS2TG SLAs with TG sea level using standard corrections.

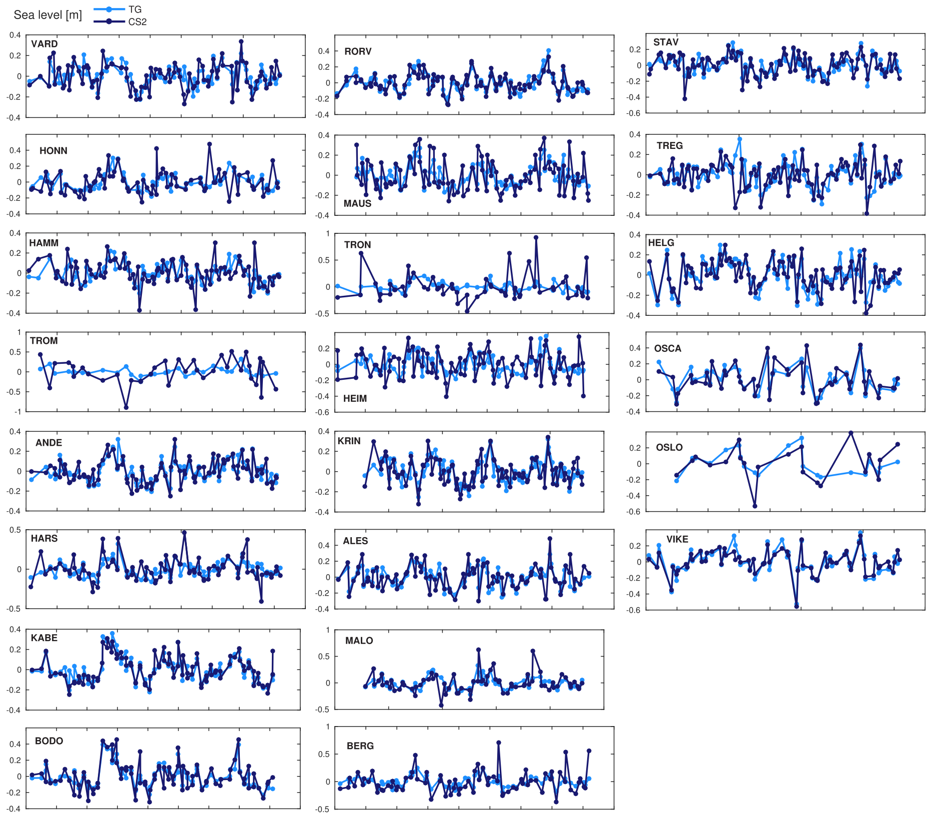

Fig. 5. As Fig. 4, but using local corrections.

tial resolution of Jason-2, its sites are typically little further from the CS2TGs than those from Envisat and SARAL/AltiKa, with a mean distance of 71 km. The mean distance for Envisat is 50 km and for SARAL/AltiKa 45 km. The largest distance between all conventional altimeters and TGs is at OSLO. Although the CS2TG at OSLO has valid observations well within the 45-km box, it is an area where CS2 also struggles due to few observations as a result of the geographical mode mask border (see Fig. 1a).

All conventional altimeters perform similarly. As with CS2, there are variations between standard deviations and correlations at different TGs. Envisat shows the largest standard deviation of differences of 18.9 cm at KRIN. Both Envisat and SARAL/AltiKa show the smallest standard deviation of differences of 5.1 cm at TROM and ANDE, respectively. Regarding correlations, Envisat shows the smallest correlation of 10% at TROM, while SARAL/AltiKa shows the largest correlation of 90% at TROM.

There is a tendency that correlation decreases and standard deviation of differences increases with increasing distance to the TG for all altimeters. These results suggest that the agreement of conventional altimetry with the TGs improves from Jason-2 through Envisat to SARAL/Altika. As mentioned earlier, the smaller footprint of SARAL/AltiKa makes it particularly suitable for coastal applications, and explains it outperforming Envisat and Jason-2. However, we note that at TGs where both altimeter sites are similarly close to the TG, the performance of the individual sites sometimes varies without obvious reason. The good performance at TGs that use common altimetry tracks (HARS, TRON, HEIM) can be seen as an indicator that the CS2TGs were not chosen too large (Section 2.3).

Similar to CS2, the mean correlation of the conventional altimeters with the TGs is 60%, but with a slightly lower mean standard deviation of differences of 11 cm. However, if the land-confined CS2TGs (e.g., TROM, TRON, HEIM, BERG), are omitted in the analysis, the CS2TGs show a mean correlation of 69%, and a mean standard deviation of differences of 12 cm (with standard corrections), and a mean correlation of 74%, and a mean standard deviation of differences of 10 cm (with local corrections). Practically

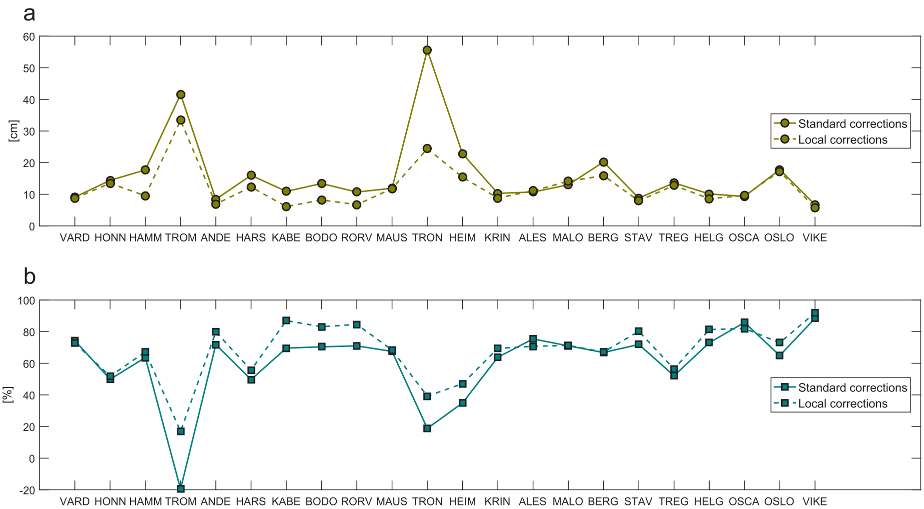

Fig. 6. Comparison of CS2 with TGs using standard and local OT and IB corrections, in terms of (a) standard deviations of differences and (b) correlations. The TGs are ordered such that the northernmost TG appears first on the left-hand side of the horizontal axis, moving southward along the Norwegian coastline.

the same results are obtained from the CS2TGs if those that use common conventional altimetry tracks are left out (HARS, TRON, HEIM, OSLO, OSCA). This suggests that, if the problematic CS2TGs are set aside, there is an improvement with CS2 as it gets closer to the coast than conventional altimeters.

As of yet, not many validation studies of CS2 SAR performance along coasts exist. Fenoglio-Marc et al. (2015) compared CS2 with the Helgoland island TG in the German Bight, and found standard deviations of differences of 6.6 cm for pseudo-LRM data and 7.7 cm for SAR-mode data (with higher range precision than our degraded SARIn observations) at a maximum distance of 20 km from the TG. As opposed to our CS2 data, a sea-state bias correction from the RADS hybrid model was applied. In a recent validation of a global CS2 geophysical ocean product (based on LRM and pseudo-LRM data), Calafat et al. (2017) found standard deviations of differences to 22 TGs spread across the globe of 7.1 cm. They also compared Jason-2 with the same set of TGs, and found a similar standard deviation of differences of 7.3 cm. Our results show a similar or better agreement (at favorable TGs), despite the complexity of the study area and the application of the degraded SARIn mode data.

In general, the observed discrepancies between altimetric SLAs and TG sea level are due to instrument noise and the fact that the altimeter and the TG sample slightly different ocean signals (Calafat et al., 2017). The latter aspect can be particularly problematic at northern high latitudes, where the baroclinic Rossby radius is expected to be smaller than 10 km (Chelton et al., 1998). At TGs where coastal or other complex ocean processes are expected to be dominant (e.g., KABE, TROM, TRON, HEIM, BERG), the observed differences between altimetry and TGs will be larger.

Furthermore, the derived time series from CS2 and the conventional altimeters are not strictly consistent with respect to the sampling interval. We practically compare instantaneous sea level observations and do not perform any temporal averaging of the altimetry observations exceeding the individual passes. However, as noted by Calafat et al. (2017), the comparison of instantaneous sea-level observations sampled with a certain periodicity is still consistent.

Finally, we emphasize a few aspects which make the conditions for the CS2TGs more challenging than for the conventional altimeters. First, the SLA observations from CS2 are taken from multiple tracks within the CS2TG. Potential errors in the MSS will appear as SLA offsets between the tracks. This, in turn, could appear as an SLA error in the comparison with the TG, making it a bigger challenge for CS2 than for conventional repeat-altimetry (Calafat et al., 2017). It becomes a serious issue close to the coast because of the interpolation error in the MSS. It is larger in the coastal areas due to missing observations and simple extrapolation. It could also be a problem for the conventional altimeters, although less so because the observations are much more concentrated in space. In addition, the conventional altimetry sites are more to the open ocean, where Smith and Scharroo (2009) found that current MSS models did not introduce significant errors in the SLAs.

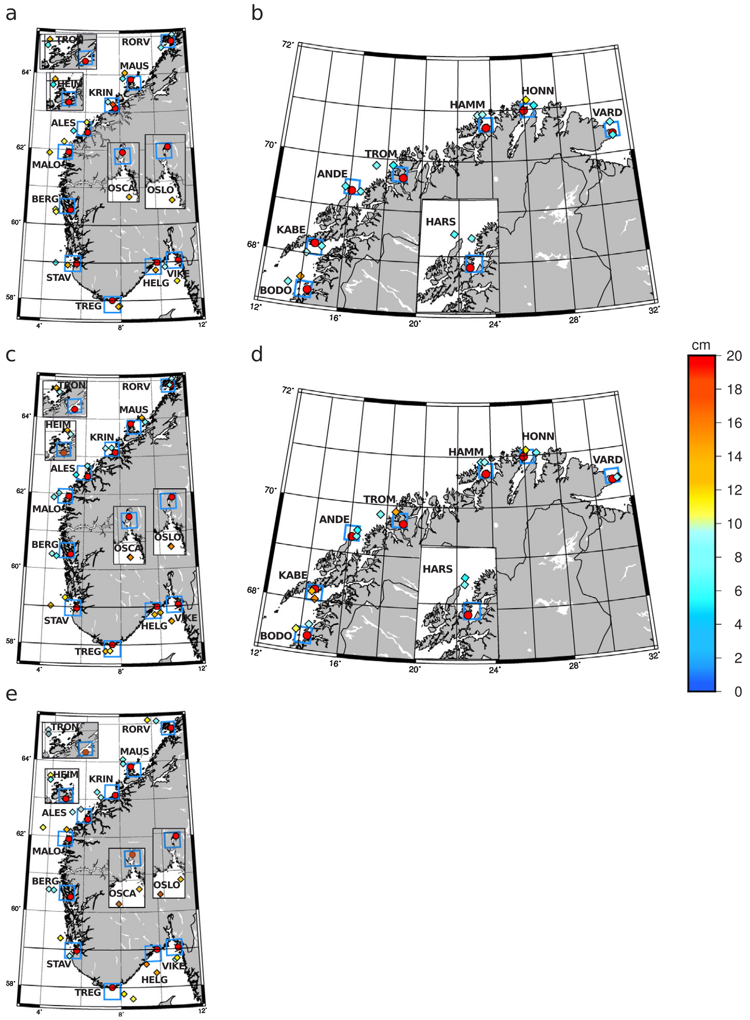

Fig. 7. TGs (red dots), CS2TGs (blue boxes) and conventional altimetry (diamond markers) along the Norwegian coast. The diamond markers, placed in the average location of the observations within the boxes, show standard deviations of differences between conventional altimetry and the 22 TGs; Envisat (a) south of 66°N, (b) north of 66°N, SARAL/AltiKa (c) south of 66°N, (d) north of 66°N, and Jason-2 (e) south of 66°N.

Second, the conventional altimetry data from RADS have robust editing criteria, and we expect these data to be of higher quality than the CS2 SARIn-mode data. The SLAs from CS2 are based on preliminary processing and data screening. The DTU Space retracking system is experimental and under development. Our editing of the CS2 degraded SARIn data is crude. A considerable amount of valid data points did not pass the editing, and reveals that CS2 targets along the Norwegian coast are noisy and prone to instrumental errors. An example of the latter is that when CS2 passes a fjord with steep mountains on either side, it will track its own noise instead of the fjord surface. Also, we have seen that a large amount of the CS2 observations well inside fjords lack OT corrections, which can be saved in post-processing by considering local OT corrections.

4. Summary and conclusions

We have performed an initial validation of CS2 along the Norwegian coast, over areas previously not monitored by conventional altimetry. The validation is done by comparing CS2 with in situ observations at 22 TGs. As pointed out by Calafat et al. (2017), CS2 has been shown to be as suitable for oceanography as are conventional altimeters. CS2 was designed for cryospheric and geodetic studies

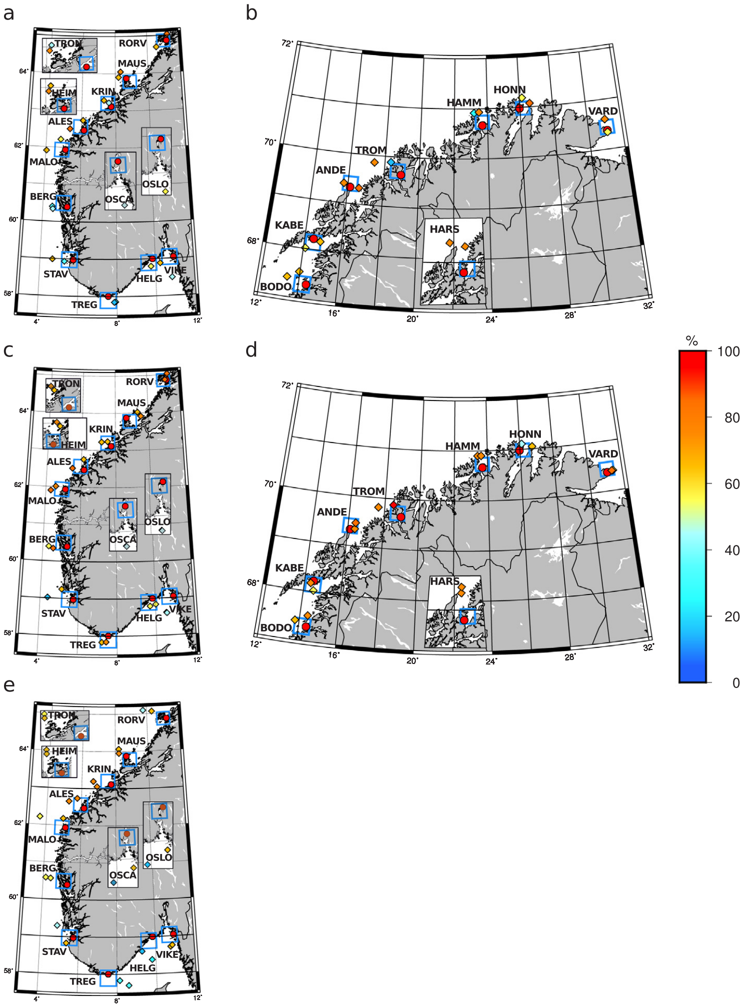

Fig. 8. As Fig. 7, but here the diamond markers show temporal correlations of conventional altimetry with the 22 TGs; Envisat (a) south of 66°N, (b) north of 66°N, SARAL/AltiKa (c) south of 66°N, (d) north of 66°N, and Jason-2 (e) south of 66°N.

which require a high spatial resolution (as opposed to studies of ocean dynamics, which require a high temporal resolution).

The entire Norwegian coast falls into the CS2 SARIn mode mask, but the phase information was not applied to these observations at the time of processing. Thus, the considered observations are a kind of degraded SARIn observations, with a noisier signal due to less waveforms that are averaged in SARIn mode than in pure SAR mode. The geodetic orbit of CS2 gives a denser spatial coverage than conventional repeat-altimetry, with an average of 4208 20 Hz SLAs within a 45×45 km area around TGs, i.e., CS2TGs. The CS2TGs are both close to the open ocean and land-confined/inside fjords. We find that the 45×45 km box is a good compromise between having a sufficient number of observations to derive meaningful statistics, and still cover a small enough area such that the OT variability within the CS2TGs is relatively similar to the OT variability at TGs.

Close to the coast, the validity of the range and geophysical corrections are of particular importance. By inspection within the CS2TGs, we confirmed that the OT and IB corrections are the largest signal contributors to the corrections, with the former being decisive along the Norwegian coast, because the OT range is large. The OT correction was missing at several land-confined TGs, so we investigated how local corrections from pressure observations and OT predictions perform within the CS2TGs. The IB correction did not change significantly when using local pressure instead of ECMWF model pressure, but the OT correction, as expected, had a significant impact. Thus, we compared CS2TGs with the TGs using both standard and local corrections.

Using standard corrections, the standard deviation of differences and correlation over all 22 TGs is 16 cm and 61%, respectively. Using local corrections, these values are 12.2 cm and 68%. We note a considerable improvement at CS2TGs that are missing standard OT corrections and have few CS2 observations, but also at reliable CS2TGs with many observations. The latter suggests a gain by a local approach to determining the OT correction.

To compare these results with conventional altimetry, the same analysis with 22 TGs was done using data from three conventional altimetry missions, Envisat, SARAL/AltiKa, and Jason-2. They show mean standard deviations of differences of 10.0 cm, 10.6 cm, and 11.0 cm, and mean correlations of 58%, 64%, and 56%, respectively. There is a tendency that standard deviation of differences increases and correlation decreases with increasing distance to the TG for all altimeters.

If the problematic CS2TGs are left out of the analysis, thus making CS2 more comparable to the conventional altimeters, the standard deviation of differences and correlation over all TGs is 12 cm and 69% (with standard corrections), and 10 cm and 74% (with local corrections).

These results confirm that CS2 SARIn-mode observations, even with their degraded range precision and without the phase information, are of comparable quality to those from conventional altimetry. A next step could be a more elaborate modeling of the DAC (including high-frequency atmospheric variations, see, e.g., Bouffard et al. (2011) or Woodworth and Horsburgh (2011)), and an improved WET correction using the national GNSS network (Obligis et al., 2011). Future improvements of the retracker system (e.g., inclusion of the phase information in the processing, giving pure SARIn observations) and the investigation of other retrackers may mitigate noise. A more elaborate statistical editing of the data, such as that employed by Nielsen et al. (2015), could also provide a larger amount of valid observations.

We have used the CS2 ice baseline B processor in this study. It has later been replaced by the ice baseline C processor (Bouffard et al., 2015). A tailored ocean processing of CS2, the CryoSat Ocean Processing (COP) baseline C, will be released in 2017 (Bouffard et al., 2016). In future coastal applications of CS2, these baselines should be considered.

The main improvement of CS2 is due to the smaller SAR footprint, enabling observations closer to the coast than conventional altimeters. As such, this study has implications for next-generation SAR altimetry missions such as Sentinel-3 and Jason-CS/Sentinel-6.

Acknowledgments

We would like to thank K. Breili at NMA, for providing TG data and helpful comments. ESA and RADS are acknowledged for providing CryoSat-2 and other altimetry data, respectively. The manuscript was considerably improved through constructive comments from two anonymous reviewers, which are gratefully acknowledged. O.B. Andersen was supported by the ESA's GOCE++DYCOT project. This study is part of the Norwegian University of Life Science's GOCODYN project, supported by the Norwegian Research Council under project number 231017.

References

Abulaitijiang, A., Andersen, O.B., Stenseng, L., 2015. Coastal sea level from inland CryoSat-2 interferometric SAR altimetry. Geophys. Res. Lett. 42 (6), 1841–1847. http://dx.doi.org/10.1002/2015GL063131.

Andersen, O.B., Knudsen, P., Stenseng, L., 2015. The DTU13 MSS (mean sea surface) and MDT (mean dynamic topography) from 20 years of satellite altimetry. In: IAG Symposia. Springer, Berlin Heidelberg. http://dx.doi.org/10.1007/1345_2015_18.

Andersen, O.B., Scharroo, R., 2011. Range and geophysical corrections in coastal regions: and implications for mean sea surface determination. In: Vignudelli, S. et al. (Eds.), Coastal Altimetry. Springer, Berlin Heidelberg, pp. 103–145. http://dx.doi.org/10.1007/978-3-642-12796-0_5.

Armitage, T.W.K., Davidson, M.W.J., 2014. Using the interferometric capabilities of the ESA CryoSat-2 mission to improve the accuracy of sea ice freeboard retrievals. IEEE Trans. Geosci. Rem. Sens. 52 (1), 529–536. http://dx.doi.org/10.1109/TGRS.2013.2242082.

Birol, F., Fuller, N., Lyard, F., Cancet, M., Niño, F., Delebecque, C., Fleury, S., Toublanc, F., Melet, A., Saraceno, M., Léger, F., 2017. Coastal applications from nadir altimetry: example of the X-TRACK regional products. Adv. Space Res. 59 (4), 936–953. http://dx.doi.org/10.1016/j.asr.2016.11.005.

Bouffard, J., Roblou, L., Birol, F., Pascual, A., Fenoglio-Marc, L., Cancet, M., Morrow, R., Ménard, Y., 2011. Introduction and assessment of improved coastal altimetry strategies: case study over the Northwestern Mediterranean Sea. In: Vignudelli, S. et al. (Eds.), Coastal Altimetry. Springer, Berlin Heidelberg, pp. 297–330. http://dx.doi.org/10.1007/978-3-642-12796-0_1.

Bouffard, J., Manner, R., Brockley, D., 2015. CryoSat-2 Level 2 Product Evolutions and Quality Improvements in Baseline C, XCRY-GSEG-EOPG-TN-15-00004 Issue 3, ESRIN, Italy.

Bouffard, J., Féménias, P., Parrinello, T., 2016. CryoSat mission: data quality status and next product evolutions. Paper presented at the European Space Agency Living Planet Symposium, Prague, May 9–13.

Calafat, F.M., Cipollini, P., Bouffard, J., Snaith, H., Féménias, P., 2017. Evaluation of new CryoSat-2 products over the ocean. Rem. Sens. Environ. 191, 131–144. http://dx.doi.org/10.1016/j.rse.2017.01.009.

Carrère, L., Lyard, F., 2003. Modeling the barotropic response of the global ocean to atmospheric wind and pressure forcing – comparisons with observations. Geophys. Res. Lett. 30 (6), 1275. http://dx.doi.org/10.1029/2002GL016473.

Chelton, D.B., Walsh, E.J., MacArthur, J.L., 1989. Pulse compression and sea level tracking in satellite altimetry. J. Atmos. Ocean. Technol. 6, 407–438. http://dx.doi.org/10.1175/1520-0426(1989)006<0407:PCASLT>2.0.CO;2.

Chelton, D.B., deSzoeke, R.A., Schlax, M.G., Naggar, K.E., Siwertz, N., 1998. Geographical variability of the first Baroclinic Rossby radius of deformation. J. Phys. Oceanogr. 28, 433–460. http://dx.doi.org/10.1175/1520-0485(1998)028<0433:GVOTFB>2.0.CO;2.

Chelton, D.B., Ries, J.C., Haines, B.J., Fu, L.-L., Callahan, P.S., 2001. Satellite altimetry. In: Fu, L.-L., Cazenave, A. (Eds.), Satellite Altimetry and Earth Sciences: A Handbook of Techniques and Applications, Int. Geophys., vol. 69. Academic Press, San Diego, California, pp. 1–131. http://dx.doi.org/10.1016/S0074-614(01)80146-7.

Dee, D.P., Uppala, S.M., Simmons, A.J., Berrisford, P., Poli, P., Kobayashi, S., Andrae, U., Balmaseda, M.A., Balsamo, G., Bauer, P., Bechtold, P., Beljaars, A.C.M., van de Berg, L., Bidlot, J., Bormann, N., Delsol, C., Dragani, R., Fuentes, M., Geer, A.J., Haimberger, L., Healy, S.B., Hersbach, H., Hólm, E.V., Isaksen, L., Kållberg, P., Köhler, M., Matricardi, M., McNally, A.P., Monge-Sanz, B.M., Morcrette, J.-J., Park, B.-K., Peubey, C., de Rosnay, P., Tavolato, C., Thépaut, J.-N., Vitart, F., . The ERA-Interim reanalysis: configuration and performance of the data assimilation system. Quart. J. R. Met. Soc. 137 (656), 553–597. http://dx.doi.org/10.1002/qj.828.

Dufau, C., Martin-Puig, C., Moreno, L., 2011. User requirements in the coastal ocean for satellite altimetry. In: Vignudelli, S. et al. (Eds.), Coastal Altimetry. Springer, Berlin Heidelberg, pp. 51–60. http://dx.doi.org/10.1007/978-3-642-12796-0_3.

European Space Agency, 2016. Geographical Mode Mask. Online at <https://earth.esa.int/web/guest/-/geographical-mode-mask-7107> (as of 27 April 2016).

Fenoglio-Marc, L., Dinardo, S., Scharroo, R., Roland, A., Dutour Sikric, M., Lucas, B., Becker, M., Benveniste, J., Weiss, R., 2015. The German bight: a validation of CryoSat-2 altimeter data in SAR mode. Adv. Space Res. 55 (11), 2641–2656. http://dx.doi.org/10.1016/j.asr.2015.02.014.

Gómez-Enri, J., Vignudelli, S., Quartly, G.D., Gommenginger, C.P., Cipollini, P., Challenor, P.G., Benveniste, J., 2010. Modeling Envisat RA-2 waveforms in the coastal zone: case study of calm water contamination. IEEE Geosci. Rem. Sens. Lett. 7 (3), 474–478. http://dx.doi.org/10.1109/LGRS.2009.2039193.

Gommenginger, C., Thibaut, P., Fenoglio-Marc, L., Quartly, G., Deng, X., Gómez-Enri, J., Challenor, P., Gao, Y., 2011. Retracking altimeter waveforms near the coasts. In: Vignudelli, S. et al. (Eds.), Coastal Altimetry. Springer, Berlin Heidelberg, pp. 61–101. http://dx.doi.org/10.1007/978-3-642-12796-0_4.

Hollander, M., Wolfe, D.A., Chicken, E., 2013. Nonparametric Statistical Methods, third ed. John Wiley & Sons, Inc., Hoboken, New Jersey.

Koch, K.-R., 1999. Parameter Estimation and Hypothesis Testing in Linear Models, Second, updated and enlarged Edition. Springer-Verlag.

Komjathy, A., Born, G.H., 1999. GPS-based ionospheric corrections for single frequency radar altimetry. J. Atmos. Sol.-Terr. Phys. 61 (16), 1197–1203. http://dx.doi.org/10.1016/S1364-6826(99)00051-6.

Lyard, F., Lefevre, F., Letellier, T., Francis, O., 2006. Modelling the global ocean tides: modern insights from FES2004. Ocean Dyn. 120 (12), 394–415. http://dx.doi.org/10.1007/s10236-006-0086-x.

Mercier, F., Dibarboure, G., Dufau, C., Carrere, L., Thibaut, P., Obligis, E., Labroue, S., Ablain, M., Sicard, P., Garcia, G., Moreau, T., Commien, L., Picot, N., Lambin, J., Bronner, E., Lombard, A., Cazenave, A., Bouffard, J., Gennero, M.C., Seyler, F., Kosuth, P., Bercher, N., 2008. Improved Jason-2 altimetry products for coastal zones and continental waters (PISTACH project). Paper presented at the Ocean Surface Topography Science Team Meeting, Nice, November 10–15.

Nielsen, K., Stenseng, L., Andersen, O.B., Villadsen, H., Knudsen, P., 2015. Validation of CryoSat-2 SAR mode based lake levels. Rem. Sens. Environ. 171, 162–170. http://dx.doi.org/10.1016/j.rse.2015.10.023.

Obligis, E., Desportes, C., Eymard, L., Fernandes, M.J., Lázaro, C., Nunes, A.L., 2011. Tropospheric corrections for coastal altimetry. In: Vignudelli, S. et al. (Eds.), Coastal Altimetry. Springer, Berlin Heidelberg, pp. 147–176. http://dx.doi.org/10.1007/978-3-642-12796-0_6.

Ophaug, V., Breili, K., Gerlach, C., 2015. A comparative assessment of coastal mean dynamic topography in Norway by geodetic and ocean approaches. J. Geophys. Res. Oceans 120 (12), 7807–7826. http://dx.doi.org/10.1002/2015JC011145.

Pugh, D., Woodworth, P.L., 2014. Sea-Level Science: Understanding Tides, Surges, Tsunamis and Mean Sea-Level Changes. Cambridge Univ. Press, Cambridge, U.K.

Revhaug, I., 2007. Outlier detection in multiple testing using Students t-test and Fisher F-test. Kart og Plan 67, 101–107.

Roblou, L., Lamouroux, J., Bouffard, J., Lyard, F., Le Hénaff, M., Lombard, A., Marsalaix, P., De Mey, P., Birol, F., 2011. Post-processing altimeter data toward coastal applications and integration into coastal models. In: Vignudelli, S. et al. (Eds.), Coastal Altimetry. Springer, Berlin Heidelberg, pp. 217–246. http://dx.doi.org/10.1007/978-3-642-12796-0_9.

Saraceno, M., Strub, P.T., Kosro, P.M., 2008. Estimates of sea surface height and near-surface alongshore coastal currents from combinations of altimeters and tide gauges. J. Geophys. Res. Oceans 113, C11013. http://dx.doi.org/10.1029/2008JC004756.

Scagliola, M., Fornari, M., 2017. Known biases in CryoSat-2 Level 1b Products. DOC: C2-TN-ARS-GS-5135, 2.1.

Scharroo, R., Leuliette, E.W., Lillibridge, J.L., Byrne, D., Naeije, M.C., Mitchum, G.T., 2013. RADS: consistent multi-mission products. In: Proc. of the Symposium on 20 Years of Progress in Radar Altimetry, ESA SP-710, ESA Publications Division, European Space Agency, Noordwijk, The Netherlands, 4 pp.

Smith, W.H.F., Scharroo, R., 2009. Mesoscale ocean dynamics observed by satellite altimeters in non-repeat orbits. Geophys. Res. Lett. 36, L06601. http://dx.doi.org/10.1029/2008GL036530.

Stenseng, L., Andersen, O.B., 2012. Preliminary gravity recovery from CryoSat-2 data in the Baffin Bay. Adv. Space Res. 50 (8), 1158–1163. http://dx.doi.org/10.1016/j.asr.2012.02.029.

Valladeau, G., Thibaut, P., Picard, B., Poisson, J.C., Tran, N., Picot, N., Guillot, A., 2015. Using SARAL/AltiKa to improve Ka-band altimeter measurements for coastal zones, hydrology and ice: the PEACHI prototype. Mar. Geod. 38, 124–142. http://dx.doi.org/10.1080/01490419.2015.1020176.

Verron, J., Sengenes, P., Lambin, J., Noubel, J., Steunou, N., Guillot, A., Picot, N., Coutin-Faye, S., Sharma, R., Gairola, R.M., Raghava Murthy, D.V.A., Richman, J.G., Griffin, D., Pascual, A., Rémy, F., Gupta, P.K., 2015. The SARAL/AltiKa altimetry satellite mission. Mar. Geod. 38, 2–21. http://dx.doi.org/10.1080/01490419.2014.1000471.

Vignudelli, S., Cipollini, P., Roblou, L., Lyard, F., Gasparini, G.P., Manzella, G., Astraldi, M., 2005. Improved satellite altimetry in coastal systems: case study of the Corsica Channel (Mediterranean Sea). Geophys. Res. Lett. 32, L07608. http://dx.doi.org/10.1029/2005GL022602.

Vignudelli, S., Kostianoy, A.G., Cipollini, P., Benveniste, J. (Eds.), 2011. Coastal Altimetry. Springer, Berlin Heidelberg. http://dx.doi.org/10.1007/978-3-642-12796-0.

Weatherall, P., Marks, K.M., Jakobsson, M., Schmitt, T., Tani, S., Arndt, J.E., Rovere, M., Chayes, D., Ferrini, V., Wigley, R., 2015. A new digital bathymetric model of the world's oceans. Earth Space Sci. 2 (8), 331–345. http://dx.doi.org/10.1002/2015EA000107.

Webb, E., Hall, A., 2016. Geophysical Corrections in Level 2 CryoSat Data Products, IDEAS-VEG-IPF-MEM-1288 Version 5.1, ESRIN, Italy.

Wingham, D.J., Francis, C.R., Baker, S., Bouzinac, C., Brockley, D., Cullen, R., de Chateau-Thierry, P., Laxon, S.W., Mallow, U., Mavrocordatos, C., Phalippou, L., Ratier, G., Rey, L., Rostan, F., Viau, P., Wallis, D.W., 2006. CryoSat: a mission to determine the fluctuations in Earth's land and marine ice fields. Adv. Space Res. 37 (4), 841–871. http://dx.doi.org/10.1016/j.asr.2005.07.027.

Woodworth, P.L., Horsburgh, K.J., 2011. Surge models as providers of improved "inverse barometer corrections" for coastal altimetry users. In: Vignudelli, S. et al. (Eds.), Coastal Altimetry. Springer, Berlin Heidelberg, pp. 177–189. http://dx.doi.org/10.1007/978-3-642-12796-0_7.

Woodworth, P.L., Hughes, C.W., Bingham, R.J., Gruber, T., 2012. Towards worldwide height system unification using ocean information. J. Geod. Sci. 2 (4), 302–318. http://dx.doi.org/10.2478/v10156-012-0004-8.

Wunsch, C., Stammer, D., 1997. Atmospheric loading and the oceanic "inverted barometer" effect. Rev. Geophys. 35 (1), 79–107. http://dx.doi.org/10.1029/96RG03037.

Paper B

AGU PUBLICATIONS

Geophysical Research Letters

RESEARCH LETTER

10.1002/2017GL073777

The coastal mean dynamic topography in Norway observed by CryoSat-2 and GOCE

Martina Idžanović[1], **Vegard Ophaug**[1], **and Ole Baltazar Andersen**[2]

[1]Faculty of Science and Technology, Norwegian University of Life Sciences (NMBU), Ås, Norway, [2]DTU Space, Technical University of Denmark, Kgs. Lyngby, Denmark

Key Points:

- CryoSat-2 delivers new data along the Norwegian coast, in areas previously not monitored by altimetry
- CryoSat-2 mean dynamic topographies agree on the 3–5 cm level with both tide-gauge geodetic and ocean mean dynamic topographies
- By comparison of geodetic and ocean mean dynamic topographies, we are able to detect errors in the coastal marine gravity field

Supporting Information:

- Supporting Information S1

Correspondence to:
M. Idžanović,
martina.idzanovic@nmbu.no

Citation:
Idžanović, M., V. Ophaug, and O. B. Andersen (2017), The coastal mean dynamic topography in Norway observed by CryoSat-2 and GOCE, *Geophys. Res. Lett.*, *44*, 5609–5617, doi:10.1002/2017GL073777.

Received 13 JAN 2017
Accepted 18 MAY 2017
Accepted article online 24 MAY 2017
Published online 11 JUN 2017

Abstract New-generation synthetic aperture radar altimetry, as implemented on CryoSat-2, observes sea surface heights in coastal areas that were previously not monitored by conventional altimetry. Therefore, CryoSat-2 is expected to improve the coastal mean dynamic topography (MDT). However, the MDT remains highly reliant on the geoid. Using new regional geoid models as well as CryoSat-2 data, we determine three geodetic coastal MDT models in Norway and validate them against independent tide-gauge observations and the operational coastal ocean model NorKyst800. The CryoSat-2 MDTs agree on the ∼3–5 cm level with both tide-gauge geodetic and ocean MDTs along the Norwegian coast. In addition, we compute geostrophic surface currents to help identifying errors in the geoid models. We find that even though the regional geoid models are all based on the latest satellite gravity data as provided by GOCE, the resulting circulation patterns differ. We demonstrate that some of these differences are due to erroneous or lack of marine gravity data. This suggests that there is significant MDT signal at spatial scales beyond GOCE, and that the geodetic approach to MDT determination benefits from the additional terrestrial gravity information provided by a regional geoid model. We also find that the border of the geographical mode mask of CryoSat-2 coincides with the Norwegian Coastal Current, making it challenging to distinguish between artifacts in the CryoSat-2 observations during mode switch and ocean signal.

1. Introduction

Although satellite altimetry is a mature technique, observing the sea surface height (SSH) globally with an accuracy of a few centimeters [*Chelton et al.*, 2001], numerous effects degrade the observations in the coastal zone [*Vignudelli et al.*, 2011]. For example, the radar footprint is contaminated by land and bright targets, and the range and geophysical corrections become difficult to model. The rugged Norwegian coast presents a further challenge, where the Norwegian Coastal Current (NCC) typically falls into a zone where conventional altimeters do not deliver reliable observations [*Ophaug et al.*, 2015].

CryoSat-2 (CS2) [*Wingham et al.*, 2006] carries a synthetic aperture interferometric radar altimeter (SIRAL) which can operate in synthetic aperture radar (SAR), interferometric SAR (SARIn), and conventional low-resolution (LR) modes. CS2 uses a geographical mode mask to decide which mode to operate in [*European Space Agency and Mullard Space Science Laboratory-University College London*, 2012]. The SAR mode improves the along-track resolution to ∼300 m through a complex Doppler processing chain. The SARIn mode has a similar resolution and also measures the phase difference of the backscattered signal at two antennas, from which the position of any backscattered point may be derived. Thus, the SARIn mode may help in discriminating and mitigating land contamination signals from off-nadir land targets (e.g., steep cliffs) [*Armitage and Davidson*, 2014] in the Norwegian coastal zone.

The geodetic dynamical ocean topography (DOT) is computed by [e.g., *Pugh and Woodworth*, 2014]

$$\mathrm{DOT} = h - N, \tag{1}$$

where h is the ellipsoidal height of sea level and N is the geoid height, all referring to the same reference ellipsoid. If we average h over a specific time period, equation (1) will give the mean dynamic topography (MDT) for that period as a difference between the mean sea surface (MSS) and the geoid. Using equation (1), the MDT has a high dependence on the geoid model.

In this work we use three state-of-the-art regional geoid models as well as CS2 data in the Norwegian coastal zone and determine coastal MDT models by equation (1). Our main goal is to validate the three CS2 MDTs against tide-gauge observations and the state-of-the-art operational coastal numerical ocean model NorKyst800.

Typically, geodesists assess the quality of regional geoid models by external validation against geometrically determined geoid heights on land, at sites observed by both Global Navigation Satellite Systems (GNSS) and leveling [*Denker*, 2013]. This approach is not ideal for assessing the regional geoid model over marine areas [*Ophaug et al.*, 2015]. Instead, we compute geostrophic surface currents from our CS2 MDTs to help identifying errors in the marine gravity field that are emphasized through the differentiation.

We compare coastal MDTs determined by the methodically different approaches of geodesy and oceanography. This work is a natural extension of such comparisons along different coasts [e.g., *Woodworth et al.*, 2012; *Higginson et al.*, 2015; *Hughes et al.*, 2015; *Lin et al.*, 2015; *Woodworth et al.*, 2015]. In particular, this work builds upon the benchmark comparison of geodetic and ocean MDTs along the Norwegian coast presented by *Ophaug et al.* [2015].

Section 2 describes the data and methods we use to determine the CS2 MDTs and validate them. The CS2 data and MDT computation is described in section 2.1. Section 2.2 presents the data used to validate the CS2 MDTs, specifically the tide-gauge geodetic MDT (section 2.2.1) and the NorKyst800 ocean MDT (section 2.2.2). In section 3 we assess the CS2 MDTs by comparing geodetic and ocean MDT profiles at tide gauges, as well as comparing flow patterns of the CS2 MDTs and NorKyst800. Finally, we discuss our results and give some concluding remarks in section 4.

2. Data and Methods

2.1. CryoSat-2 MDT

While equation (1) seems computationally simple, it is important that h and N cover the same wavelengths. Typically, when using satellite-only geoid models, h contains small-scale features that N lacks, requiring a suitable filtering of h to reduce the error of N.

In order to resolve the smallest spatial scales of the gravity field and thus reduce the filtering need, we have referenced ellipsoidal sea level to three regional geoid models, namely, the operational regional geoid model for Norway, NMA2014, as described in *Ophaug et al.* [2015], the Nordic Geodetic Commission NKG2015 model [*Ågren et al.*, 2016], and the European Gravimetric Geoid EGG2015 [*Denker*, 2016], see supporting information Table S1. All are based on fifth release data from the European Space Agency (ESA) satellite gravity mission Gravity and steady-state Ocean Circulation Explorer (GOCE) [*Drinkwater et al.*, 2003]. The geoid heights were transformed from the zero-tide system to the mean tide (MT) system using *Ekman* [1989, equation (17)]. They refer to the WGS84 ellipsoid.

CS2 operates in LR mode (LRM) over most of the Norwegian Sea, and in SAR mode in the North Sea and Skagerrak area. It switches to SARIn mode in the Norwegian coastal areas. SARIn data points are available in a zone stretching out ~40 km off the Norwegian coast (Figure 3b). Thus, we have used SSH observations obtained in all three modes in this work.

The LR and SAR mode data were obtained through the Radar Altimeter Database System (RADS) [*Scharroo et al.*, 2013a]. It contains 1 Hz values referring to the TOPEX ellipsoid and was referenced to WGS84 by considering an average difference of 0.686 m between WGS84 and TOPEX [*Ophaug et al.*, 2015]. RADS provides SAR mode observations as so-called pseudo-LRM observations; i.e., they are reduced SAR observations using an incoherent processing of the pulse-limited echoes, similar to the conventional LRM processing [*Scharroo et al.*, 2013b]. Therefore, we will refer to all RADS data as LRM data in the following.

SARIn mode observations were obtained from the ESA Grid Processing On Demand (GPOD) CryoSat-2 service [*Benveniste et al.*, 2016], which provides CS2 data in two modes, Level 1 (L1) and Level 2 (L2). The data processing is based on the L2 data set, as well as the 1 Hz L1b data set, which is retracked using the SAR Altimetry Mode Studies and Applications (SAMOSA) 2 physical retracker [*Ray et al.*, 2015]. The SARIn off-nadir range correction was applied in the processing [*Armitage and Davidson*, 2014; *Abulaitijiang et al.*, 2015]. To obtain a reliable temporal mean (see below), we let our CS2 data set cover the 2010–2015 period. This slightly translates the temporal mean epoch by a year as compared to the tide-gauge geodetic and ocean MDTs. The time difference corresponds to a negligible difference of ∼2 mm in SSH due to regional sea-level rise [*Simpson et al.*, 2015].

As opposed to the LRM data obtained from RADS, no editing or quality assessment has been performed on the SARIn data. We have considered standard range and geophysical corrections for both LRM and SARIn data sets, see supporting information Table S2 [*Cartwright and Tayler*, 1971; *Cartwright and Edden*, 1973; *Wahr*, 1985]. We first removed all observations over land, giving 21,535 data points over the ocean. Next, by visual inspection of the data set, we identified a bias in the SARIn data and removed outliers within $0\text{ m} \geq N \geq 0.6\text{ m}$. In addition, we performed a within-track outlier removal by multiple Student's *t* test (two-tailed, with $\alpha = 0.05$) [e.g., *Koch*, 1999]. This two-step outlier removal led to a ∼45% reduction in the SARIn data points.

Geoid heights from each geoid model were interpolated to the location of CS2 SSH observations, from which they were subsequently subtracted. Due to the geodetic orbit of CS2, we need to spatially average the DOT values to get a temporal mean and avoid striping effects. Therefore, all observations were combined and averaged in 20 × 20 km bins and interpolated onto a regular grid with 30-arc sec resolution, within an area delimited by $55.8092° \leq \varphi \leq 73°$ and $0° \leq \lambda \leq 34°$. The interpolation was done using least-squares collocation [*Moritz*, 1980], see supporting information Text S1 [*Forsberg and Tscherning*, 2008; *Moritz*, 1980; *Wunsch and Stammer*, 1998]. CS2 MDTs based on NKG2015, EGG2015, and NMA2014 will be referred to as $C2_{NKG}$, $C2_{EGG}$, and $C2_{NMA}$ in the following.

We have chosen to compare flow patterns in the form of geostrophic surface currents, see supporting information Text S1. Under the geostrophic assumption we look at the surface component of the flow. We are aware that the geostrophic assumption is not necessarily valid close to the coast [e.g., *Lin et al.*, 2015]. However, we determine the currents mainly to facilitate our assessment of the regional geoid models, as any error in the geoid will be emphasized through the differentiation.

2.2. Validation Data

2.2.1. Tide-Gauge MDT

We have considered a subset of 19 tide-gauges (TGs) on the Norwegian mainland in this work, see Figure 1a and supporting information Table S3. Thereby, we have omitted four TGs due to their location well inside fjords that are not sufficiently covered by altimetry data [*Ophaug et al.*, 2015]. Monthly sea-level observations for 2012–2015 were obtained from the Permanent Service for Mean Sea Level (PSMSL) [*Holgate et al.*, 2013] at http://www.psmsl.org/data/obtaining/. Local pressure observations with 10-min temporal resolution have been obtained from the database of the Norwegian Mapping Authority (NMA) (K. Breili, personal communication, 2016). As Mausund data are not yet available at PSMSL, these data were obtained from the NMA database. The pressure observations were used to correct sea level for the ocean's inverted barometer (IB) effect, following the approach of *Idžanović et al.* [2016].

The sea-level observations are given as heights *H* in the national height system, NN2000. As none of the considered TGs have been observed directly by GNSS with sufficient accuracy, we have derived ellipsoidal heights *h* of mean sea level (MSL) using the Norwegian height reference surface HREF2016A [*Solheim*, 2000], and the simple relation $h = H + \text{HREF}$, following the approach of *Ophaug et al.* [2015]. NKG2015, EGG2015, and NMA2014 were linearly interpolated to the tide-gauge sites, and by equation (1), TG_{NKG}, TG_{EGG}, and TG_{NMA} were determined, respectively.

2.2.2. NorKyst800

We have considered the operational coastal ocean model of MET Norway, NorKyst800, based on the Regional Ocean Modeling System (ROMS) [*Haidvogel et al.*, 2008]. It was obtained from http://met.no/Hav_og_is/English/Access_to_data/, where it is available in the form of daily mean values since July 2nd 2012.

NorKyst800 uses a polar stereographic grid delimited by $55.8092° \leq \varphi \leq 75.2419°$ and $-1.5651° \leq \lambda \leq 38.0339°$, at an eddy-resolving resolution of 800 m. The applied version of NorKyst800 uses atmospheric forcing by *Røed and Debernard* [2004] and additionally considers a sea ice component [*Budgell*, 2005]. It includes tidal forcing from the global TPXO model [*Egbert and Erofeeva*, 2002] and freshwater runoff from a hydrological model discharge at 256 main catchment areas.

To make our validation easier, NorKyst800 was resampled to a regular grid with 30-arc sec resolution using the NEARNEIGHBOR routine of the Generic Mapping Tools (GMT) [*Wessel et al.*, 2013]. As NorKyst800 is forced by

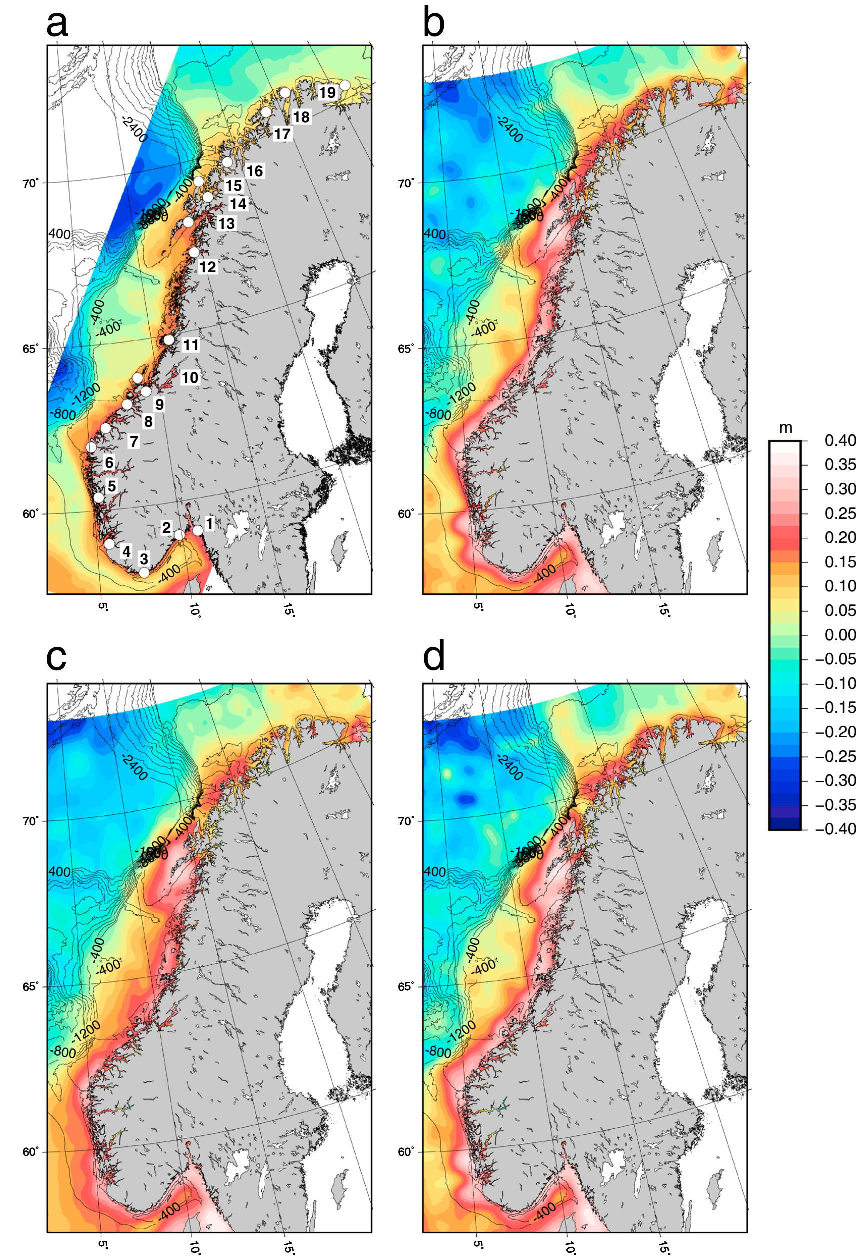

Figure 1. Coastal MDTs in Norway; (a) ocean, based on NorKyst800, and geodetic, based on (b) $C2_{NKG}$, (c) $C2_{EGG}$, and (d) $C2_{NMA}$. The mean value, given in supporting information Table S4, has been removed in all cases. The tide gauges considered in this work are shown in Figure 1a, for which a code is given in Figure 2. In all (Figures 1a–1d), 400 m isobaths from the 2014 General Bathymetric Charts of the Oceans (GEBCO) [*Weatherall et al.*, 2015] grid are shown.

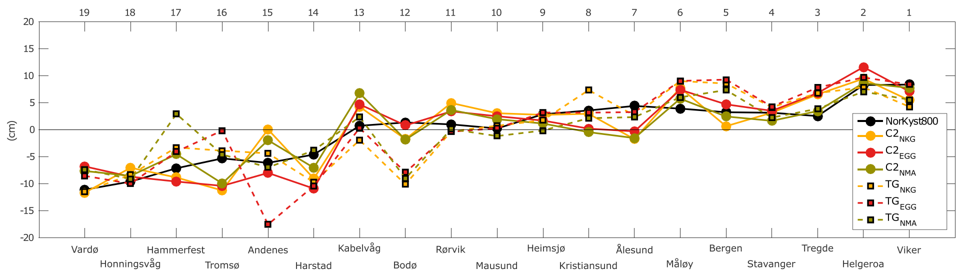

Figure 2. Tide-gauge MDT profiles using geodetic and ocean estimates, arranged and numbered from north to south, as shown in Figure 1a. For all profiles the mean value has been removed. Tide gauge (TG) names and IDs are given on the bottom and top *x* axis, respectively.

atmospheric pressure, it includes the IB effect. We corrected NorKyst800 for the IB effect by applying *Wunsch and Stammer* [1997, equation (1)] to a 0.25° × 0.25° mean sea-level pressure field for the 2012–2015 period, obtained from the European Centre for Medium-Range Weather Forecasts (ECMWF) Interim Reanalysis (ERA Interim) [*Dee et al.*, 2011].

3. Results

The CS2 MDTs (Figures 1b–1d) are generally consistent with NorKyst800 (Figure 1a), with slightly larger values in the coastal zone (up to ~40 km off the coast) and smaller values to the open ocean. The general pattern of the Norwegian Sea circulation is evident in all MDTs; we trace the Norwegian Atlantic Current (NwASC) northward and observe its branching at the Barents Sea Opening around 72°N, as well as the NCC originating in the Baltic Sea around 58°N flowing northward along the coast all the way to its final destination in the Barents Sea. In comparison with NorKyst800, $C2_{EGG}$ shows a slightly larger ~7 cm standard deviation of differences than the other two geodetic MDTs (~6 cm), see supporting information Table S4. All geodetic MDTs show areas along the coast with smaller values than expected. For example, a fall toward the coast between 65 and 70°N, as well as along the northeastern coast, is evident in all geodetic MDTs, although with slight variations. The most striking coastal feature of $C2_{EGG}$ and $C2_{NMA}$ is an MDT low seen in the area between the Lofoten-Vesterålen area and Senja island, roughly at 69°N, between 15 and 20°E. This feature is much less visible in $C2_{NKG}$.

The ocean and geodetic MDT profiles at TGs are shown in Figure 2. The coastal MDT profile obtained from NorKyst800 is smoother compared to the MDT profiles obtained from TGs and CS2. In accordance with the findings of *Ophaug et al.* [2015], we observe a 10 cm rise toward Kabelvåg, a flattening toward Stavanger, and another 10 cm rise toward Viker. We note the largest differences in the Lofoten-Vesterålen area (~10 cm). The geodetic MDTs show a large spread at Hammerfest, Andenes, and Bodø, but agree well at Honningsvåg, Mausund, Heimsjø, and Stavanger. We further observe a polarization of TG and CS2 MDTs at some TGs. At Tromsø, Rørvik, and Ålesund the TG MDTs agree more with NorKyst800 than the CS2 MDTs, while the converse holds true at Bodø and Bergen. In comparison with their respective TG MDT, $C2_{NKG}$, $C2_{EGG}$, and $C2_{NMA}$ show profile standard deviations of differences of 4.5 cm, 4.7 cm, and 3.9 cm, respectively. In comparison with NorKyst800, $C2_{NKG}$, $C2_{EGG}$, and $C2_{NMA}$ show values of 3.6 cm, 3.4 cm, and 3.2 cm, respectively. TG_{NKG}, TG_{EGG}, and TG_{NMA} show profile standard deviations of differences of 4.1 cm, 4.7 cm, and 3.9 cm to NorKyst800, respectively. We regard these numbers as promising considering previous studies of coastal MDT, which have shown an agreement between tide-gauge geodetic and ocean MDTs on the ~2–14 cm level [e.g., *Woodworth et al.*, 2012; *Higginson et al.*, 2015; *Lin et al.*, 2015; *Ophaug et al.*, 2015; *Woodworth et al.*, 2015], and between altimetric geodetic and ocean MDT on the ~5–11 cm level [e.g., *Ophaug et al.*, 2015; *Woodworth et al.*, 2015].

To facilitate the MDT diagnostics, we derived geostrophic velocity fields, see supporting information Text S1 and Figure 3. Prior to the differentiation, all MDTs were slightly filtered using a Gaussian kernel with a filter width of 12 km. The general pattern of the Norwegian Sea circulation is evident in NorKyst800, $C2_{NKG}$, and $C2_{NMA}$. We trace the NwASC northward and observe its branching at the Barents Sea Opening around 72°N, as well as the hot spots at Svinøy around 62.5°N and the Lofoten-Vesterålen area. We also see the NCC originating in the Baltic Sea around 58°N, flowing northward, splitting from the NwASC at Svinøy and connecting with it again in the Lofoten-Vesterålen area, and continuing toward the Barents Sea. The strongest and most

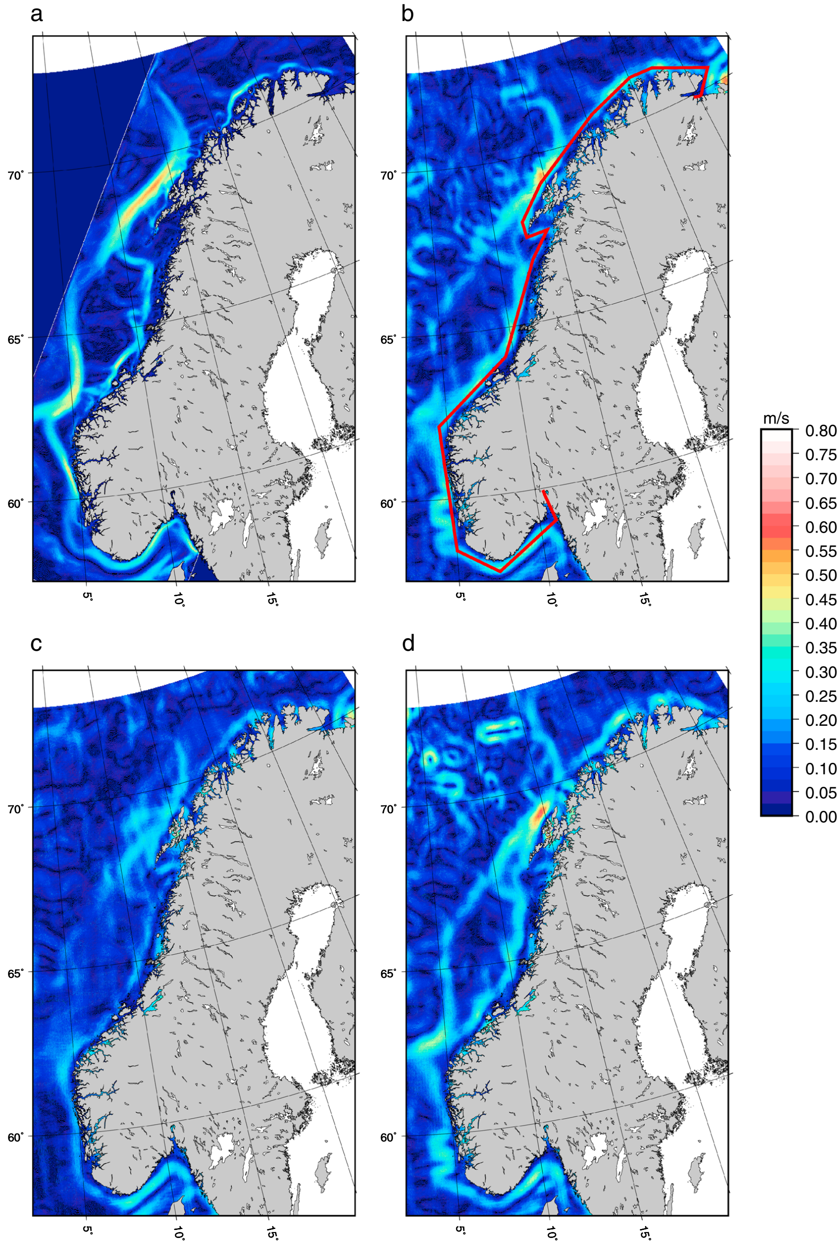

Figure 3. Geostrophic ocean surface currents derived from (a) NorKyst800, (b) $C2_{NKG}$, (c) $C2_{EGG}$, and (d) $C2_{NMA}$. The red line in Figure 3b shows the CS2 SARIn mode border, using the geographical mode mask version 3.8 [*ESA*, 2016].

well-defined currents are visible in NorKyst800, which are highly correlated with the bathymetry (compare with Figure 1a). $C2_{NMA}$ shows the strongest currents and most distinct pattern of the geodetic MDTs, followed closely by $C2_{NKG}$. $C2_{EGG}$ also shows the NCC, but the open-ocean circulation pattern is more or less absent, apart from the hot spot in the Lofoten-Vesterålen area.

By considering the geostrophic surface current patterns, we try to distinguish dynamical features that are actual ocean signal from artificial features related to errors in the marine gravity field. As noted for $C2_{EGG}$ and $C2_{NMA}$, we see the MDT lows in the area between Lofoten-Vesterålen and Senja island translate into small currents. In addition, we observe several eddy-like current features in $C2_{NMA}$ north of 70°N, between 5 and 15°E, which are much less prominent in $C2_{NKG}$, and not visible in $C2_{EGG}$. Thus, they are likely to be artificial ocean signal related to geoid errors. On the other hand, the eddy feature with a center at 69°N, 4°E is visible in all geodetic MDTs and is most prominent in $C2_{NKG}$. This feature is the so-called Lofoten Vortex, a major quasi-permanent mesoscale eddy in the Nordic Seas [*Raj et al.*, 2015]. We note two prominent current signals in $C2_{NKG}$ and $C2_{NMA}$ south of 60°N and west of 5°E which are not seen in $C2_{EGG}$ but tend to be present in NorKyst800 and therefore possibly related to actual ocean signal. Finally, the transition zone between the CS2 geographical mask modes seems to translate into a current which largely follows the path of the NCC. This effect is most prominent in $C2_{EGG}$, where the ocean signal is weaker and less visible in $C2_{NKG}$ and $C2_{NMA}$.

4. Summary and Discussion

In this work, we have shown the promising abilities of CS2 SAR(In) altimetry to recover MDT closer to the Norwegian coast than conventional altimetry, even in skerry landscapes and fjords. At tide gauges, the CS2 MDTs agree on the ∼3–5 cm level with both tide-gauge and ocean MDTs, which are determined using fundamentally different methods. We determine geostrophic surface currents to further assess the MDTs, as both ocean and artificial signals are enhanced through the differentiation. The general circulation pattern is revealed in the geodetic MDTs. However, in spite of these encouraging results, our CS2 MDTs show different artifacts related to the resolution and accuracy of the marine geoid. These variations are observed even though we have restricted ourselves to using new high-resolution gravimetric geoid models which are all based on the same satellite gravity information. This suggests that there is significant MDT signal at smaller spatial scales than those resolved by GOCE, and that the geodetic MDT can be improved by considering regional geoid models which include terrestrial gravity data.

As mentioned in section 3, Figure 2 reveals a polarization of TG and CS2 MDTs at some sites. In some cases, the TG MDTs agree more with NorKyst800 than the CS2 MDTs. As all geodetic MDTs are based on the same geoid models, this suggests that the CS2 MDTs are off due to noisy CS2 targets rather than geoid errors. Using the same argument, in case the CS2 MDTs agree more with NorKyst800 than the TG MDTs, this suggests that there could be an error in the ellipsoidal height of MSL. Our method for determining the ellipsoidal height of MSL at the tide gauges makes these values dependent on HREF accuracy, which in turn is dependent on GNSS/leveling and errors in the geoid it is based on. We continue to stress that ellipsoidal heights at tide gauges are best determined directly by GNSS, simplifying the error budget of the geodetic MDT.

The three regional geoid models in this work are mostly based on the same terrestrial gravity data. Therefore, varying data, weighting and interpolation methods used for their determination are likely to affect the observed variation in the geodetic MDTs. NKG2015 and NMA2014 are both almost completely free of altimetry-derived gravity information (and thus independent of the altimetry observations they are subtracted from). They differ in that the terrestrial gravity database has been updated for NKG2015, and a different gravity interpolation technique was used for its determination. In general, gravity data are sparse in a small coastal gap between observations on land and on the open ocean, which might affect the gravity interpolation there. The MDT low in $C2_{NMA}$ in the area between Lofoten-Vesterålen and Senja, mentioned in section 3, is likely due to a gravity data interpolation issue in the computation of NMA2014, as gravity data are sparse in this particular area (O. C. D. Omang, NMA, personal communication, 2016). This seems to have been resolved in the more recent NKG2015. Furthermore, the eddy-like current features in $C2_{NMA}$ might be linked to undetected systematics in shipborne gravity in that area, which have been addressed in NKG2015. EGG2015 differs from NKG2015 and NMA2014 in that it is heavily based on altimetry-derived gravity. Looking at Figure 3c, we note that the branching of the NwASC is less emphasized in $C2_{EGG}$, and north-south flows generally seem less distinct. The prominent current signals in $C2_{NKG}$ and $C2_{NMA}$ which are slightly correlated with the current seen in NorKyst800 are not seen in $C2_{EGG}$. This could, in part, be owing to the way gravity is derived from altimetry.

Another challenge is posed by the geographical mode mask of CS2. The SARIn mode only stretches out to roughly ∼40 km off the coast, where it blends into the LR or SAR mode. In addition, being more sparse at the border, the SARIn and LRM/SAR observations are also more uncertain in this area, as SIRAL is in the process of switching modes. Notably, in $C2_{EGG}$, the border area gives an artificial contribution to the NCC. $C2_{NKG}$ and $C2_{NMA}$ are less affected. EGG2015 has a slightly coarser resolution than NKG2015 and NMA2014 and is expected to be smoother due to the incorporation of altimetry-derived gravity. This might be a reason why the artificial signal caused by the CS2 geographical mode mask is emphasized in $C2_{EGG}$. As the CS2 geographical mask border largely coincides with the NCC, the combination of CS2 modes will always require special attention in studies of Norwegian coastal dynamics. This suggests that in the future, the SARIn mask should stretch further out from the coast than it presently does.

Finally, our CS2 MDTs are based on novel SARIn processing and data screening. Our editing of the CS2 SARIn data is crude, and only ∼55% of the raw CS2 data (omitting points on land) are used. This not only suggests that a considerable amount of valid data points did not pass the editing but also reveals that the CS2 targets along the Norwegian coast are generally noisy. Also, a large amount of CS2 observations inside fjords do not have a valid ocean tide (OT) correction, as they are outside the coverage of the standard global OT model. These observations have been disregarded in this work but could be included in the future by considering local ocean tide corrections [*Idžanović et al.*, 2016].

At this point, we would like to stress that NorKyst800 errors also form a component of our MDT error estimates. Using the simple error budgeting approach of *Ophaug et al.* [2015], which relates the empirical standard deviation of differences to the formal error propagation, we get a 2–3 cm error contribution from NorKyst800. Thus, we have used our MDT profile standard deviations and assume equal error contributions from ellipsoidal sea level, geoid model, and NorKyst800.

We have shown that by using oceanographic results, we are able to constrain the regional geoid models, and for the first time we are able to identify errors in the regional geoid models through this approach. Using the traditional external geoid validation method by comparison with GNSS/leveling, we would not be able to unveil artifacts related to systematics in old shipborne marine gravity data or marine gravity data gaps.

At the current stage our results highlight the great improvement in coastal MDT determination due to new regional geoid models and the SAR(In) altimeter on board CS2. The continued improvement of the former remains decisive for the coastal MDT. We relate the main improvement of the latter to the smaller SAR footprint, giving valid observations closer to the coast than conventional altimeters. As such, this study has implications for new-generation SAR altimetry such as the Sentinel-3 and Jason-CS/Sentinel-6 missions of ESA, European Organisation for the Exploitation of Meteorological Satellites, NASA, and NOAA.

Acknowledgments
We acknowledge the open data policy of ESA, MET Norway, PSMSL, and RADS. We would like to thank K. Breili at the Norwegian Mapping Authority for providing data and helpful comments. Figures were drafted using GMT. Data used to produce Figures 1–3 and supporting information Table S4 are available upon request. O. B. Andersen was supported by the European Space Agency's GOCE++DYCOT project. This work is part of the Norwegian University of Life Science's GOCODYN project, supported by the Norwegian Research Council under project number 231017. Finally, we would like to thank two anonymous reviewers for helpful comments that greatly improved the manuscript.

References

Abulaitijiang, A., O. B. Andersen, and L. Stenseng (2015), Coastal sea level from inland CryoSat-2 interferometric SAR altimetry, *Geophys. Res. Lett.*, *42*, 1841–1847, doi:10.1002/2015GL063131.

Ågren, J., et al. (2016), On the development of the new Nordic gravimetric geoid model NKG2015, paper presented at the IAG Symposium on Gravity, Geoid and Height Systems, Thessaloniki, Greece, 19–23 Sept.

Armitage, T. W. K., and M. W. J. Davidson (2014), Using the interferometric capabilities of the ESA CryoSat-2 mission to improve the accuracy of sea ice freeboard retrievals, *IEEE Trans. Geosci. Remote Sens.*, *52*(1), 529–536, doi:10.1109/TGRS.2013.2242082.

Benveniste, J., A. Ambrózio, M. Restano, and S. Dinardo (2016), SAR processing on demand service for CryoSat-2 and Sentinel-3 at ESA G-POD. Geophysical Research Abstracts vol. 18, EGU2016-13084 presented at 2016 EGU General Assembly, Vienna Austria, 17–22 Apr.

Budgell, W. P. (2005), Numerical simulation of ice-ocean variability in the Barents Sea region. Towards dynamical downscaling, *Ocean Dyn.*, *55*(3), 370–387, doi:10.1007/s10236-005-0008-3.

Cartwright, D. E., and A. C. Edden (1973), Corrected tables of tidal harmonics, *Geophys. J. Int.*, *33*(3), 253–264, doi:10.1111/j.1365-246X.1973.tb03420.x.

Cartwright, D. E., and R. J. Tayler (1971), New computations of the tide-generating potential, *Geophys. J. Int.*, *23*(1), 45–73, doi:10.1111/j.1365-246X.1971.tb01803.x.

Chelton, D. B., J. C. Ries, B. J. Haines, L.-L. Fu, and P. S. Callahan (2001), Chapter 1 satellite altimetry, in *Satellite Altimetry and Earth Sciences—A Handbook of Techniques and Applications*, edited by L.-L. Fu and A. Cazenave, pp. 1–131, Academic Press, San Diego, Calif., doi:10.1016/S0074-6142(01)80146-7.

Dee, D. P., et al. (2011), The ERA-Interim reanalysis: Configuration and performance of the data assimilation system, *Q. J. R. Meteorol. Soc.*, *137*, 553–597, doi:10.1002/qj.828.

Denker, H. (2013), Regional gravity field modeling: Theory and practical results, in *Sciences of Geodesy—II*, edited by G. Xu, pp. 185–291, Springer, Berlin, doi:10.1007/978-3-642-28000-9_5.

Denker, H. (2016), A new European gravimetric (quasi)geoid EGG2015, paper presented at the IAG Symposium on Gravity, Geoid and Height Systems, Thessaloniki, Greece, 19–23 Sept.

Drinkwater, M. R., R. Floberghagen, R. Haagmans, D. Muzi, and A. Popescu (2003), GOCE: ESA's first Earth Explorer Core mission, in *Earth Gravity Field from Space — From Sensors to Earth Sciences*, edited by G. Beutler et al., pp. 419–432, Springer, Netherlands. Space Sci. Ser. of ISSI., doi:10.1007/978-94-017-1333-7_36.

Egbert, G. D., and S. Y. Erofeeva (2002), Efficient inverse modeling of barotropic ocean tides, *J. Atmos. Oceanic Technol.*, *19*, 183–204, doi:10.1175/1520-0426(2002)019<0183:EIMOBO>2.0.CO;2.

Ekman, M. (1989), Impacts of geodynamic phenomena on systems for height and gravity, *Bull. Geod.*, *63*(3), 281–296, doi:10.1007/BF02520477.

European Space Agency (2016), Geographical mode mask. [Available at https://earth.esa.int/web/guest/-/geographical-mode-mask-7107, last accessed 27 April 2016.]

European Space Research Institute (ESRIN) – European Space Agency, and Mullard Space Science Laboratory – University College London (2012), CryoSat product handbook, London, U. K. [Available at: http://emits.sso.esa.int/emits-doc/ESRIN/7158/CryoSat-PHB-17apr2012.pdf, last accessed 29 May 2017.]

Forsberg, R., and C. C. Tscherning (2008), An Overview Manual for the GRAVSOFT Geodetic Gravity Field Modelling Programs, 2nd ed., Contract Report to JUPEM, Copenhagen, Denmark. [Available at: http://cct.gfy.ku.dk/publ_cct/cct1792.pdf, last accessed 29 May 2017.]

Haidvogel, D. B., et al. (2008), Ocean forecasting in terrain-following coordinates: Formulation and skill assessment of the Regional Ocean Modeling System, *J. Comput. Phys.*, *227*(7), 3595–3624, doi:10.1016/j.jcp.2007.06.016.

Higginson, S., K. R. Thompson, P. L. Woodworth, and C. W. Hughes (2015), The tilt of mean sea level along the east coast of North America, *Geophys. Res. Lett.*, *42*, 1471–1479, doi:10.1002/2015GL063186.

Holgate, S. J., A. Matthews, P. L. Woodworth, L. J. Rickards, M. E. Tamisiea, E. Bradshaw, P. R. Foden, K. M. Gordon, S. Jevrejeva, and J. Pugh (2013), New data systems and products at the Permanent Service for Mean Sea Level, *J. Coastal Res.*, *29*(3), 493–504, doi:10.2112/jcoastres-d-12-00175.1.

Hughes, C. W., R. J. Bingham, V. Roussenov, J. Williams, and P. L. Woodworth (2015), The effect of Mediterranean exchange flow on European time mean sea level, *Geophys. Res. Lett.*, *42*, 466–474, doi:10.1002/2014GL062654.

Idžanović, M., V. Ophaug, and O. B. Andersen (2016), Coastal sea level in Norway from CryoSat-2 SAR altimetry, paper presented at 2016 European Space Agency Living Planet Symposium, ESA Special Publication SP-740 on CD-ROM, Prague, Czech Republic, 9–13 May.

Koch, K.-R. (1999), *Parameter Estimation and Hypothesis Testing in Linear Models*, Springer, Berlin.

Lin, H., K. R. Thompson, J. Huang, and M. Véronneau (2015), Tilt of mean sea level along the Pacific coasts of North America and Japan, *J. Geophys. Res. Oceans*, *120*, 6815–6828, doi:10.1002/2015JC010920.

Moritz, H. (1980), *Advanced Physical Geodesy*, Herbert Wichmann, Karlsruhe, Germany.

Ophaug, V., K. Breili, and C. Gerlach (2015), A comparative assessment of coastal mean dynamic topography in Norway by geodetic and ocean approaches, *J. Geophys. Res. Oceans*, *120*, 7807–7826, doi:10.1002/2015JC011145.

Pugh, D., and P. L. Woodworth (2014), *Sea-Level Science: Understanding Tides, Surges, Tsunamis and Mean Sea-Level Changes*, Cambridge Univ. Press, Cambridge, U. K.

Raj, R. P., L. Chafik, J. E. Ø. Nilsen, T. Eldevik, and I. Halo (2015), The Lofoten vortex of the Nordic seas, *Deep Sea Res, Part I*, *96*, 1–14, doi:10.1016/j.dsr.2014.10.011.

Ray, C., C. Martin-Puig, M. P. Clarizia, G. Ruffini, S. Dinardo, C. Gommenginger, and J. Benveniste (2015), SAR altimeter backscattered waveform model, *IEEE Trans. Geosci. Remote Sens.*, *53*(2), 911–919, doi:10.1109/TGRS.2014.2330423.

Røed L. P., and J. Debernard (2004), Description of an integrated flux and sea-ice model suitable for coupling to an ocean and atmosphere model, Meteorol. No Rep. 4/2004, 56 pp., Norwegian Meteorol. Inst., Oslo, Norway.

Scharroo, R., E. W. Leuliette, J. L. Lillibridge, D. Byrne, M. C. Naeije, and G. T. Mitchum (2013a), RADS: Consistent multimission products, paper ESA SP-710 presented at Symposium on 20 Years of Progress in Radar Altimetry, ESA Special Publication, Venice, Italy, 20–28 Sep.

Scharroo, R., W. H. F. Smith, E. W. Leuliette, and J. L. Lillibridge (2013b), RADS: The performance of CryoSat as an ocean altimeter. Paper ESA SP-717 presented at 3rd CryoSat-2 User Workshop, ESA Special Publication, Dresden, Germany, 12–14 Mar.

Simpson, M. J. R., J. E. Ø. Nilsen, O. R. Ravndal, K. Breili, H. Sande, H. P. Kierulf, H. Steffen, E. Jansen, M. Carson, and O. Vestøl (2015), Sea level change for Norway: Past and present observations and projections to 2100, Norwegian Cent. for Clim. Serv. Rep. 1/2015, Norwegian Cent. for Clim. Serv., Oslo, Norway.

Solheim, D. (2000), New height reference surfaces for Norway, in *Report on the Symposium of the IAG Subcommission for Europe (EUREF) in Tromsø, 22–24 Jun.*, edited by J. A. Torres and H. Hornik, pp. 154–158, Verlag der Bayerischen Akademie der Wissenschaften, Munich, Germany.

Vignudelli, S., A. G. Kostianoy, P. Cipollini, and J. Benveniste (Eds.) (2011), Coastal altimetry,Springer, Berlin, doi:10.1007/978-3-642-12796-0.

Wahr, J. M. (1985), Deformation induced by polar motion, *J. Geophys. Res.*, *90*(B11), 9363–9368, doi:10.1029/JB090iB11p09363.

Weatherall, P., K. M. Marks, M. Jakobsson, T. Schmidt, S. Tani, J. E. Arndt, M. Rovere, D. Chayes, V. Ferrini, and R. Wigley (2015), A new digital bathymetric model of the world's oceans, *Earth Space Sci.*, *2*, 331–345, doi:10.1002/2015EA000107.

Wessel, P., W. H. F. Smith, R. Scharroo, J. Luis, and F. Wobbe (2013), Generic mapping tools: Improved version released, *Eos Trans. AGU*, *94*(45), 409–410, doi:10.1002/2013EO450001.

Wingham, D. J., et al. (2006), CryoSat: A mission to determine the fluctuations in Earth's land and marine ice fields, *Adv. Space Res.*, *37*(4), 841–871, doi:10.1016/j.asr.2005.07.027.

Woodworth, P. L., C. Hughes, R. J. Bingham, and T. Gruber (2012), Towards worldwide height system unification using ocean information, *J. Geod. Sci.*, *2*(4), 302–318, doi:10.2478/v10156-012-0004-8.

Woodworth, P. L., M. Gravelle, M. Marcos, G. Wöppelmann, and C. W. Hughes (2015), The status of measurement of the Mediterranean mean dynamic topography by geodetic techniques, *J. Geod.*, *89*(8), 811–827, doi:10.1007/s00190-015-0817-1.

Wunsch, C., and D. Stammer (1997), Atmospheric loading and the oceanic "inverted barometer" effect, *Rev. Geophys.*, *35*(1), 79–107, doi:10.1029/96RG03037.

Wunsch, C., and D. Stammer (1998), Satellite altimetry, the marine geoid, and the oceanic general circulation, *Annu. Rev. Earth Planet. Sci.*, *26*, 219–253, doi:10.1146/annurev.earth.26.1.219.

Paper C

Analysis of Glacial Isostatic Adjustment in Fennoscandia: Comparison of Model Results and Observational Evidence

Analyse des glazial-isostatischen Ausgleichs in Fennoskandien: Vergleich von Modellresultaten und Beobachtungsdaten

Martina Idžanović, Christian Gerlach

Glacial isostatic adjustment is the ongoing response of the Earth and the ocean to the melting of Pleistocene ice sheets. This unloading initiated an uplift of the crust close to the centers of former ice sheets. Today, vertical surface velocities in Fennoscandia reach values up to around 1 cm/year and are dominated by post-glacial rebound, while additional signals caused, e.g., by the elastic rebound from contemporary melting of glaciers, tectonic processes or hydrological loading contribute less.

Using ice histories from the ICE-x series (specifically ICE-5G and ICE6G_C) along with the related rheological profiles (VMx), we predict vertical velocity fields as well as time series of relative sea level change (RSL). Computations are performed with the open source sea level equation solver (SELEN) and validated against external data, namely the semi-empirical land-uplift model NKG2016LU_abs (representing present-day vertical crustal velocities) and geological RSL reconstructions. Because NKG2016LU_abs fits the actual vertical velocity field best, we also use the underlying rheological profiles as alternatives to the VMx profiles. In order to quantify the significance of some of the assumptions and approximations in SELEN, we compare our processing results with published grids of vertical velocities derived by other authors with other software solutions.

In general, all software solutions agree on a ~ 1 mm/yr level with NKG2016LU_abs in terms of standard deviations of differences. The agreement between predictions from SELEN and external data is highly dependent on the implemented ice model. We find that all vertical velocity fields as well as RSL predictions calculated with ICE6G_C show a considerably better fit to NKG2016LU_abs and RSL data than model results of ICE-5G, which confirms the improvement within the ICE-x series. For both ice models, predictions of present-day vertical velocities based on VMx rheological profiles agree better with observations (NKG2016LU_abs) than predictions based on NKG rheologies. Considering predictions of RSL between the last glacial maximum and present day, the opposite holds true. Here, predictions with NKG rheologies, on average, fit better to RSL data than predictions with VMx rheologies.

Keywords: Ice models, rheology, uplift rates, RSL, Fennoscandia

Glazial-isostatischer Ausgleich bezeichnet die laufende Reaktion der Erde und des Ozeans auf das Schmelzen der pleistozänen Eisschilde. Die damit einhergehende Entlastung der Erdkruste führt zu einer Anhebung der Oberfläche in der Nähe der früheren Eisschilderzentren. Heute erreichen die vertikalen

Oberflächengeschwindigkeiten in Fennoskandien Werte bis etwa 1 cm/Jahr, wobei der Hauptanteil auf den glazial-isostatischen Ausgleich zurückgeführt werden kann. Zusätzliche Signale, die z.B. durch tektonische Prozesse oder durch elastische Reaktionen auf zeitvariable Auflasten oder den aktuellen Rückzug heutiger Gletscher verursacht werden, liefern geringere Beiträge zur Landhebung.

Unter Verwendung von Eismodellen der ICE-x-Serie (nämlich ICE-5G und ICE6G_C) und den dazugehörigen Rheologieprofilen (VMx) werden vertikale Geschwindigkeitsfelder und Zeitreihen der relativen Meeresspiegeländerung (RSL) für Fennoskandien berechnet. Hierfür wurde die Open-Source-Software SELEN (Sea Level Equation Solver) verwendet. Ergebnisse werden gegenüber dem semi-empirischen Landhebungsmodell NKG2016LU_abs und gegenüber geologischer Küstenlinienrekonstruktionen validiert. Da das Modell NKG2016LU_abs als derzeit beste Darstellung des vertikalen Geschwindigkeitsfelds in Fennoskandien angesehen werden kann, haben wir zusätzliche Berechnungen durchgeführt, in denen das für NKG2016LU_abs verwendete Rheologieprofil als Alternative zu den VMx-Profilen genutzt wird. Um den Einfluss verschiedener Annahmen und Näherungen in SELEN zu quantifizieren, wurden die eigenen Berechnungen mit den publizierten Ergebnissen anderer Gruppen verglichen, die auf anderen Softwarelösungen beruhen.

Im Allgemeinen stimmen alle Softwarelösungen auf einem Niveau von ~ 1 mm/Jahr (Standardabweichungen der Differenzen) mit den Vertikalgeschwindigkeiten aus NKG2016LU_abs überein. Die Übereinstimmung zwischen den mit SELEN berechneten Lösungen und den externen Daten hängt stark vom implementierten Eismodell ab. Wir stellen fest, dass alle mit ICE6G_C berechneten Vertikalgeschwindigkeitsfelder sowie RSL-Prädiktionen eine wesentlich bessere Übereinstimmung mit NKG2016LU_abs und RSL-Daten zeigen als Modelle, die auf ICE-5G basieren, was die Verbesserung der Eishistorien innerhalb der ICE-x Serie bestätigt. Für beide Eismodelle zeigt sich, dass die auf den VMx-Rheologien basierenden vertikalen Geschwindigkeitsfelder besser zu den Beobachtungsdaten (NKG2016LU_abs) passen, als die auf den NKG-Rheologien basierenden. Anders verhält es sich bei den RSL-Prädiktionen, die sich auf den Zeitraum seit dem letzten glazialen Maximum beziehen. Hier schneiden Lösungen mit NKG-Rheologien im Mittel besser ab, als diejenigen mit VMx-Rheologien.

Schlüsselwörter: *Eismodelle, Rheologie, Landhebungsraten, RSL, Fennoskandien*

1 INTRODUCTION

The Earth is subject to a series of ice cycles over millions of years. Over the last several million years, each cycle lasts ~ 100 000 years (100 ka), including a long glaciation phase (~ 90 ka) and a much shorter deglaciation phase. The deglaciation phase of the current ice age started ~ 20 ka before present (BP), at the last glacial maximum (LGM), and ended ~ 8 ka BP /Tsuji et al. 2009/. Canada and the northeastern United States, Scotland, Fennoscandia, as well as Greenland and Antarctica were covered with major continental ice sheets at the LGM /Steffen & Wu 2011/, /Tsuji et al. 2009/. Ice cover forced mantle material under the ice sheets to flow from regions beneath to surrounding regions forming forebulges. Ice-sheet melting induces a reverse process, where the mantle material flows back to the former glaciated areas. The unloading starts an uplift of the crust near the centers of former ice sheets and subsidence of former bulges. Glacial Isostatic Adjustment (GIA) includes a wide range of phenomena associated with the isostatic disequilibrium induced by ice melting. GIA is related to (i) temporal changes of the Earth's gravitational field on a global and regional scale, (ii) three-dimensional (3D) displacements of the Earth's surface in the near and far field of former ice sheets, (iii) stress variations in the crust and mantle, and (iv) fluctuations of the Earth's rotational axis /Spada 2017/. Present-day climate-change related ice melting induces elastic GIA effects, while paleo-GIA effects describe the ongoing viscous response to past ice-sheet changes /Purcell et al. 2016/.

In the following, we are presenting some basic definitions and equations used in GIA modelling. Thereby, we follow the presentation and notation in /Spada 2017/, where an overview of GIA modelling is given, along with some notes on the development of theory and numerical implementation. For more details, we refer to /Spada 2017/ and references therein. The absolute sea level (SL) is given as an offset between two surfaces:

$$SL(\omega,t) = R_{SS}(\omega,t) - R_{SE}(\omega,t), \tag{1}$$

where $\omega \equiv (\theta,\lambda), \theta$ is colatitude and λ longitude, t is time, and R_{SS} and R_{SE} are radii of the equipotential sea surface (SS) and the solid surface of the Earth (SE), respectively, both relative to the Earth's center of mass.

Sea-level change S at a given time BP t_{BP} is the variation of absolute sea level SL relative to an arbitrary time t_0:

$$S(\omega,\ t_{BP}) = SL(\omega,\ t_{BP}) - SL(\omega,\ t_0). \tag{2}$$

For the present time t_P we can similarly write

$$S(\omega,\ t_P) = SL(\omega,\ t_P) - SL(\omega,\ t_0). \tag{3}$$

The relative sea level (RSL) at a given epoch t_{BP} is defined as the past sea level referred to the present-day sea level:

$$RSL(\omega,\ t_{BP}) = SL(\omega,\ t_{BP}) - SL(\omega,\ t_P). \tag{4}$$

According to Eq. (*2*) and Eq. (*3*), *RSL* in Eq. (*4*) can be directly related to the sea-level change *S* as

$$RSL(\omega,\ t_{BP}) = S(\omega,\ t_{BP}) - S(\omega,\ t_P). \tag{5}$$

In addition, using Eq. (*1*), *S* can be written as a difference between the sea-surface variation *N* and the vertical displacements of the solid Earth *U:*

$$S(\omega,\ t) = N(\omega,\ t) - U(\omega,\ t). \tag{6}$$

An approximation to the rate of vertical uplift $\dot{U}$ can be obtained by dividing the vertical displacement *U* between subsequent time steps t_i and t_{i-1} by the time increment $\Delta t = t_i - t_{i-1}$:

$$\dot{U}(\omega,t_i) = \frac{U(\omega,t_i) - U(\omega,t_{i-1})}{\Delta t}. \tag{7}$$

The rates of sea-level change $\dot{S}$ and of geoid change $\dot{N}$ can be obtained accordingly. The time increment is determined by the time increment of the employed ice-history model.

Eq. (*6*) represents the simplest form of the sea level equation (SLE) /Spada & Melini 2013/. The SLE is a linear, integral equation for modelling sea-level variations, vertical displacements of the solid Earth, and geoid variations as a response to ice-sheet melting /Spada & Stocchi 2007/. A widely used tool to solve the SLE is the pseudo-spectral approach /Mitrovica & Milne 2003/. For its numerical implementation, the temporal discretization is made by assuming that the variables vary stepwise in time while the spatial discretization is accomplished by expressing all involved variables in terms of spherical harmonic expansion up to a maximum harmonic degree /Farrell & Clark 1976/, /Spada & Stocchi 2006/. Since the SLE has an integral form, it involves an iterative solution scheme in which an initial guess of the sea-level change is refined /Mitrovica & Milne 2003/.

We use the open source sea level equation solver (SELEN) 2.9 /Spada & Stocchi 2007/ to calculate rates of vertical uplift $\dot{U}$ given in Eq. (*7*) and RSL predictions in Eq. (*5*) in Fennoscandia. SELEN solves the SLE adopting the pseudo-spectral method for a spherically layered, non-rotating Earth with an incompressible Maxwell viscoelastic rheology /Spada & Melini 2013/, assuming fixed shorelines. In contrast to SELEN, the software from /Peltier 2004/ and the CALSEA software /Lambeck et al. 2003/ take shoreline migration (the shape of shorelines changes as the sea level changes) as well as rotational feedback (time variations in global mass distribution change the direction of the Earth's rotational axis, thus affecting the equipotential sea level through changes in the centrifugal potential) into account. The discrepancy in the rotational-term calculation has an amplitude of less than 0.2 mm/yr /Purcell et al. 2016/. The difference between the SLE solution incorporating shoreline migration and solving the SLE with fixed shorelines gives a discrepancy of 0.9 mm/yr along the coast in the Gulf of Bothnia. This value was calculated using the modelled relation between gravity and height rates of change of −0.163 µGal/mm for GIA /Olsson et al. 2015, Tab. 5/ and the quantified effect in terms of gravity rates from /Olsson et al. 2012, Fig. 8/. The input parameters for each SLE solver are ice histories and rheological profiles. The ice models represent loading/unloading in time steps of 1 ka from the LGM until today, while the rheological profiles define the Earth's response to this loading/unloading.

In order to quantify the significance of differences in the various software packages, we first compare vertical velocity fields that are determined by: (i) SELEN, (ii) the software used in /Peltier 2004/, and (iii) CALSEA. Because SELEN is an open-source software, we performed all SELEN runs ourselves. This is not possible for software packages (ii) and (iii) because they are not freely available. Therefore, we used results published by the groups of Peltier and Lambeck in form of gridded maps of vertical velocities and compared those to SELEN solutions based on the same input parameters (ice model and rheology).

Secondly, we calculate rates of vertical uplift with SELEN by applying different input parameters and compare them with independent data sets, i. e., the state-of-the-art semi-empirical land-uplift model NKG2016LU_abs based on geodetic observations; we also compare RSL derived by SELEN with radiocarbon-controlled RSL data at the Fennoscandian sites from the global /Tushingham & Peltier 1992/ database.

Section 2 describes the models and data we used to determine and validate vertical uplift rates and RSL predictions. The two input parameters: ice histories and rheological profiles are described in Section 2.1. Section 2.2 presents the data used for validation, specifically the semi-empirical land-uplift model NKG2016LU_abs and the geological RSL data set. In Section 3, we compare our results with validation data sets. We discuss results and give some concluding remarks in Section 4.

2 MODELS AND DATA: ICE MODELS, RHEOLOGICAL PROFILES, AND VALIDATION DATA

2.1 Ice models and rheological profiles

Variations in ice thickness change the total amount of water stored in the ocean and, in addition, affects the solid Earth by vertical displacements of the topography, which in turn change the geoid, i. e., the sea surface. Our task is to describe the sea-level change *S* as a function of ice thickness and rheology assumed for the mantle and lithosphere.

Ice models represent ice-thickness changes as a function of position and time. In GIA, two approaches for ice modelling exist: (i) classical and (ii) thermo-mechanical. Ice models determined by the classical approach are adjusted with the SLE and the solution fits the available RSL and tide-gauge data /Steffen 2014/. These ice models strongly contain Earth model information since their determination is based on a particular initial Earth model. The initial Earth model is then iteratively refined through inversion /Steffen & Wu

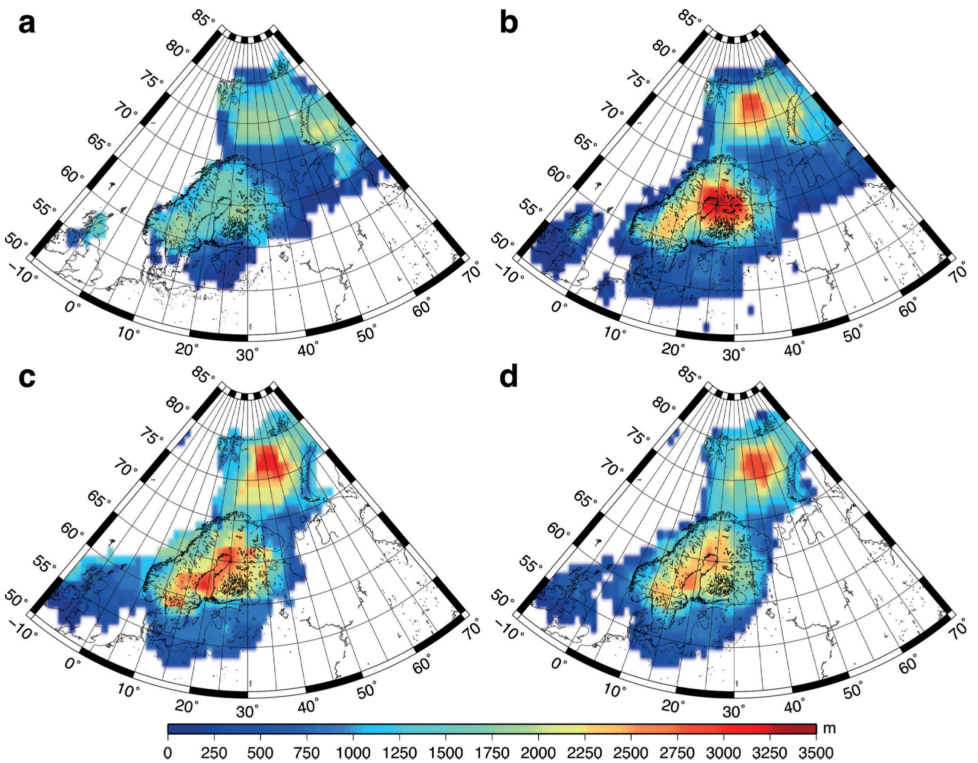

Fig. 1 | Overview of ice models given as ice thickness in meters at the LGM in Fennoscandia: (a) ICE-3G /Tushingham & Pelier 1991/ (not used in this study), (b) ICE-4G /Peltier 1994/ (not used in this study), (c) ICE-5G /Peltier 2004/, and (d) ICE6G_C /Argus et al. 2014/, /Peltier et al. 2015/

2011/. The ICE-x (ICE-3G, ICE-4G, ICE-5G, and ICE6G_C) models are classical ice models and differ in the a priori assumption of the rheological profile, the RSL data sets they were constrained by, and the approaches for solving the SLE /Spada 2017/ and references therein. In the second approach, 3D thermo-mechanically climate-forced models are tuned to ice-margin information, present-day uplift, and RSL records. In comparison to classical models, thermo--mechanical ice models contain Earth model information mainly due to topography information /Steffen 2014/.

Fig. 1 presents the ICE-x models at the LGM in Fennoscandia. ICE-4G /Peltier 1994/, ICE-5G /Peltier 2004/, and ICE6G_C /Argus et al. 2014/, /Peltier et al. 2015/ are updated versions of ICE-3G from /Tushingham & Peltier 1991/ /Steffen & Wu 2011/. ICE-5G and ICE6G_C, which were used in this study, are given on a global $1° \times 1°$ grid, describing changes in the ice thickness of major ice sheets over North America and Greenland, Fennoscandia, the Barents Sea, British Isles, and Antarctica from the LGM to present in time steps of 1 ka. In our study region Fennoscandia, the delimitation of ice-covered areas in the different ice models is similar, with smaller deviations at the ice bridge between the Scottish and Norwegian ice sheets. ICE-4G and ICE-5G have ice-sheet maxima of 3649 m and 3084 m at the LGM, respectively. ICE-3G and ICE6G_C are less thick with 1905 m and 2694 m, respectively. In all ice models except ICE-3G, the ice-sheet maxima are placed over central Sweden and the Gulf of Bothnia. For ICE-3G, the maximum is shifted to the east and located in central Finland. In comparison to older ICE-x model versions, an extensive set of geodetic data (e. g., GPS (Global Positioning Satellite) and GRACE (Gravity Recovery and Climate Experiment)) was used to constrain the ICE6G_C reconstruction /Abe-Ouchi et al. 2015/.

The widely used model for the Earth's response to loading is a spherically symmetric, radially layered Maxwell viscoelastic body, with an elastic lithosphere and a liquid core. The relaxation for this kind of body is described through viscoelastic Love numbers by solving the Laplace-transformed governing equations using an elastic structure and inverting into the time domain /Wu & Peltier 1982/. The applied rheological profiles in SELEN are employed as three-, four- or five-parameter models. The models differ in the lithospheric thickness (LT), as well as the number and viscosity values of mantle layers. The corresponding Earth's rheological structure for ICE-3G is VM1 /Tushingham & Peltier 1991/ (dark red line in *Fig. 2*), for ICE-5G VM2a /Peltier 2004/ (dashed blue line in *Fig. 2*), and for ICE6G_C VM5a /Peltier et al. 2015/, /Purcell et al. 2016/ (coral pink line in *Fig. 2*). Their lithospheric thicknesses (LTs) range between 65 and 120 km. VM1, VM2a, and VM5a have between two and four mantle layers. VM5a has a transition zone

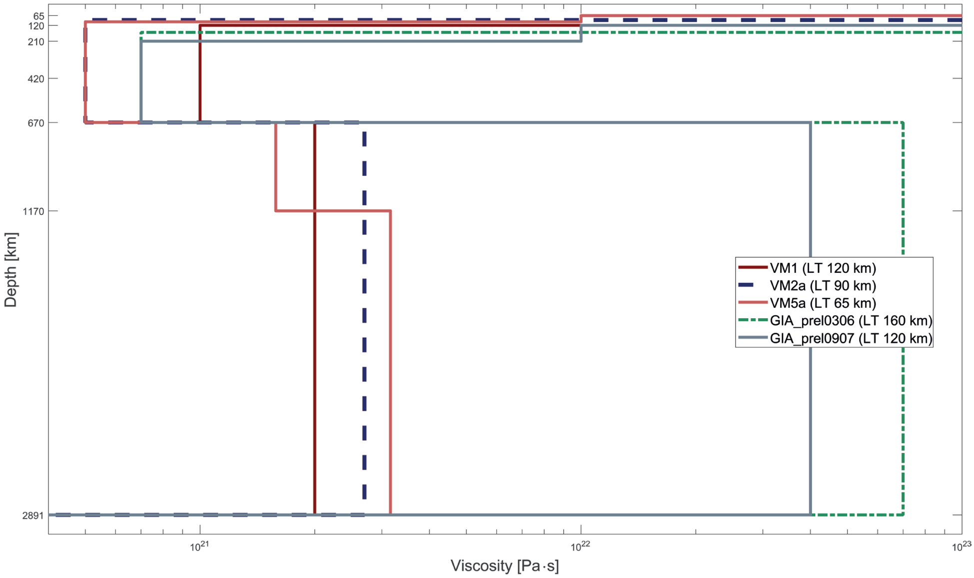

Fig. 2 | Logarithmic representation of rheological profiles used in this study: VM1 /Tushingham & Peltier 1991/, VM2a /Peltier 2004/, VM5a /Peltier et al. 2015/, /Purcell et al. 2016/, GIA_prel0306 /Vestøl et al. 2016/, and GIA_prel0907 /H. Steffen, personal communication, 2017/

defined between the upper and lower mantle, with a viscosity half of that for the lower mantle. Earth models corresponding to ICE-x ice histories are termed VMx rheological profiles in the following.

In addition to the VMx rheologies, two other rheological profiles from the Nordic Geodetic Commission (NKG) were used, namely GIA_prel0306 /Vestøl et al. 2016/ (dashed green line in *Fig. 2*) and GIA_prel0907 (H. Steffen, personal communication, 2017, gray line in *Fig. 2*), with LTs of 160 km and 120 km, respectively. GIA_prel0306 was found as the best fitting model (in central Fennoscandia) to GNSS (Global Navigation Satellite System) uplift rates and Fennoscandian RSL data /Vestøl et al. 2016/. For more details about the computation of NKG2016GIA_prel0306, see Section 2.2. VM5a and GIA_prel0907 have a thin layer (35 km thick for VM5a and 90 km for GIA_prel0907) below the lithosphere, i. e., the asthenosphere. This additional layer in GIA_prel0907 was introduced to tune a one-dimensional model towards a good fit to horizontal velocities /Vestøl et al. 2016/. The most obvious difference of the NKG rheologies compared to the VMx profiles is the much higher viscosity in the lower mantle. This, in general, results in slowing down the rebound over the whole deglaciation phase, implying higher present-day velocities. The upper-lower mantle boundary is defined at 670 km depth for all rheological profiles. For all Earth models used in this study, elastic-model parameters as well as density are volume-averaged mean values of the Preliminary reference Earth model /Dziewonski & Anderson 1981/.

2.2 Validation data

To validate vertical uplift rates and RSL predictions, we used two independent data sets. First, we compare the semi-empirical land-uplift model NKG2016LU_abs /Vestøl et al. 2016/ for the Nordic-Baltic region, based on GNSS and levelling, with calculated land-uplift rates. We use NKG2016LU_abs for validation because we assume, it is the currently best representation of present-day land uplift. Secondly, we use the database of geological RSL data from /Tushingham & Peltier 1992/ to validate our RSL predictions. We use the /Tushingham & Peltier 1992/ data set for our comparison since it is, at the moment, the only one available for the Fennoscandian area (updates, beyond the contents of the database are, to our knowledge, only available outside our study area).

NKG2016LU is a semi-empirical land-uplift model, released by NKG, which combines an empirical land-uplift model with NKG2016GIA_prel0306 by applying the remove-compute-restore technique. First, the empirical model was directly computed from BIFROST (Baseline Inferences for Fennoscandian Rebound Observations, Sea Level, and Tectonics) GNSS velocities /Kierulf et al. 2014/ and levelling by least-squares collocation (LSC). Secondly, the GIA model was removed from the empirical model in the observation points and LSC was applied to model the residual surface. Finally, the GIA model was added back to the residual-surface grid to get the final land-uplift grid. The model gives uplift rates as (i) absolute land uplift NKG2016LU_abs in ITRF2008 (*Fig. 3a*) and (ii) levelled land uplift NKG2016LU_lev relative to the geoid. The statistics of the NKG2016LU_abs signal over land points is given in *Tab. 3*. The underlying GIA model was computed applying the ICEAGE software /Kaufman 2004/, using the viscoelastic normal-mode (VNM)

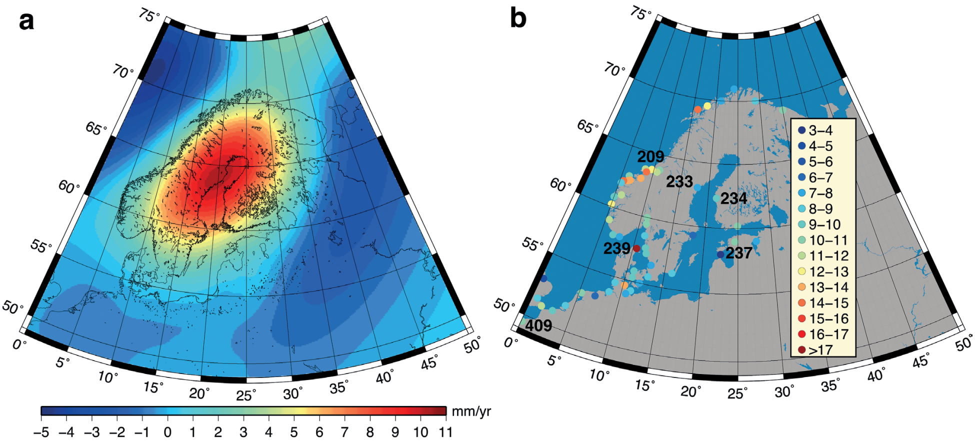

Fig. 3 | Validation data sets used in this study: (a) Absolute land-uplift model NKG2016LU_abs in ITRF2008, (b) Geological RSL sites from the /Tushingham & Peltier 1992/ database and their geographical distribution in Fennoscandia. The calibrated age BP (in ka) of the oldest available observation per RSL site is marked with a colored dot. Only RSL sites used for the comparison in Section 3.2 are numbered (*Fig. 7*). The corresponding name for each RSL site can be found in /Tushingham & Peltier 1992/.

method. The spherical-harmonic expansion was truncated at degree 192. For the rheology, the three-layered GIA_prel0306 model was used. The #71340 GLAC ice history for Fennoscandia and the Barents Sea by L. Tarasov was used in the calculation, while other parts of the world were taken from ICE-5G /Vestøl et al. 2016/. The #71340 GLAC ice history is a thermo-mechanical ice model. This type of model is dynamically more consistent than the ICE-x models because it represents the dynamic response of a real ice sheet to climate forcing. Despite the fact that thermo-mechanical models are also based on some certain rheology, there is a smaller interdependency between ice model and rheology /Schmidt et al. 2014/ than in case of ICE-x and VMx, which are iteratively tuned to fit geological and/or geodetic data using the SLE.

In the database from /Tushingham & Peltier 1992/, 392 globally non-uniformly distributed radiocarbon-controlled RSL histories are available, covering a time span of 0–15 ^{14}C ka BP. Relict shoreline deposits were identified and dated radiometrically from associated carbonate or organic material by geomorphological methods. The results are given as relative heights in meters referenced to modern mean sea level /Tushingham & Peltier 1992/, i. e., RSL. We used 55 RSL sites within an area delimited by $49° < \varphi < 75°$ and $0° < \lambda < 50°$ for our comparison (*Fig. 3b*). The RSL ages are given as ^{14}C ages and were calibrated to calendar years using the Calib 7.1 program /Stuiver & Reimer 1993/ following the approach described in /Alves et al. 2018/. We employed a regional mean reservoir correction based on 125 data points from the Marine Reservoir Database (http://calib.org/marine, with references for each value therein). The RSL sites in Fennoscandia have a varying number of observations and cover different time spans, where the oldest available RSL data reach back to ~ 17.3 ka BP.

3 COMPARISON OF MODEL RESULTS WITH EXTERNAL DATA

Validation of model results is achieved by forming differences ε between external data and model results. These differences are empirical measures for errors in the validation data as well as in the model results. Modelling errors can be further attributed to errors in ice histories and rheologies as well as to approximations of the applied software packages. Additional discrepancies may arise from non-GIA related processes, like tectonics, which contribute to observed temporal variations. Thus, we may write

$$\varepsilon = \varepsilon_{\text{NKG2016LU\_abs}} + \varepsilon_{\text{ICE}} + \varepsilon_{\text{RHEO}} + \varepsilon_{\text{SOFT}} + \varepsilon_{\text{non-GIA}}, \qquad (8)$$

where $\varepsilon_{\text{NKG2016LU\_abs}}$ represents errors of NKG2016LU_abs and depends on the accuracy of geodetic data and the underlying GIA model NKG2016GIA_prel0306, ε_{ICE} and $\varepsilon_{\text{RHEO}}$ are errors of ice models and rheological profiles. $\varepsilon_{\text{SOFT}}$ are approximations in the software, including approximations in the mathematical model and its numerical implementation, as well as temporal and spatial discretization; $\varepsilon_{\text{non-GIA}}$ are contributions of non-GIA effects. Eq. (*8*) represents the full empirical error budget.

Besides the validation with external data, we also perform comparisons of different model results. Thereby, terms of the full error budget in Eq. (*8*), which are identical in both model runs, drop out. When comparing uplift rates between different software solutions that include same input parameters (ice model and rheological profile) the error budget in Eq. (*8*) reduces to $\varepsilon_{\text{SOFT}}$, thus allowing to quantify the significance of the software component in the full error budget. Determining differences of uplift rates calculated with the same software, varying the ice model/rheology combinations, gives insight into the sensitivity of results to ice models and/or rheological profiles. These differences do, however, only reflect the level of similarity/disagreement between different models and do not give information about which model is correct.

3.1 Comparison of vertical uplift rates

We compare vertical velocity fields that were calculated applying different software packages and assumptions. The vertical velocity fields were determined using ICE-5G and ICE6G_C, and their corresponding VMx rheological profiles. Uplift rates from three different software packages are compared: software from /Peltier 2004/, SELEN /Spada & Stocchi 2007/, and CALSEA /Lambeck et al. 2003/. We calculated uplift rates applying only SELEN and did not run the /Peltier 2004/ or CALSEA software but used published grids of vertical-displacement rates. We denote the present-day radial-velocity field based on ICE-5G from /Peltier 2004/ $\dot{U}_{ICE5G}$ and the one calculated with SELEN $\dot{U}_{ICE5G\_S}$. The parameter overview for determining the vertical displacements $\dot{U}$ applying ICE-5G (VM2 or VM2a) is given in *Tab. 1*. In addition, we denote the present-day radial-velocity field based on ICE6G_C from /Peltier et al. 2015/ $\dot{U}_{ICE6G\_C}$, the CALSEA solution $\dot{U}_{ICE6G\_ANU}$, and the one calculated using SELEN $\dot{U}_{ICE6G\_S}$. Input parameters for $\dot{U}_{ICE6G\_C}$, $\dot{U}_{ICE6G\_ANU}$, and $\dot{U}_{ICE6G\_S}$ are given in *Tab. 2*.

The statistics of all uplift-rate differences between NKG2016LU_abs and modeled values was calculated over land points within an area delimited by $49° < \varphi < 73°$ and $4° < \lambda < 35°$ because only there is NKG2016LU_abs constrained by geodetic observations. *Figs. 4a – 4c* present differences between NKG2016LU_abs and uplift rates calculated with ICE6G_C. Comparing *Fig. 4a* and *Fig. 4b*, we note similar geographical structures with an offset between the velocity fields. This is also reflected in *Fig. 4d* (difference between $\dot{U}_{ICE6G\_C}$ and $\dot{U}_{ICE6G\_ANU}$) and in the corresponding statistics in *Tab. 3*. The clear correlation between the velocity fields derived by Peltier's and Lambeck's software might be related to the fact that both take some effects into account, which are neglected in SELEN. The SELEN solution (*Fig. 4c*) gives a less correlated velocity field but still reflects the main features, having a standard deviation of differences of ~ 0.6 mm/yr when compared to Lambeck's solution (*Fig. 4e*). Comparing the statistics of differences between $\dot{U}_{ICE6G\_C}$ and $\dot{U}_{ICE6G\_ANU}$ with the numbers presented in /Purcell et al. 2016/, we find a slight disagreement, which we ascribe to the selection of somewhat varying sections of the Fennoscandian area for evaluation of the statistics.

Tab. 1 shows the statistics of differences between NKG2016LU_abs and vertical uplift rates using ICE-5G (VM2/VM2a) and *Tab. 2* shows differences based on ICE6G_C (VM5a). The differences in *Tab. 1* vary between –4.2 mm/yr and 2.9 mm/yr, and in *Tab. 2* between –2.2 mm/yr and 2.6 mm/yr. Those are relatively large values, considering that the largest uplift rates in Fennoscandia are around 10 mm/yr (see

Vertical uplift rates		$\dot{U}_{ICE5G}$	$\dot{U}_{ICE5G\_S}$
Software package		/Peltier 2004/	SELEN /Spada & Stocchi 2007/
Method		pseudo-spectral	pseudo-spectral
Rheological profile		VM2	VM2a [a]
Truncation degree and order		256	256
$\Delta\varphi \times \Delta\lambda$		1° × 1°	$r = 44$ [b]
Number of iterations		–	3
Shoreline migration		Yes /Peltier 1998/	No
Paleo-topography and grounded ice		Yes	No
Rotational feedback		Yes	No
Differences to NKG2016LU_abs [c]	min	–2.18 mm/yr	–4.23 mm/yr
	max	2.94 mm/yr	0.95 mm/yr
	mean	0.14 mm/yr	–0.67 mm/yr
	std	1.15 mm/yr	0.95 mm/yr

[a] a volume-averaged version of the VM2 viscosity profile /Spada & Melini 2013/

[b] corresponds to 0.5° × 1°, see /Spada & Melini 2013/ for more details

[c] over land points within an area delimited by $49° < \varphi < 73°$ and $4° < \lambda < 35°$ where NKG2016LU observations are available

Tab. 1 | Parameter overview of calculated uplift rates $\dot{U}$ using ICE-5G (VM2/VM2a) and statistics of differences to NKG2016LU_abs

Vertical uplift rates		$\dot{U}_{ICE6G\_C}$	$\dot{U}_{ICE6G\_ANU}$	$\dot{U}_{ICE6G\_S}$
Software package		/Peltier 2004/	CALSEA (version 33) /Lambeck et al. 2003/	SELEN /Spada & Stocchi 2007/
Method		pseudo-spectral	–	pseudo-spectral
Rheological profile		VM5a	VM5a	VM5a
Truncation degree and order		512	256	256
$\Delta\varphi \times \Delta\lambda$		1° × 1°	1° × 1°	$r = 44$ [a]
Number of iterations		–	–	3
Shoreline migration		Yes /Peltier 1998/	Yes /Lambeck et al. 2003/	No
Paleo-topography and grounded ice		Yes	GEBCO_08/BEDMAP [b]	No
Rotational feedback		Yes	Yes [c]	No
Differences to NKG2016LU_abs [d]	min	–1.53 mm/yr	–2.07 mm/yr	–2.22 mm/yr
	max	2.63 mm/yr	1.97 mm/yr	2.21 mm/yr
	mean	0.21 mm/yr	–0.02 mm/yr	–0.03 mm/yr
	std	1.00 mm/yr	0.90 mm/yr	0.89 mm/yr

[a] corresponds to 0.5° × 1°, see /Spada & Melini 2013/ for more details

[b] GEBCO_08 was used north of 60° S and BEDMAP south of 60° S

[c] the applied geoid velocity corrections are /Purcell et al. 2016/: $\dot{C}_{21}^{rot} = -1{,}75 \times 10^{-9}$, $\dot{S}_{21}^{rot} = -1{,}75 \times 10^{-8}$

[d] over land points within an area delimited by by $49° < \varphi < 73°$ and $4° < \lambda < 35°$ where NKG2016LU observations are available

Tab. 2 | Parameter overview of calculated uplift rates $\dot{U}$ using ICE6G_C (VM5a) and statistics of differences to NKG2016LU_abs

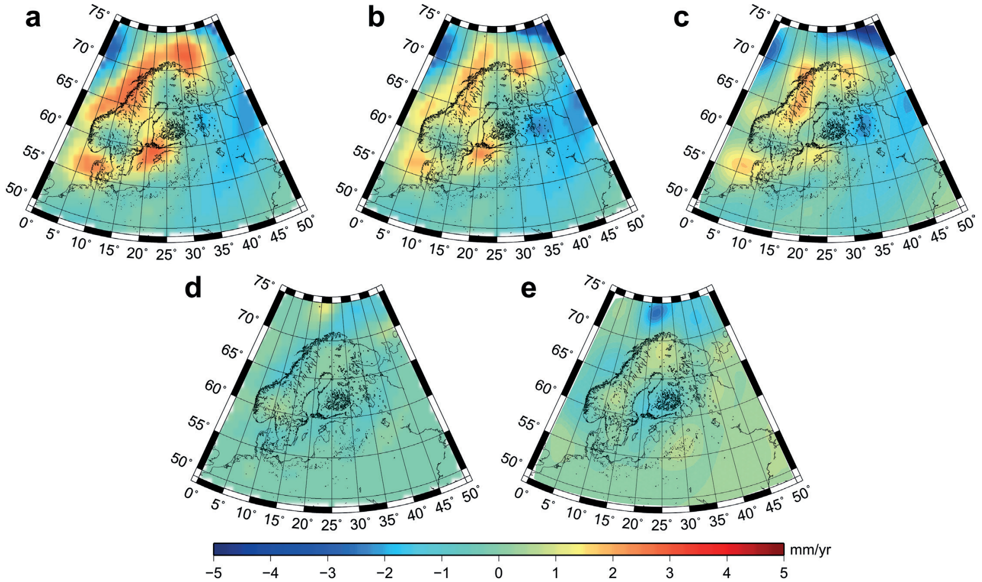

Fig. 4 | The first row shows differences between NKG2016LU_abs and (a) $\dot{U}_{ICE6G\_C}$, (b) $\dot{U}_{ICE6G\_ANU}$, and (c) $\dot{U}_{ICE6G\_S}$. The second row shows differences between software solutions: (d) $\dot{U}_{ICE6G\_C}$ and $\dot{U}_{ICE6G\_ANU}$ (difference between *Fig. 4a* and *Fig. 4b*), and (e) $\dot{U}_{ICE6G\_ANU}$ and $\dot{U}_{ICE6G\_S}$ (difference between *Fig. 4b* and *Fig. 4c*). See *Tab. 1* and *Tab. 2* for an overview of applied software and assumptions.

	min	max	mean	std
NKG2016LU_abs [a]	–1.80 mm/yr	10.29 mm/yr	2.60 mm/yr	3.47 mm/yr
$\dot{U}_{ICE5G} - \dot{U}_{ICE5G\ S}$	–4.35 mm/yr	1.34 mm/yr	–0.56 mm/yr	1.23 mm/yr
$\dot{U}_{ICE6G\ C} - \dot{U}_{ICE5G\ ANU}$	–1.63 mm/yr	1.10 mm/yr	–0.24 mm/yr	0.37 mm/yr
$\dot{U}_{ICE6G\ ANU} - \dot{U}_{ICE6G\ S}$	–2.65 mm/yr	0.84 mm/yr	–0.05 mm/yr	0.56 mm/yr

[a] over land points within an area delimited by $49° < \varphi < 73°$ and $4° < \lambda < 35°$ where NKG2016LU observations are available

Tab. 3 | Statistics of NKG2016LU_abs signal, and statistics of differences between $\dot{U}_{ICE5G}$ and $\dot{U}_{ICE5G\_S}$, $\dot{U}_{ICE6G\_C}$ and $\dot{U}_{ICE6G\_ANU}$ (*Fig. 4d*), and $\dot{U}_{ICE6G\_ANU}$ and $\dot{U}_{ICE6G\_S}$ (*Fig. 4e*)

Tab. 3). However, one must consider that the ICE-x (VMx) models are derived from a best fit towards geological and geodetic data in a global sense, while we restrict our comparison to Fennoscandia.

Based on the statistics in *Tab. 1* and *Tab. 2*, we do not observe that the less complex software (SELEN) gives the worst results in all cases. In terms of the average velocity field, Peltier's solution fits considerably better to NKG2016LU_abs than SELEN when using ICE-5G (VM2). However, using ICE6G_C (VM5a) results in the worst fit of Peltier's solution, while the ANU (Australian National University) and SELEN solutions give a much better fit. In terms of standard deviations of differences to NKG2016LU_abs, we find a slightly different picture but still no clear deficiency of SELEN compared to the more advanced software packages. Using ICE-5G (VM2) results even in a considerably smaller standard deviation for SELEN compared to Peltier's solution. For the combination ICE6G_C (VM5a), Peltier's solution shows the largest standard deviation, while the SELEN solution has the lowest value (hardly smaller than ANU's solution).

Comparison of different packages, as just shown, requires using the same combination of ice history and rheology for all solutions. In order to investigate the significance of different ice histories and rheologies, we carry out computations based on various combinations of ice history and rheology. Uplift rates derived from those combinations undergo external and internal validation. Differences between uplift rates from NKG2016LU_abs and the various SELEN solutions represent the external validation, while the internal comparison is done by choosing one SELEN solution as reference and determining differences between velocity fields of this reference and other SELEN solutions. Statistics of the external comparisons is given in *Tab. 4*, the internal one in *Tab. 5*. The corresponding geographic maps of differences are shown in *Fig. 5* (external) and *Fig. 6* (internal). Thereby, only maps based on ICE-5G are shown, because maps based on ICE6G_C show very similar geographical patterns. The VM1-based combinations are chosen as reference solutions for the internal comparisons because they fit NKG2016LU_abs best in terms of the average velocity field of both ice models (*see Tab. 4*).

Fig. 5 shows the comparison of calculated SELEN uplift rates (using ICE-5G) with NKG2016LU_abs. Similar geographical patterns for the group of vertical velocity fields calculated using VMx rheologies are notable *(Figs. 5a–5c*). The group of NKG rheological profiles (*Fig. 5d and Fig. 5e*) also results in similar patterns. In *Figs. 5a–5c*, we notice a low over Finland, while this low is more significant in *Fig. 5d* and *Fig. 5e*, and expands over the Barents and Norwegian Sea. The average velocity fields based on ICE6G_C fit better to NKG2016LU_abs than ICE-5G solutions. Comparison of

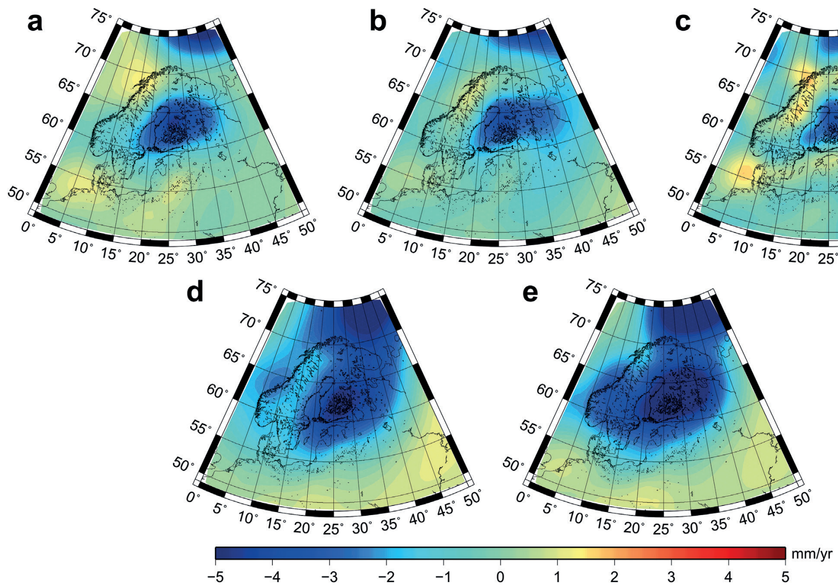

Fig. 5 | Differences between NKG2016LU_abs and (a) $\dot{U}_{I5G(VM1)}$, (b) $\dot{U}_{I5G(VM2a)}$, (c) $\dot{U}_{I5G(VM5a)}$, (d) $\dot{U}_{I5G(prel0306)}$, and (e) $\dot{U}_{I5G(prel0907)}$

NKG2016LU_abs – …[a]	Ice model	Rheology	min	max	mean	std
$\dot{U}_{I5G(VM1)}$	ICE-5G	VM1	–4.73 mm/yr	1.49 mm/yr	–0.39 mm/yr	1.28 mm/yr
$\dot{U}_{I5G(VM2a)}$		VM2a	–4.23 mm/yr	0.94 mm/yr	–0.67 mm/yr	0.95 mm/yr
$\dot{U}_{I5G(VM5a)}$		VM5a	–3.79 mm/yr	1.93 mm/yr	–0.51 mm/yr	1.07 mm/yr
$\dot{U}_{I5G(prel0306)}$		GIA_prel0306	–5.08 mm/yr	0.92 mm/yr	–1.36 mm/yr	1.69 mm/yr
$\dot{U}_{I5G(prel0907)}$		GIA_prel0907	–6.49 mm/yr	1.07 mm/yr	–1.64 mm/yr	2.15 mm/yr
$\dot{U}_{I6G(VM1)}$	ICE6G_C	VM1	–2.40 mm/yr	1.78 mm/yr	–0.04 mm/yr	0.74 mm/yr
$\dot{U}_{I6G(VM2a)}$		VM2a	–1.71 mm/yr	1.63 mm/yr	–0.14 mm/yr	0.73 mm/yr
$\dot{U}_{I6G(VM5a)}$		VM5a	–2.22 mm/yr	2.22 mm/yr	–0.04 mm/yr	0.89 mm/yr
$\dot{U}_{I6G(prel0306)}$		GIA_prel0306	–3.75 mm/yr	0.76 mm/yr	–0.87 mm/yr	1.13 mm/yr
$\dot{U}_{I6G(prel0907)}$		GIA_prel0907	–4.71 mm/yr	0.88 mm/yr	–1.15 mm/yr	1.51 mm/yr

[a] over land points within an area delimited by 49° < φ < 73° and 4° < λ < 35° where NKG2016LU observations are available

Tab. 4 | Statistics of differences over land points between NKG2016LU_abs and calculated vertical uplift rates $\dot{U}$ based on ICE-5G and ICE6G_C

the mean values *in Tab. 4* reveals an offset in the order of 0.5 mm/yr between ICE6G_C and ICE-5G solutions. This shift of the present-day mean velocity field can be ascribed to differences in total ice load between the two models (*see Fig. 1*). However, *Tab. 4* shows negative mean values for all solutions, i. e., they all have, on average, greater present-day uplift rates than NKG2016LU_abs, implying a too slow relaxation process. Considering the standard deviations of differences to NKG2016LU_abs, *Tab. 4* shows smaller values for ICE6G_C than for ICE-5G. This indicates that not only the total ice load but also the spatial distribution and the deglaciation history of ICE6G_C is more realistic than of ICE-5G.

After the comparison of different SELEN solutions with NKG2016LU_abs, we perform internal comparisons amongst the SELEN solutions. For both ice models, the combination with the VM1 rheology serves as a reference solution. *Tab. 5* shows the statistics of differences, while *Fig. 6* shows the corresponding geographic maps (again only for the ICE-5G solutions). Looking at *Fig. 6*, we observe two groups of geographical patterns: the first for VMx rheologies and the second for NKG rheological profiles. Few high peaks appear when calculating differences between VM1 and the other two VMx rheological profiles (*Fig. 6a* and *Fig. 6b*). Negative values in the ocean area occur when forming differences between VM1 and NKG rheologies that have one-magnitude higher lower-mantle viscosities than VM1 (*Fig. 6c* and *Fig. 6d*). A decreasing similarity from VM2a over VM5a and GIA_prel0306 to GIA_prel0907 with VM1 is notable for both ice models (*Tab. 5 and Fig. 6*). Except the difference to $\dot{U}_{I6G(VM2a)}$, all differences calculated with ICE6G_C show slightly smaller standard deviations of differences than the ones determined with ICE-5G. The smallest differences occur between solutions derived applying VM1 and VM2a independent from the employed

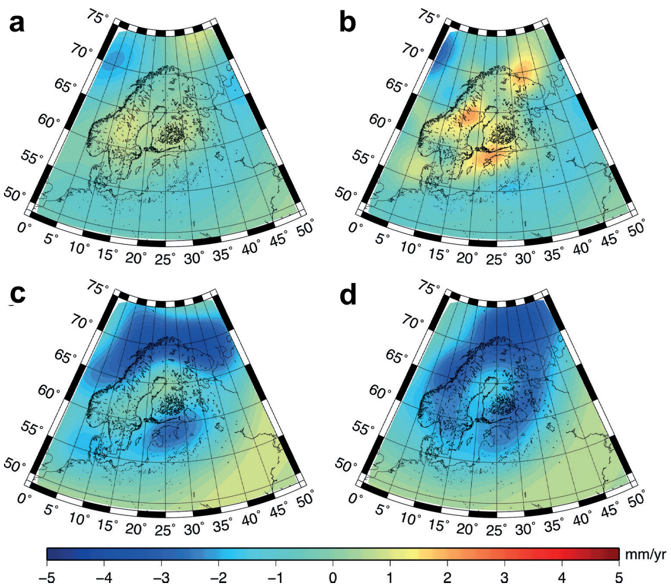

Fig. 6 | Comparison of values calculated with SELEN where ICE-5G was used. The rheology profile VM1 was chosen as a reference and differences to calculated $\dot{U}$ values based on (a) VM2a, (b) VM5a, (c) GIA_prel0306, and (d) GIA_prel0907 are shown.

ice model. Although VM1 and GIA_prel0907 both have a LT of 120 km, the difference between uplift rates calculated applying them are the most significant with largest standard deviations of differences of ~1.3 mm/yr for ICE-5G and ~1.2 mm/yr for ICE6G_C. The upper-mantle viscosities of those rheological profiles are similar but differ in the lower-mantle viscosities. Looking at the mean values of differences for both ice models in *Tab. 5*, VM2a and VM5a both differ on average ~ 0.2 mm/yr from VM1, while GIA_prel0306 and GIA_prel0907 differ ~ 0.9 mm/yr. In general, uplift rates calculated with VM1 are smaller in comparison to other uplift rates.

	Ice model	Rheology	min	max	mean	std
$\dot{U}_{I5G(VM1)} - \dots$ [a]	ICE-5G	VM1				
$\dot{U}_{I5G(VM2a)}$		VM2a	–1.72 mm/yr	0.92 mm/yr	–0.40 mm/yr	0.57 mm/yr
$\dot{U}_{I5G(VM5a)}$		VM5a	–1.59 mm/yr	2.21 mm/yr	–0.12 mm/yr	0.92 mm/yr
$\dot{U}_{I5G(prel0306)}$		GIA_prel0306	–3.82 mm/yr	0.97 mm/yr	–0.66 mm/yr	1.16 mm/yr
$\dot{U}_{I5G(prel0907)}$		GIA_prel0907	–3.77 mm/yr	0.67 mm/yr	–1.25 mm/yr	1.25 mm/yr
$\dot{U}_{I6G(VM1)} - \dots$	ICE6G_C	VM1				
$\dot{U}_{I6G(VM2a)}$		VM2a	–1.71 mm/yr	1.17 mm/yr	–0.33 mm/yr	0.62 mm/yr
$\dot{U}_{I6G(VM5a)}$		VM5a	–1.16 mm/yr	2.33 mm/yr	–0.07 mm/yr	0.83 mm/yr
$\dot{U}_{I6G(prel0306)}$		GIA_prel0306	–3.44 mm/yr	1.00 mm/yr	–0.60 mm/yr	1.09 mm/yr
$\dot{U}_{I6G(prel0907)}$		GIA_prel0907	–3.48 mm/yr	0.64 mm/yr	–1.18 mm/yr	1.21 mm/yr

[a] over land points within an area delimited by $49° < \varphi < 73°$ and $4° < \lambda < 35°$ where NKG2016LU observations are available

Tab. 5 | Statistics of differences between calculated $\dot{U}$ rates based ICE-5G and ICE6G_C. The rheology profile VM1 was chosen as a reference and differences relative to it were computed.

3.2 Comparison of relative sea level

We have computed differences between geological RSL data at 55 sites in Fennoscandia, shown in *Fig. 3b*, and RSL predictions from SELEN using different ice histories and rheologies. *Tab. 6* shows the statistics of these differences. Their values vary between –147.01 m and 89.43 m. In general, ICE6G_C solutions give a considerably better fit to RSL data than ICE-5G solutions in terms of both mean values as well as standard deviations of differences. This holds for all VMx rheologies. On average, there is a slight increase in the standard deviation of differences for NKG rheologies when using ICE6G_C instead of ICE-5G. In view of mean values and standard deviations of differences, the RSL predictions based on NKG rheologies show a better agreement to RSL data than the ones based on VMx rheologies. The smoother NKG-based RSL-prediction curves in *Fig. 7* show a slower reaction to the unloading with consequently smaller mean values that fit the RSL data better than the VMx-based predictions. A slower reaction of NKG rheologies due to larger LTs and lower-mantle viscosities means also higher present-day vertical-uplift rates, which is notable in *Fig. 5* and *Tab. 4*.

Fig. 7 shows the fit between RSL data and calculated RSL curves using ICE-5G and ICE6G_C with different rheological profiles at chosen sites (numbered sites in *Fig. 3b*). All RSL curves in *Fig. 7* show values relative to

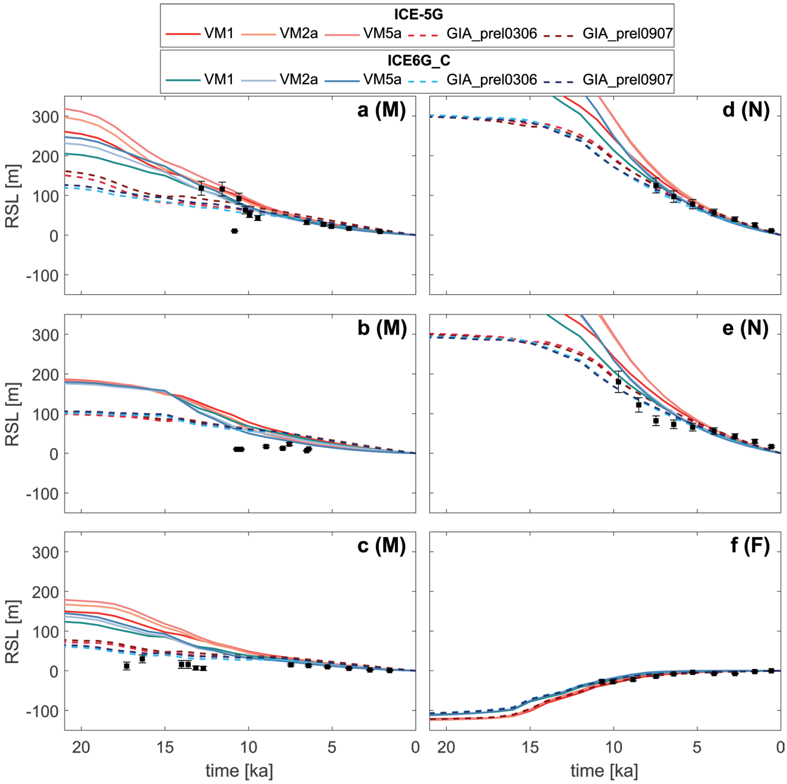

Fig. 7 | Variation of RSL curves at sites (a) 209, (b) 237, (c) 239, (d) 233, (e) 234 and (f) 409 in meters, and their comparison with geological RSL data (including RSL error bars). See *Fig. 3b* for site locations. Red nuances represent RSL curves calculated using ICE-5G, while blue-nuances RSL-curves are computed applying ICE6G_C. M, N, and F define site locations in respect to the former ice sheet: m stands for ice-sheet margin, N for near field, and F for far field.

the present-day sea-level change (Eq. (*5*)). The presented sites were chosen depending on the distance to the former ice sheet. Hence, they represent regions of ice-sheet margin (M), near field (N), and far field (F). For regions far from the former ice sheet (F), we predict that RSL was ~100 m lower at the LGM than today (*Fig. 7f*). There, melting of ice sheets caused a RSL rise, mainly due to the increasing amount of water in the oceans, accompanied by a small secondary effect from increased loading at the ocean bottom. In the ice-margin area (M), we predict a RSL fall between ~100 m to ~300 m since the LGM (*Figs. 7a–7c*). This is caused by the rebound of the crust after its unloading, which is superimposed by an absolute sea-level fall caused by depression of the equipotential surface due to mass loss. In the near field (N), we predict a RSL fall of even more than 300 m because land uplift and sea-level fall have a bigger impact than in the margin area (*Fig. 7d* and *Fig. 7e*). This general behavior is also well described in the literature, e.g., /Lambeck 1993/, /Steffen & Wu 2011/. In general, RSL-prediction curves in *Fig. 7* have larger discrepancies over the period before ~8 ka BP. The LGM ended ~8 ka BP, when almost all ice masses disappeared. In the period after that, the relaxation process is only affected by rheology. RSL-prediction curves of older periods (before 8 ka BP) reflect combined effects of ice-history variations as well as rheology, showing therefore a wider spread over those periods.

The dependence of RSL predictions on ice model and/or rheology is different in regions of far field, ice-sheet margin, and near field. The RSL predictions in the far field are not affected by rheology. The dominant parameter there is the ice model, which determines the amount of

RSL data	Ice model	Rheology	min	max	mean	std
$RSL_{I5G(VM1)}$	ICE-5G	VM1	–116.88 m	39.94 m	–11.68 m	21.11 m
$RSL_{I5G(VM2a)}$		VM2a	–136.57 m	44.29 m	–11.28 m	21.39 m
$RSL_{I5G(VM5a)}$		VM5a	–147.01 m	42.38 m	–11.78 m	22.60 m
$RSL_{I5G(prel0306)}$		GIA_prel0306	–56.66 m	83.88 m	–4.67 m	18.29 m
$RSL_{I5G(prel0907)}$		GIA_prel0907	–70.91 m	76.43 m	–7.77 m	17.98 m
$RSL_{I6G(VM1)}$	ICE6G_C	VM1	–87.42 m	59.62 m	–5.92 m	16.53 m
$RSL_{I6G(VM2a)}$		VM2a	–95.87 m	55.89 m	–5.00 m	15.94 m
$RSL_{I6G(VM5a)}$		VM5a	–102.72 m	51.45 m	–4.80 m	15.91 m
$RSL_{I6G(prel0306)}$		GIA_prel0306	–48.22 m	89.43 m	–1.83 m	18.70 m
$RSL_{I6G(prel0907)}$		GIA_prel0907	–58.02 m	79.65 m	–4.27 m	17.72 m

Tab. 6 | Statistics of differences between RSL data and predictions melted ice entering the oceans. We observe in *Fig. 7f* a slight grouping of RSL predictions according to the applied ice model and its ice-sheet distribution/thickness. RSL predictions obtained using ICE-5G (red-nuances curves) show larger RSL changes than predictions based on ICE6G_C (blue-nuances curves) due to thicker ice-sheets of ICE-5G (compare *Fig. 1c* and *Fig. 1d*). At the ice-sheet margin and in the near field area, we note two branches of RSL-prediction curves (*Figs. 7a–7e*). The first branch gathers RSL curves of VMx rheologies and the second one gathers RSL curves based on NKG rheologies. The variations of RSL-prediction curves within each branch in the ice-margin area are harder to distinguish than in the near field region. Significant differences of RSL predictions in the near field region (which is dominated by land uplift) are highly dependent on rheology. The LT, asthenosphere, and lower-mantle viscosity are affecting the behavior of RSL-prediction curves there. First, RSL curves are gathering according to the LT; a larger LT (*Fig. 2*) results in smaller RSL changes. Secondly, GIA_prel0907 that assumes an additional layer under the lithosphere shows smaller RSL predictions in comparison to GIA_prel0306, although the first has a thinner lithosphere. Finally, RSL predictions based on GIA_prel0306 and GIA_prel0907 with one-magnitude higher lower-mantle viscosities show the smallest RSL-change values. In general, the model with larger total ice masses, i.e., ICE-5G results in greater RSL changes.

4 SUMMARY AND DISCUSSION

In this work, our main interest was to quantify the sensitivity of present-day geodetic variations, i.e., vertical land uplift and RSL in Fennoscandia as a function of Earth's rheology and ice history, and to validate calculated quantities against independent observations. Input parameters for the SLE solvers were ICE-5G and ICE6G_C ice histories, and rheological profiles: VM1, VM2a, VM5a, GIA_prel0306, and GIA_prel0907. The validation of model results was accomplished by forming differences between external data and model results, where these differences represent measures for errors in the validation data as well as in model results.

First, we compare vertical velocity fields that were determined by different software packages. We calculated vertical velocity fields for ICE-5G (VM2a) and ICE6G_C (VM5a) running SELEN, while velocity-field grids determined by /Peltier 2004/ and the CALSEA software were downloaded. The software packages differ in the method for solving the SLE as well as particular approximations and assumptions. SELEN assumes a linear incompressible rheology, and solves the SLE for fixed shorelines and a non-rotating Earth. Although /Peltier 2004/ and CALSEA both consider the effects of shoreline migration and rotational feedback, the standard deviation of differences of their velocity fields is 0.4 mm/yr. Despite the fact that /Peltier 2004/ and CALSEA provide similar vertical velocity fields, comparing to NKG2016LU_abs, they show significant differences in Fennoscandia. In the external validation, NKG2016LU_abs and the software solutions for both ice models agree on average on a ~1 mm/yr level in terms of standard deviations of differences. Considering that the maximum uplift rate is ~10 mm/yr and its signal standard deviation is 3.5 mm/yr, a misfit of 1 mm/yr seems to be quite large. However, one needs to consider that the employed ice histories (ICE-x) and rheological profiles (VMx) are tuned to best fit the observational data on a global scale, which does not necessarily lead to a good fit on a regional scale.

Secondly, we compare uplift rates based on different ice models and rheologies. Calculations were preformed with SELEN and externally validated with NKG2016LU_abs. The application of both ICE-5G and ICE6G_C gives similar geographical patters. Overall, SELEN solutions assume larger present-day velocity fields than the observations in NKG2016LU_abs reflect. On average, the vertical velocity fields calculated with ICE-5G and ICE6G_C fit the observations on a ~1.2 mm/yr level in terms of standard deviations of differences. In the internal comparison of different SELEN solutions, we took the velocity field calculated applying VM1 as a reference. In general, uplift rates calculated with VM1 show smaller values than uplift rates calculated with other rheologies. The reason might be greater lower-mantle viscosities in all other rheological profiles, which cause the present-day vertical velocities to be larger since the mantle needs more time for relaxation. In addition to the comparison of uplift rates, we compare RSL predictions with geological RSL data at 55 sites in Fennoscandia. In terms of mean values of differences between RSL predictions and RSL data, NKG rheologies fit the RSL data significantly better than VMx rheologies, but in terms of standard deviations of differences, the NKG rheological profiles show just a slightly better agreement. RSL curves computed using the NKG rheological profiles are smoother in comparison to curves of VMx rheologies. The NKG rheologies have greater LT values, which reduce the flexure at the LGM and slow down the relaxation process. Looking at the agreement between RSL curves and RSL geological data at different time spans (*Fig. 7*), the RSL curves differ more over older periods (before ~8 ka BP). At ~8 ka BP, almost all ice masses are gone, which means that the relaxation process is only dependent on rheology. Older epochs show larger discrepancies between RSL predictions, reflecting the combined effects of varying ice histories and rheologies. Moreover, the curves show variations with respect to present day and thus represent an accumulation of the reversed relaxation process back in time. Thus, it is clear that all curves agree on the right-hand side of the figure (the reference epoch at present day), while the accumulation of differences in RSL predictions build up as one moves back in time to the left-hand side of the figure. RSL curves in the near field (N) show a high sensitivity to varying rheological profiles as well as to the local ice distribution. In the margin area (M), RSL curves are more sensitive to rheology, while RSL curves in the far field (F) vary only slightly due to the chosen ice model (there, the rheology has no effect).

The level of agreement with NKG2016LU_abs is highly dependent on the implemented ice model. In view of ice models, all uplift rates as well as RSL predictions calculated with ICE6G_C show a considerably better fit to NKG2016LU_abs and the RSL data than model results of ICE-5G. In the ICE6G_C reconstruction, GPS data were used to provide additional constraints, which could explain the better fit of ICE6G_C to NKG2016LU_abs. The agreement of NKG-2016GIA_prel0306 and the BIFROST GNSS stations is 0.6 mm/yr /Vestøl et al. 2016/, where a thermo-mechanical ice model was used. Implementing the ICE-x models, the fit between NKG2016LU_ abs and $\dot{U}_{I5G(prel0306)}$ is 1.7 mm/yr, and between NKG2016LU_abs and $\dot{U}_{I6G(prel0306)}$ 1.1 mm/yr. As mentioned in Section 1, the ICE-x models were built by the classical approach, meaning that based on an initial Earth model, ice model and rheology are iteratively tuned (using the SLE) to fit geological and/or geodetic data. Using this kind of ice models with various rheological profiles does not reflect a fully independent picture of the significance of rheology in our results. Therefore, the use of thermo-mechanical models, where the interdependency between the ice and Earth model is smaller, could be considered in the future.

Considering the spatial scale, we use ice models that were optimally fitted to global RSL and tide-gauge data, and look into variations at regional scales, which do not have to reflect the same behavior as global variations. Moreover, rheological profiles that fit RSL data over a time scale of thousands of years do not necessarily agree with the present-day geodetic observations. Regarding rheological profiles, vertical velocity fields calculated with VMx rheologies have a better agreement with NKG2016LU_abs than the ones calculated with NKG rheologies in terms of standard deviations of differences. The opposite holds for the agreement between RSL predictions and RSL observations, where the NKG rheologies agree slightly better. Finally, we would like to stress that the presented differences reflect the level of agreement between various model results and observations, and do not necessarily imply the correctness of a certain solution, respectively a certain input model or a model parameter, in the absolute sense.

ACKNOWLEDGMENTS

We would like to thank H. Steffen at Lantmäteriet for providing data. Maps were drawn in Generic Mapping Tools. This study is part of the Norwegian University of Life Sciences' GOCODYN project, supported by the Norwegian Research Council under project number 231017. The manuscript was considerably improved through constructive comments from an anonymous reviewer, which are gratefully acknowledged.

REFERENCES

Abe-Ouchi, A.; Saito, F.; Kageyama, M.; Braconnot, P.; Harisson, S. P.; Lambeck, K.; Otto-Bliesner, B. L.; Peltier, W. R.; Tarasov, L.; Peterschmitt, J.-Y.; Takahashi, K. (2015): Ice-sheet configuration in the CMIP5/PMIP3 Last Glacial Maximum experiments. In: Geoscientific Model Development 8(2015), 3621 – 3637. DOI: 10.5194/gmd-8-3621-2015.

Alves, E. Q.; Macario, K.; Ascough, P.; Bronk Ramsey, C. (2018): The Worldwide Marine Radiocarbon Reservoir Effect: Definitions, Mechanisms, and Prospects. In: Reviews of Geophysics 56(2018)1, 278 – 305. DOI: 10.1002/2017RG000588.

Argus, D. F.; Peltier, W. R.; Drummond, R.; Moore, A. W. (2014): The Antarctica component of postglacial rebound model ICE-6G_C (VM5a) based on GPS positioning, exposure age dating of ice thicknesses, and relative sea level histories. In: Geophysical Journal International 198(2014)1, 537 – 563. DOI: 10.1093/gji/ggu140.

Dziewonski, A. M.; Anderson, D. L. (1981): Preliminary reference Earth model. In: Physics of the Earth and Planetary Interiors 25(1981)4, 297 – 356. DOI: 10.1016/0031-9201(81)90046-7.

Farrell, W. E.; Clark, J. A. (1976): On Postglacial Sea Level. In: Geophysical Journal International 46(1976)3, 647 – 667. DOI: 10.1111/j.1365-246X.1976.tb01252.x.

Kaufman, G. (2004): Program package ICEAGE, Version 2004, Manuscript. Institut für Geophysik, Universität Göttingen, 40 pp.

Kierulf, H. P.; Steffen, H.; Simpson, M. J. R.; Lidberg, M.; Wu, P; Wang, H. (2014): A GPS velocity field for Fennoscandia and a consistent comparison to glacial isostatic adjustment models. In: Journal of Geophysical Research: Solid Earth 119(2014)8, 6613 – 6629. DOI: 10.1002/2013JB010889.

Lambeck, K. (1993): Glacial rebound and sea-level change: An example of a relationship between mantle and surface processes. In: Tectonophysics 223(1993)1-2, 15 – 37. DOI: 10.1016/0040-1951(93)90155-D.

Lambeck, K.; Purcell, A.; Johnston, P.; Nakada, M.; Yokoyama, Y. (2003): Water-load definition in the glacio-hydro-isostatic sea-level equation. In: Quaternary Science Reviews 22(2003)2-4, 309 – 318. DOI: 10.1016/S0277-3791(02)00142-7.

Mitrovica, J. X.; Milne, G. A. (2003): On post-glacial sea level: I. General theory. In: Geophysical Journal International 154(2003)2, 253 – 267. DOI: 10.1046/j.1365-246X.2003.01942.x.

Olsson, P.-A.; Ågren, J.; Scherneck, H.-G. (2012): Modelling of the GIA-induced surface gravity change over Fennoscandia. In: Journal of Geodynamics 61(2012), 12 – 22. DOI: 10.1016/j.jog.2012.06.011.

Olsson, P.-A.; Milne, G.; Scherneck, H.-G.; Ågren, J. (2015): The relation between gravity rate of change and vertical displacement in previously glaciated areas. In: Journal of Geodynamics 83(2015), 76 – 84. DOI: 10.1016/j.jog.2014.09.011.

Peltier, W. R. (1994): Ice Age Paleotopography. In: Science 265(1994)5169, 195 – 201. DOI: 10.1126/science.265.5169.195.

Peltier, W. R. (1998): "Implicit ice" in the global theory of glacial isostatic adjustment. In: Geophysical Research Letters 25(1998)21, 3955 – 3958. DOI: 10.1029/1998GL900076.

Peltier, W. R. (2004): Global Glacial Isostasy and the Surface of the Ice-Age Earth: The ICE-5G (VM2) Model and GRACE. In: Annual Review of Earth and Planetary Sciences 32(2004), 111 – 149. DOI: 10.1146/annurev.earth.32.082503.144359.

Peltier, W. R.; Argus, D. F.; Drummond, R. (2015): Space geodesy constrains ice age terminal deglaciation: The global ICE-6G_C (VM5a) model. In: Journal of Geophysical Research: Solid Earth 120(2015)1, 450 – 487. DOI: 10.1002/2014JB011176.

Purcell, A.; Tregoning, P.; Dehecq, A. (2016): An assessment of the *ICE6G_C(VM5a)* glacial isostatic adjustment model. In: Journal of Geophysical Research: Solid Earth 121(2016)5, 3939 – 3950. DOI: 10.1002/2015JB012742.

Schmidt, P.; Lund, B.; Näslund, J.-O.; Fastook, J. (2014): Comparing a thermo-mechanical Weichselian Ice Sheet reconstruction to reconstructions based on the sea level equation: aspects of ice configurations and glacial isostatic adjustment. In: Solid Earth 5(2014), 371 – 388. DOI: 10.5194/se-5-371-2014.

Spada, G. (2017): Glacial Isostatic Adjustment and Contemporary Sea Level Rise: An Overview. In: Surveys in Geophysics 38(2017)1, 153 – 185. DOI: 10.1007/s10712-016-9379-x.

Spada, G.; Melini, D. (2013): SELEN: A program for solving the "Sea-Level Equation". User Manual for version 2.9. Retrieved from https://geodynamics.org/cig/software/selen/selen-manual.pdf.

Spada, G.; Stocchi, P. (2006): The Sea Level Equation. Theory and Numerical Examples. 1st Edition. Rome, ARACNE editrice S. r. l.

Spada, G.; Stocchi, P. (2007): SELEN: A Fortran 90 program for solving the "sea-level equation". In: Computers & Geosciences 33(2007)4, 538 – 562. DOI: 10.1016/j.cageo.2006.08.006.

Steffen, H. (2014): On the accuracy of Glacial Isostatic Adjustment models with special attention to ice models. Paper presented at EUREF 2014 Symposium, June 3–7, 2014, Vilnius, Lithuania.

Steffen, H.; Wu, P. (2011): Glacial isostatic adjustment in Fennoscandia – A review of data and modeling. In: Journal of Geodynamics 52(2011)3-4, 169–204. DOI: 10.1016/j.jog.2011.03.002.

Stuiver, M.; Reimer, J. P. (1993): Extended ^{14}C Data Base and Revised CALIB 3.0 ^{14}C Age Calibration Program. In: Radiocarbon 35(1993)1, 215–230. DOI: 10.1017/S0033822200013904.

Tushingham, A. M.; Peltier, W. R. (1991): Ice-3G: A new global model of Late Pleistocene deglaciation based upon geophysical predictions of post-glacial relative sea level change. In: Journal of Geophysical Research: Solid Earth 96(1991)B3, 4497–4523. DOI: 10.1029/90JB01583.

Tushingham, A. M.; Peltier, W. R. (1992): Validation of the ICE-3G Model of Würm-Wisconsin Deglaciation using a global data base of relative sea level histories. In: Journal of Geophysical Research: Solid Earth 97(1992)B3, 3285–3304. DOI: 10.1029/91JB02176.

Tsuji, L. J. S.; Gomez, N.; Mitrovica, J. X.; Kendall, R. (2009): Post-Glacial Isostatic Adjustment and Global Warming in Subarctic Canada: Implications for Islands of the James Bay Region. In: Arctic 62(2009)4, 458–467. DOI: 10.14430/arctic176.

Vestøl, O.; Ågren, J.; Steffen, H; Kierulf, H.; Lidberg, M.; Oja, T.; Rüdja, A.; Kall, T.; Saaranen, V.; Engsager, K.; Jepsen, C.; Liepins, I.; Paršeliunas, E.; Tarasov, L. (2016): NKG2016LU, an improved postglacial land uplift model over the Nordic-Baltic region. Paper presented at the NKG Joint WG Workshop on Postglacial Land Uplift Modelling, December 1–2, 2016, Gävle, Sweden.

Wu, P.; Peltier, W. R. (1982): Viscous gravitational relaxation. In: Geophysical Journal International 70(1982)2, 435–485. DOI: 10.1111/j.1365-246X.1982.tb04976.x.

M. Sc. Martina Idžanović

NORWEGIAN UNIVERSITY OF LIFE SCIENCES
FACULTY OF SCIENCE AND TECHNOLOGY

Drøbakveien 31 | 1433 Ås, Norway
maid@nmbu.no

Dr.-Ing. Christian Gerlach

BAVARIAN ACADEMY OF SCIENCES AND HUMANITIES – RESEARCH GROUP FOR GEODESY & GLACIOLOGY

Alfons-Goppel-Str. 11 | 80539 Munich
gerlach@keg.badw.de

Manuskript eingereicht: 16.02.2018 | Im Peer-Review-Verfahren begutachtet

Paper D

remote sensing

MDPI

Article

An Attempt to Observe Vertical Land Motion along the Norwegian Coast by CryoSat-2 and Tide Gauges

Martina Idžanović [1,*], Christian Gerlach [1,2], Kristian Breili [1,3] and Ole Baltazar Andersen [4]

1 Faculty of Science and Technology, Norwegian University of Life Sciences (NMBU), P.O. Box 5003, 1432 Ås, Norway; gerlach@badw.de (C.G.); kristian.breili@kartverket.no (K.B.)
2 Geodesy and Glaciology, Bavarian Academy of Sciences and Humanities (BAdW), 80539 Munich, Germany
3 Norwegian Mapping Authority (NMA), 3507 Hønefoss, Norway
4 DTU Space, Technical University of Denmark, 2800 Kgs. Lyngby, Denmark; oa@space.dtu.dk
* Correspondence: maid@nmbu.no; Tel.: +47-672-316-04

Received: 11 February 2019; Accepted: 22 March 2019; Published: 27 March 2019

Abstract: Present-day climate-change-related ice-melting induces elastic glacial isostatic adjustment (GIA) effects, while paleo-GIA effects describe the ongoing viscous response to the melting of late-Pleistocene ice sheets. The unloading initiated an uplift of the crust close to the centers of former ice sheets. Today, vertical land motion (VLM) rates in Fennoscandia reach values up to around 10 mm/year and are dominated by GIA. Uplift signals from GIA can be computed by solving the sea-level equation (SLE), $\dot{S} = \dot{N} - \dot{U}$. All three quantities can also be determined from geodetic observations: relative sea-level variations ($\dot{S}$) are observed by means of tide gauges, while rates of absolute sea-level change ($\dot{N}$) can be observed by satellite altimetry; rates of VLM ($\dot{U}$) can be determined by GPS (Global Positioning System). Based on the SLE, $\dot{U}$ can be derived by combining sea-surface measurements from satellite altimetry and relative sea-level records from tide gauges. In the present study, we have combined 7.5 years of CryoSat-2 satellite altimetry and tide-gauge data to estimate linear VLM rates at 20 tide gauges along the Norwegian coast. Thereby, we made use of monthly averaged tide-gauge data from PSMSL (Permanent Service for Mean Sea Level) and a high-frequency tide-gauge data set with 10-min sampling rate from NMA (Norwegian Mapping Authority). To validate our VLM estimates, we have compared them with the independent semi-empirical land-uplift model NKG2016LU_abs for the Nordic-Baltic region, which is based on GPS, levelling, and geodynamical modeling. Estimated VLM rates from 1 Hz CryoSat-2 and high-frequency tide-gauge data reflect well the amplitude of coastal VLM as provided by NKG2016LU_abs. We find a coastal average of 2.4 mm/year (average over all tide gauges), while NKG2016LU_abs suggests 2.8 mm/year; the spatial correlation is 0.58.

Keywords: CryoSat-2; tide gauges; Norwegian coast; vertical land motion; land-uplift model

1. Introduction

Vertical land motion (VLM) and changing sea levels result from a complex interplay of thermal expansion of ocean water, changing ice reservoirs, glacial isostatic adjustment (GIA), tectonic motion, and anthropogenic effects [1]. VLM is a key for understanding long-term relative sea-level changes, and, in Fennoscandia, it is dominated by GIA. The present effect of GIA reaches values of up to 10 mm/year in the Gulf of Bothnia (center of former ice sheet) and decreases to nearly zero at the edges of the former ice sheet. Uplift signals from GIA can be computed by solving the sea-level equation (SLE): $\dot{S} = \dot{N} - \dot{U}$. All three quantities of the SLE can be determined directly by time-series analysis of geodetic observations. Tide-gauge records constrain the relative sea-level change ($\dot{S}$), which is the variation of the sea surface relative to the solid Earth [1]. Tide gauges are attached to the Earth's crust making their measurements affected by VLM. On the other hand, satellite altimetry and GPS

(Global Positioning System) provide independent measurements of sea-level change $\dot{N}$ and VLM $\dot{U}$, respecively, with respect to a global geocentric reference frame. Based on the SLE, the combination of sea-surface measurements from altimetry and relative sea-level records from tide gauges can be used to isolate the VLM component $\dot{U}$ [2]. This method has been applied in previous studies, using point observations or gridded sea-level anomalies from conventional altimetry (e.g., Kuo et al. [1], Nerem and Mitchum [2], Pfeffer and Allemand [3]).

Nerem and Mitchum [2] used a ∼7.5 years long time series of observations from TOPEX/POSEIDON (T/P) (with 10-days sampling interval) in combination with (daily averaged) measurements from 114 globally distributed tide gauges to compute VLM. The mean total error of the VLM estimates was 2.6 mm/year. Fenoglio-Marc et al. [4] estimated VLM from T/P (1993–2001) and de-seasoned monthly tide-gauge data at 24 tide gauges in the Mediterranean Sea, which passed predefined selection criteria. Accounting for the serial correlation, the mean uncertainty of rates was 2.3 mm/year. Kuo et al. [1] also combined T/P altimetry data from 1992 to 2001 with monthly averaged tide-gauge records at 25 sites in the Baltic Sea region. The estimated VLM rates ranged from −7.5 to 13.4 mm/year and had an average uncertainty of 4.6 mm/year. The average uncertainty of VLM rates was significantly reduced to 0.4 mm/year by applying a network adjustment algorithm. The algorithm exploited long-term (>40 years) tide-gauge records to link relative VLM between all the involved tide gauges. The application of this approach is only possible in areas with long tide-gauge records available. An improved algorithm was used by Kuo et al. [5], which presented a VLM solution for Fennoscandia, with an average uncertainty of 0.5 mm/year. Ostanciaux et al. [6] combined 16 years of T/P, Jason-1, and Jason-2 data with annual tide-gauge records at 641 globally distributed sites including 64 sites in Fennoscandia south of 66°N. At those sites, the VLM rates ranged from −12.8 to 11.3 mm/year, with an average VLM rate of 1.6 mm/year. Pfeffer and Allemand [3] combined 20 years (1992–2013) of monthly averaged sea-level anomalies from a multi-satellite altimetry grid and monthly tide-gauge observations to evaluate VLM rates. Uncertainties of VLM rates ranged from 0.3 to 7.4 mm/year, with a mean uncertainty of 0.9 mm/year. Breili et al. [7] compared sea-level rates from two sets of altimetry data (1993–2016) along the Norwegian coast with sea-level rates estimated from 19 tide-gauge records corrected for VLM. The coastal averages of the sea-level rates were within errors, indicating that no systematic errors are present in the observations nor in the applied corrections.

In this study, we explore the potential of using tide-gauge observations in combination with data from the European Space Agency (ESA) CryoSat-2 (CS2) [8] to calculate VLM rates at 20 tide gauges along the Norwegian coast. The CS2 data have several advantages we will benefit from when combining it with tide-gauge observations. First, due to the orbit configuration of CS2, areas north of 66°N are covered by observations and its 369-days repeat orbit implies dense sampling of the ocean. Furthermore, CS2 has a synthetic aperture interferometric radar altimeter (SIRAL) that can be operated in three modes: low resolution, synthetic aperture radar (SAR), and interferometric SAR (SARIn). In SAR and SARIn modes, the footprint in the along-track direction is ∼300 m, in contrast to ∼8 km in the low-resolution mode. Smaller footprints reduce the risk of data contaminated by back-scattered energy from land features in the coastal zones, and allow the sea-surface height to be sampled closer to land. As a result of this, CS2 SARIn observations are available in a zone stretching out ∼40 km off the coast [9] (see Figure 1b), opposed to conventional altimetry that provides observation points, which are on average ∼54 km from the Norwegian tide gauges [10] and need to be extrapolated towards the coast. Our results will be compared to independent VLM rates from a land-uplift model based on GPS, levelling, and geophysical modeling. We will test the existence of systematic errors in our results and investigate whether CS2 in combination with tide-gauge data is able to sample the spatial variation in VLM along the Norwegian coast. In addition to providing new estimates of VLM at Norwegian tide gauges, the present study demonstrates the coastal accuracy of CS2 data and its retracker.

Section 2 describes data and methods used to determine VLM rates. Section 2.4 presents data used to validate our VLM rates, i.e., the absolute land-uplift model for the Nordic-Baltic region

NKG2016LU_abs [11]. Comparison results are shown in Section 3. Finally, we discuss our results and give concluding remarks in Section 4.

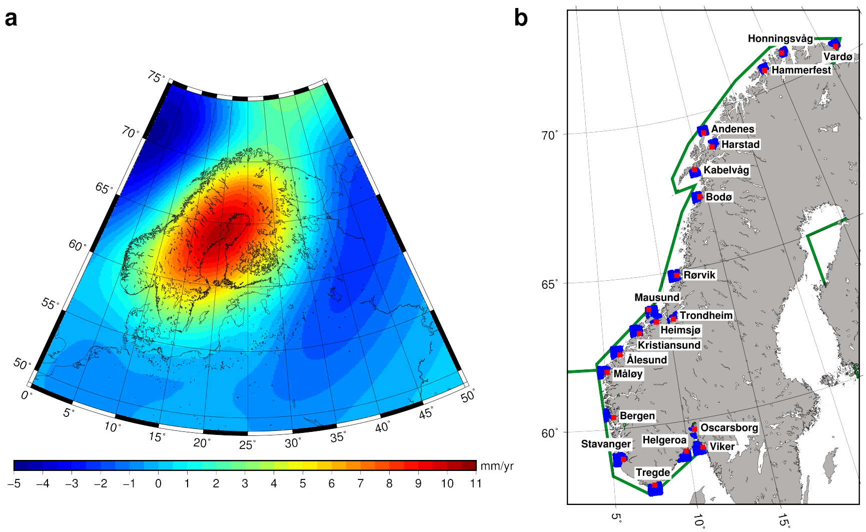

Figure 1. (**a**) The absolute land-uplift model for the Nordic-Baltic region NKG2016LU_abs [11] in ITRF2008. (**b**) Blue dots indicate available CS2 SARIn observations in 45 km × 45 km CS2 boxes around 20 Norwegian tide gauges. Red squares indicate the tide-gauge locations (see Supplementary Materials Table S1). The green line shows the CS2 SARIn-mode border, using the geographical mode mask version 3.9 [12].

2. Data and Methods

2.1. CryoSat-2 SARIn Data Processing

In this study, CS2 SARIn sea-level anomalies were obtained from the ESA Grid Processing on Demand (GPOD) service [13]. We used 1 and 20 Hz Level-2 products derived from the CS2 Level-1B products in SARIn mode for the period between July 2010 and December 2017. Three processing stages were included in the downloaded data set: reprocessing (RPRO), off-line routine operations (OFFL), and long-term archive (LTA). The SAR Altimetry Mode Studies and Applications (SAMOSA) 2 physical retracker [14] was applied as well as the SARIn off-nadir range correction [15,16]. The downloaded CS2 sea-level anomalies were computed with respect to the DTU15 mean sea surface (MSS) [17], and corrected for dry and wet tropospheric refraction, ionospheric delay computed from the global ionospheric model [18], ocean tides provided by the FES2004 model [19], long-period ocean tides, ocean-tide loading, solid Earth tides, pole tides, and dynamic atmosphere correction (DAC). The DAC consisted of a high-frequency part that is provided by MOG2D [20] and a low-frequency part, inverted barometer (IB), provided by the European Centre for Medium-Range Weather Forecasts (ECMWF) [21]. The sea state bias correction was not available.

No a priori data editing or quality assessment has been applied to the downloaded SARIn data. Therefore, we first removed all observations over land applying a land mask. Secondly, observations flagged as contaminated echoes or unclear ocean signals were rejected. The LTA data covered a time span between July 2010 and February 2015, OFFL from May 2012 until December 2017, and RPRO from July 2010 to January 2012. For the period before August 2013, there were some LTA observations that had epochs identical to observation epochs in the RPRO and OFFL data sets. Mean sea-level anomaly (SLA) differences for the overlapping time stamps were less than 0.2 cm. To avoid epochs with duplicated observations, we eliminated LTA observations for these time stamps.

Next, we rejected all |SLA| > 1 m. To identify and eliminate outliers, we used the same approach as outlined in Idžanović et al. [22]. With this method, the multiple Student's *t* test [23] was applied to the sea-level anomalies in each individual satellite pass. In the last step, we established 45 km × 45 km boxes around each tide gauge containing CS2 observations and formed "CS2 tide gauges", see Figures 1b and 2. The positions and dimension of the CS2 boxes are equivalent to those defined in Idžanović et al. [22]. Using the 20 Hz CS2 data, we have significantly more CS2 observations available in our CS2 boxes (see Table 1), and can gain a few kilometers towards the tide gauges. Therefore, we used both 1 and 20 Hz data to determine VLM rates.

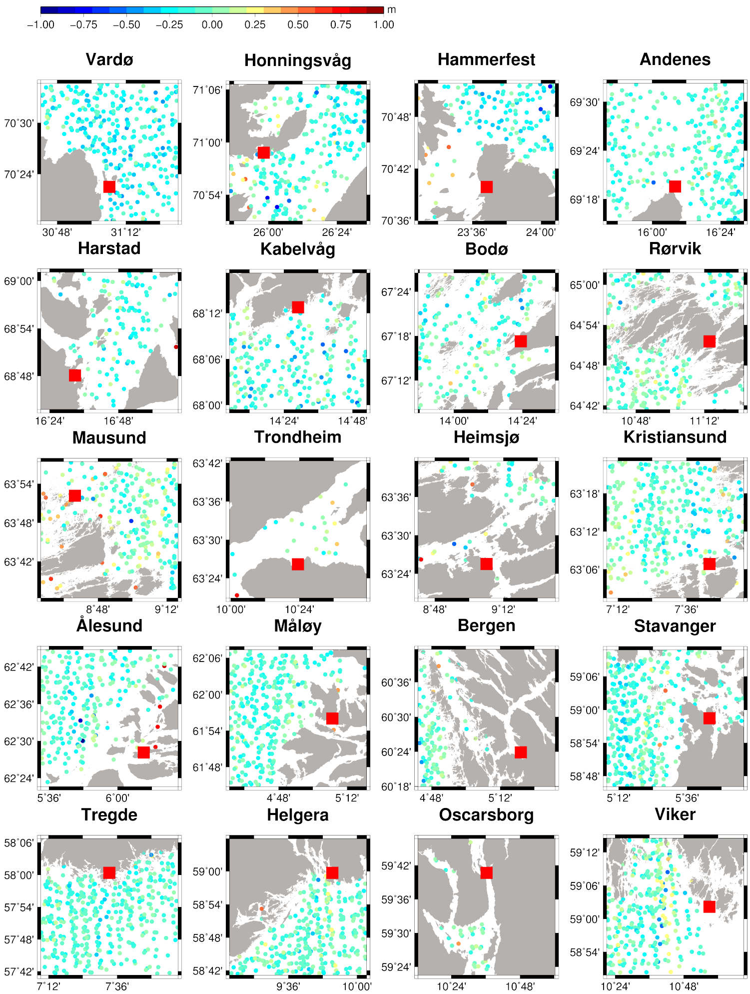

Figure 2. 1 Hz CS2 SARIn sea-level anomalies around 20 Norwegian tide gauges in 45 km × 45 km CS2 boxes. Red squares indicate the tide-gauge locations.

2.2. Tide-Gauge Data

There are in total 23 tide gauges along the Norwegian coast. The tide gauges in Tromsø, Narvik, and Oslo are located inside fjords and do not have enough CS2 observations available for trend computations. Thus, we used a subset of 20 tide gauges to estimate VLM rates (see Figure 1b and Supplementary Materials Table S1). Two tide-gauge data sets were used in this study: (i) monthly averaged sea-level observations obtained from the Permanent Service for Mean Sea Level (PSMSL) [24] at http://www.psmsl.org/data/obtaining/ and (ii) 10-min sea-level observations obtained from the database of the Norwegian Mapping Authority (NMA). Both data sets cover the same period as the CS2 observations, i.e., from 2010 to 2018. The NMA tide-gauge data are given as observed water levels referred to tide-gauge zero. To each tide-gauge record from NMA, ocean-tide (OT) corrections were applied. These corrections were estimated in a harmonic analysis of several years of water-level observations from the current tide gauge. OT corrections were not applied to PSMSL observations since the strongest tidal constituents will be close to zero in monthly averages of tide-gauge observations [3,4]. The IB corrections were applied to neither PSMSL nor NMA tide-gauge records. At the tide gauge in Mausund, monthly sea-level observations are not available in the archives of PSMSL. Thus, monthly averages were computed from the NMA record with 10-min sampling interval instead. For consistency between altimetry and tide-gauge data sets, the DAC correction provided by GPOD was added back to the sea-level anomalies, meaning that the CS2 observations were not corrected for DAC [1].

2.3. Rates of Vertical Land Motion

The PSMSL and NMA tide-gauge data were interpolated using nearest-neighbor interpolation onto 1 and 20 Hz time stamps of CS2 SARIn observations. VLM rates and standard deviations of residuals, s_e, were then computed by fitting a linear regression model to the differences. To account for serial correlation in the time series, final rate uncertainties (σ) were estimated by:

$$\sigma = s_e \sqrt{\frac{1+r^1}{1-r^1}}, \tag{1}$$

where r^1 is the lag-1 autocorrelation coefficient computed from the residuals of the regression [25]. In the following, $\mathrm{VLM}_{1\mathrm{HzPSMSL}}$ and $\mathrm{VLM}_{1\mathrm{HzNMA}}$ refer to VLM rates estimated from tide-gauge observations from PSMSL and NMA, respectively, and 1 Hz CS2 data. Similarly, $\mathrm{VLM}_{20\mathrm{HzPSMSL}}$ and $\mathrm{VLM}_{20\mathrm{HzNMA}}$ are calculated from 20 Hz CS2 observations.

2.4. Validation Data

We used the absolute land-uplift model NKG2016LU_abs [11] for the Nordic-Baltic region to validate our calculated VLM rates. NKG2016LU_abs is a semi-empirical land-uplift model, which combines an empirical land-uplift model with a GIA model. The empirical model is based on BIFROST (Baseline Inferences for Fennoscandian Rebound Observations, Sea Level, and Tectonics) GPS velocities [26] and levelling, and does not include sea-level data. In the first step, estimates of vertical velocities were derived from GPS and levelling at the corresponding observation sites over land. In the next step, residuals with respect to vertical velocities derived from a GIA model were formed. These residuals were filtered and gridded by least-squares collocation, thus reducing the noise of the geodetic observations. In the final step, velocities of the GIA model were restored, yielding a smooth gridded surface representation of present-day VLM. The underlying GIA model, NKG2016GIA_prel0306, was computed applying the ICEAGE software [27]. This model uses a three-layered rheology and a thermo-mechanical ice history for Fennoscandia and the Barents Sea compiled by L. Tarasov [11]. The uncertainty of the VLM rates from NKG2016LU_abs was calculated to 0.6 mm/year by Olsson et al. [28], taking into account internal uncertainty (0.2 mm/year), as well as drift in the ITRF2008 reference frame's origin (0.5 mm/year) and scale (0.3 mm/year). Notice that the land-uplift model provides both (i) absolute land-uplift rates in ITRF2008 (NKG2016LU_abs, Figure 1a) and (ii) levelled land-uplift rates relative to the geoid (NKG2016LU_lev). In the following, when referring in the text to the NKG uplift model, the absolute land-uplift model NKG2016LU_abs is meant.

3. Results

Table 1 gives an overview of the amount of available 1 and 20 Hz CS2 SARIn observations within CS2 boxes as well as the mean difference and mean correlation between CS2 and tide-gauge time series computed over 20 Norwegian tide gauges. Generally, both 1 and 20 Hz CS2 time series agree well with the NMA tide-gauge time series. Averaged over all tide gauges, the 1 Hz CS2 time series show a standard deviation of differences and correlation of 11.9 cm and 0.82, respectively. The 20 Hz CS2 time series show a standard deviation of 12.1 cm and a correlation of 0.77. The agreement between 1 and 20 Hz CS2 time series with PSMSL is poorer. The 1 Hz CS2 time series show a standard deviation of 17.5 cm and a correlation of 0.53, while the 20 Hz time series show a standard deviation and correlation of 16.7 cm and 0.50, respectively. Hence, the tide-gauge time series from both NMA and PSMSL agree better with 1 Hz CS2 time series than with 20 Hz time series in terms of mean correlations.

Linear rates as well as associated uncertainties of VLM from the NKG uplift model and CS2 combined with tide-gauge records over the period 2010–2018 are illustrated in Figure 3. The upper and lower panels show VLM rates based on 1 and 20 Hz CS2 time series, respectively. The NKG land-uplift model shows positive rates (from 1.3 mm/year at Måløy to 4.7 mm/year at Trondheim) for all 20 tide gauges. This is also confirmed by the majority of our estimated VLM rates. The rate uncertainties calculated by Equation (1) take into account serial correlations of measurements. The uncertainties range from 3.1 to 27.1 mm/year when using 1 Hz CS2 sea-level anomalies and from 1.1 to 18.5 mm/year when using 20 Hz CS2 data. Largest uncertainties occur at tide gauges with few CS2 observations available, i.e., at Trondheim, Heimsjø, Oscarsborg, and Hammerfest (see Figure 2).

Table 2 lists key numbers from the comparison between our VLM estimates and rates from the NKG uplift model. VLM rates based on both 1 and 20 Hz CS2 data in combination with NMA tide-gauge measurements (VLM_{1HzNMA} and $VLM_{20HzNMA}$) agree with the NKG uplift model within uncertainties for most of the sites. Their differences range from −13.9 to 8.1 mm/year. When using PSMSL tide-gauge data for the VLM estimation ($VLM_{1HzPSMSL}$ and $VLM_{20HzPSMSL}$), differences range between −23.2 and 16.3 mm/year. The standard deviations of differences between the NKG uplift model and rates of VLM based on PSMSL tide-gauge records are twice as large as the standard deviations of differences between the land-uplift model and rates from NMA tide-gauge data.

The last two columns of Table 2 list coastal averages of VLM and uncertainties defined in Equation (1), where both quantities represent values averaged over tide gauges. We notice that the mean uncertainties when using 20 Hz CS2 observations are almost half of the mean uncertainties when using 1 Hz CS2 sea-level anomalies. The NKG uplift model has a coastal average of 2.8 mm/year over all 20 tide gauges. $VLM_{1HzPSMSL}$ shows a coastal average of 4.4 mm/year and VLM_{1HzNMA} of 2.4 mm/year. VLM rates based on 20 Hz CS2 data show coastal averages of 5.5 mm/year ($VLM_{20HzPSMSL}$) and 3.4 mm/year ($VLM_{20HzNMA}$). We used the Welch's unequal variances *t* test [29] (two-tailed, with $\alpha = 0.05$) to check whether the coastal averages of estimated VLM rates are significantly different from the coastal average of the NKG uplift model rates. The average rates of our four VLM solutions along the Norwegian coast were not significantly different from the coastal average of the NKG uplift model at the 95% level. Though the coastal averages of VLM rates calculated with PSMSL data ($VLM_{1HzPSMSL}$ and $VLM_{20HzPSMSL}$) differ more from the coastal average of the NKG uplift model, they were not significantly different. This is most likely due to the high spread of the PSMSL-based VLM rates, and the fact that two most different estimates may pass the Welch's unequal variances *t* test if one of the two data sets has a large variance. The mean Spearman's rank correlation coefficient between VLM estimates based on PSMSL data and the NKG uplift model is 0.53 when using 1 Hz CS2 data, and 0.46 when using the 20 Hz CS2 observations (Figure 4a,c). Employing NMA tide-gauge records, the mean correlation between VLM rates and the NKG uplift model over all tide gauges is 0.58 and 0.43 for 1 and 20 Hz CS2 data, respectively (Figure 4b,d). The mean correlations calculated for the Norwegian coast are lower than 0.77 obtained by Pfeffer and Allemand [3] at 113 GPS sites. At the same time, they outperform the results by Nerem and Mitchum [2] (0.35 at 33 nearby GPS and DORIS sites) and Ostanciaux et al. [6] (0.40 at 57 GPS sites).

At Vardø, Harstad, Rørvik, Ålesund, Bergen, and Viker, for at least three out of four VLM solutions, differences to the NKG uplift model are maximum 5 mm/year or less. Although most of those tide gauges are inside fjords and land-confined (except Vardø and Viker), they show a good agreement to the NKG uplift model. At Honningsvåg, Hammerfest, Trondheim, Kristiansund, Måløy, Stavanger, and Tregde, the differences to the NKG uplift model range between 2 and 10 mm/year for three or four VLM solutions. Most of these tide gauges are land-confined, except Kristiansund and Tregde. In turn, high discrepancies between the NKG uplift model and VLM rates from CS2 and tide-gauge data are found at both tide gauges that are land-confined and located to the open ocean. For all four solutions, the largest misfits to the NKG uplift model are observed at Trondheim, Heimsjø, and Oscarsborg, all located deeply inside fjords. Leaving out these tide gauges, the coastal average of the NKG uplift model drops from 2.8 to 2.6 mm/year. Excluding Trondheim, Heimsjø, and Oscarsborg from the comparison reduces the minima and standard deviations of differences for all VLM solutions considerably (see lower part of Table 2). A decrease in the coastal averages of estimated VLM rates is noted as well as reduced uncertainties. Unlike the mean values of differences calculated over all tide gauges, the mean values after excluding Trondheim, Heimsjø, and Oscarsborg are all positive, implying that all VLM solutions have consistently smaller rates than the observations in the NKG uplift model reflect. $VLM_{1HzPSMSL}$ and VLM_{1HzNMA} differ on average 1.4 and 1.5 mm/year from the NKG uplift model, respectively. $VLM_{20HzPSMSL}$ differs on average 0.1 mm/year from the NKG uplift model and $VLM_{20HzNMA}$ 0.3 mm/year. The agreement of mean values between differences of estimated VLM rates and the NKG uplift model is also reflected in the agreement between their coastal averages. VLM rates based on 1 Hz CS2 data show coastal averages of 1.2 mm/year ($VLM_{1HzPSMSL}$) and 1.1 mm/year (VLM_{1HzNMA}), while estimates of VLM based on 20 Hz data have coastal averages of 2.5 mm/year ($VLM_{20HzPSMSL}$) and 2.3 mm/year ($VLM_{20HzNMA}$).

Table 1. Number of available CS2 SARIn observations in CS2 boxes and the overall agreement (mean Spearman's rank correlation coefficient and mean standard deviation) between CS2 and tide-gauge time series at 20 Norwegian tide gauges.

	No. of CS2 Observations			Mean Corr.	Mean Std (cm)	Mean Corr.	Mean Std [cm]
CS2	**Min**	**Max**	**Mean**	**PSMSL**		**NMA**	
1 Hz	24	402	218	0.53	17.55	0.82	11.89
20 Hz	269	6738	3359	0.50	16.70	0.77	12.12

Table 2. Statistics of NKG2016LU_abs signal as well as statistics of differences between NKG2016LU_abs and VLM rates based on CS2 observations and tide-gauge data along the Norwegian coast in mm/year. The upper part of the table shows the statistics over all 20 tide gauges, while the lower part shows the statistics excluding Trondheim, Heimsjø, and Oscarsborg. The last two columns represent the coastal averages and uncertainties (defined in Equation (1) for estimated VLM rates and adopted from Olsson et al. [28] for NKG2016LU_abs) calculated over tide gauges.

	Min	Max	Mean	Std	Coastal Average	Uncertainty
NKG2016LU_abs	1.3	4.7	-	1.1	2.8	0.6
NKG2016LU_abs - ...						
$\mathbf{VLM_{1HzPSMSL}}$	−23.2	16.3	−1.5	11.0	4.4	10.8
$\mathbf{VLM_{1HzNMA}}$	−13.9	8.1	0.4	4.8	2.4	6.2
$\mathbf{VLM_{20HzPSMSL}}$	−23.2	14.5	−2.7	10.0	5.5	6.2
$\mathbf{VLM_{20HzNMA}}$	−10.5	6.5	−0.5	4.1	3.4	3.2
NKG2016LU_abs [a]	1.3	4.3	-	1.0	2.6	0.6
NKG2016LU_abs - ... [a]						
$\mathbf{VLM_{1HzPSMSL}}$	−12.3	16.3	1.4	8.7	1.2	9.5
$\mathbf{VLM_{1HzNMA}}$	−3.9	8.1	1.5	3.5	1.1	5.3
$\mathbf{VLM_{20HzPSMSL}}$	−13.1	14.5	0.1	7.7	2.5	4.4
$\mathbf{VLM_{20HzNMA}}$	−5.5	6.5	0.3	3.4	2.3	2.3

[a] Trondheim, Heimsjø, and Oscarsborg were excluded.

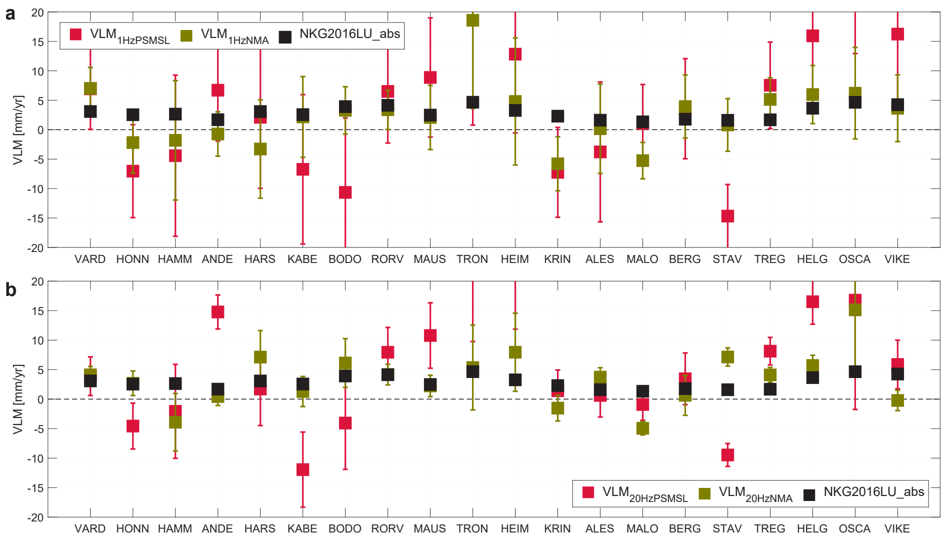

Figure 3. Rates of VLM at 20 Norwegian tide gauges. Black squares represent rates from NKG2016LU_abs, while red and green squares represent VLM calculated from tide-gauge data provided by PSMSL and NMA, respectively, and CS2 sea-level anomalies. (**a**) VLM rates based on 1 Hz CS2 time series. (**b**) VLM rates based on 20 Hz CS2 time series. The size of squares corresponds to 2 mm/year. The error bars indicate the associated uncertainties σ calculated by Equation (1), taking into account serial correlations in the measurements. The uncertainty of VLM rates from NKG2016LU_abs is 0.6 mm/year [28].

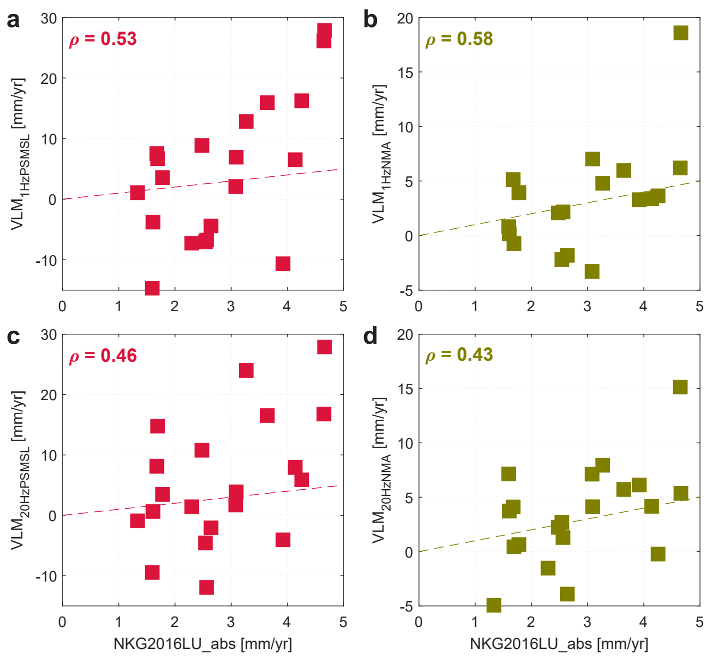

Figure 4. Comparison of estimated VLM rates with rates from NKG2016LU_abs. Spearman's rank correlation coefficient ρ is shown, which was computed over all 20 tide gauges.

4. Summary and Discussion

We have assessed VLM at 20 tide gauges along the Norwegian coast by computing linear trends of differences between CS2 and tide-gauge time series for the period 2010–2018. Two tide-gauge data sets have been used: (i) monthly sea-level observations from PSMSL and (ii) 10-min sea-level measurements obtained from NMA. The agreement between the CS2 and tide-gauge time series is given in Table 1. The resulting VLM rates with associated uncertainties are shown in Figure 3 and Supplementary Materials Table S1, while the statistics of the comparison with the NKG uplift model is given in Table 2 and Figure 4.

The 1 Hz CS2 data agree better with the tide-gauge time series than the 20 Hz data in terms of mean correlations. The agreement between the 20 Hz CS2 data and tide-gauge data from NMA (mean standard deviation of 12.1 cm and mean correlation of 0.77) represents encouraging improvements compared to the results in Idžanović et al. [22]. For the same 20 tide gauges, they obtained a mean standard deviation of 14.7 cm and a mean correlation of 0.64 using standard CS2 corrections and the simple threshold retracker. Our results demonstrate that the SAMOSA 2 retracker has improved the coastal performance compared to the empirical retracker. Furthermore, the tide-gauge data with 10-min sampling interval agree significantly better with CS2 measurements than the monthly PSMSL time series. The smaller correlation and higher standard deviation between CS2 and the PSMSL time series (see Table 1) can be explained by most different sampling rates. The 1 or 20 Hz sampling frequencies of CS2 imply that the altimetry observations include ocean signals, which are averaged to nearly zero in the monthly tide-gauge data. Consequently, differential ocean signals may be introduced in the series of differences between CS2 and the monthly tide-gauge data. This, in turn, may lead to less accurate VLM estimates and a possibly poorer fit to the NKG uplift model.

Our results are encouraging and suggest that CS2 in combination with the high-frequency NMA tide-gauge data can reflect the coastal average of VLM over 20 tide gauges along the Norwegian coast. At Honningsvåg, Kabelvåg, Rørvik, Mausund, and Viker, are differences between VLM rates based on NMA data and the NKG uplift model within the uncertainty of the land-uplift model. In addition, the agreement between the NKG uplift model and NMA-based VLM solutions indicates that there are no systematic errors in the Norwegian national sea-level observing system. Furthermore, the results obtained along the coast demonstrate that altimetry in combination with tide-gauge data can be used to determine VLM at tide gauges where there are no nearby GPS receivers nor rates available from a VLM model.

In general, the spread of rates from CS2 and tide gauges is larger than that of the NKG uplift model. This is especially notable for the PSMSL-based VLM rates, where the combination of CS2 with PSMSL tide-gauge records does not observe the VLM at some tide gauges. However, the NMA-based VLM solutions show a much smaller spread of differences to the NKG uplift model and a high spatial correlation. The comparison between estimated VLM rates and the NKG uplift model indicates that largest differences occur at tide gauges with an insufficient number of CS2 observations, i.e., at Trondheim, Heimsjø, and Oscarsborg. Excluding those tide gauges, the NKG uplift model shows a coastal average of 2.6 mm/year. Omitting Trondheim, Heimsjø, and Oscarsborg from the comparison, the standard deviations of differences decrease along with a significant drop in the mean uncertainties. In addition, eliminating Trondheim, Heimsjø, and Oscarsborg, the largest improvement is found for the PSMSL-based VLM solutions. Combining 1 and 20 Hz data with tide-gauge data provided by NMA gives coastal averages of 1.1 and 2.3 mm/year, respectively. VLM rates calculated combining tide-gauge measurements from PSMSL with 1 and 20 Hz CS2 data show coastal averages of 1.2 and 2.5 mm/year, respectively. In case of omitting the problematic tide gauges, we note a stronger dependence of VLM estimates to the CS2 sampling, and a better fit of VLM rates based on 20 Hz data to the NKG uplift model.

Different OT corrections applied to CS2 (FES2004) and tide-gauge measurements (OT corrections provided by NMA) are possible reasons for the misfit between the NKG uplift model and calculated VLM rates at some tide gauges. Particularly at Hammerfest, Trondheim, Heimsjø, and Kristiansund, discrepancies between signal standard deviations of FES2004 and local OT corrections within CS2 boxes are ranging from 6.7 to 28.5 cm. At these stations, we also find the largest differences to the NKG uplift model. In addition, the CS2 sea-surface observations come from multiple tracks within the CS2 boxes. Potential MSS errors will appear as SLA offsets between individual tracks, possibly introducing SLA errors [30] and, in turn, affecting the VLM estimation. Especially at the coast, it becomes a problem where no observations are available, and the MSS is simply extrapolated. In general, the observed discrepancies between altimetric sea-level anomalies and tide-gauge sea level, and in turn the large spread of estimated VLM rates not seen in the NKG uplift model, might be due to an insufficient number of CS2 observations within CS2 boxes, instrument noise and complex ocean [22] or other coastal processes (e.g., local subsidence not represented by the NKG uplift model).

The estimated errors of VLM rates are strongly dependent on the number of CS2 observations available in each CS2 box. Consequently, mean uncertainty estimates based on 20 Hz data (6.2 mm/year for $VLM_{20HzPSMSL}$ and 3.2 mm/year for $VLM_{20HzNMA}$) are much smaller than those based on 1 Hz data (10.8 mm/year for $VLM_{1HzPSMSL}$ and 6.2 mm/year for VLM_{1HzNMA}). Extension of the CS2 data span would improve the accuracy of the estimated VLM rates [5]. A next step in the VLM estimation from CS2 and tide gauges could be a link of relative VLM between tide gauges, as presented in Kuo et al. [1], using additional conditions and taking advantage of long-term tide-gauge records available in Fennoscandia. In addition, replacing the standard CS2 OT correction with a local one, as demonstrated in Idžanović et al. [22], could possibly lead to a better agreement of estimated VLM rates with the NKG uplift model. Especially at tide gauges, where discrepancies between standard and local OT corrections are large. Furthermore, expanding the estimation of VLM rates using CS2 and tide-gauge measurements to the Baltic Sea region will be considered in the future, where the VLM signal reaches values up to $\sim$10 mm/year.

Supplementary Materials: The following is available online at http://www.mdpi.com/2072-4292/11/7/744/s1, Table S1: Location of 20 tide gauges along the Norwegian coast as well as estimated linear VLM rates and corresponding uncertainties at tide gauges in mm/year.

Author Contributions: Conceptualization, M.I.; Methodology, M.I.; Software, M.I.; Validation, M.I.; Formal Analysis, M.I., C.G., K.B., and O.B.A.; Investigation, M.I.; Resources, M.I., C.G., K.B., and O.B.A.; Data Curation, M.I.; Writing—Original Draft Preparation, M.I.; Writing—Review & Editing, C.G., K.B., and O.B.A.; Visualization, M.I.; Supervision, C.G., K.B., and O.B.A.; Project Administration, C.G. and K.B.; Funding Acquisition, C.G., K.B., and O.B.A.

Funding: This work is part of the Norwegian University of Life Sciences' GOCODYN project, supported by the Norwegian Research Council under project number 231017.

Acknowledgments: We acknowledge the open data policy of ESA and PSMSL. Maps were drafted using Generic Mapping Tools. The manuscript was considerably improved through constructive comments from two anonymous reviewers, which are gratefully acknowledged.

Conflicts of Interest: The authors declare no conflict of interest.

References

1. Kuo, C.Y.; Shum, C.K.; Braun, A.; Mitrovica, J.X. Vertical crustal motion determined by satellite altimetry and tide gauge data in Fennoscandia. *Geophys. Res. Lett.* **2004**, *31*, L01608. [CrossRef]
2. Nerem, R.S.; Mitchum, G.T. Estimates of vertical crustal motion derived from differences of TOPEX/POSEIDON and tide gauge sea level measurements. *Geophys. Res. Lett.* **2002**, *29*, 40-1–40-4. [CrossRef]
3. Pfeffer, J.; Allemand, P. The key role of vertical land motions in coastal sea level variations: A global synthesis of multisatellite altimetry, tide gauge data and GPS measurements. *Earth Planet. Sci. Lett.* **2016**, *439*, 39–47. [CrossRef]
4. Fenoglio-Marc, L.; Dietz, C.; Groten, E. Vertical Land Motion in the Mediterranean Sea from Altimetry and Tide Gauge Stations. *Mar. Geod.* **2004**, *27*, 683–701. [CrossRef]
5. Kuo, C.-Y.; Shum, C.K.; Braun, A.; Cheng, K.-C.; Yuchan, Y. Vertical Motion Determined Using Satellite Altimetry and Tide Gauges. *Terr. Atmos. Ocean. Sci.* **2008**, *19*, 21–35. [CrossRef]

6. Ostanciaux, É.; Husson, L.; Choblet, G.; Robin, C.; Pedoja, K. Present-day trends of vertical ground motion along the coast lines. *Earth-Sci. Rev.* **2012**, *110*, 74–92. [CrossRef]
7. Breili, K.; Simpson, M.J.R.; Nilsen, J.E.Ø. Observed Sea-level Changes along the Norwegian Coast. *J. Mar. Sci. Eng.* **2017**, *5*, 29. [CrossRef]
8. Wingham, D.J.; Francis, C.R.; Baker, S.; Bouzinac, C.; Brockley, D.; Cullen, R.; de Chateau-Thierry, P.; Laxon, S.W.; Mallow, U.; Mavrocordatos, C.; et al. CryoSat: A mission to determine the fluctuations in Earth's land and marine ice fields. *Adv. Space Res.* **2006**, *37*, 841–871. [CrossRef]
9. Idžanović, M.; Ophaug, V.; Andersen, O.B. The coastal mean dynamic topography in Norway observed by CryoSat-2 and GOCE. *Geophys. Res. Lett.* **2017**, *44*, 5609–5617. [CrossRef]
10. Ophaug, V.; Breili, K.; Gerlach, C. A comparative assessment of coastal mean dynamic topography in Norway by geodetic and ocean approaches. *JGR Oceans* **2015**, *120*, 7807–7826. [CrossRef]
11. Vestøl, O.; Ågren, J.; Steffen, H.; Kierulf, H.; Lidberg, M.; Oja, T.; Rüdja, A.; Kall, T.; Saaranen, V.; Engsager, K.; et al. NKG2016LU, an improved postglacial land uplift model over the Nordic-Baltic region. In Proceedings of the NKG Joint WG Workshop on Postglacial Land Uplift Modelling, Gävle, Sweden, 1–2 December 2016.
12. European Space Agency. Geographical Mode Mask. 2018. Available online: https://earth.esa.int/web/guest/-/geographical-mode-mask-7107 (accessed on 25 January 2018).
13. Benveniste, J.; Ambrózio, A.; Restano, M.; Dinardo, S. SAR processing on demand service for CryoSat-2 and Sentinel-3 at ESA G-POD. In *Geophysical Research Abstracts, EGU2016-13084, 2016 EGU General Assembly, Vienna, Austria, 17–22 April 2016*; EGU: Göttingen, Germany, 2016; Volume 18.
14. Ray, C.; Martin-Puig, C.; Clarizia, M.P.; Ruffini, G.; Dinardo, S.; Gommenginger, C.; Benveniste, J. SAR altimeter backscattered waveform model. *IEEE Trans. Geosci. Remote Sens.* **2016**, *53*, 911–919. [CrossRef]
15. Armitage, T.W.K.; Davidson, M.W.J. Using the interferometric capabilities of the ESA CryoSat-2 mission to improve the accuracy of sea ice freeboard retrievals. *IEEE Trans. Geosci. Remote Sens.* **2014**, *52*, 529–536. [CrossRef]
16. Abulaitijiang, A.; Andersen, O.B.; Stenseng, L. Coastal sea level from inland CryoSat-2 interferometric SAR altimetry. *Geophys. Res. Lett.* **2015**, *42*, 1841–1847. [CrossRef]
17. Andersen, O.B.; Stenseng, L.; Piccioni, G.; Knudesn, P. The DTU15 MSS (Mean Sea Surface) and DTU15LAT (Lowest Astronomical Tide) reference surface. In Proceedings of the ESA Living Planet Symposium 2016, Prague, Czech Republic, 9–13 May 2016.
18. Komjathy, A.; Born, G.H. GPS-based ionospheric corrections for single frequency radar altimetry. *J. Atmos. Sol.-Terr. Phys.* **1999**, *61*, 1197–1203. [CrossRef]
19. Lyard, F.; Lefevre, F.; Letellier, T.; Francis, O. Modelling the global ocean tides: Modern insights from FES2004. *Ocean Dyn.* **2006**, *56*, 394–415. [CrossRef]
20. Carrère, L.; Lyard, F. Modeling the barotropic response of the global ocean to atmospheric wind and pressure forcing—Comparisons with observations. *Geophys. Res. Lett.* **2003**, *30*, 1275. [CrossRef]
21. Dee, D.P.; Uppala, S.M.; Simmons, A.J.; Berrisford, P.; Poli, P.; Kobayashi, S.; Andrae, U.; Balmaseda, M.A.; Balsamo, G.; Bauer, P.; et al. The ERA-Interim reanalysis: Configuration and performance of the data assimilation system. *Q. J. R. Meteorol. Soc.* **2011**, *137*, 553–597. [CrossRef]
22. Idžanović, M.; Ophaug, V.; Andersen, O.B. Coastal sea level from CryoSat-2 SARIn altimetry in Norway. *Adv. Space Res.* **2018**, *62*, 1344–1357. [CrossRef]
23. Koch, K.-R. *Parameter Estimation and Hypothesis Testing in Linear Models*; Springer: Berlin, Germany, 1999; pp. 271–309.
24. Holgate, S.J.; Matthews, A.; Woodworth, P.L.; Rickards, L.J.; Tamisiea, M.E.; Bradshaw, E.; Foden, P.R.; Gordon, K.M.; Jevrejeva, S.; Pugh, J. New data systems and products at the Permanent Service for Mean Sea Level. *J. Coast. Res.* **2013**, *29*, 493–504. [CrossRef]
25. Wilks, D.S. *Statistical Methods in the Atmospheric Sciences*; International Geophysics Series; Academic Press: San Diego, CA, USA, 2006; Volume 59, pp. 131–177.
26. Kierulf, H.P.; Steffen, H.; Simpson, M.J.R.; Lidberg, M.; Wu, P.; Wang, H. A GPS velocity field for Fennoscandia and a consistent comparison to glacial isostatic adjustment models. *JGR Solid Earth* **2014**, *119*, 6613–6629. [CrossRef]
27. Kaufman, G. *Program Package ICEAGE*, version 2004; Manuscript; Institut für Geophysik, Universität Göttingen: Göttingen, Germany, 2004; 40p.

28. Olsson, P.-A.; Breili, K.; Ophaug, V.; Steffen, H.; Bilker-Koivula, M.; Nilsen, E.; Oja, T.; Timmen, L. Postglacial gravity change in Fennoscandia—Three decades of repeated absolute gravity observations. *Geophys. J. Int.* **2019**, *217*, 1141–1156. [CrossRef]
29. Welch, B.L. The generalization of "Student's" problem when several different population variances are involved. *Biometrika* **1947**, *34*, 28–35. [CrossRef] [PubMed]
30. Calafat, F.M.; Cipollini, P.; Bouffard, J.; Snaith, H.; Féménias, P. Evaluation of new CryoSat-2 products over the ocean. *Remote Sens. Environ.* **2017**, *191*, 131–144. [CrossRef]

ISBN: 978-82-575-1641-3
ISSN: 1894-6402

Norwegian University
of Life Sciences

Postboks 5003
NO-1432 Ås, Norway
+47 67 23 00 00
www.nmbu.no

105181 / ANDVORDGRAFISK.NO